

## **Turbulent flow through a ribbed pipe**

### **An experimental study**

Schenker, M.C.

**DOI**

[10.4233/uuid:50a1ca63-83c5-4603-9680-a11277f828a6](https://doi.org/10.4233/uuid:50a1ca63-83c5-4603-9680-a11277f828a6)

**Publication date**

2022

**Document Version**

Final published version

**Citation (APA)**

Schenker, M. C. (2022). *Turbulent flow through a ribbed pipe: An experimental study*. [Dissertation (TU Delft), Delft University of Technology]. <https://doi.org/10.4233/uuid:50a1ca63-83c5-4603-9680-a11277f828a6>

**Important note**

To cite this publication, please use the final published version (if applicable). Please check the document version above.

**Copyright**

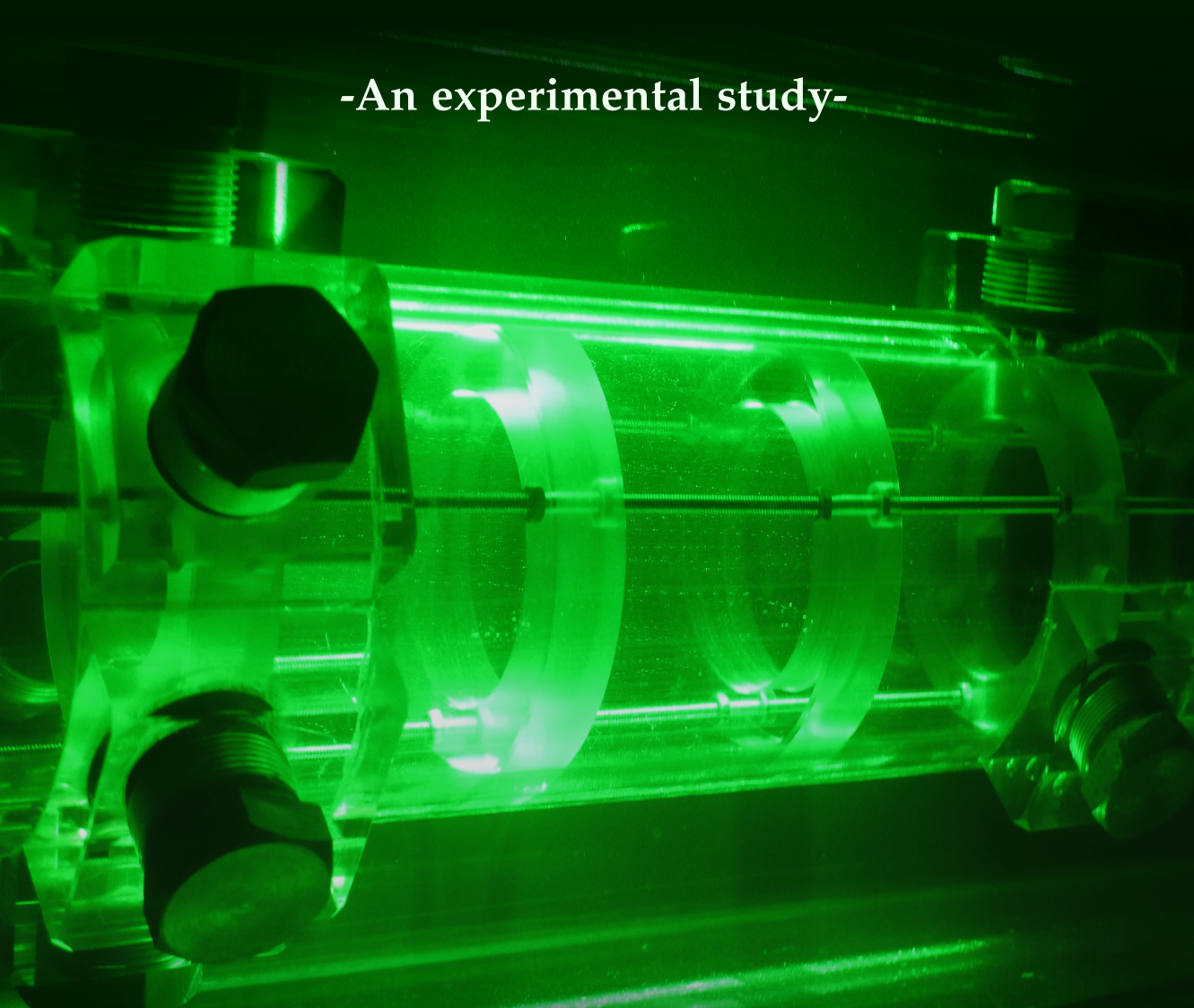
Other than for strictly personal use, it is not permitted to download, forward or distribute the text or part of it, without the consent of the author(s) and/or copyright holder(s), unless the work is under an open content license such as Creative Commons.

**Takedown policy**

Please contact us and provide details if you believe this document breaches copyrights. We will remove access to the work immediately and investigate your claim.

# Turbulent flow through a ribbed pipe

-An experimental study-



Marieke Carolien Schenker- van Rossum



# **Turbulent flow through a ribbed pipe**

**-An experimental study-**

PROEFSCHRIFT

ter verkrijging van de graad van doctor  
aan de Technische Universiteit Delft,  
op gezag van de Rector Magnificus prof.dr.ir. T.H.J.J. van der Hagen,  
voorzitter van het College voor Promoties,  
in het openbaar te verdedigen op  
maandag 19 september 2022 om 15 uur

door

**Marieke Carolien SCHENKER - van ROSSUM**

Ingenieur Werktuigbouwkunde, Technische Universiteit Delft, Nederland  
geboren te Rotterdam, Nederland.

Dit proefschrift is goedgekeurd door de promotor:  
Prof. dr. ir. J. Westerweel

Samenstelling promotiecommissie:

Rector Magnificus,	voorzitter
Prof. dr. ir. J. Westerweel,	Technische Universiteit Delft, promotor
Dr. R. Delfos,	Technische Universiteit Delft, co-promotor
Prof. dr. ir. R.A.W.M. Henkes	Technische Universiteit Delft
Prof. dr. ir. W.S.J. Uijttewaal	Technische Universiteit Delft
Prof. dr. ir. C.H. Venner	University of Twente
Prof. dr. ir. D.M.J. Smeulders	Technische Universiteit Eindhoven
Dr. ir. A. Twerda	TNO
Prof. dr. ir. B.J. Boersma	Technische Universiteit Delft, reservelid

The work presented in this thesis was part of the FLUVAWINT project. A cooperation between TNO, the TU Delft, Bluewater B.V and Gutteling Hoses B.V.

Copyright © 2022 by M.C.Schenker- van Rossum  
All rights reserved.  
ISBN 978-94-6419-562-0

Printed by Gildeprint, Enschede

# Contents

<b>List of Figures</b>	<b>iv</b>
<b>List of Tables</b>	<b>xiii</b>
<b>Summary</b>	<b>xvii</b>
<b>Samenvatting</b>	<b>xix</b>
<b>Nomenclature</b>	<b>xxi</b>
<b>1 Introduction</b>	<b>1</b>
1.1 The challenge: transport of liquefied natural gas . . . . .	1
1.2 Turbulent wall-bounded flow . . . . .	3
1.3 Wall roughness . . . . .	6
1.4 Parameters describing flows over rough walls . . . . .	8
1.5 Beyond wall roughness . . . . .	14
1.6 Cavitation & impact . . . . .	18
1.7 Current research . . . . .	20
<b>2 Static and dynamic pressure measurements</b>	<b>21</b>
2.1 Experimental set-up and design . . . . .	21
2.2 Configurations and measurements . . . . .	26
2.3 Convergence, uncertainties and corrections . . . . .	27
2.4 Static measurements: pressure losses, friction factors and geometric scaling . . . . .	30
2.5 Orifice losses or flow over a single rib . . . . .	42
2.6 Cavitation impact . . . . .	46
2.7 Dynamic pressure . . . . .	47

<b>3</b>	<b>Two-dimensional flow field measurements</b>	<b>53</b>
3.1	Set-up and experimental parameters . . . . .	53
3.2	Image pre-processing . . . . .	61
3.3	Image correlation with boundaries . . . . .	63
3.4	Vector validation . . . . .	63
<b>4</b>	<b>PIV: time-averaged patterns and profiles</b>	<b>69</b>
4.1	Mean velocity fields for ribbed sections . . . . .	69
4.2	Shear stresses of the mean flow . . . . .	73
4.3	Cavity flow pattern evaluation . . . . .	80
4.4	Flow axisymmetry . . . . .	85
4.5	Mean flow for orifice flows . . . . .	93
4.6	Local mean profiles . . . . .	100
4.7	Axial spatial averaging . . . . .	109
4.8	Summary of results and preliminary conclusions . . . . .	125
<b>5</b>	<b>PIV: temporal fluctuations</b>	<b>129</b>
5.1	Statistical analysis of the flow dynamics: joint probability density functions . . . . .	129
5.2	Quadrant analysis . . . . .	137
5.3	Dynamic flow behaviour . . . . .	144
5.4	Coherent structures . . . . .	146
<b>6</b>	<b>Conclusions</b>	<b>159</b>
6.1	Outlook . . . . .	163
<b>A</b>	<b>Pressure tap location</b>	<b>165</b>
<b>B</b>	<b>Overheating correction</b>	<b>171</b>
<b>C</b>	<b>Line fit method to the dynamic pressure spectrum</b>	<b>173</b>
	<b>Bibliography</b>	<b>173</b>

# List of Figures

1.1	Schematic cut-through structure of bellow-type (left) and composite-type (right) corrugated hoses. The dash-dotted line indicates the pipe axis. . . . .	2
1.2	Outer structure (a) and inner shape (b) of composite corrugated hoses. . . . .	3
1.3	Velocity profile in a turbulent boundary layer, scaled with inner-layer variables. Image from Kundu et al. (2012). . . . .	5
1.4	Visualization by a passive scalar of the instantaneous flow patterns and mean flow streamlines of (from top to bottom) d-type, intermediate and k-type ribbed surfaces. Adopted from Leonardi et al. (2007). . . . .	13
1.5	Typical spectrum of pressure fluctuations, adopted from Rockwell (1977). . . . .	17
2.1	Schematic overview of the flow loop. A: optional connection to vacuum pump, B: (low-pressure) reservoir, C: de-aeration section, D: measurement section, E: static differential pressure sensor, F: dynamic pressure taps, G: inflow length, H: centrifugal pump, I: flow meter, J: diffuser. . . . .	22
2.2	Rib configuration and attachment to the pipe. . . . .	23
2.3	The three types of ribs used in the measurement section, with their cross-sectional shape indicated schematically (on scale). EL & RL geometries: $9.5 \times 7.5$ mm ( $\varnothing_{in} = 35$ mm), RS: $9.5 \times 11.25$ mm ( $\varnothing_{in} = 27.5$ mm). . . . .	24
2.4	Dynamic pressure sensors mounted on the pipe wall. . . . .	25
2.5	Schematic of flow redevelopment downstream of the ribs. The arrow below the pipe indicates the redevelopment length. . . . .	29
2.6	Dimensionless loss factor $K_r$ vs $Re_r$ in sections of 8 ribs of type EL with various pitches. . . . .	31
2.7	Dimensionless loss factor $K_r$ vs $Re_r$ in sections of 8 ribs of type RL with various pitches. . . . .	31
2.8	Example of the fitting procedure used to determine the flow loss per rib for developed flow behaviour. $p = 25$ mm, $Re_r = 2.8 \cdot 10^5$ , rib type EL . . . . .	32

2.9	Darcy-Weissbach friction factor $f_D$ for ribs of the EL type. The error bars are indicative and for clarity only depicted every 7th datapoint. The grey dotted lines are the Colebrook friction correlations for several values of the equivalent relative sand-grain roughness. The values in the legend indicate the pitch of the geometry. . . . .	33
2.10	Darcy-Weissbach friction factor $f_D$ for ribs of the RL type. The error bars are indicative and for clarity only depicted every 7th datapoint. The gray dotted lines are the Colebrook friction correlations for several values of the equivalent relative sand-grain roughness. The values in the legend indicate the pitch of the geometry. . . . .	34
2.11	Friction factor $f_{D,r}$ as calculated based on the inner rib diameter for rectangular ribs (type EL). . . . .	35
2.12	Two approaches to describe the roughness of a smooth pipe containing ribs. . . . .	35
2.13	Plateau values of $K_r'$ (a) and $f_D$ (b) as obtained from their plots versus $Re$ , as a function of pitch for rectangular ribs (EL geometry). Note that this graph includes data for $p = 12,5$ mm; the corresponding curve is, for clarity, omitted in Figs 2.9 and 2.11. . . . .	38
2.14	Maximum values of $K_r$ (a) and $f_D$ (b) as a function of pitch for the RL geometry. . . . .	38
2.15	Maximum values of $K_r$ (a) and $f_D$ (b) as a function of pitch for the RS geometry. . . . .	39
2.16	Rib geometries used for single-rib experiments. All ribs have a maximum width of 9.5 mm. The flow direction with respect to the ribs is indicated by the grey arrow in the upper right drawing. . . . .	42
2.17	Single-rib losses for various rib shapes. Labels A-F refer to the shapes shown in Fig. 2.16. All ribs have a 35-mm inner diameter. Dot-dashed and dashed lines indicate the losses for thin and thick orifices according to Eqs (1.20) and (1.21), respectively. . . . .	43
2.18	Dimensionless loss factor $K_r$ versus Reynolds number (a) and cavitation number (b). The ribbed segment is of the EL type with 5 ribs for all presented data. For clarity some intermediate curves were omitted from (b). The absolute pressures as displayed in the legend of (a) are measured in the de-aeration segment as indicated in Fig. 2.1. . . . .	46
2.19	Fluctuation strength $\sigma$ of the dynamic pressure. Blue and red symbols indicate two different sensors, located at the wall in successive cavities. Their positions relative to the ribs vary with pitch. . . . .	48
2.20	Contours of the normalized power spectrum of the dynamic pressure as a function of $V_r$ . . . . .	49
2.21	Strouhal number ( $Sr = \frac{f_p}{V_r}$ ) as a function of pitch $p$ . . . . .	50

3.1	Optical box in position. A test-section of three ribs is placed inside the pipe, using bolted attachments that are located within the optical box. The box is not fully filled with water in this image, resulting in a thin layer of air between water and upper wall of the box. . . . .	54
3.2	Principles of a conventional lens and a telecentric lens. . . . .	56
3.3	Typical images produced by a conventional lens and a telecentric lens. . .	57
3.4	Image calibration to enable PIV measurements. . . . .	61
4.1	Mean axial (a) and wall-normal (b) velocity for rectangular ribs (EL geometry), $p = 20$ mm, $Re_r = 1.6 \times 10^5$ . Dimensions in metres, direction of the flow from left to right. . . . .	70
4.2	Mean axial (a) and radial (b) velocity for rectangular ribs (EL geometry), $p = 30$ mm, $Re_r = 1.6 \times 10^5$ . Dimensions are in metres, direction of the flow from left to right. Note: the "wiggle" in the lower right-hand corner of the images is identified as an artefact of the measurement and not further discussed. . . . .	71
4.3	Mean axial (a) and radial (b) velocity for rectangular ribs (EL geometry), $p = 40$ mm, $Re_r = 1.6 \times 10^5$ . Dimensions in metres, direction of the flow from left to right. . . . .	71
4.4	Axial velocities in RL (left) and EL (right) geometries for different Reynolds numbers and $p = 25$ mm. Dimensions in metres, flow direction from left to right. The region downstream of the second rib suffers from measurement artefacts. . . . .	72
4.5	Axial velocities in RL (left) and EL (right) geometries for different Reynolds numbers and $p = 40$ mm. Dimensions in metres, flow direction from left to right. The region downstream of the second rib suffers from measurement artefacts. . . . .	73
4.6	Mean horizontal shear $\frac{\partial U}{\partial y}$ for $Re_r = 1.6 \times 10^5$ and different rib geometries and pitches 20 - 30 mm. Dimensions in metres, flow direction from left to right. . . . .	74
4.7	Mean horizontal shear $\frac{\partial U}{\partial y}$ for $Re_r = 1.6 \times 10^5$ and different rib geometries and pitches 35- 45 mm. Dimensions in metres, flow direction from left to right. . . . .	75
4.8	Reynolds stress $-\rho \overline{u'v'}$ for $Re_r = 1.6 \times 10^5$ and different geometries and pitches 20 - 30 mm. Dimensions in metres, flow direction from left to right. 76	76
4.9	Reynolds stress $-\rho \overline{u'v'}$ for $Re_r = 1.6 \times 10^5$ and different geometries and pitches 35-45 mm. Dimensions in metres, flow direction from left to right. 77	77
4.10	Mean-flow $Q$ criterion for $Re_r = 1.6 \times 10^5$ for EL and RL, with $p = 20$ mm, superimposed with streamlines of the mean flow. Dimensions in metres, flow direction from left to right. . . . .	78

4.11	Mean-flow $Q$ criterion for $Re_r = 1.6 \times 10^5$ for EL and RL, with $p = 30$ and 40 mm, superimposed with streamlines of the mean flow. Dimensions in metres, flow direction from left to right. . . . .	79
4.12	Mean flow streamlines for the EL geometry at $Re_r = 1.6 \times 10^5$ , $p = 20$ -35 mm. Similar to all contour plots, the dimensions are in metres and the flow direction is from left to right. . . . .	81
4.13	Mean flow streamlines for the EL geometry at $Re_r = 1.6 \times 10^5$ , $p = 40$ -45 mm. Similar to all contour plots, the dimensions are in metres and the flow direction is from left to right. . . . .	82
4.14	Mean flow streamlines for the RL geometry with $p = 25$ mm (left panels) and 35 mm (right panels). Dimensions in metres and flow direction from left to right . . . . .	83
4.15	Mean flow streamlines for the RL geometry with $p = 45$ mm. Dimensions in metres and flow direction from left to right . . . . .	84
4.16	Mean flow streamlines superimposed on the mean radial velocity for a single cavity. $Re_r = 1.6 \times 10^5$ , $p = 25 - 30$ mm, dimensions in metres and flow from left to right. . . . .	85
4.17	Mean flow streamlines superimposed on the mean radial velocity for a single cavity. $Re_r = 1.6 \times 10^5$ , $p = 35 - 40$ mm, dimensions in metres and flow from left to right. Color scale according to Fig. 4.16 . . . . .	86
4.18	Azimuthal velocity gradient $\frac{1}{r} \frac{\partial V}{\partial \theta}$ for $p = 25 - 35$ mm. the EL geometry. $Re_r = 1.6 \times 10^5$ , dimensions in metres, flow from left to right. Color scale according to Fig. 4.19 . . . . .	87
4.19	Azimuthal velocity gradient $\frac{1}{r} \frac{\partial V}{\partial \theta}$ for $p = 40 - 45$ mm. the EL geometry. $Re_r = 1.6 \times 10^5$ , dimensions in metres, flow from left to right. . . . .	88
4.20	Schematic azimuthal triple symmetry for the configuration used in most measurements, with the observer on the left hand side of the image, the brown dots denoting the rib-connecting rods and the red line indicating the image plane. . . . .	89
4.21	Azimuthal flow direction and direction of acceleration/deceleration as assumed based on the geometry and azimuthal gradient magnitude. The green arrow is the overall flow direction. . . . .	90
4.22	Instantaneous, smoothed and mean volume flux. The flux is directed outward in azimuthal direction and inward in radial direction with respect to the control volume in the cavity. The smooth line is obtained by a moving average with a span of 0.01 s. . . . .	91
4.23	Mean radial outflow velocity normalized with the bulk velocity $V_b$ as a function of pitch. $Re = 1.6 \times 10^5$ . . . . .	92

4.24	Mean axial velocity for all single-orifice geometries. Rib geometries are shown in black and referred to according to Table 2.5. $Re_r = 1.6 \times 10^5$ , flow direction from left to right. . . . .	94
4.25	Mean Reynolds stress for all single-orifice geometries. Rib geometries are shown in black and referred to according to Table 2.5. $Re_r = 1.6 \times 10^5$ , flow direction from left to right. . . . .	95
4.26	Streamlines for all single-orifice geometries. Geometries are referred to according to Table 2.5, $Re_r = 1.6 \times 10^5$ and flow direction from left to right. 96	
4.27	Comparison between the axial velocity, mean Reynolds stress and streamline pattern for ribbed section EL (left) and single-orifice geometry E (right). The colour range for the velocity plots is identical to that of Fig. 4.24. $Re = 1.6 \times 10^5$ , dimensions in metres and flow from left to right. . .	98
4.28	Comparison between the axial velocity, mean Reynolds stress and streamline pattern for a RL-type ribbed section and orifice geometry F. The colour range for the velocity is identical to that in Figure 4.24, $Re = 1.6 \times 10^5$ , dimensions in metres and flow from left to right. . . . .	99
4.29	Mean axial (solid lines) and radial (dashed lines) velocity for EL geometries. $Re_r = 1.6 \times 10^5$ , $p = 20$ and 25 mm. Blue: upstream quarter; green: cavity centre; red: downstream quarter. Data for $p = 45$ mm not available up to the centre line (wall-normal positions $> 0,022$ m). . . . .	101
4.30	Mean axial (solid lines) and radial (dashed lines) velocity for EL geometries. $Re_r = 1.6 \times 10^5$ , $p = 35$ and 45 mm. Blue: upstream quarter; green: cavity centre; red: downstream quarter. Data for $p = 45$ mm not available up to the centre line (wall-normal positions $> 0,022$ m). . . . .	101
4.31	Mean axial (solid lines) and radial (dashed lines) velocity for RL geometries. $Re_r = 7.3 \times 10^4$ . Blue: upstream quarter; green: cavity centre; red: downstream quarter. Data for $p = 45$ mm is not available up to the centre line (wall-normal positions $> 0,022$ m). . . . .	102
4.32	Mean axial (solid lines) and radial (dashed lines) velocity for RL geometries. $Re_r = 2.5 \times 10^5$ . Blue: upstream quarter; green: cavity centre; red: downstream quarter. Data for $p = 45$ mm is not available up to the centre line (wall-normal positions $> 0,022$ m). . . . .	102
4.33	Reynolds stress at three axial locations for rectangular ribs (EL geometry) at $Re_r = 1.6 \times 10^5$ . Blue: upstream quarter; green: cavity centre; red: downstream quarter. Data for $p = 45$ mm not available up to the centre line (wall-normal positions $> 0,022$ m). . . . .	104

- 4.34 Reynolds stress at three axial locations for rounded ribs (RL geometry). Left column:  $p = 25$  mm; right column:  $p = 45$  mm. Blue: upstream quarter; green: cavity centre; red: downstream quarter. Data in panels e and f not available up to the centre line. . . . . 105
- 4.35 Axial velocity profile at four axial locations for the six types of orifices studied. The axial positions are chosen to match the 1/4th, 2/4th, 3/4th and 4/4th cavity length for a 45-mm pitch geometry.  $Re_r = 1.6 \cdot 10^5$ . . . . 106
- 4.36 Reynolds stress profile at four axial locations for the six types of orifices studied. The positions match 1/4th, 2/4th, 3/4th and 4/4th cavity length for a 45-mm pitch geometry.  $Re_r = 1.6 \cdot 10^5$ . . . . . 108
- 4.37 Axially spatially averaged axial (red) and wall-normal (blue) velocity for the EL geometry at  $Re_r = 1.6 \times 10^5$ . . . . . 111
- 4.38 Bulk velocity  $V_b$  for all available EL measurements. Comparison between PIV results for the upper ( $\times$ ) and lower ( $\times$ ) halves of the velocity field and the flow meter results ( $\circ$ ). The three horizontal rows of data correspond to  $Re_r = 7.3 \times 10^4$  (bottom),  $1.6 \times 10^5$  (middle) and  $2.5 \times 10^5$  (top). . . . . 112
- 4.39 Spatially averaged Reynolds stress (magenta), dispersive stress (dark-blue) and total stress (light blue) for EL geometries at  $Re_r = 1.6 \times 10^5$ . . . . . 114
- 4.40 Effective mixing lengths  $l_m$  (blue) and  $l_{m,tot}$  (red). The black dash line indicates the rib crest height. The green dashed line represents the fit of Eq. (4.6) to the linear region of the mixing length. The magenta line represents the same fit, but assuming  $\kappa = 0.41$ . . . . . 116
- 4.41 Von Kármán constant  $\kappa$  obtained by fitting Eq. (4.6) for rectangular ribs (EL geometry). Open symbols: upper half of the pipe; crosses: lower part of the pipe. . . . . 117
- 4.42 Displacement height  $d$  obtained by fitting Eq. (4.6) for rectangular ribs (EL geometry). Open symbols: upper half of the pipe; crosses: lower part of the pipe. . . . . 118
- 4.43 The relation  $f(p) = d - A\kappa$ , defined in Eq. (4.8). Open symbols: upper half of the pipe; crosses: lower half of the pipe. . . . . 119
- 4.44 Displacement height  $d$  (a) and von Kármán constant  $\kappa$  (b) as obtained by the two procedures to fit Eq. (4.6): without (blue) and with (green) forcing  $\kappa = 0.41$ . . . . . 119
- 4.45 Spatial average velocity represented in logarithmic form for  $Re_r = 1.6 \times 10^5$  and  $p = 30$  mm. The dotted and dash-dotted black lines indicate the rib crest height of the upper rib cross section and centre line of the pipe, respectively. The red line is a fit to Eq. (4.9). . . . . 121

4.46	Friction factor as a function of pitch for rectangular ribs (EL geometry) as obtained from PIV measurements. Open circles: upper half of the pipe; crosses: lower half of the pipe. Also included are the friction factors derived from the pressure measurements and fitted trend as shown before in Fig. 2.13b. . . . .	122
4.47	Roughness function $\Delta u^+$ as a function of pitch. Open circles: upper half of the pipe; crosses: lower half of the pipe. . . . .	123
4.48	Measured ( $\times$ ) and fitted (+) values of $\Delta u^+$ . Fits obtained by fitting the data to Eq. (4.9) and by using Eq. (4.11) with $B'=0$ and $h=8.1$ mm. Dashed line: fit obtained by Perry et al. (1969) with $B'=-0.4$ . . . . .	124
4.49	Additive constant $F$ compared with the results for two-dimensional ribs from Coleman et al. (2007). The three colours correspond to the three Reynolds numbers investigated (blue = $Re_r = 4.3 \times 10^4$ ; green = $Re_r = 1.6 \times 10^5$ ; red = $Re_r = 2.5 \times 10^5$ ). The black symbols correspond to results from studies for two-dimensional rectangular rib roughness on one side of a channel flow as included in Coleman et al. (2007). They correspond to the following relative rib heights: $\bullet$ : $h/H = 0.09$ (free surface flow); $\square$ and $\triangle$ : $h/H = 0.1$ ; $\circ$ : $h/H = 0.06$ ; solid line: theoretic limit for $h/H = 0$ . . . . .	125
5.1	Example of a jpdf (a) and corresponding Reynolds stress contribution (b). Case: EL geometry, $p = 25$ mm, $Re_r = 1.6 \times 10^5$ . Position: rib-crest height and axial cavity centre. . . . .	130
5.2	Effect of threshold fraction on the jpdf ellipsoid origin (circles) and size (lines). The lines for threshold fractions 0.01 and 0.001 overlap due to the limited resolution of the distribution. The major and minor axes are not shown for clarity. . . . .	131
5.3	Jpdf evolution versus wall-normal position $y$ . Case: EL geometry, $p = 25$ mm, $Re_r = 1.6 \times 10^5$ . Position: axial cavity centre. . . . .	132
5.4	Jpdf evolution versus wall-normal position $y$ . Case: EL geometry, $p = 25$ mm, $Re_r = 1.6 \times 10^5$ . Position: axial cavity centre. Continuation of Fig. 5.3	133
5.5	Ellipse properties versus wall-normal position. Case: EL geometry, $p = 25$ mm, $Re = 1.6 \times 10^5$ . . . . .	134
5.6	Ellipse properties versus wall-normal position. Case: EL geometry, $p = 25$ mm, $Re = 1.6 \times 10^5$ . (Continuation of Fig. 5.5) . . . . .	135
5.7	Jpdf parameters as a function of pitch. Case: rectangular ribs (EL geometry). $Re = 7.3 \times 10^4$ (blue), $1.6 \times 10^5$ (green), $2.5 \times 10^5$ (red). . . . .	137
5.8	Schematic layout of the 4 quadrants Q1-Q4. . . . .	138
5.9	Quadrant analysis at cavity centre for $Re_r = 1.6 \times 10^5$ , EL geometry, $p = 25$ mm. . . . .	140

5.10	Quadrant analysis at cavity centre for $Re_r = 1.6 \times 10^5$ , EL geometry, $p = 40$ mm. . . . .	141
5.11	Fraction of occurrence of Q2 (solid lines) and Q4 (dashed lines) around the rib crest height, displayed for three axial locations: 1/4th, 1/2nd and 3/4th of the cavity. Data for the EL geometry, $p = 40$ mm, $Re = 1.6 \times 10^5$ . . . . .	142
5.12	Sketch of the mechanism of quadrant occurrence in a vortex shed from the cavity edge. . . . .	143
5.13	Vorticity and Q criterion for 2 uncorrelated snapshots. EL geometry, $p = 40$ mm, $Re = 1.6 \times 10^5$ . Dimensions in meters, flow direction from left to right. . . . .	145
5.14	Different representations of a typical snapshot (EL geometry, $p = 40$ mm, $Re = 1.6 \times 10^5$ ). The snapshot is the same as shown in Figs 5.13a and 5.13b. Dimensions in metres, flow direction from left to right. . . . .	147
5.15	Instantaneous snapshot showing a strong Q2 and Q4 event. The colour scales are the same as those in Fig. 5.14. Case: EL geometry, $p = 40$ mm, $Re = 1.6 \times 10^5$ . Dimensions in metres, flow direction from left to right. . . . .	149
5.16	Instantaneous snapshot showing a dominant Q2 event. The colour scales are the same as those in Fig. 5.14. Case: EL geometry, $p = 40$ mm, $Re = 1.6 \times 10^5$ . Dimensions in metres, flow direction from left to right. . . . .	150
5.17	Instantaneous snapshot showing a dominant Q2 event in the core region. The colour scales are the same as those in Fig. 5.14. Case: EL geometry, $p = 40$ mm, $Re = 1.6 \times 10^5$ . Dimensions in metres, flow direction from left to right. . . . .	151
5.18	Example of a vortex train. The colour scales are the same as those in Fig. 5.14. Case: EL geometry, $p = 40$ mm, $Re = 1.6 \times 10^5$ . Dimensions in metres, flow direction from left to right. . . . .	152
5.19	Example of the pdf of the fraction of occurrence of each stress contribution for all four quadrants. EL geometry, $p = 40$ mm, $Re = 1.6 \times 10^5$ . . . . .	154
5.20	Fraction of occurrence of Q2 minus fraction of occurrence of Q4 for 4 wall-normal positions. EL geometry, $p = 40$ mm, $Re = 1.6 \times 10^5$ . . . . .	155
5.21	Contribution of Q2 minus contribution of Q4 organized by event strength for 4 wall-normal positions. EL geometry, $p = 40$ mm, $Re = 1.6 \times 10^5$ . . . . .	156
5.22	Normalized cumulative distribution of the contribution to the Reynolds stresses. EL geometry, $p = 40$ mm, $Re = 1.6 \times 10^5$ . Lighter colours signify increasing wall-normal location, from inside the cavity (black) to the centre of the pipe (yellow). . . . .	157

5.23	Normalized cumulative distribution of the contribution to the Reynolds stresses. EL geometry, $p = 25$ mm, $Re = 1.6 \times 10^5$ . Lighter colours signify increasing wall-normal location, from inside the cavity (black) to the centre of the pipe (yellow). The two innermost points (corresponding to the two darkest lines in Fig. 5.22), located in a strong recirculation region within the cavity, are removed for clarity. . . . .	158
A.1	Pressure recovery downstream of the ribbed pipe segment. CFD-calculation for EL geometry with 7 ribs and $p = 15, 25, 40$ and $45$ mm. $V_b = 2.15$ m/s. . . . .	165
A.2	Total pressure drop $\Delta p$ at a bulk velocity, $V_b = 2.15$ m/s, for EL geometry with 7 ribs . . . . .	166
A.3	Pressure recovery half-distance as a function of rib-pitch . . . . .	167
A.4	Original nondimensional pressure loss $K_r$ vs number of ribs and the same result corrected for the pressure recovery when applicable, for a geometry with 25 mm pitch at $Re_b = 1.65 \times 10^5$ . . . . .	168
B.1	Non-dimensional pressure loss $K_r$ for $p = 45$ mm before and after the overheating incident and subsequent adjustment of the outer rib diameter. . . . .	171
C.1	Example of the line fit method to determine the harmonics in the dynamic pressure spectrum for $p = 22.5$ mm. . . . .	174
C.2	Scalar describing the linear frequency trend ( $p = 22.5$ mm and peak of this function as a function of pitch. . . . .	175



# List of Tables

2.1	Types of ribs within the ribbed pipe segment . . . . .	24
2.2	Numbers of ribs within the ribbed pipe segment. . . . .	26
2.3	Experimental parameters for the pressure measurements. . . . .	27
2.4	Pitch, physical rib height, mean roughness height and equivalent roughness for all rib geometries, calculated based on either the outer ( $R$ ) or inner ( $r$ ) diameter of the ribs. All values are in mm. . . . .	36
2.5	Adjustment factor for the contraction coefficient $c_\sigma$ and empirical constant $\zeta$ needed to match the measured results for single ribs with Eq. (1.21). . . . .	44
3.1	Parameters for PIV experiments . . . . .	59



# Summary

## **Turbulent flow through a ribbed pipe:**

### **An experimental study**

This thesis describes the results of an experimental study of turbulent flow through a ribbed pipe. The ribbed pipe used is a pipe segment of 50 mm inner diameter with ribs inserted at various pitches (15 to 50 mm). Rectangular and rounded ribs are used, with a rib height of 7.5 or 11 mm.

Pressure measurements result in friction factors showing a strong dependency on rib shape and pitch, and for the rounded rib shape also a dependency on Reynolds number. Dynamic pressure measurements show the presence of a frequency that coincides with second harmonic of vortex shedding of the ribs. Measurements with single ribs, rather than ribbed segments, show that the friction behaviour of a ribbed segment cannot be predicted based on a single rib, as the observed friction behaviour scales differently.

With PIV measurements, mean flow patterns, shear strength and Reynolds Stress distributions are obtained, confirming the significant impact of rib pitch and shape on the behaviour of the flow that was indirectly observed during the pressure measurements. For the rectangular shaped ribs, axially averaging the results over one pitch flow length results in flow and stress profiles. These profiles are used as input in the theoretical description of flow over a rough wall. With some adjustment, specifically fitting the Von Kármán constant instead of assuming a value a-priori, the results fit within the theoretical description. The friction factors derived in this way, agrees well with the friction factors based on the pressure measurements up to a pitch of 35 mm.

A statistical analysis of the flow dynamics shows that the large contributions to the stresses are caused by relatively rare but strong fluctuations, which are, depending on the location in the flow, either ejections or sweeps. The observation of these fluctuations and their location in the flow match with the second harmonic vortex shedding that was hypothesised based on the frequencies in the dynamic pressure spectrum.



# Samenvatting

## **Turbulente stroming door een geribbelde buis: Een experimenteel onderzoek**

Dit proefschrift beschrijft de resultaten van een experimenteel onderzoek naar turbulente stroming door een geribbelde buis. De gebruikte geribbelde buis is een segment met een binnendiameter van 50 mm, met daarin ribben geplaatst met een variabele afstand (15 tot 50 mm). Er is gebruik gemaakt van rechthoekige en afgeronde ribben, met een ribhoogte van 7,5 of 11 mm.

Drukmetingen resulteren in wrijvingsfactoren die een sterke afhankelijkheid van ribvorm en onderlinge afstand vertonen, en bij de afgeronde ribben ook een afhankelijkheid van het Reynolds getal. Dynamische drukmetingen tonen de aanwezigheid van een frequentie die samenvalt met die van tweede harmonische frequentie van wervelloslating van de ribben. Metingen met één enkele rib, in plaats van een geribbeld segment, laten zien dat het wrijvingsgedrag van een geribbeld segment niet kan worden voorspeld op basis van meting met één enkele rib, omdat het wrijvingsgedrag anders schaal.

Met PIV metingen zijn gemiddelde stromingsvelden, schuifspannings- en Reynolds spanningsverdelingen verkregen. Deze bevestigen de significante invloed van de vorm en afstand van de ribben op het stromingsgedrag, zoals indirect uit de drukmetingen was waargenomen.

Bij de rechthoekige ribben zijn met het in axiale richting over één ribafstand middelen van de resultaten de stromings- en spanningsprofielen verkregen. Deze profielen zijn gebruikt als input in de theoretische beschrijving van stroming over een ruwe wand. Met enkele aanpassingen, specifiek het fitten van de Von Kármán constante in plaats van het vooraf vastleggen van de waarde daarvan, passen de resultaten goed in het theoretische model. De wrijvingsfactoren die op deze manier zijn afgeleid komen goed overeen met de wrijvingsfactoren gebaseerd op de drukmetingen, tot aan een ribafstand van 35 mm.

Een statistische analyse van de stroming toont aan dat de grote bijdragen aan de spanningen in de stroming worden veroorzaakt door relatief zeldzame maar

sterke fluctuaties. Deze fluctuaties zijn, afhankelijk van de locatie in de stroming, ofwel zogenoemde "ejections" ofwel "sweeps". De observatie van deze fluctuaties en hun positie in de stroming komen overeen met de tweede harmonische frequentie wevelafscheiding die was voorspeld op basis van het spectrum van de dynamische drukfluctuaties.

# Nomenclature

## Symbols

Symbol	Description	Unit
$A$	orifice surface area	$\text{m}^2$
$A_{\text{vena}}$	orifice vena contracta surface area	$\text{m}^2$
$B'$	constant, characteristic of the roughness	-
$C$	constant in the law of the wall	-
$ca$	cavitation number	-
$ca_d$	cavitation number addition due to diffuser	-
$d$	displacement height	m
$D$	pipe diameter	mm
$\epsilon$	$h - d$	m
$\epsilon$	eccentricity	-
$F$	roughness parameter	-
$f_D$	Darcy-Weissbach friction factor	-
$f_{D,r}$	$f_D$ defined using radius $r$ instead of pipe radius $R$	-
$G_r, G_b$	normalization factor for the pressure based on rib and pipe bulk velocity: $\frac{1}{2}\rho V_{r/b}^2$	Pa
$h$	roughness height	m
$H$	relevant large normal geometric scale ( $\delta$ or radius)	m
$\kappa$	Von Kármán constant	-
$K_r, K_b$	total pressure loss normalized with $G_r$ or $G_b$ respectively	-

Symbol	Description	Unit
$K_r^r, K_b^r$	$K_r$ or $K_b$ per rib instead of the total of the ribbed segment	-
$k_s$	equivalent roughness	m
$l$	cavity length ( $l = p - w$ )	m
$L_e$	entrance length	m
$m, n$	two-directions window shift in PIV correlation	pixels
$N$	neighbourhood size for several computational operations	-
$p$	symbol for the pitch	m
$p_v$	vapour pressure	Pa
$\Delta p$	pressure loss over the measured section	Pa
$\Delta p_d$	pressure loss over the diffusor	Pa
$\Pi$	wake function	-
$r$	inner radius of a rib	mm
$R$	pipe radius	mm
$Re_r, Re_b$	Reynolds number, based on $d$ and $V_r$ or on $D$ and $V_b$ , respectively	-
$\rho$	fluid density	kg/m <sup>3</sup>
$s$	window size ( $s \times s$ ) in the PIV procedure	pixels
$\sigma_c$	contraction coefficient	-
$\Delta t$	time difference between two laser pulses	s
$\Delta T$	time difference between two camera frames	s
$u$	local instantaneous axial velocity	m/s
$u_\tau$	friction velocity $\sqrt{\tau_0/\rho}$	m/s
$u_{\tau^*}$	effective friction velocity $u_\tau \sqrt{1 - d/H}$	m/s
$\bar{U}$	local mean axial velocity	m/s
$u'$	instantaneous velocity, relative to local mean $\bar{U}$	m/s
$\bar{u}'$	instantaneous velocity, relative to spatially averaged mean $\bar{U}$	m/s
$\bar{U}$	mean axial velocity spatially averaged in axial direction	m/s
$V_b$	bulk velocity defined using the inner diameter of the pipe	m/s

Symbol	Description	Unit
$V_r$	bulk velocity defined using the inner diameter of the rib	m/s
$v$	local instantaneous wall-normal velocity	m/s
$V$	local mean wall-normal velocity	m/s
$v'$	instantaneous velocity, relative to local mean $V$	m/s
$\bar{v}'$	instantaneous velocity, relative to spatially averaged mean $\bar{V}$	m/s
$\bar{V}$	mean wall-normal velocity spatially averaged in axial direction	m/s
$w$	rib width	m
$y_0$	roughness length	m
$\zeta$	empirical constant (0 to 1) in the Borda-Carnot equation	-

# Chapter 1

## Introduction

Flows through rough-walled pipes constitute a rather broad class of flows. They are used in a wide variety of industrial installations and equipment, and are relevant to many research fields. Because of this broad applicability, much research has been performed, in theoretical, numerical or experimental form, on rough-walled pipe flows. Nonetheless, there are still gaps in our knowledge about this type of flow. This is mostly caused by the amount of possibilities within the class and the many parameters that are involved. Specific problems aren't typically investigated thoroughly until their industrial or scientific relevance becomes apparent.

The work in this thesis is inspired by such a specific application of rough-walled pipe flow: the short-distance transport of *liquefied natural gas* (LNG) through flexible corrugated hoses. The combination of geometrical and other physical parameters in this application presents us with an example of a situation that is yet not fully understood and requires further research.

### 1.1 The challenge: transport of liquefied natural gas

The topic of this thesis arises from a specific problem in industry: the unpredictable behaviour of turbulent flow of LNG through corrugated hoses (van Bokhorst and van Osch, 2011). There are two features that separate this type of flow from the typical rough-walled flows found in other industrial applications:

- The short-distance transport of LNG is often done using corrugated hoses rather than smooth solid pipes.

- LNG is a liquefied gas and transported at low pressures, in a near-boiling state.

A corrugated hose is a more or less flexible pipe with a relatively large internal structure, inherent to its mechanical construction. Currently there are two main types of large-scale industrial corrugated hoses available on the market: bellow-type hoses and composite-type hoses (Fig. 1.1). Although the dimensions of hoses may differ between brands, specific purposes and hose diameters, the main differences between the two types are presented in Fig. 1.1. A bellow-type hose consists of metal plates shaped into so-called bellows to provide flexibility. Composite hoses are constructed using an inner and outer metal wire, both wound into spirals, and a thick layer of different impermeable fabrics wrapped in between those spirals.

The roughness aspect ratio (rib height divided by rib pitch) of bellow-type hoses is larger than that of composite hoses, and the relative roughness height of the bellow type is typically a few times larger than that of a composite hose of the same diameter (van der Putte, 2015a).

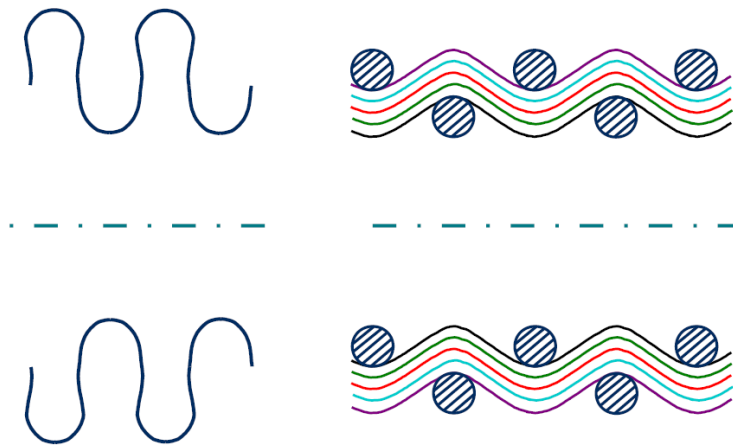


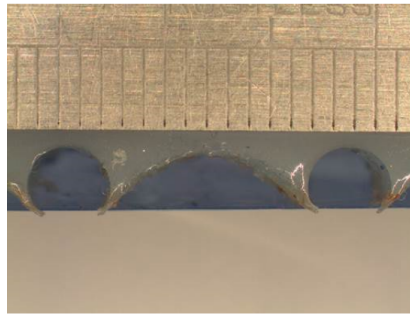
Figure 1.1: Schematic cut-through structure of bellow-type (left) and composite-type (right) corrugated hoses. The dash-dotted line indicates the pipe axis.

Besides the roughness, another difference between the two types of hoses concerns their inner surface structure. In the case of a bellow-type hose, the material of the surface is comparable to that of commonly used straight industrial pipes. However, for composite hoses, part of the hose has a surface made from fabrics with a roughness depending on the fabric type used. In general, these fabrics

have a large roughness compared to the metal surfaces of bellow-type hoses. Fig. 1.2a shows the wire-and-fabric roughness of a typical composite hose.



(a) Photograph of the outer structure of a composite LNG hose with a diameter of 3 inch (7.6 cm) (Gutteling BV)



(b) Mold of the inner hose structure of a 4-inch composite hose, very similar to the one shown in (a). Scale of the ruler is in mm. Image from van der Putte (2015a)

Figure 1.2: Outer structure (a) and inner shape (b) of composite corrugated hoses.

The second feature that distinguishes LNG flow from most other flows is the transported liquid. As the name indicates, LNG is a liquefied gas, a state typically reached by lowering the temperature below  $-163^{\circ}\text{C}$  at near-atmospheric pressures.

What is most important for the remainder of this thesis is that small changes in pressure or temperature can lead to the formation of gas (i.e. vapour), either temporary ("cavitation") or increasing in volume throughout the course of the flow ("boil-off"). Of course, a combination of the two gas formation processes can also occur, in which case only a part of the formed gas re-liquefies within the flow.

The above describes the challenge we address: **we aim to understand flows experiencing two specific interacting aspects: a rib-like wall geometry and a near-boiling or cavitating liquid state.**

To be able to study the interaction between the two aspects, we first need to understand them independently from each other. The current work focuses mainly on the impact of the pipe wall geometry.

## 1.2 Turbulent wall-bounded flow

The geometry of a ribbed pipe can be interpreted as a wall roughness acting on the flow. This section gives an overview of relevant work on rough-wall flows.

We briefly introduce wall-bounded flow in general, followed by an overview of relevant aspects of flows moving over rough surfaces.

In the current work, the focus is on fully developed wall-bounded flows. Fully developed means that there is no mean velocity gradient in the axial direction  $x$  and no mean velocity in wall-normal direction  $y$ . If we define  $u$  as the local axial and  $v$  as local wall-normal velocity, this can be written as:  $\frac{d\bar{u}}{dx} = 0$  and  $\bar{v} = 0$ .

The entrance length  $L_e$  is the distance travelled by the flow before this fully developed state is reached. For turbulent flow through a smooth-walled pipe of diameter  $D$ , the entrance length is dependent on the Reynolds number  $Re$  (White, 2008):

$$L_e \approx 4.4DRe^{1/6} \quad (1.1)$$

In general, the velocity profile within a developed turbulent flow can be described using two sub-layers: an inner layer and an outer layer (Schlichting, 1979b; Nieuwstadt, 2016; Tennekes and Lumley, 1999). At sufficiently high Reynolds numbers, the two layers overlap, giving rise to a third layer: the overlap region. The inner-layer flow scales with inner-wall units:  $y^+ = \frac{yu_\tau}{\nu}$ , with the friction velocity  $u_\tau$  defined as:

$$u_\tau = \sqrt{\tau_0/\rho}, \quad (1.2)$$

where  $\tau_0$  is the wall shear stress,  $\rho$  the fluid density and  $\nu$  the kinematic viscosity. The outer-layer velocity profile scales with  $\eta = \frac{y}{\delta}$ , where  $\delta$  is the characteristic scale of the flow, i.e. the pipe radius (or boundary layer thickness in the case of a turbulent boundary layer).

The inner and outer layers can roughly be defined as:

$$\begin{aligned} \text{inner layer: } & y/\delta < \approx 0.1 - 0.15 \\ \text{outer layer: } & y^+ > 30 \end{aligned}$$

In the overlapping region, both the functional dependencies on inner layer ( $y^+$ ) and outer layer ( $\eta$ ) variables are valid. Matching those dependencies results in a logarithmic velocity distribution, and therefore this overlap layer is commonly referred to as the "logarithmic layer":

$$u^+(y) = \frac{1}{\kappa} \ln y^+ + C \quad (\text{expressed in inner layer variables}), \quad (1.3)$$

where  $\kappa$  and  $C$  are constants.

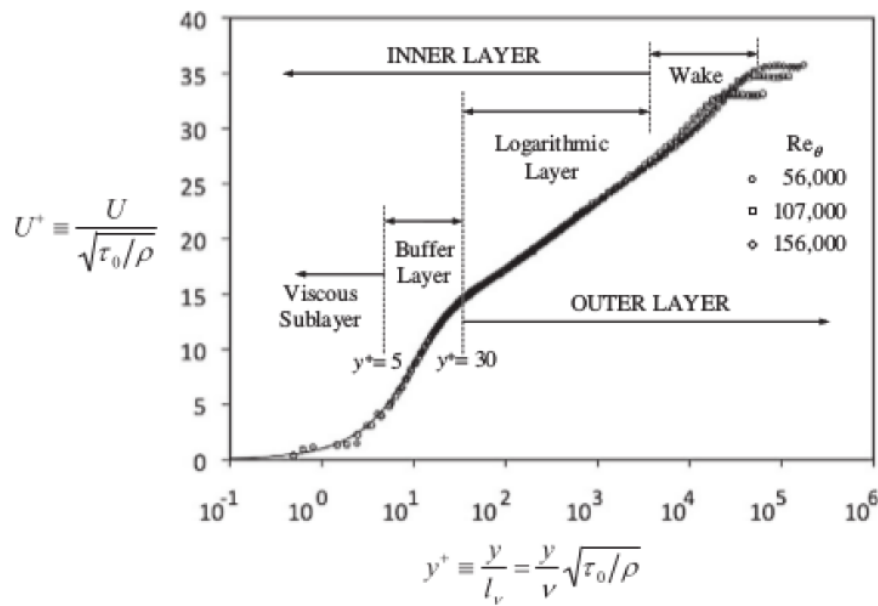


Figure 1.3: Velocity profile in a turbulent boundary layer, scaled with inner-layer variables. Image from Kundu et al. (2012).

The outer layer beyond the logarithmic layer can be expressed as:

$$u^+(y) = \frac{1}{\kappa} \ln(y^+) + C + \frac{2\Pi}{\kappa} W(\eta) \quad (\text{outer layer}) \quad (1.4)$$

Here,  $\Pi$  and  $W$  are called the wake strength and wake function, respectively.  $\kappa$  and  $C$  are generally considered to be universal constants, at least in flows over smooth walls. Their values are:  $\kappa = 0.41$  and  $C = 5.1$  or  $5.5$  (Kundu et al., 2012; Nieuwstadt, 2016; Pope, 2000). The constant  $\kappa$  is called the von Kármán constant.

The layers are indicated in the velocity profile shown in Fig. 1.3. As can be seen, the inner layer is divided in a viscous sub-layer and a buffer layer. In the viscous layer, which extends to  $y^+ = 5$ , viscous effects dominate the flow. In the buffer layer, both viscous friction and turbulent fluctuations influence the flow, whereas beyond the buffer layer viscous stresses become negligible and the flow is dominated by turbulent stresses.

### 1.3 Wall roughness

The velocity profiles derived in Section 1.2 are valid for flows over smooth surfaces. However, when a surface has a roughness of a size that is significant with respect to the thickness of the viscous layer ( $y^+ \approx 5$ ), the equations discussed in Section 1.2 are no longer valid (Schlichting and Kersten, 2001).

#### 1.3.1 General rough-wall velocity profile

Although the universal flow profiles have been derived for smooth walls, the flow over a rough surface exhibits similar layers as in the smooth-walled case. The outer layer is described by the same equation but now with an additional parameter  $\Delta u^+$ , called the roughness function (Jiménez, 2004):

$$u^+(y) = \frac{1}{\kappa} \ln(y^+) + C - \Delta u^+ + \frac{2\Pi}{\kappa} W(\eta) \quad (1.5)$$

The wall friction velocity  $u_\tau$ , which is used to normalize the velocity and obtain  $u^+$ , is now defined using the total surface friction, thus including the added resistance due to roughness effects. Similarly, the logarithmic layer is expressed using the smooth-wall equation and the added roughness function. The inner region is no longer dominated by viscous effects, but by the roughness geometry. The viscous layer (see Fig. 1.3) is substituted by a layer determined by a combination of viscous and roughness effects.

When the impact of the surface roughness is negligibly small, we speak of a "hydraulically smooth wall". When roughness and viscous wall effects are both important, we speak of transitional roughness, and when the viscous wall effects are negligible small, the wall surface is considered "fully rough". For the work described in this thesis, all flows can be considered as flows over a fully rough surface and transitional roughness is not considered any further.

#### 1.3.2 Equivalent roughness

A first methodical quantification of roughness scaling for a pipe flow was reported by Nikuradse (1933). He used different sand grain sizes as a well-defined roughness, covering roughness heights relative to the pipe radius ranging from 1/500 to 1/15. Based on the measurements by Nikuradse, the parameter  $k^+ = \frac{ku_\tau}{\nu}$  was introduced, with  $k$  the characteristic grain size of the sand roughness.

The three roughness regimes as introduced in Section 1.3 can be quantified based on this non-dimensional roughness:

$$\begin{aligned}
k^+ < 3 & \text{ hydraulically smooth regime} \\
3 < k^+ < 70 & \text{ transition regime} \\
k^+ > 70 & \text{ fully rough regime}
\end{aligned} \tag{1.6}$$

This dependence of the type of regime on a dimensionless roughness is also evident for flows over types of roughness other than only sand-grain-type wall roughness. This is the basis for the well-known Moody diagram, which displays the Darcy-Weissbach friction factor  $f_D$  as a function of Reynolds number for a range of equivalent roughnesses:

$$f_D = \frac{\Delta p D_h}{\frac{1}{2} \rho L V_b^2} \tag{1.7}$$

Here,  $L$  is the pipe length, and  $D_h$  the hydraulic diameter, which is equal to  $D$  in circular pipes. In the rough and transitional rough regime, the Moody diagram displays the so-called Colebrook-White equation (Colebrook, 1939), which was derived based on the data from Nikuradse (1933):

$$\frac{1}{\sqrt{f_D}} = -2 \log_{10} \left( \frac{k}{3.7D} + \frac{2.51}{Re \sqrt{f_D}} \right) \tag{1.8}$$

Beyond the transitional regime, the friction factors reach a regime in which they become a constant: the fully rough regime.

For other roughness types, an equivalent sand-grain roughness  $k_s$  has been introduced. This equivalent surface roughness is chosen such that Eq. (1.8) matches the measured friction factor. In case of sand-type roughness,  $k_s$  thus matches the true geometrical sand grain size  $k$ . However, for other roughness types,  $k_s$  can differ significantly from the actual roughness height  $h$ . For certain roughness patterns, the relation between the actual roughness height and the equivalent sand grain roughness can be found in literature.

In the fully rough regime, the Reynolds number dependency of the friction coefficient is negligible. This confirms that indeed the influence of viscous effects is not significant, and the wall friction is caused by pressure drag on the roughness elements (Leonardi and Castro, 2010).

In the description of the velocity profile, the innermost layer is now determined by the roughness, unlike the viscous layer before. However, the outer and overlap layers can be expressed analogously to those in hydrodynamically smooth wall flow. The rough overlap layer can be expressed using the equivalent sand grain roughness as (Schlichting, 1979a):

$$u^+ = \frac{1}{\kappa} \ln(y^+) + C^+(k_s^+) = \frac{1}{\kappa} \ln\left(\frac{y}{k_s}\right) + \frac{1}{\kappa} \ln(k_s^+) + C^+(k_s^+) \quad (1.9)$$

Since viscosity is not a relevant parameter for a flow over a fully rough surface,  $k_s^+$  cannot be a scaling parameter either. The term  $C^+(k_s^+) + \frac{1}{\kappa} \ln(k_s^+)$  thus becomes constant. Based on experiments, this constant, called  $B$ , has been determined empirically to be approximately 8-8.5 (Schlichting and Kersten, 2001; Nikuradse, 1933).

The equivalent sand-grain roughness is a frequently used way to describe the effect of wall roughness on flows. Other, often equivalent, notations are commonly used as well. For example, the classification in Eq. (1.5), introducing the roughness function, is completely equivalent to Eq. (1.9). Which description is used depends on the field of science and specific aim of a study. Both roughness functions are

Reynolds number-independent for fully rough flow. The roughness function can be determined empirically, but attempts have been made to obtain geometric dependencies to determine its value for specific roughness geometries (e.g. Webb, 1971; Jackson, 1981; Karwa et al., 1999).

## 1.4 Parameters describing flows over rough walls

As shown in Section 1.3, the flow over a rough surface can be described using several parameters. Here we further clarify three important parameters: the displacement height, the roughness length and the wall friction velocity. Next, we proceed to discuss the stress distribution, mixing length and friction correlations.

### 1.4.1 Displacement height

In many descriptions of flow over a rough wall, a so-called displacement height  $d$  is used. This displacement height is the shift of the origin of the described velocity profile with respect to the base of the roughness (Perry et al., 1969; Jackson, 1981):

$$u^+(y) = \frac{1}{\kappa} \ln((y - d)^+) + C - \Delta u^+ \quad (1.10)$$

The wall-normal coordinate is thus relative to this shifted origin. Offset  $d$  is often used but not always explicitly defined. Perry et al. (1969) and Jackson (1981) also use the displacement height in their description for the roughness function  $\Delta U^+$  itself, with only a constant factor remaining to be determined:

$$\Delta u^+ = \frac{1}{\kappa} \ln (h - d)^+ + B' = \frac{1}{\kappa} \ln \epsilon^+ + B' \quad (1.11)$$

Although this method gives a more intuitive description of the effect of roughness, the number of unknown parameters remains the same, and empirical fitting of the velocity profile to obtain the constants is still required.

Due to its Reynolds number-independence, the expression in Eq. (1.11) must be proportional to  $h$ , as was already mentioned by Leonardi et al. (2007). The proportionality constant is unknown and depends on the characteristics of the geometry.

The determination of the displacement height is less straightforward than might be expected. It is a parameter that depends on the geometry of the flow domain, but not like a geometric parameter such as height, plan area coverage density or solidity; the latter two being geometrical parameters describing the relative roughness area and relative frontal projected roughness area. Jackson (1981) associates  $d$  with the height at which the mean stress acts on the wall surface. Although this approach does not lead to an a-priori determination of the parameter, it provides insight in the mechanism causing the changes in the various flow layers described previously. A complete measurement of friction and pressure along a representative part of the rough wall would then provide the displacement height. It is more common to determine the displacement height assuming the commonly used value for the Von Kármán constant  $\kappa$  of 0.41, and fitting the data to Eq. (1.10) to obtain the displacement height. This method is often referred to as Clauser-chart or Clauser-plot method (Castro, 2009). For some data sets, the two methods provide similar results, but most often there is a discrepancy and no consensus on the matter. Castro (2009) and Leonardi and Castro (2010) argue that the universality of  $\kappa$  is not generally confirmed for all flow types, and might break down for some roughness geometries. On the other hand, e.g. Cheng et al. (2007) do not address the matter of  $\kappa$ -universality, and therefore implicitly reject the interpretation of Jackson (1981) and thus the derivation of  $d$  based on drag momentum. The derivation of  $d$  based on computing all stresses and pressures locally around the roughness elements is very challenging, especially with experimental data, so in practice  $d$  is mostly computed using the Clauser-chart method. However, it should be kept in mind that this method is not fully without controversy, and results might show trends or errors introduced by the assumptions of the method itself. Coceal et al. (2007) summarize the discussion clearly and state that the currently obtained data is insufficient to conclude on the matter; either  $\kappa$  is not universally constant or the explanation of the displacement height has shortcomings. Both may apply as well.

An important note to add is that the Clauser-chart method can lead to a negative

displacement height for certain types of roughness (Leonardi et al., 2007; Coleman et al., 2007), which is in disagreement with the physical interpretation of  $d$ , i.e. corresponding to the height of the mean acting force as described previously.

In practice, many authors use the height at which the mean velocity becomes zero as the displacement height, then referred to as the "virtual origin". This approximation often provides a reasonable estimate of  $d$  but can differ significantly from the displacement height as computed with either of the previous two methods.

## 1.4.2 Roughness length

The roughness length  $y_0$  is a characteristic length that describes the impact of roughness on the flow characteristics. It is an alternative method to express the roughness function (e.g. Castro (2007)). The expressions are equivalent and both depend on all aspects of the roughness geometry. When choosing the roughness length and displacement height as variables, the expression for the logarithmic flow region becomes:

$$u^+(y) = \frac{1}{\kappa} \ln((y-d)^+) + C - \Delta u^+ = \frac{1}{\kappa} \ln\left(\frac{y-d}{y_0}\right) \quad (1.12)$$

Using this equation, the effect of roughness is split up into a displacement and an overall impact factor, which might be an appropriate way to envision the total effect of the roughness.

Using the logarithmic description for the roughness function as given in Eq. (1.11), the roughness length can be defined as follows:

$$y_0 = \epsilon e^{\kappa(B'-C)} \quad (1.13)$$

Here,  $C$  is the same universal constant as present in the description for hydraulically smooth flow in Eq. (1.3). The constant  $B'$  depends on the roughness geometry. The expression in Eq. (1.13) is similar to relations used in the atmospheric sciences (e.g. De Bruin and Moore (1985)), where  $y_0$  is defined as the height at which the mean flow is theoretically zero, extrapolating the logarithmic layer towards the ground. Since the roughness length is typically well within the roughness height itself, the logarithmic expression is not valid at that height anymore, and this extrapolated value thus may differ from the actual height at which the mean flow vanishes.

### 1.4.3 Friction velocity

For all velocity profiles thus far, the velocities and coordinates are normalized with the friction velocity  $u_\tau$  and the expression  $\frac{v}{u_\tau}$ , respectively. For flows over hydraulically smooth walls, the friction velocity is defined based on the total wall friction and the fluid density (see Eq. (1.2)). For flows over rough walls, the same expression is valid although not all flow resistance is due to viscous friction. The effect of the roughness is to alter the flow shear stress. Since the flow through a rough-walled pipe effectively occupies a smaller region, Coceal et al. (2006) argue that the origin of the linear stress profile is shifted with the displacement height  $d$  as well, and this should be reflected in the friction velocity. Without changing the definition of the friction velocity itself, this implies changing the definition of the wall shear stress by changing the diameter into an effective diameter. For a pipe flow, this would result in  $u_{\tau^*} = u_\tau \sqrt{1 - d/R}$ , with  $R$  the height occupied by the flow or the pipe radius. Especially with a relatively large roughness height, this factor can lead to a significant change in the effective friction velocity, which then directly influences the other fitting parameters.

### 1.4.4 Stress distribution

The Reynolds stress is an effective stress as a result of turbulent fluctuations which lead to a dissipation of energy. These turbulent fluctuations are typically defined as the temporal fluctuations with respect to the local time-averaged velocities. Coceal et al. (2006) use a slightly different definition for the fluctuations; they define them with respect to the streamwise mean of the time-averaged flow, rather than with respect to the local time-averaged velocities.

Using this approach, an additional stress term called dispersive stress arises, describing separately the effect of spatial variation. Introducing this separate term provides insight in the impact of the periodicity of the wall on the total stresses in the flow.

It has been shown for cubical roughness (Coceal et al., 2006) that the dispersive stresses are negligible compared to the Reynolds stresses everywhere outside the roughness layer; within the roughness layer they significantly contribute to the total stresses. For repeated rib roughness, such as investigated by us, no study reporting the dispersive stresses is available.

### 1.4.5 Mixing length

The mixing length  $l$  is a flow parameter that is used to describe and model turbulent flows. It describes the macro-scale of turbulent energy transport:

$$l = \sqrt{\langle -u'v' \rangle} / (dU/dy) \quad (1.14)$$

As with the Reynolds stresses, Coceal et al. (2006) introduce a spatially averaged mixing length  $l_m$ , defined as

$$l_m = \sqrt{\langle -\bar{u}'\bar{v}' \rangle} / (d\bar{U}/dy), \quad (1.15)$$

with  $\bar{u}'$  and  $\bar{v}'$  the temporal deviations from mean velocities  $\bar{U}$  and  $\bar{V}$ , spatially averaged in the axial direction. Using the assumption that Eq. (1.10) applies, Coceal et al. (2006) show that a linear profile of the effective mixing closely above the location of the displacement height is equivalent to the direct fitting of a logarithmic velocity profile.

#### 1.4.6 Ribbed-wall flow friction correlations

Webb (1971) performed a systematic investigation of flows through ribbed-wall tubes specifically for roughness due to rectangular-shaped ribs. He found a simple correlation for relative rib sizes of  $k^+ > 35$  and  $p/h > 10$ , corresponding to the fully developed regime:

$$\frac{1}{\sqrt{f}} = \frac{1}{2\sqrt{2}\kappa} \ln\left(\frac{R}{h}\right) - \frac{3}{4\sqrt{2}\kappa} + \frac{0.95}{2\sqrt{2}} \left(\frac{p}{h}\right)^{0.53}, \quad (1.16)$$

with  $p$  the rib pitch and  $h$  the rib height of the roughness geometry.

Han et al. (1978) extended the research by Webb (1971) and included the angle of attack, two smaller pitch-to-rib-height ratios and some aspects of the rib shape to the correlation. Both investigations, however, treat relatively small roughness heights ( $k/D = 0.01 - 0.04$ ) and a  $p/h$  ratio of more than 5, limiting the applicability of the obtained correlations.

Flow through tubes with similar range in relative pitch and rib height as Han et al. (1978) was investigated by Ryu et al. (2007), with an extended range of the relative pitch down to  $p/h = 5$  and with the inclusion of variations in rib shape. Their results indicate a regime change towards smaller pitch and a significant influence of rib shape. However, no parametric roughness function model was proposed.

Many investigations studying square ribs use the distinction between d-type, intermediate and k-type ribbed flows, as introduced by Perry et al. (1969). In this classification, the velocity profile of flow over d-type ribs does not scale with the roughness height  $h$ , whereas the profile of flow over k-type ribs does scale with  $h$ . The d-type ribs are roughly the case for  $p/h$  smaller than 4, while k-type ribs are

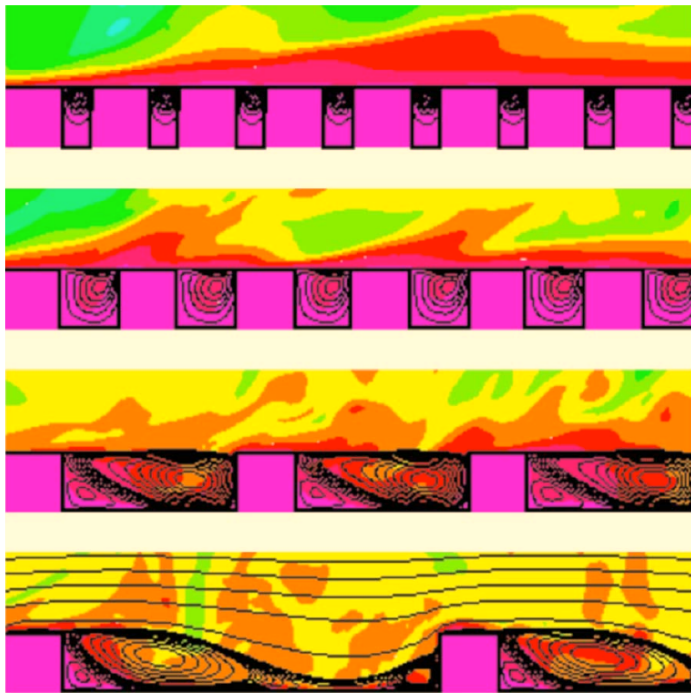


Figure 1.4: Visualization by a passive scalar of the instantaneous flow patterns and mean flow streamlines of (from top to bottom) d-type, intermediate and k-type ribbed surfaces. Adopted from Leonardi et al. (2007).

defined as ribs with  $p/h$  larger than 4 (e.g. Cui et al., 2003; Jiménez, 2004). An intermediate regime between d and k-type roughness is often defined as well (e.g. Perry et al., 1969; Jiménez, 2004), shifting the actual k-type roughness to larger aspect ratios (i.e. a cavity width  $\sim 3 - 4$  times the rib height (Jiménez, 2004)). This coarse classification is widely discussed, as are the mechanisms responsible for the change in behaviour. Typical mean flow streamlines of the three cases can be seen in Fig. 1.4. Although most recent studies (e.g. Cui et al., 2003) agree that this classification is an oversimplification, it is still often used to characterize a ribbed surface (e.g. Leonardi et al., 2007). The friction correlation by Webb (1971), Eq. (1.16), and the studies by Han et al. (1978) and Ryu et al. (2007) all correspond to a k-type rough flow.

## 1.5 Beyond wall roughness

The topic discussed thus far is that of a flow over a rough wall, establishing the flow parameters in a spatially averaged sense. However, the key to understanding the global behaviour might be in the details within the roughness region. In addition, there is a lower limit of the ratio  $\delta/h$  up to which the rough-wall approximation with velocity profiles divided in an inner, overlapping and outer layer remains applicable.

The question is whether this limit is reached for either the specific case of corrugated hoses or the experiments performed within the current experimental work.

### 1.5.1 The limit of rough-walled flow

Jiménez (2004) argues that for the rough-wall approximation to be applicable, the direct impact of the roughness should not extend beyond half the thickness of the logarithmic layer, and assumes a roughness impact region of  $3h$ . In that case, the relative roughness  $\delta/h > 40$  would be the limit for the use of the rough-wall approximation. In a pipe-flow,  $\delta$  equals the pipe radius; for a typical corrugated tube with a diameter of 10 inch (0.25 m), the roughness should not extend beyond 3.1 mm, while for a 4 inch hose this would be 1.2 mm. Considering the multi-composite hose described in Section 1.1, the diameter of the wire that shapes the roughness is approximately 2 mm. Hence, the roughness clearly does not stay within the limit given above. In the laboratory experiments described in Chapter 2, the relative roughness is even larger, and certainly beyond the "classical" roughness size.

The analysis by Jiménez (2004) does not take into account the shift in origin of the velocity profiles. Some authors (Lee et al., 2011; Coleman et al., 2007) show that similarity expressions do exist and a logarithmic layer can be found, also for roughness beyond this limit of  $\delta/h > 40$ . This does not necessarily imply that the resulting logarithmic functions have characteristics identical to the cases below the roughness limit.

### 1.5.2 Orifice flow

Another way to approach a pipe with repeated ribs is describing it as a series of repeated orifices. Single-orifice flows have been investigated thoroughly in the scope of their application in flow meters, and empirical correlations are available for the pressure loss and wall pressure (White, 2008).

The "single rib" in an orifice flow meter is designed to show similar behaviour over a large range of Reynolds numbers. This results in a specific geometry with a plate thickness less than 0.05 times the pipe diameter, slanted orifice edges and a limited range for the inner diameter of the orifice – not representative for orifice geometries of other diameters and shapes.

The non-recoverable energy loss for a generic orifice is computed using a combination of the Bernoulli equation, mass conservation and momentum conservation, resulting in the Borda-Carnot equation:

$$\Delta E = \zeta \frac{1}{2} \rho (\Delta V)^2, \quad (1.17)$$

where  $0 \leq \zeta \leq 1$  is an empirical constant. Eq. (1.17) assumes that the flow is uniform across the cross section of the pipe.

From the point of view of the flow, an orifice is a sequence of a sudden contraction and a sudden expansion. At the contraction edge, the flow separates, forming a recirculation bubble. When the flow reattaches within the orifice, the geometry is referred to as a thick orifice. This reattachment occurs approximately when the orifice width divided by the inner diameter of the orifice is larger than 0.5 (Roul and Dash, 2012; Fossa and Guglielmini, 2002; Jianhua et al., 2010). A thin orifice has a very low  $w/h$  ratio, where  $w$  is the thickness of the orifice and  $h$  the "rib height" defined as  $\frac{1}{2}(D - d)$ . The influence of the orifice is described solely by the diameter ratio. Between the thick and thin-orifice geometries, an intermediate range is present, with less clearly defined characteristics.

The smallest flow diameter, which is determined by the size of the recirculation, is referred to as the *vena contracta*. The surface area of this vena contracta is expressed using the actual flow area ratio  $\sigma = (d/D)^2$  and a contraction coefficient  $\sigma_c$ :

$$A_{\text{vena}} = A \sigma \sigma_c \quad (1.18)$$

For thin orifices, this coefficient is estimated using the empirically derived Chisholm expression (Chisholm, 1983):

$$\sigma_c = \frac{1}{0.639(1 - \sigma)^{0.5} + 1} \quad (1.19)$$

and the unrecoverable pressure loss for a thin orifice is described by Roul and Dash (2012):

$$\Delta P = \frac{\rho V_b^2}{2} \left[ \frac{1}{\sigma \sigma_c} - 1 \right]^2 \quad (1.20)$$

Applying Eq. (1.17) to the flow through a thick orifice requires an extra stage in the calculation. First the contraction, without significant losses, then an expansion

from the vena contracta to the orifice diameter, followed by a second expansion from the orifice diameter to the pipe diameter. For the case of sudden expansions, the empirical constant is equal to 1, which is also applied to the intermediate expansion for thick orifices. Using this approach, the pressure loss for a thick orifice can be described by Roul and Dash (2012):

$$\Delta P = \frac{\rho V_b^2}{2} \left[ \left( \frac{1}{\sigma \sigma_c} \right)^2 - 1 - \frac{2}{\sigma^2} \left( \frac{1}{\sigma_c} - 1 \right) - 2 \left( \frac{1}{\sigma} - 1 \right) \right] \quad (1.21)$$

For orifices that are neither thick nor very thin, the presence of a freely expanding flow, either within the orifice or in the full pipe, is obstructed. This might influence both the contraction coefficient and the empirical constant  $\zeta$  in Eq. (1.17).

There is thus a range of orifices that qualify as neither thick nor thin, and no established correlations are available describing the discharge behaviour of such orifices. In the experiments described in this thesis (see Section 2.1.2), the ribs are in this intermediate range. However, the correlations for thin and thick orifices can be used as a guideline for comparing intermediate orifice flows.

### 1.5.3 Cavity flow oscillations

Similar to describing ribbed flow as flow through a series of consecutive single orifices, we can also describe the geometry as a series of consecutive axisymmetric cavities. Cavity flows are known for displaying oscillatory behaviour which can be divided in three categories: fluid-dynamical interaction, fluid resonance and fluid-elastic coupling (Rockwell and Naudascher, 1978).

In the current research, only the fluid-dynamic flow interaction is of interest, since the Mach number (maximum  $\approx 0.03$ ) is too low for compressibility effects to be important and thus acoustic resonance to be significant.

Cavity oscillations in fluid-dynamic interaction mode occur in discrete modes at frequencies which cause impingement of shed vortices to have a phase delay of approximately  $\pi$  rad with respect to the upstream edge of the cavity (Naudascher and Rockwell, 1994; Rockwell, 1977). The most significant parameters are the cavity gap length and the convection velocity of the shed vortices. However, more flow parameters such as the approaching momentum thickness and the angle of the approaching streamlines are important. The frequency and amplification of the cavity modes are influenced by the average momentum thickness across the cavity and thus by the cavity length, depth and shape as well (Rockwell, 1977).

Typically 1 or 2 "cavity modes" are clearly present in the spectrum; which mode is most dominant depends on the geometry and approaching flow conditions.

Figure 1.5 shows a typical spectrum of the wall pressure at the downstream edge of a cavity with resonance modes 2 and 3 clearly present.

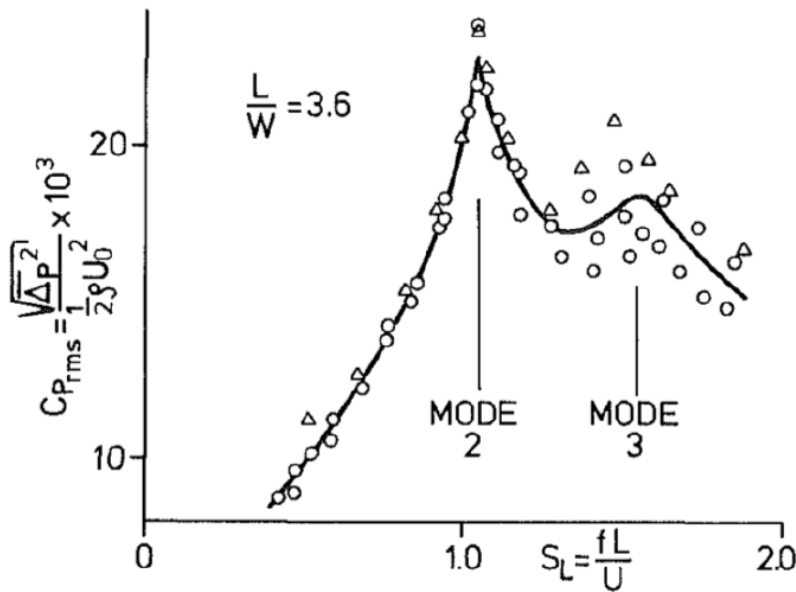


Figure 1.5: Typical spectrum of pressure fluctuations, adopted from Rockwell (1977).

The peaks in the pressure fluctuations are often expressed in the form of a Strouhal number:

$$Sr = \frac{fL}{V}, \quad (1.22)$$

in which the geometric parameter  $L$  is typically the cavity length and  $V$  the free stream velocity or bulk velocity. When applying the theory of single-cavity oscillation to a ribbed pipe, significant differences in amplification and mode frequency can be expected, because the approach conditions differ from those of an approaching boundary layer. In addition, interaction between subsequent cavities might impact the fluctuations by either mutual suppression or amplification.

#### 1.5.4 Coherent structures in flows with obstacles

In any wall-bounded turbulent flow, patterns can be found in the fluctuating part of the velocities. In a flow through a rough or structured surface, distinct

patterns can be found, both in the mean and in the fluctuating components of the velocities.

In the mean flow field, structures such as recirculation regions, attachment lines, secondary flows, impingement regions and strong shear layers can be observed (e.g. Leonardi and Castro, 2010). In an instantaneous sense, shedding vortices are a good example of a flow structure typical for a wall with a ribbed or blocked roughness structure. The patterns in the instantaneous velocity components are called "coherent structures".

The strength, occurrence and characteristics of the patterns are determined by the geometry and often used as a way of classifying the roughness. For example, the transition from intermediate to k-type ribbed flow is typically defined by the presence of a reattachment point in the cavity between two subsequent ribs.

Visualization of coherent structures can be done using various quantities: velocity, vorticity,  $\lambda_2$  criterion, turbulent kinetic energy or instantaneous streamlines (e.g. Wang et al., 2007, 2010; Cardwell and Vlachos, 2011; Coceal et al., 2007; Cui et al., 2003; Fröhlich et al., 2005). More quantitative characterization methods include but are not limited to 2-point correlations (e.g. Coceal et al., 2007; Wang et al., 2010), quadrant analysis (e.g. Coceal et al., 2007; Leonardi and Castro, 2010; Cardwell and Vlachos, 2011; Pokrajac et al., 2007), conditional averaging (Coceal et al., 2007), spectral analysis (Fröhlich et al., 2005) and proper orthogonal decomposition (POD) (Wang et al., 2010). Similar to the introduction of dispersive stresses in Section 1.4.4, the fluctuations can be defined with respect to the local or spatially averaged mean, resulting in different structures and interpretations. Another type of coherent structure often described for turbulent wall-bounded flow is the Uniform Momentum Zone (UMZ) (de Silva et al., 2016; Adrian et al., 2000). An interesting characteristic of UMZs is that they can be identified consistently in the temporal instants of a measured velocity field, even when the time-averaged flow is featureless (e.g. in a flat-walled boundary layer).

## 1.6 Cavitation & impact

The second aspect of interest in this investigation, besides the wall geometry, is the occurrence of cavitation within the flow and its impact on the flow parameters. Although it is a similar process, cavitation is not the same as boiling. Though the result of both processes are similar (i.e. the formation of vapour out of a liquid), the mechanisms themselves can display very different behaviour and their effect on the surrounding flow differs as well.

Boiling is a process caused by an increase in temperature that crosses the vapour-liquid interface. Cavitation is generally speaking an inertia-driven process. Rather

than an increase in temperature, the liquid now experiences a decrease in pressure, also leading to vaporization.

The difference in bubble growth and impact on behaviour of the surrounding flow originates from this difference in thermodynamic path (Brennen, 1995). Boiling is a process depending on heat transport. This is typically due to heat transfer at a solid-liquid interface and diffusion driven, and therefore relatively slow. In contrast, cavitation is inertia driven; when the cavitation commences at a location of lowest pressure, this can happen almost instantly. A cavitation bubble can therefore grow very fast compared to a bubble in a boiling liquid, and vice versa, also shrink much faster. Cavitation thus behaves typically much more "violent" than boiling; so violent that imploding cavitation bubbles can generate high-pressure shock waves in the surrounding liquid. In this way, the cavitation bubbles interact strongly with each other, and a cloud of cavitation bubbles has a significant impact on the dynamics of the surrounding flow characteristics.

Cavitation impact on flows is widely studied for so-called "sheet cavitation" behind bluff bodies due to its significance in industry. While for bubble cavitation the occurrence of cavitation is often studied, the feedback mechanism of the cavitation with the flow is not. An exception to this is the study of acoustic interference and effective sound velocity due to cavitation (Brennen, 1995) and the work by Lyster and Ceccio (2002) describing a cavitating shear layer. At TNO, measurements were performed to test the effect of the downstream absolute pressure on the pressure losses for three types of corrugated hose (van der Putte, 2015b). They observed a decrease in friction factor with a decrease in absolute pressure. However, the results differed strongly between the different hose geometries and multiple effects took place simultaneously, such as a hose elongation for higher pressures and velocities. No conclusion regarding the mechanisms responsible for the change in flow losses can be drawn from these results.

A dimensionless parameter used to characterize the susceptibility of a flow to cavitation is the cavitation number (White, 2008):

$$Ca = \frac{p - p_v}{\frac{1}{2}\rho V^2}, \quad (1.23)$$

with  $p_v(T)$  the vapour pressure of the fluid and  $V$  the characteristic flow velocity. Smaller cavitation numbers indicate a higher susceptibility for the occurrence of cavitation; above a value of  $\sim 1$ , cavitation is not likely to occur.

## 1.7 Current research

The experiments described in the following chapters aim towards answering the following questions:

1. Can the flow through a ribbed pipe be described using the classical roughness descriptions?
  - if yes:
    - Is the physical interpretation and parameterization of these descriptions similar to that of classical roughness?
    - How do the descriptive parameters relate to the geometrical parameters of the ribs?
    - How do the descriptive parameters relate to both static and dynamic characteristics of the flow?
  - if no:
    - How can the flow best be characterized, other than using a rough-wall approach?
2. How does the occurrence of cavitation influence the flow? And how does the flow influence the occurrence of cavitation?

The investigation in this thesis focuses on the flow through a ribbed pipe segment; not with a one-to-one resemblance with a corrugated hose but with more generic geometric properties. The ratio  $h/D$  of the ribs in the experiments is also significantly larger than for corrugated transport hoses. This large rib size enables a more detailed analysis of all effects introduced to the flow by the presence of the ribs.

### 1.7.1 Thesis outlook

Chapter 2 describes the pressure measurements, both static (i.e. through pressure drop measurements) and dynamic (i.e. through high frequency pressure measurements). The static measurements provide a quantitative overview of the friction scaling of the flow. The dynamic results serve to study the presence of periodic fluctuations, which can reveal aspects of the link between the flow and the occurrence of cavitation. Chapters 3, 4, and 5 describe flow field measurements by Particle Image Velocimetry. These results are used to derive the characteristic patterns and motions of the flow, in relation to the geometric dependency and frictional behaviour obtained in chapter 2. In chapter 6 a discussion based on the results of the previous chapters is held, drawing conclusions, identifying remaining gaps and suggesting further research.

## Chapter 2

# Static and dynamic pressure measurements

This chapter discusses flow-resistance measurements through a ribbed pipe. First, Sections 2.1, 2.2 and 2.3 introduce the experimental set-up, parameters and applied corrections, respectively. In the subsequent two sections, the results can be found for static losses (Section 2.4) and dynamic pressure measurements (Section 2.7).

### 2.1 Experimental set-up and design

All experiments described in this thesis were performed using the same experimental test set-up, although some adaptations and alterations were made over the course of the experiments. This set-up is a ribbed pipe segment, representing a generic scaled-up model of a corrugated pipe (see Section 1.7).

In this section, we discuss the pipe segment built for this purpose and the design and implementation of the measurements.

#### 2.1.1 Flow loop

Figure 2.1 shows the flow loop and the main experimental components in a schematic view. The dimensions of the flow loop are indicated in the figure and the components labelled A-J are explained in the figure caption.

The diffuser (J) is mainly installed to remove bubble entrapment in the recirculation regions downstream of the sudden expansion.

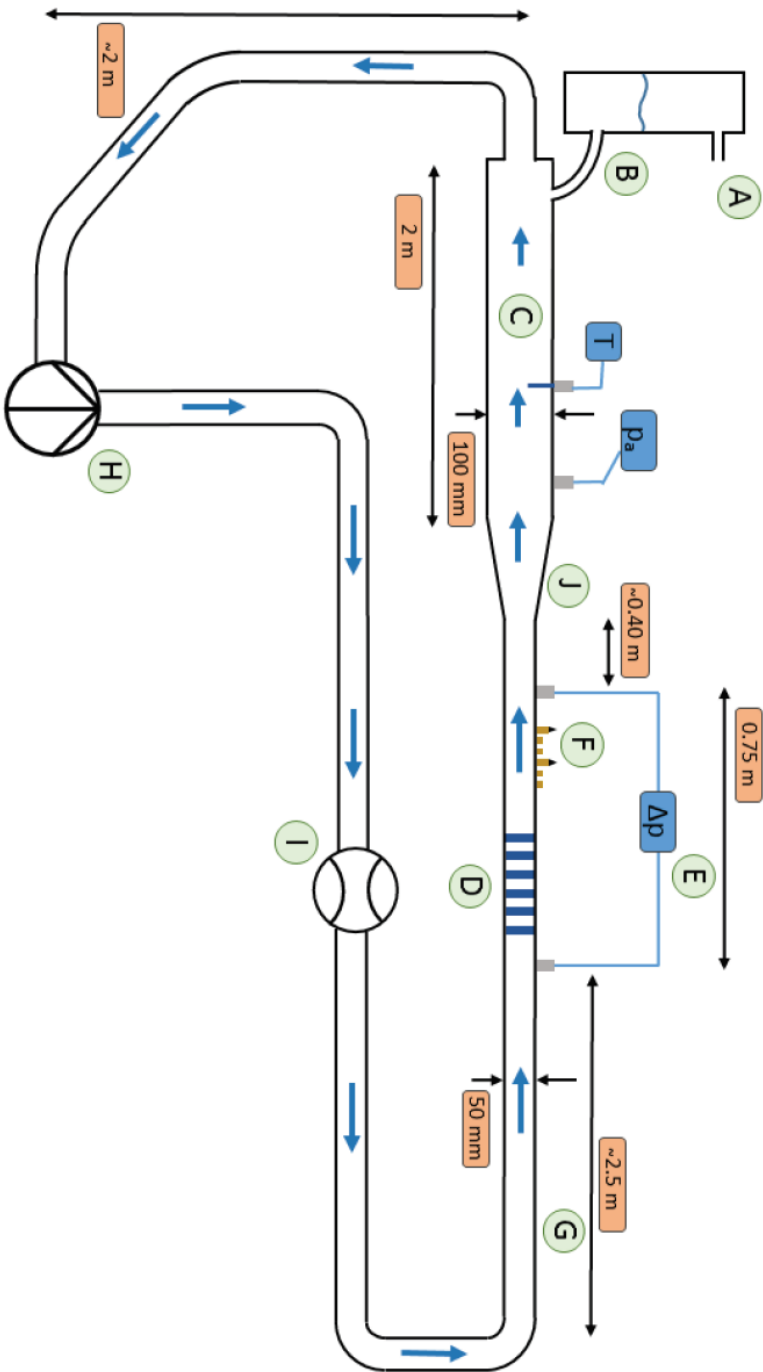
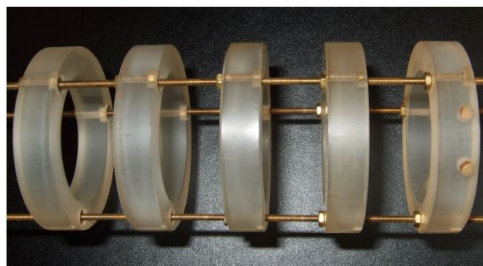


Figure 2.1: Schematic overview of the flow loop. A: optional connection to vacuum pump, B: (low-pressure) reservoir, C: de-aeration section, D: measurement section, E: static differential pressure sensor, F: dynamic pressure taps, G: inflow length, H: centrifugal pump, I: flow meter, J: diffuser.

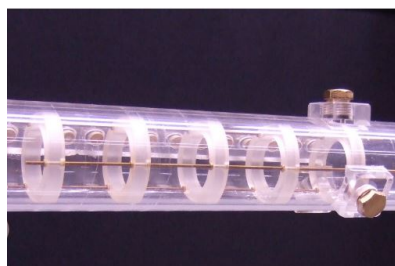
Some of the experiments require the system to be operated at a low system pressure. For this to be possible, the flow loop has to be fully closed, and the pump driving the system has to be suitable for operation under low pressure, which is not an apparent feature for commonly used pumps. The lowest desired system pressure approaches vacuum ( $\sim 0.1$  bara), which would put an unrealistic requirement on the pump specifics. To loosen this requirement, a hydrostatic head of almost 2 metres is included in the system as indicated in Fig. 2.1, shifting the required specifics for the pump to an inflow pressure of at least  $\sim 0.3$  bara. To generate a low system pressure, a vacuum pump is connected to the loop through a vacuum tank (connections B and A in Fig. 2.1). The water level imposes a small hydrostatic head with respect to the adjustable pressure in the vacuum tank. The tank also serves as de-aeration device during the preparations before each experiment and serves as a buffer for the vacuum pump, which is only capable of handling gases.

### 2.1.2 Pipe segment

As shown in Fig. 2.2, the measurement section consists of a straight pipe segment with inserted ribs. The ribs are only attached to each other and not to the pipe, with the exception of one rib that is connected to the pipe wall. This enables the variation of shape, number, position and relative distance of the ribs in between experiments. The rib interconnections need to be very rigorous to withstand the large pressure differences over the ribbed section during the experiments. The ribs are therefore connected to each other using three metal rods. The rib that is connected to the pipe is fixed using screws with metal pins piercing through the pipe wall into the rib.



(a) Example of a ribbed section ( $p = 25$  mm); the flow is from right to left.



(b) Placement of a ribbed section ( $p = 50$  mm) in the pipe.

Figure 2.2: Rib configuration and attachment to the pipe.

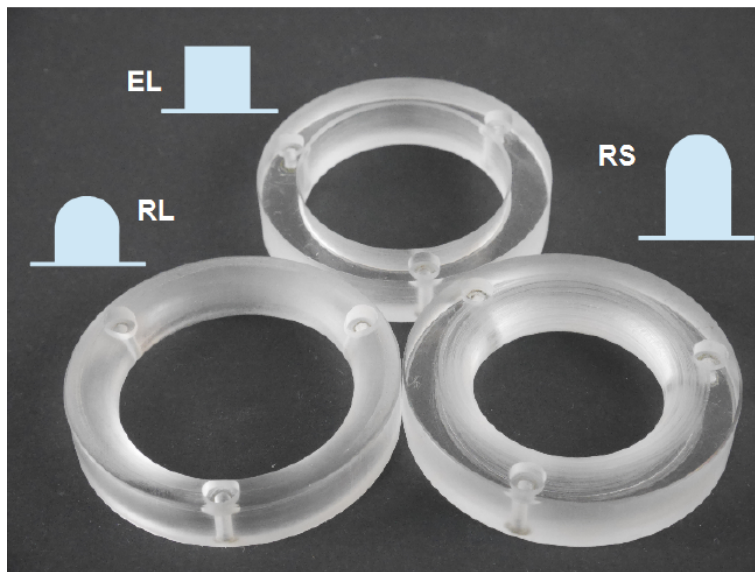


Figure 2.3: The three types of ribs used in the measurement section, with their cross-sectional shape indicated schematically (on scale). EL & RL geometries:  $9.5 \times 7.5$  mm ( $\varnothing_{in} = 35$  mm), RS:  $9.5 \times 11.25$  mm ( $\varnothing_{in} = 27.5$  mm).

### 2.1.3 Ribs

Three types of ribs were used for the majority of the experiments, as indicated in the table below:

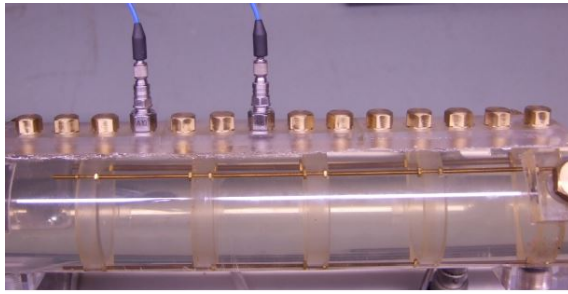
Table 2.1: Types of ribs within the ribbed pipe segment

Cross section	Inner diameter	Referred to as
Rectangular	35 mm	Edged large (EL)
Rounded	35 mm	Rounded large (RL)
Rounded	27.5 mm	Rounded small (RS)

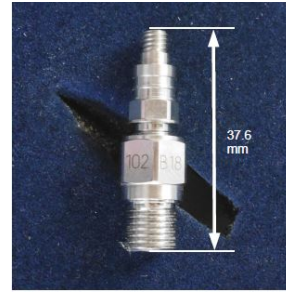
The adjectives "large" and "small" thus refer to the inner diameter of the ribs. The three types of ribs are shown in Fig. 2.3.

All three rib types have a width  $w$  of  $9.5 \pm 0.5$  mm, the rounded ribs have a curved profile that is half a circle with diameter  $w$ . The outer diameter of all ribs is slightly smaller than the inner diameter of the pipe to enable placement.

Additional experiments are performed with single orifices. The rib geometries used for those experiments are shown in Fig. 2.16.



(a) Slots in the pipe wall with two dynamic sensors mounted.



(b) A dynamic pressure sensor.

Figure 2.4: Dynamic pressure sensors mounted on the pipe wall.

### 2.1.4 Sensors

The static pressure difference over the measurement section is measured using a differential diaphragm pressure transducer<sup>1</sup> connected to two pressure taps in the pipe wall, labelled "E" in Fig. 2.1. For some of the measurements, we also measure the local pressure fluctuations. Two or three dynamic pressure sensors<sup>2</sup> are flush-mounted with the wall at different positions within the pipe segment. These sensors are capable of capturing fluctuations above  $\sim 0.5$  Hz up to over 500 kHz.

Because the rib locations are not fixed within the pipe, the mounting locations of the dynamic sensors need to be adjustable as well. The sensors can be mounted at specific positions over a section length of approximately 25 cm. In this manner, at least one sensor can be located in between two ribs without overlapping with a rib at the pipe surface. The sensor and the mounting slots are shown in Fig. 2.4. During all experiments, the flow rate is measured halfway the flow loop, downstream of the pump and upstream from the measurement section, see "I" in Fig. 2.1.

For the experiments involving cavitation, the absolute pressure is obtained by connecting an analog manometer to the pipe downstream of the measurement section, close to the connection with the vacuum tank, as indicated with  $p_a$  in Fig. 2.1. The pressure is regulated through a connection to the same section of the flow loop. Thus, the absolute pressure is independent of the flow velocity. Between the measurement section and the pressure regulation, the flow passes a diffuser with a diameter ratio of 2.

<sup>1</sup>Validyne, DP15 Variable Reluctance Pressure Sensor, with a #42 (0-140 kPa) membrane

<sup>2</sup>PCB, type 102B18

The water temperature is measured using a PT100 thermometer submerged in the flow at the low-speed section (large diameter) of the flow (indicated with  $T$  in Fig. 2.1). The measurement of the temperature is necessary to be able to determine the viscosity, density and saturated vapour pressure of the water.

## 2.2 Configurations and measurements

The pressure measurements are divided in two types: static and dynamic. The static pressure difference is measured over the full test section only. This includes a smooth pipe section up and downstream of the ribbed segment. Because of the relatively large aspect ratio between the ribs and the pipe diameter, the measured pressure loss over the ribs dominates the results, while the frictional contribution of the smooth pipe sections is negligible<sup>3</sup>. However, the added losses caused by the in and outflow of the ribbed section are not negligible. To be able to quantify these contributions and exclude them from the desired flow losses, measurements are performed with different section lengths, i.e. number of ribs, for each configuration. The dynamic pressure is measured locally within the ribbed section and is therefore independent of the static pressure contribution due to the in and outflow regions.

Table 2.2: Numbers of ribs within the ribbed pipe segment.

rib type	pitch [mm]								
	12.5	15	20	25	30	35	40	45	50
<b>EL</b>	5, 7	5-10	5-10	5-10	7-10	5-10	5, 7-10	5-10	5-7
<b>RL</b>	-	-	6-9	6-9	6-9	6-9	6-9	6-9	-
<b>RS</b>	-	-	6-8	6-8	6-8	6-8	6-8	6-8	-

As described in Section 2.1.3, we use three types of ribs for ribbed segment measurements. An overview of all rib configurations is given in Table 2.2. The numbers in this table indicate the number of ribs in the pipe section used in the measurements.

For the rectangular ribs (EL geometry), sections with 5 to 10 ribs were used in the measurements. For rounded ribs with large (RL) and small (RS) inner diameter, 5 to 9 and 5 to 8 ribs were used, respectively. The rib pitch is defined by the period

<sup>3</sup>This was tested using the set-up without ribs. The flow losses were even smaller than could be reliably measured with the pressure transducer used, but of the order of magnitude expected for a smooth pipe flow.

of the roughness and thus includes the cavity length and the width of a single rib.

Table 2.3 provides an overview of the range of parameters that were used.

Table 2.3: Experimental parameters for the pressure measurements.

Parameter	Value
working fluid	water
working temperature	15-25 °C
acquisition time static pressure	10-20 s
acquisition time dynamic pressure	10 s
acquisition frequency dynamic pressure	10 kHz
acquisition frequency static pressure	10 or 4 kHz
maximum flow rate	$\approx 9.0$ l/s
maximum $Re$	$\approx 3.6 \times 10^5$
pipe diameter	50 mm

## 2.3 Convergence, uncertainties and corrections

Before looking at the results, the sources for possible errors and uncertainties in the data are briefly discussed. These include: convergence, influence of tap location, temperature effects and two experimental problems, i.e. leakage and system overheating.

### 2.3.1 Spatial convergence

In the context of a ribbed pipe, "fully developed" does not imply that there is no axial dependency of the statistical properties of the flow. Instead, it implies that the spatial dependency becomes, after a certain inflow region, periodic with the pitch of the ribbed geometry.

When the flow reaches this developed state within the measurement section, each added rib should add the same amount of drag to the system, implying a linear relation between total drag and the number of ribs. Whether the fully developed state has been reached can thus be checked by measuring drag versus number of ribs. Preparatory measurements with rectangular ribs showed that a section length of 5 ribs is sufficient to obtain developed behaviour for all geometries, while for a larger pitch a section of 4 ribs is sufficient.

### 2.3.2 Temporal convergence

The pressure difference over the measurement section is measured for 10 or 20 seconds with 10 or 4 kHz acquisition rates, respectively (see also Table 2.3), with the measurement length restricted by the internal memory of the camera and the highest acquisition frequency to allow simultaneous dynamic pressure measurements. A low-pass filter is used to remove fluctuations at frequencies above the cut-off frequency of the pressure sensor, which is estimated at  $\approx 100$  Hz. For most measurements, the remaining signal is reasonably flat, with an RMS error below 4%. However, some of the measurements show a small but significant increasing or decreasing trend, suggesting that those measurements were performed before a steady-state flow was established. These measurements were removed before further analyses were performed.

The dynamic pressure is measured over the same temporal range as the static pressure component, i.e. 10 seconds with a 10 kHz acquisition rate. With a lower cut-off frequency of 0.5 Hz embedded in the sensors, any low-frequency fluctuations in the flow have no significant influence on the recorded signal.

### 2.3.3 Temperature variations

The temperature measured in the flow (see Section 2.1.4) varies significantly, both within a single measurement (i.e. a full test with steps in a range from 0 to  $V_{\max}$ ) and between measurements (e.g. for different geometries). The variation in density within the observed temperature range, although included in the computations, is small. The influence of temperature on the viscosity is much larger and can deviate up to 18% within a measurement and up to 33% between measurements. Although the viscosity is not included in the expression for the friction factor, it is a parameter in the Reynolds number and thus reflected in the results. For the measurements concerning cavitation, the measured temperature is used to determine the actual value of the vapour pressure  $p_v$ .

### 2.3.4 Corrections for the pressure tap position and pipe deformation

The flow experiences a redevelopment region when exiting the ribbed section, schematically represented in Fig. 2.5.

In order to distinguish the drag contribution of this redevelopment region from that of the ribbed section, we note that we expect this contribution to be equal for all measurements corresponding to the same geometry (i.e., the same  $p$  and rib type). If the pressure tap is located beyond the redevelopment length, this

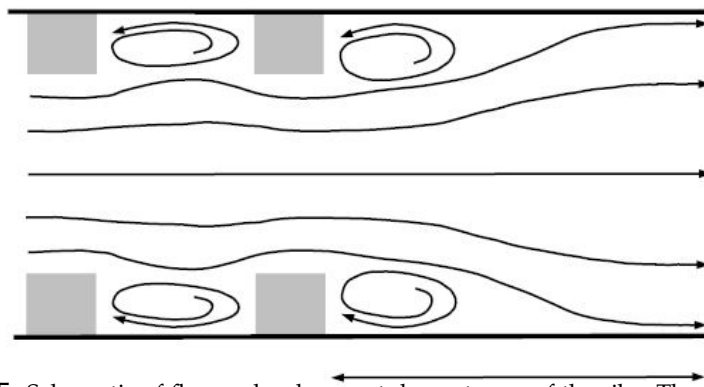


Figure 2.5: Schematic of flow redevelopment downstream of the ribs. The arrow below the pipe indicates the redevelopment length.

condition is fulfilled, given the negligible contribution of the developed flow through the smooth pipe. However, in some of the performed experiments the downstream pressure tap is unfortunately located within the redevelopment length. To be able to consistently include the full entrance and exit flow behaviour in every measurement, a correction is introduced. Appendix A explains the corrections we performed, which are, where necessary, applied to all data reported in the results further in this chapter.

Halfway the experimental campaign, an unfortunate incident happened and the pipe system reached temperatures high enough to locally cause small deformations in the perspex pipe. A small decrease in the outer diameter of the ribs was required to be able to fit the ribs through the slightly deformed pipe and continue the experiments. This change in set-up inevitably had some effect on the characteristics of the flow. For a few measurements, a proper comparison between the total pressure loss before and after the heating incident could be made.

Based on these data sets, assumptions regarding the effect of the adaptation of the ribs on the flow were extrapolated to the full set of measurements. Details on this procedure can be found in Appendix B. The obtained correction is applied to all relevant measurements.

### 2.3.5 System air-tightness

During the low-pressure experiments intended to study the impact of cavitation, it was crucial that no air was present in the system. This proved to be an experimental challenge, eventually severely limiting the scope of the experiments. During the earlier experiments that were performed, the amount of air that

leaked into the system was very small, and low-pressure experiments could be performed with reasonable results. Rapid deterioration of the original pump required the use of another type of pump, which was, on paper, suited for a low entrance pressure and was installed using a larger hydrostatic head.

Unfortunately, the adjusted set-up showed a larger leakage of air than the original set-up. Although many efforts were done and some significant improvements were made, to date the locations of the remaining leaks have not yet been found, severely diminishing the possibilities of further low-pressure experiments.

## 2.4 Static measurements: pressure losses, friction factors and geometric scaling

The pressure drop  $\Delta p$ , obtained for every geometry and corrected according to the procedures mentioned in Section 2.3.4, is expressed as a dimensionless loss factor  $K$ :

$$K = \frac{\Delta p}{\frac{1}{2}\rho V^2} \quad (2.1)$$

The velocity  $V$  can be chosen according to several definitions. In this chapter, unless indicated otherwise, the rib bulk velocity  $V_r = Q/\pi r^2$ , with  $r$  the inner diameter of the ribs, is used. The corresponding values for  $K$  and Reynolds number  $Re$  based on the same diameter are referred to as  $K_r$  and  $Re_r$ , respectively. Figs 2.6 and 2.7 show a selection of results obtained for ribbed sections of type EL and RL (rectangular and rounded ribs with  $r = 35$  mm). These figures show the non-dimensionalized pressure loss as a function of Reynolds number for a full ribbed section (in this case, 8 ribs in length) including the contributions of the in and outflow regions.

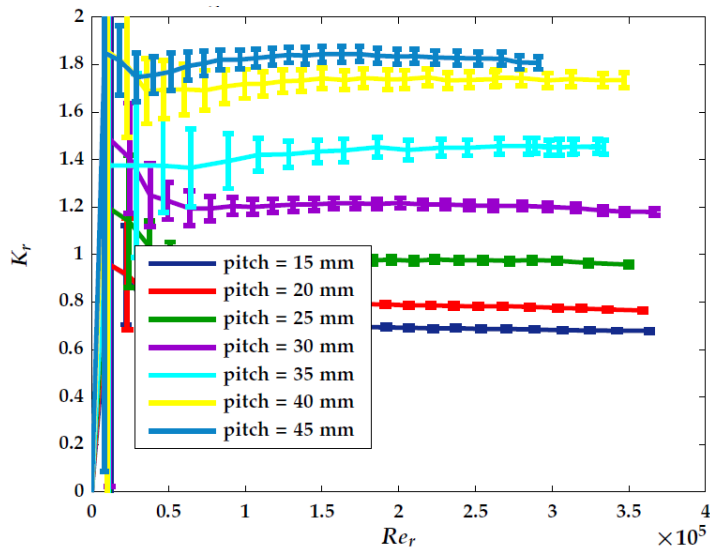


Figure 2.6: Dimensionless loss factor  $K_r$  vs  $Re_r$  in sections of 8 ribs of type EL with various pitches.

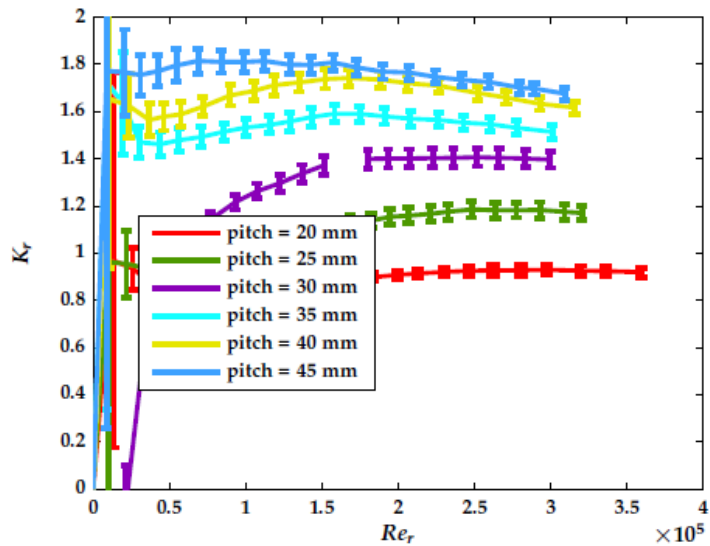


Figure 2.7: Dimensionless loss factor  $K_r$  vs  $Re_r$  in sections of 8 ribs of type RL with various pitches.

### 2.4.1 Loss per rib

The pressure losses, such as those for 8 ribs in Figs 2.6 and 2.7, include the inflow and outflow effects discussed in Section 2.3.1. By repeating measurements for

multiple section lengths as indicated in Table 2.2, we can remove these effects and evaluate the behaviour of a fully developed flow. With multiple sections of 5 or more ribs available, the linear trend between the number of ribs and total drag can be derived. The slope of this trend provides the static flow loss per rib;  $K_r/\text{rib}$  or  $K_r'$ , which can be determined for every available Reynolds number.

An example of the fitting procedure is shown in Fig. 2.8, where the slope of the dashed line yields  $K_r'$ .

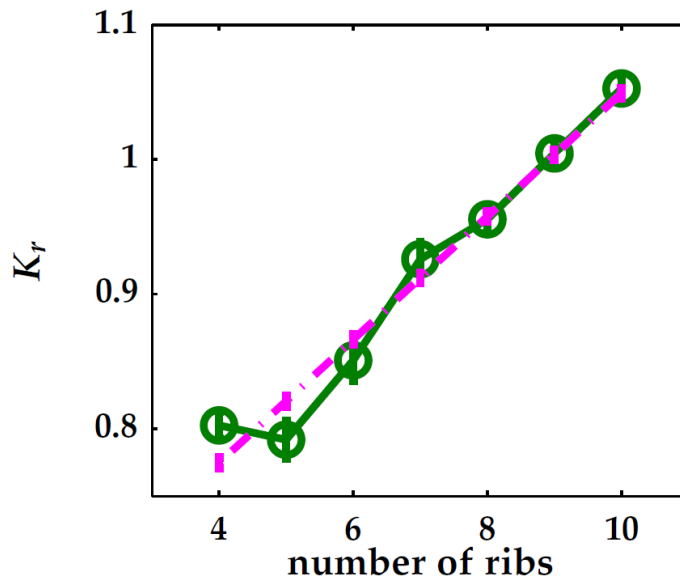


Figure 2.8: Example of the fitting procedure used to determine the flow loss per rib for developed flow behaviour.  $p = 25$  mm,  $Re_r = 2.8 \cdot 10^5$ , rib type EL

The uncertainty of the outcome is a combination of the regression uncertainty of the least squares fit and the uncertainty of the individual points, which in turn are a direct result of the measurement uncertainty as shown in Figs 2.6 and 2.7.

The linear regime to which the trend is fitted is present for every geometry (i.e. pitch and shape), which is an indication that the in/outflow contributions and the extra loss of every added rib becomes constant for sufficiently long pipe sections. In this regime, the flow is considered fully developed. The fitted line also never crosses near the origin of the graph showing  $K_r$  vs number of ribs, which means that the magnitude of the contribution of the in and outflow regions to the losses is far from negligible.

### 2.4.2 Friction factor

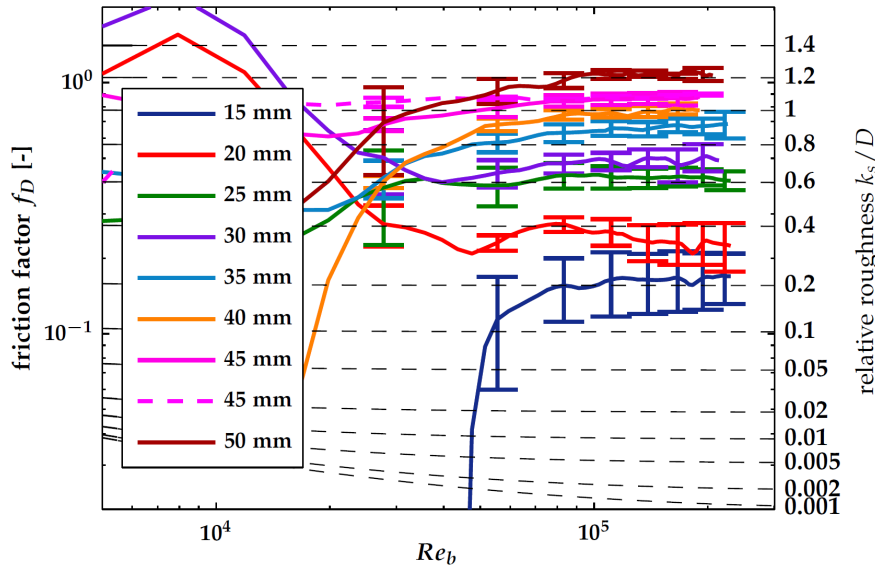


Figure 2.9: Darcy-Weissbach friction factor  $f_D$  for ribs of the EL type. The error bars are indicative and for clarity only depicted every 7th datapoint. The grey dotted lines are the Colebrook friction correlations for several values of the equivalent relative sand-grain roughness. The values in the legend indicate the pitch of the geometry.

The values for  $K_r'$ , obtained for every available Reynolds number, are transformed to the Darcy-Weissbach friction factor  $f_D$  (see also Eq. (1.7)). This representation enables a direct comparison with generic rough flows such as through pipe with a sand grain-type roughness. In general, the Darcy-Weissbach friction factor for any surface is defined using the pipe diameter. However, when using  $K_r'$ , the conversion involves an additional geometric multiplication, which depends on the inner rib diameter:

$$f_D = K_r' \frac{D R^4}{p r^4}, \quad (2.2)$$

with  $R = D/2$  and  $p$  the pitch.

Figures 2.9 and 2.10 show the friction factor as a function of bulk Reynolds number  $Re_b$  for rounded and rectangular ribs, respectively. Included in the graphs is the Colebrook friction correlation (see Eq. (1.8)) for several values of relative roughness  $k_s/D$ .

Representing the friction factors obtained with the Colebrook relation as in Figs 2.9 and 2.10 implies that the geometry is interpreted as a pipe with diameter  $D$

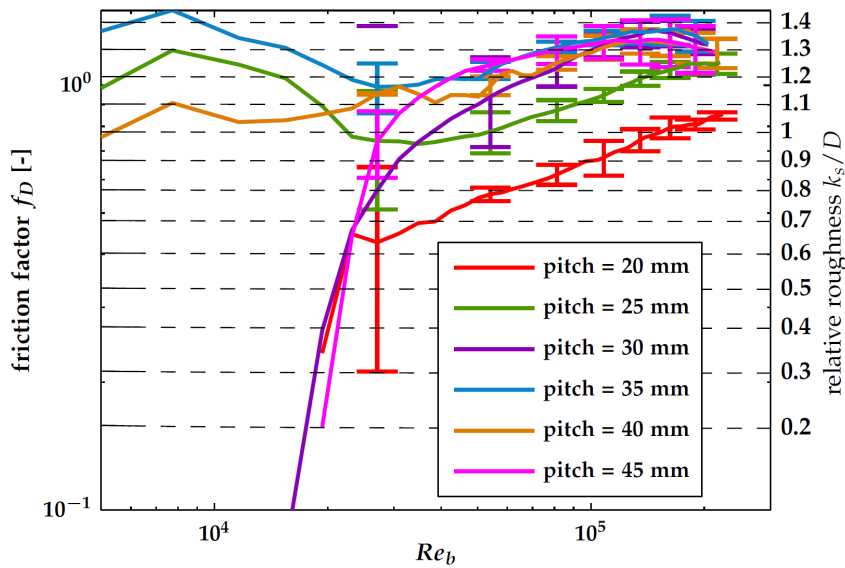


Figure 2.10: Darcy-Weissbach friction factor  $f_D$  for ribs of the RL type. The error bars are indicative and for clarity only depicted every 7th datapoint. The gray dotted lines are the Colebrook friction correlations for several values of the equivalent relative sand-grain roughness. The values in the legend indicate the pitch of the geometry.

and a roughness (due to the ribs) extending inwards from the surface. As can be seen from the magnitudes of the relative equivalent roughness indicated on the right hand side of graphs 2.9 and 2.10, this method of representation does not lead to a meaningful comparison as any relative roughness above 0.5 is not physically possible.

Figure 2.11 shows the results for EL-type ribs, based on the same data as in Fig. 2.9 but with a different interpretation: the pipe diameter is now set to be  $2r$ , and the cavities between the ribs are the roughness elements extruding outwards. This change in interpretation results in adjustment factors from  $Re_b$  to  $Re_r$  of  $\frac{R}{r}^5$  and from  $f_D$  to the friction factor based on the inner rib diameter  $f_{D,r}$  of  $\left(\frac{r}{R}\right)^5$ . The difference between the two approaches is schematically indicated in Fig. 2.12. The obtained results now appear shifted relative to the Colebrook friction correlation as can be seen in Fig. 2.11. The equivalent sand-grain roughness for both approaches can be calculated using Eq. (1.8). Similar to the significant difference in friction factor due to the geometric scaling, the equivalent roughnesses differ significantly.

In Table 2.4, the equivalent roughness for the EL, RL and RS geometries is

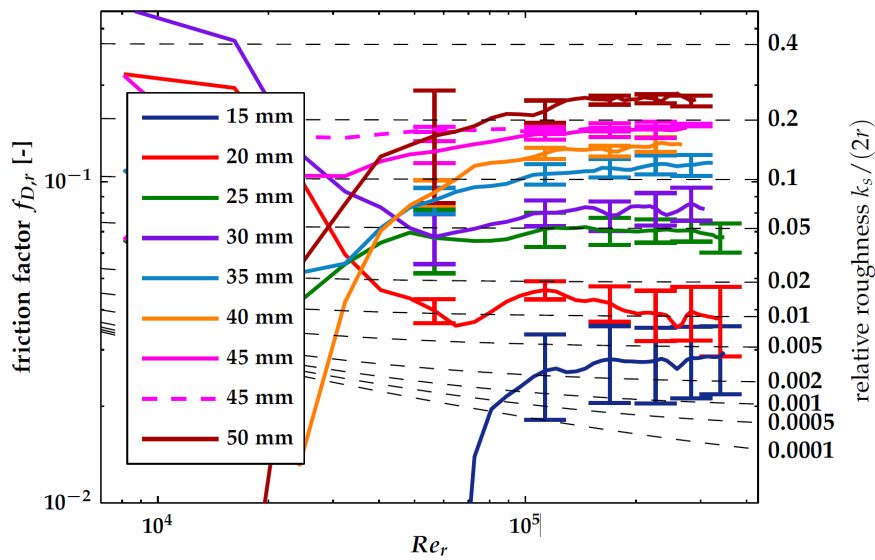


Figure 2.11: Friction factor  $f_{D,r}$  as calculated based on the inner rib diameter for rectangular ribs (type EL).

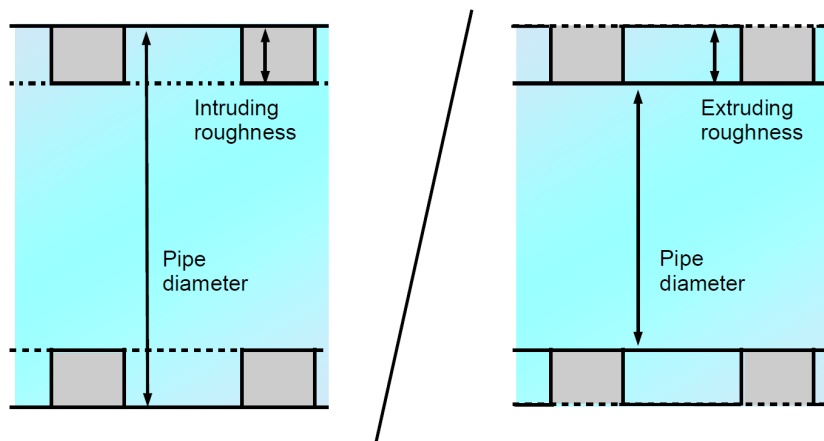


Figure 2.12: Two approaches to describe the roughness of a smooth pipe containing ribs.

provided for both friction factor definitions; the roughnesses are denoted as  $k_s(R)$  and  $k_s(r)$  to indicate the radius used in the corresponding definition. The Table also provides values for the rib pitch  $p$ , physical rib height  $h$  and mean roughness height  $h_m$ . Similarly to the two definitions for the pipe friction factor, the mean roughness height can be expressed according to both diameters, referred to as

$h_m(R)$  and  $h_m(r)$ . In the second definition, with the pipe diameter defined as the inner diameter of the ribs, the mean roughness height is defined as the mean cavity depth.

Table 2.4: Pitch, physical rib height, mean roughness height and equivalent roughness for all rib geometries, calculated based on either the outer ( $R$ ) or inner ( $r$ ) diameter of the ribs. All values are in mm.

geometry	$p$	$h$	$h_m(R)$	$h_m(r)$	$k_s(R)$	$k_s(r)$
EL	15	7.5	4.8	2.8	12.9	0.2
	20	7.5	3.6	3.9	16.8	0.4
	25	7.5	2.9	4.7	31.2	1.7
	30	7.5	2.4	5.1	35.6	2.3
	35	7.5	2.0	5.5	44.8	4.0
	40	7.5	1.8	5.7	49.4	4.9
	45	7.5	1.6	5.9	53.8	6.3
	50	7.5	1.4	6.1	60.8	8.5
RL	20	7.5	3.1	4.4	53.4	6.4
	25	7.5	2.5	5.0	62.6	9.1
	30	7.5	2.1	5.4	68.9	11.6
	35	7.5	1.8	5.7	68.7	11.5
	40	7.5	1.5	6.0	66.7	10.7
	45	7.5	1.4	6.1	67.0	10.9
RS	20	11	6.2	4.7	86.6	4.1
	25	11	3.8	7.2	98.2	7.0
	30	11	3.2	7.8	101.1	8.1
	35	11	2.7	8.3	104.2	9.0
	40	11	2.4	8.6	103.5	8.7
	45	11	2.1	8.9	105.5	9.4

### 2.4.3 Relevance of the friction factor definitions

The equivalent sand-grain roughness is a measure for the "effective" roughness of the geometry. In this context, Table 2.4 clearly shows that using  $k_s(R)$  is not a proper way to describe the geometry. In all cases,  $k_s(R)$  exceeds  $h$  by at least a factor of 2, and in most cases,  $k_s(R)$  extends far beyond 25 mm, indicating a roughness larger than the radius of the pipe.  $k_s(r)$  yields much more realistic results, with a similar order of magnitude as both the physical height  $h$  and the mean roughness height  $h_m(r)$ . Only for the EL geometry with  $p = 15$  and 20,  $k_s(r)$  is very small compared to both geometrical roughnesses. This observation is not surprising, since these geometries are likely to correspond to the d-type flow regime, a regime in which the strong separation between cavity and core flow dismisses the cavity depth as a relevant parameter for the contributions to the flow drag (see also Section 1.4.6).

$k_s$  can never relate directly to the physical rib height only due to the additional dependence of flow drag on rib shape and pitch. The mean roughness height  $h_m$  takes into account the roughness density and is thus a simple attempt to incorporate the pitch in the roughness description.  $h_m(R)$  is clearly not a proper parameter, since the drag increases with pitch, while the roughness density decreases.  $h_m(r)$  might be a better choice, with a positive trend between pitch and drag. However, the mean roughness height, regardless of the choice of effective pipe diameter, will always converge towards a constant value (e.g.  $h$  for  $h_m(r)$  and 0 for  $h_m(R)$ ), whereas the equivalent sand-grain roughness does not.

### 2.4.4 Pressure loss and friction versus pitch

From Figs 2.9 and 2.10 it is clear that the ribs with rounded (RL/RS) and rectangular (EL) cross sections induce very different flow behaviour within the investigated range of Reynolds numbers.

For the rectangular ribs,  $K_r'$ ,  $f_D$  and  $f_{D,d}$  converge to a Reynolds number-independent plateau, the value of which depends on pitch as shown in Fig. 2.13.

For the rounded ribs (RL/RS; see Fig. 2.10), there is no convergence towards a Reynolds number-independent regime within the measured Reynolds number range. Results equivalent to those in Figs 2.13a and 2.13b can thus not be generated for the rounded ribs. However, the flow loss  $K_r$  does reach a maximum within the measured velocity range for all data sets except  $p = 20$  mm.

Using this maximum as a characteristic flow loss for the geometry, Figs 2.14 and 2.15 are obtained for the RL and RS geometries, respectively.

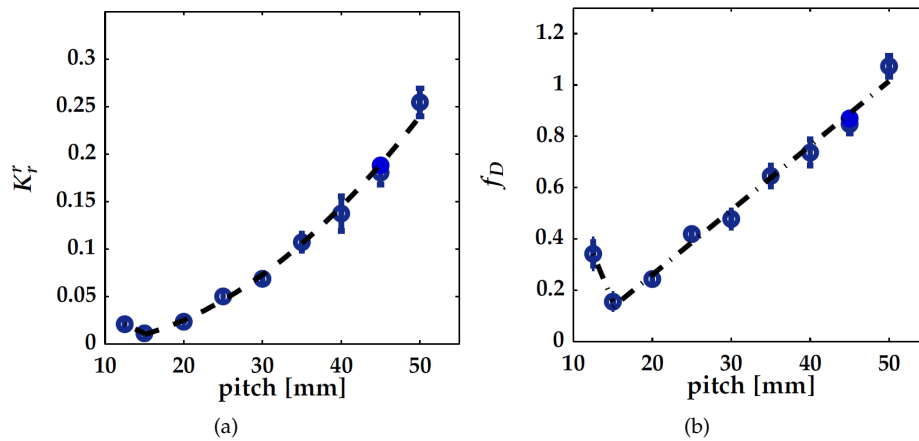


Figure 2.13: Plateau values of  $K_r'$  (a) and  $f_D$  (b) as obtained from their plots versus  $Re$ , as a function of pitch for rectangular ribs (EL geometry). Note that this graph includes data for  $p = 12,5$  mm; the corresponding curve is, for clarity, omitted in Figs 2.9 and 2.11.

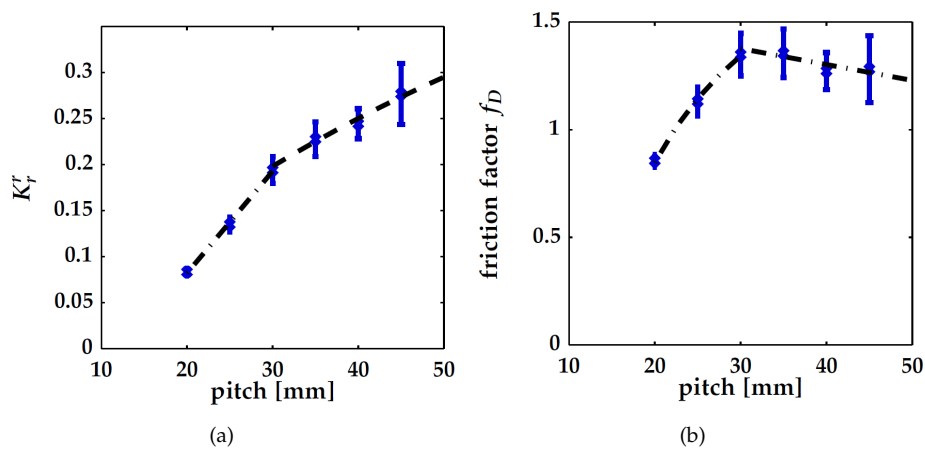


Figure 2.14: Maximum values of  $K_r$  (a) and  $f_D$  (b) as a function of pitch for the RL geometry.

## 2.4.5 Scaling trends for rectangular ribs

For rectangular ribs (EL), Fig. 2.13b displays a linear trend of the friction factor with pitch, with the exception of the data for  $p = 12,5$  mm. This indicates a

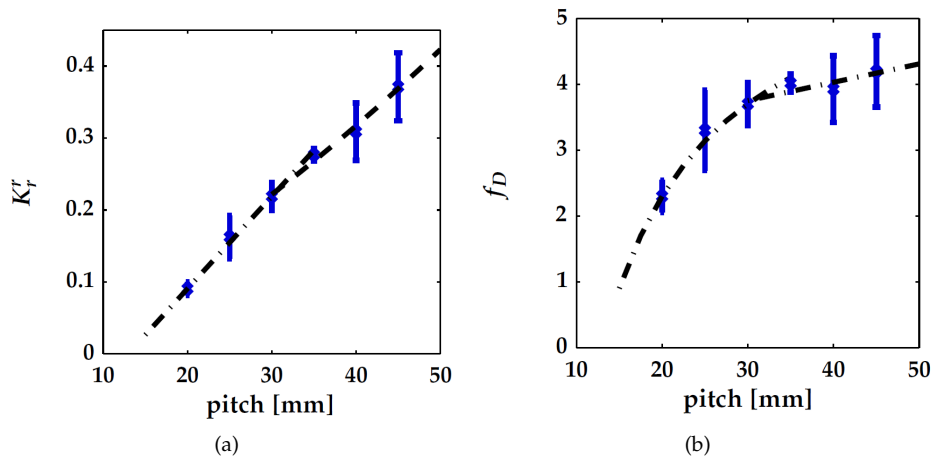


Figure 2.15: Maximum values of  $K_r$  (a) and  $f_D$  (b) as a function of pitch for the RS geometry.

change in regime, coinciding approximately with the boundary between d-type and intermediate-type roughness found in literature (see Section 1.4.6). In Fig. 2.13a, the approximately constant flow loss in the first regime strengthens this observation; in the d-type regime, the flow loss per rib is independent of pitch.

The linear trend in the second regime for  $f_D$  vs  $p$  crosses zero at a pitch of approximately 10 mm, corresponding to the width of the ribs. This suggests that the physically most relevant parameter for the frictional scaling is the cavity width  $l = p - w$ , rather than the pitch of the ribs. The flow loss for each individual rib thus scales according to  $l \times p$ , which resembles the quadratic dependency on  $p$  as visible in Fig. 2.13a.

This scaling does not correspond to the results for k-type roughness from e.g. Webb (1971), who reports inverse dependencies on the pitch, i.e. a decreasing friction coefficient with increasing pitch for  $p/h > 10$ . Han et al. (1978) do provide a positive correlation between  $f_D$  and  $p$  for  $10 > p/h > 5$ , but much weaker than the linear dependency observed here. The results for the pressure drag by Cui et al. (2003) match a linear dependency on cavity width for two available measurements with  $p/h = 2$  and  $p/h = 5$ .

The observed regime thus matches the characteristics of an intermediate roughness. The transition from intermediate-type to k-type roughness is, based on literature, expected to occur at a pitch of approximately 40-45 mm (Jiménez, 2004). Based on the current results, the presence of this transition cannot be confirmed.

### 2.4.6 Scaling trends for rounded ribs

As is the case for rectangular ribs (EL), two regimes can be determined for rounded ribs (RL and RS), although the scaling within those regimes is very different.

A change in regime for RL and RS occurs around a pitch of 30 mm. The first regime shows, similar to the results for the second regime for EL, a linear trend with the cavity width, rather than the pitch. This suggests that, similar to the situation for EL, the regime corresponds to an intermediate regime.

The first regimes of RL and RS, when expressed as  $K_r'$ , are almost identical. The mechanisms responsible for the most significant contributions to the losses in this regime are independent of the cavity depth. The losses in this regime are not independent of the pitch or cavity width, and therefore indeed do not correspond to a d-type regime, as was observed for the first regime for EL.

In the second regime of RL and RS, the trend of  $K_r'$  with pitch flattens, although there is still a positive trend. As the k-type regime is valid also for much larger  $p/h$  ratios (e.g. Webb, 1971), the value of  $K_r'$  must eventually, for larger values of  $p$ , converge to a constant, assuming the friction of the smooth pipe section to be negligible. The presence of a positive and linear trend for  $K_r'$  in the second regime thus indicates that a transition to a k-type regime has not fully occurred yet. However, especially for RL, the change in trend indicates that either at least a second intermediate regime occurs, or the transition to a k-type flow is not well defined and evolves gently with increasing pitch.

### 2.4.7 Reynolds number dependency and analogy with cylinder flow for rounded ribs

The friction factor as observed for both RS and RL geometries, other than for the EL geometry, depend on the Reynolds number over the full measured range of Reynolds numbers (see Figs 2.9 and 2.10). Where the rectangular ribs most likely have a flow separation at the upstream edge of each rib (see Sections 2.7.2 and 2.7.3 for further explanation), this separation point is not fixed for the rounded ribs. A small shift of the separation point with increasing Reynolds number is possible and most likely a cause of the Reynolds number-dependent friction behaviour.

The RL and RS configurations are in some aspects comparable with that of one half of the flow around a cylinder. To explore this similarity, the Reynolds number must be defined using the "cylinder diameter" or in this case the rib thickness and the bulk velocity based on the inner diameter of the ribs. The range of Reynolds numbers of interest hereby converts from  $3 \times 10^4 - 4 \times 10^5$  to  $1.2 \times 10^4 - 8 \times 10^4$ .

This range corresponds, for a flow past a circular cylinder, to that of a fully turbulent wake, and remains below the threshold at which the boundary layer itself becomes turbulent (e.g. Schlichting, 1979a; Kundu and Cohen, 2008). In this regime, the separation point is more or less Reynolds number-independent, as is the drag coefficient, although the latter does increase slightly with Reynolds number according to measurements as shown in Schlichting (1979a) or Kundu and Cohen (2008).

This means that the steady increase in friction factor with Reynolds number as observed in the current measurements is not explained by a direct analogy with a flow past a cylinder. However, for the RL geometries with a larger pitch, the friction factor shows a decreasing trend with Reynolds number for the highest Reynolds numbers within the range. In e.g. Kundu and Cohen (2008), it is mentioned that the drag crisis and the corresponding drop in friction coefficient around  $Re = 3 \times 10^5$  are sensitive to multiple factors.

Given the differences between the present geometry and a true cylinder wake-flow, it is probable that this observed decrease in friction is still related to the occurrence of a mechanism similar to the drag crisis of the flow around a cylinder.

#### 2.4.8 Interpretation for rectangular versus rounded ribs

In general, the pressure losses for rounded ribs (RL and RS geometries) are much higher than for rectangular ribs (EL geometry). It is plausible that, with increasing pitch, the shear layer originating from the ribs can penetrate deeper into each cavity, influencing the impingement area and leading to an increase in drag with increasing cavity width. This is valid for all three geometries. The mechanism can continue to dominate until the shear layer reaches the cavity bottom, which is probably the point of transition to a k-type roughness.

The analogy with flow past a cylinder does help to interpret the strong differences between the scaling with pitch in the intermediate regimes for EL ( $p = 15 - 20$  mm) and RL ( $p = 20 - 30$  mm). The relatively large differences in losses can be attributed to the presence of a broad 'wake' behind the rounded ribs, as opposed to a sharper and less diffuse shear layer originating from the sharp edge of the EL geometry.

The flow penetration into the cavity also results in a pitch-dependency of the approach angle of the flow onto the ribs. In the case of RL, this results in a shift of the point of separation, whereas for EL the separation point is fixed. A separation point further upstream of the rib leads to a larger wake region, which increases the total drag, similar to the case of flow past a cylinder. This mechanism might be the cause for the stronger increase of  $K_f^*$  with  $p$  for RL in comparison with EL.

## 2.5 Orifice losses or flow over a single rib

Next to measurements on ribbed segments, we study the effects of single ribs. A single orifice can be seen as the limiting case for a ribbed section with a pitch reaching infinity.

For these results, no analysis similar to that described previously for the ribbed segments, resulting in a friction factor, can be performed. However, a direct comparison of the non-dimensional losses over a single rib — stated otherwise: the flow through a single orifice — can be made for the various rib shapes. Fig. 2.16 shows the single-rib geometries used. Geometries A and C are asymmetric and were measured in two configurations, referred to as geometries A/B and C/D, respectively. Geometries E and F are identical to those used in the ribbed segments EL and RL discussed before. All used rib geometries have an inner diameter of 35 mm.

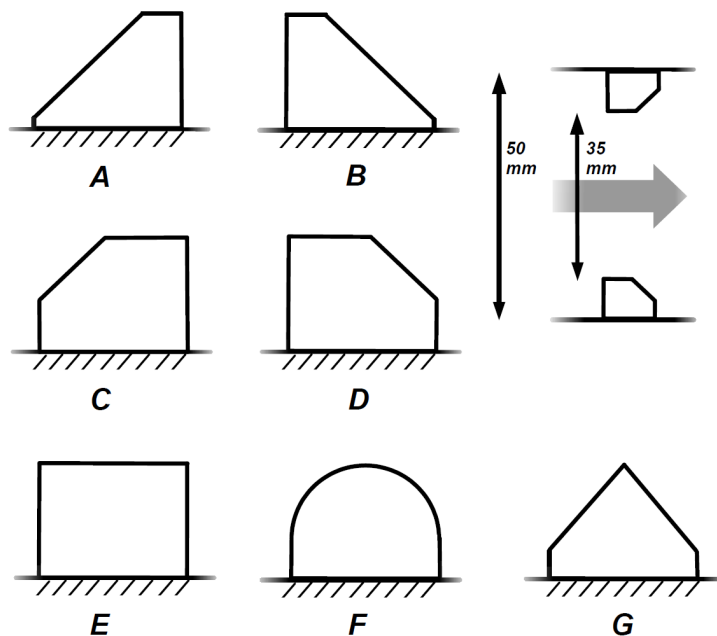


Figure 2.16: Rib geometries used for single-rib experiments. All ribs have a maximum width of 9.5 mm. The flow direction with respect to the ribs is indicated by the grey arrow in the upper right drawing.

Figure 2.17 shows the non-dimensional pressure loss  $K_r$  as a function of  $Re_r$  for all

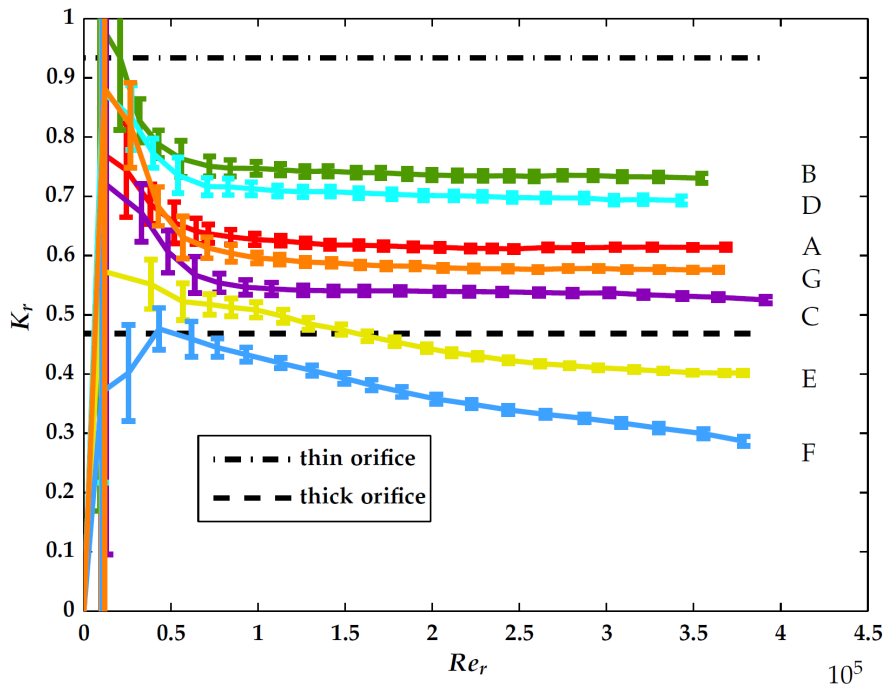


Figure 2.17: Single-rib losses for various rib shapes. Labels A-F refer to the shapes shown in Fig. 2.16. All ribs have a 35-mm inner diameter. Dot-dashed and dashed lines indicate the losses for thin and thick orifices according to Eqs (1.20) and (1.21), respectively.

available geometries. The figure also includes the correlations for non-recoverable pressure loss for a thick and thin orifice as described in Section 1.5.2.

The shape of orifice geometry E is similar to the ribs used for the thin and thick rib correlations indicated in Fig. 2.17. Although the criterion for a thick orifice, i.e.  $w/d > 0,5$ , is not fulfilled, the relative proximity of the result to the relation for a thick orifice suggests that the flow does reattach within the orifice.

All other geometries have a very small inner orifice surface, at most  $w/d = 0,27$ , making such a reattachment very unlikely. The best applicable reference geometry would thus be a thin orifice. For comparison, the thin-orifice correlation (Eqs (2.3) or (1.20)) is used as a reference case for the evaluation of all orifice geometries:

$$\Delta P = \frac{\rho \zeta V_b^2}{2} \left[ \frac{1}{\sigma \sigma_c} - 1 \right]^2 \quad (2.3)$$

An adjustment of either the contraction coefficient  $\sigma_c$  for a thin orifice determined by the Chisholm correlation (Eq. 1.19) or the empirical constant  $\zeta$ , which is, for

Table 2.5: Adjustment factor for the contraction coefficient  $c_\sigma$  and empirical constant  $\zeta$  needed to match the measured results for single ribs with Eq. (1.21).

rib shape		$c_\sigma$	$\zeta$
B		1.08	0.78
D		1.10	0.74
A		1.14	0.65
G		1.17	0.62
C		1.20	0.56
E		1.30	0.43
F		1.42	0.31

a thin orifice, equal to one, or a simultaneous adjustment of both is required to match the results to this equation. Table 2.5 shows the adjustment factors  $c_\sigma$  applied to the contraction coefficient and  $\zeta$  required to match the single-rib measurements to the thin-orifice correlation. Both factors are computed independent of each other, not taking into account a simultaneous application of both adjustments for  $c_\sigma$  and  $\zeta$ .

For the rounded rib (geometry F), no Reynolds number-independent region is present and the displayed value matches the value at the highest available Reynolds number.

Some trends related to the rib shape can be distinguished for the single-rib measurements. Geometries A, C and G, each with a slanted edge on the upstream side, cause less drag than geometries B and D, which only have a slanted edge on the downstream side. However, all geometries with a slanted edge induce a higher drag than the rounded and rectangular rib shapes.

Comparing geometries A with G and B with D reveals that a longer slanted edge results in additional drag. The result of geometry G does not, as might be expected, sum the drag-increasing effects of both slanted edges. This indicates that the mechanisms responsible for the increase in drag of the slanted geometries with respect to the rectangular rib do not occur independently from each other.

Using the adjustment factors  $c_\sigma$  listed in Table 2.5 as a measure, it is expected that the orifice measurement results predict the magnitude of the flow contraction.

Where the change in vena contracta is not responsible, the parameter  $\zeta$ , describing the efficiency of the contraction and expansion, must have changed.

The two geometries with the highest losses, B and D, closest to that of a thin orifice, are effectively a thin rib with a wedge added on the downstream side. The three following geometries, A, G and C, each have a ramp on the upstream side of the orifice. It is likely that the first two geometries, B and D, mainly feel an effect in the expansion region, not affecting the vena contracta itself, thus attributing the difference with a thin orifice to a change in  $\zeta$ . In the second group, the vena contracta is presumably less strong due to the change in inflow direction, which enables the flow to follow the geometry better, creating a thinner recirculation area.

### 2.5.1 Comparing orifice flow and flow through a ribbed section

As mentioned above, a single orifice can be seen as the limiting case for a ribbed section with  $p \rightarrow \infty$ . The results for the single-rib geometries thus correspond to a different flow regime than the results for the intermediate regime for EL-type multi-rib sections (Section 2.4.5). However, the second regime for RL and RS geometries does, as argued in Section 2.4.6, correspond to the onset of a k-type roughness. This suggests that  $K_r^r$  in Fig. 2.14a converges to a value of  $\sim 0,36$ , obtained for geometry F from Fig. 2.17 at  $Re_r \sim 2 \times 10^5$ , that is the Reynolds number corresponding to the location of the maximum in Fig. 2.9. The proximity of this value to the value for  $p = 45$  mm strengthens the hypothesis that the behaviour shown in Fig. 2.14a indeed corresponds to a transition towards k-type roughness. The regime observed for EL in Section 2.4.5 is clearly not a k-type regime. However, the transition to a k-type flow is likely to occur for slightly larger pitch. For that regime, the asymptote value of  $K_r^r \sim 0,4$ , obtained for geometry E in Fig. 2.17, applies. Whether this occurs through a smooth transition, an abrupt one or even a overshoot, cannot be concluded from the available results.

The Reynolds dependency observed for single-orifice geometry F, corresponding to the RL geometry, is very similar to the Reynolds dependency of the RL results. This indicates that the Reynolds dependency is caused by the rib directly, not by interactions with up/downstream cavities or the recirculation area within the cavity. From the fact that this dependency is only strongly present for geometry F, we conclude that the similarity explanation of Section 2.4.7, using the wake mechanics of a cylinder in a free flow as a reference, remains a plausible explanation.

## 2.6 Cavitation impact

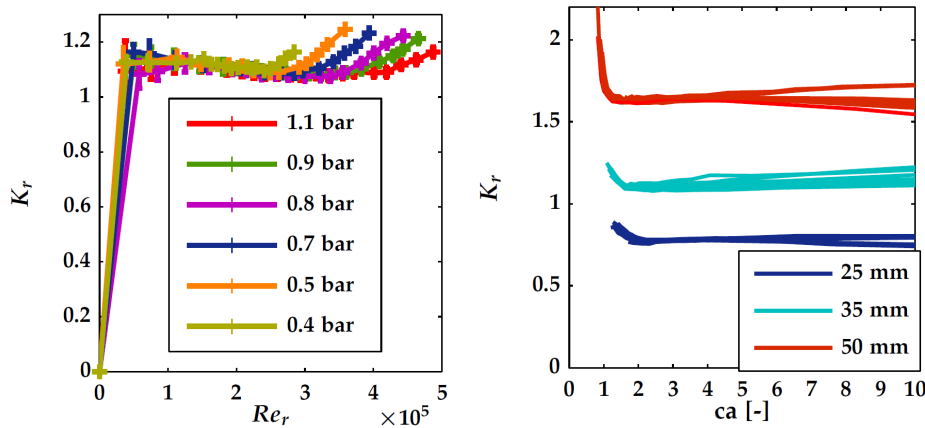
In the preparatory experiments, some measurements were included intended to examine the impact of absolute pressure on the flow losses. Fig. 2.18a shows the impact of absolute pressure on the flow losses for a single-rib geometry.

The results for lower pressures deviate from those for ambient conditions, with the onset of the deviation occurring at lower Reynolds numbers for lower absolute pressures. The measurements are also compared using the cavitation number  $Ca$  rather than the Reynolds number:

$$Ca = \frac{p - p_0}{\frac{1}{2}\rho V_r^2}, \quad (2.4)$$

with  $p_0$  the vapour pressure of the water.

The result is shown in Fig. 2.18b for three geometries over a range of absolute pressures between 0.33 and 1.07 bara. The curves for the same geometry at various pressures collapse; a behaviour observed for all three pitches investigated.



(a)  $K_r$  vs  $Re_r$  for six absolute pressures as indicated in the legend.  $p = 35$  mm.

(b)  $K_r$  vs  $Ca$  for three pitches as indicated in the legend. All absolute pressures as indicated in (a) are included; for  $p = 25$  mm, only 3 pressures are available.

Figure 2.18: Dimensionless loss factor  $K_r$  versus Reynolds number (a) and cavitation number (b). The ribbed segment is of the EL type with 5 ribs for all presented data. For clarity some intermediate curves were omitted from (b). The absolute pressures as displayed in the legend of (a) are measured in the de-aeration segment as indicated in Fig. 2.1.

The absolute pressure and pressure difference are not measured at the same

location. This means that the change in diameter through the diffuser is not taken into account in the absolute pressure relevant for the vaporization. This pressure difference is independent of geometry. The offset it causes in the cavitation number is given by:

$$Ca_o = \frac{\Delta p_d}{\frac{1}{2}\rho V_r^2} \approx C \quad (2.5)$$

with  $\Delta p_d$  the pressure loss over the diffuser. Although  $\Delta p_d$  can be estimated based on the diffuser geometry, this is not necessary because its effect on the results is by creating an offset, not by influencing the overall trends. The collapse of the curves confirms that the measured differences are indeed due to cavitation. However, whether the impact is solely an effect of the increased total volume caused by the local presence of gas bubbles or a more complex form of flow interaction with the cavitating regions can not be determined based on the available results.

Surprisingly, lowering the absolute pressure leads to an increase of pressure loss, which is a trend opposite to that encountered in flow tests for LNG hoses (see Section 1.6). The current experiments do not suffer from an important secondary effect which was present in those experiments: a change in the hose geometry as a function of both absolute pressure and flow velocity. It is therefore likely that the results for the LNG hose were dominated by the effects caused by the changes in geometry, while the current experiments solely observe the impact of the cavitation itself.

## 2.7 Dynamic pressure

We measure the dynamic pressure for the rectangular rib geometry, at a location within the ribbed section where the flow is fully developed (as defined in Section 2.3.1). The pressure reading contains information about both strength and frequency of the pressure fluctuations in the flow, locally at the position of the sensor.

### 2.7.1 Fluctuation strength

The signal amplitude is a function of both flow velocity and geometry. While the velocity dependency is evaluated, a firm evaluation of the fluctuation strength as a function of pitch is not possible. This is due to the variation in position of the sensor with respect to the ribs, which is inevitable with the limited amount of sensor slots in the pipe wall (see Fig. 2.4).

In Fig. 2.19a, the velocity dependency of the RMS of the dynamic pressure fluctuations is shown for a pitch of 35 mm.

The trend of the fluctuation strength with flow velocity seems to be similar to that of the pressure loss. Indeed, when normalized with the square of the bulk velocity, a flat plateau emerges similar to that observed for  $K_r$  vs  $Re_r$  curves in Section 2.4. This behaviour is observed for every pitch that was investigated.

Figure 2.19b depicts the plateau value of these normalized fluctuation strengths as a function of pitch, showing a general increase of fluctuation magnitude with pitch. The influence of position with respect to the geometry on the measured fluctuations is demonstrated by comparing 2 simultaneous measurements in successive "cavities" by 2 identical sensors. For the particular geometry of Fig. 2.19a, the two sensors were located in very similar positions within the cavity, hence the similar results for both sensors. The large variation between the locations of the two sensors throughout the data sets prohibits a more precise evaluation of these results.

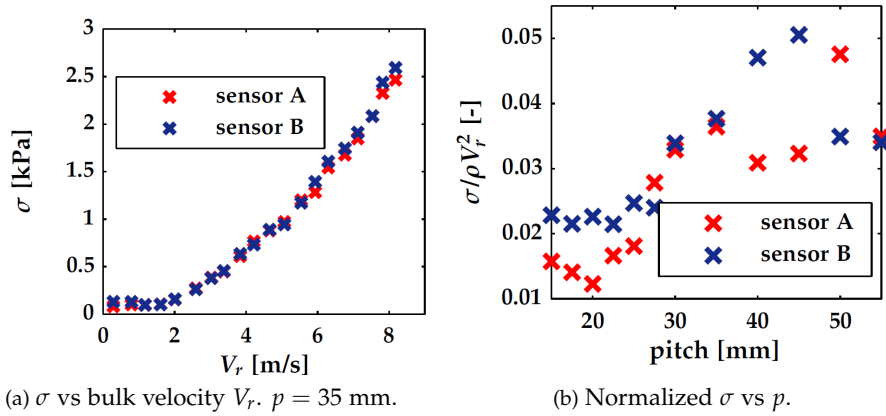


Figure 2.19: Fluctuation strength  $\sigma$  of the dynamic pressure. Blue and red symbols indicate two different sensors, located at the wall in successive cavities. Their positions relative to the ribs vary with pitch.

## 2.7.2 Frequency content

To determine the dominant frequencies, a power spectrum of the measured signals is computed and normalized with  $V_r^4$ . This equalizes the contribution at different velocities using the quadratic velocity dependency of the dynamic signal amplitude as discussed in Section 2.7.1.

Although the signals are very noisy, and looking at individual spectra reveals little information, clear trends emerge when displaying the power spectra for a single geometry at all available velocities in a single contour plot.

Figure 2.20a shows an example of such a plot for a pitch of 35 mm. As visible in Fig. 2.19a, the quadratic trend for this geometry disappears below approximately 2 m/s, and the spectrum normalization with  $V_r^2$  no longer suffices. For clarity, this region is omitted from Fig. 2.20a.

Two linear trends are visible, both of which cross the origin of the graph. One in the low-frequency range, reaching up to approximately 20 Hz at  $V_r = 8$  m/s and the second trend reaching higher frequencies up to 200 Hz for the same  $V_r$ .

Some of the geometries show more trends than visible in Fig. 2.20a. Fig. 2.20b shows this behaviour for a pitch of 17.5 mm. Now three similar linear trends are visible, reaching approximately 20, 180 and 400 Hz, respectively, at a velocity of  $V_r = 8$  m/s.

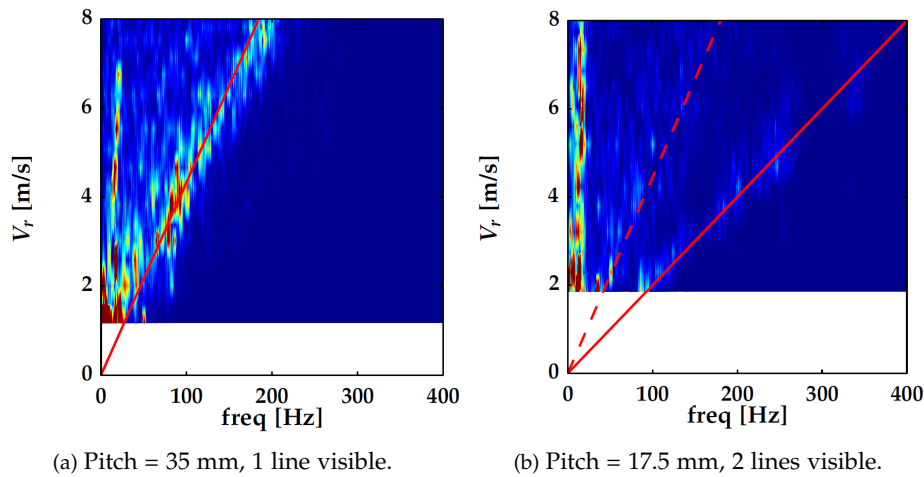


Figure 2.20: Contours of the normalized power spectrum of the dynamic pressure as a function of  $V_r$ .

The features most of interest are the frequencies that originate from flow-geometry interaction. Based on Section 1.5.3, this interaction consists of vortex shedding and impingement, which, in the fully developed regime, indeed result in an oscillation frequency that increases linearly with velocity as observed in Fig. 2.20.

The slope of the observed trends  $\frac{f_{peak}}{V_r}$  is a function of geometry, and can be expressed in the form of a Strouhal number as:

$$\frac{f_{peak} p}{V_r} \quad (2.6)$$

In Appendix C, the method used to obtain the desired slope from the available data is explained in more detail.

The trends visible in the low-frequency region do not display behaviour correlated with pitch. From this it is derived that, although the peak frequencies corresponding to this trend depend on velocity, they do not correspond to the vortex impingement behaviour.

For most geometries, only a single trend is clearly observed. The Strouhal numbers obtained from the clearest trend are displayed in Fig. 2.21. In the cases with two remaining trends visible, their slopes differ by approximately a factor 2, suggesting that those trends correspond to consecutive harmonics.

For the measurement with a 15-mm pitch, no trend other than the low-frequency region can be distinguished and therefore this result is connected by a dashed line in Fig. 2.21.

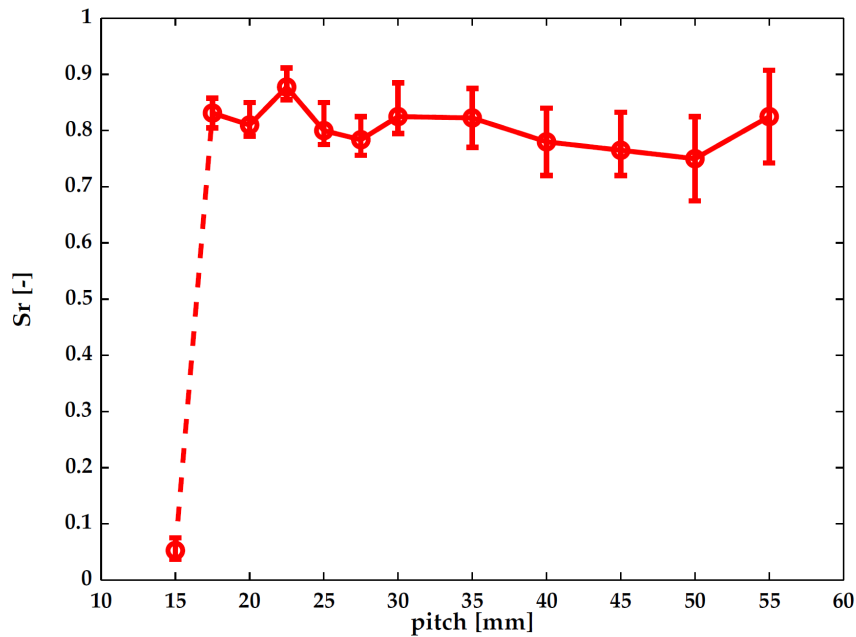


Figure 2.21: Strouhal number ( $Sr = \frac{f p}{V_r}$ ) as a function of pitch  $p$ .

### 2.7.3 Dynamic results

The linear trend in the dominant frequency of the dynamic power spectrum is attributed to vortices shedded on each rib and impinging on the next.

In Fig. 2.21, we deliberately use the pitch and not the cavity length, as would be the case for a single-cavity flow, as a geometric parameter in determining the Strouhal number. This results, as shown in Fig. 2.21, in a Strouhal number independent of the geometry. The dependency on pitch, rather than cavity width, indicates that the shedded vortices originate at the downstream edge of each rib. These vortices travel at the local flow velocity at rib crest height. This velocity is not known at this point. However, an estimate based on the geometry and bulk velocity can be made, based on the assumption of a parabolic flow profile with a zero crossing at half the rib height due to the presence of a recirculation region. This model results in a velocity at crest height of approximately  $0.43 V_r$ . Using this velocity rather than  $V_r$  itself in the computation of the Strouhal number as done in Fig. 2.21 thus results in  $1/0.43$  higher values, yielding a Strouhal number around  $St = 1.8$ . A single vortex, travelling and impinging, would result in  $St = 1$ , which implies that the second shedding mode, with two simultaneously present vortices, gives  $St = 2$ . The value of 1.8, taking into account the crude assumptions regarding the vortex travelling velocity, is close to 2, suggesting that the observed frequency trends correspond to the second harmonic. This also explains the presence of a weaker second trend, as observed in for example Fig. 2.20b, which is then related to the first harmonic shedding mode.



## Chapter 3

# Two-dimensional flow field measurements

In Chapter 2, the flow is investigated by means of pressure measurements, delivering global scaling behaviour of the flow through ribbed pipes. In this chapter, the method to obtain the flow field itself is described. The results of these measurements are reported and analysed in Chapter 4.

Particle Image Velocimetry (PIV) is a quantitative technique measuring flow velocities in a plane or volume. We apply planar PIV, monitoring two velocity components in a plane aligned with the axial flow direction. This chapter focusses on the adaptations of the experimental set-up and the specific measurement conditions used in the current work.

### 3.1 Set-up and experimental parameters

All measurements are done using the flow loop introduced in Section 2.1.1.

For the PIV measurements, always the most upstream mounting position on the pipe is used, which enables optical access to the pipe without obstructions due to the mounting positions of the dynamic sensors. This implies automatically that the optical measurements are performed without simultaneous dynamic pressure measurements. To enable PIV measurements, some additional components are added to the set-up: PIV measurements require optical access, a laser, a camera, flow seeding, a calibration procedure and a timing system, all of which are briefly discussed in the sections below.

### 3.1.1 Optical access: optical box & telecentric lens

The curvature of the pipe wall creates a large optical distortion. To minimize this distortion it is common practice to add a so-called 'optical box', consisting of a thin-walled rectangular box filled with the same liquid as the working fluid, i.e. water. Due to the location of attachment of the ribs to the pipe, the set-up requires the use of a detachable optical box, rather than a more convenient and robust box permanently fixed to a section of the pipe. In Fig. 3.1, the detachable optical box as used in our set-up is shown.

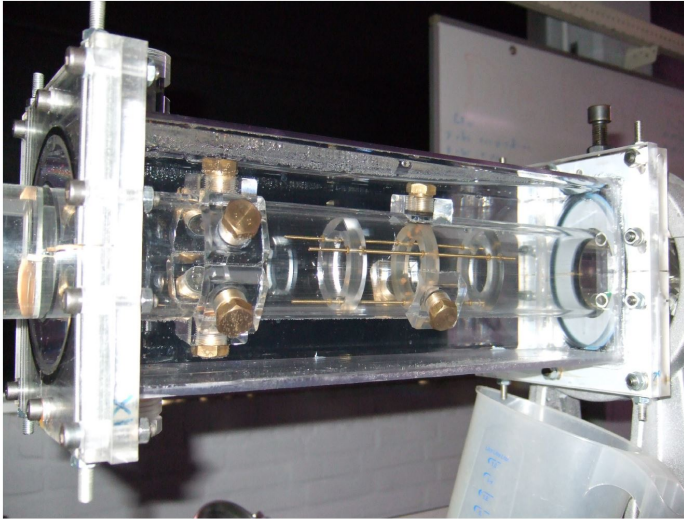


Figure 3.1: Optical box in position. A test-section of three ribs is placed inside the pipe, using bolted attachments that are located within the optical box. The box is not fully filled with water in this image, resulting in a thin layer of air between water and upper wall of the box.

The ribs inserted in the pipe form an optical obstruction. To have an unobstructed view through them, despite the many curves and edges present on the ribs, would require not only perfect transparency, but also a refractive index of the rib material matched to that of the water. Since neither conditions could be fulfilled, a non-visible area, also partially covering the cavity regions between the ribs, is unavoidable.

A telecentric lens (Vicotar, T240/0,27a) is used in the measurements to obtain a better view of the cavity regions (i.e. the axial pipe locations without a rib present). In contrast to a regular lens, a telecentric lens has a viewing angle

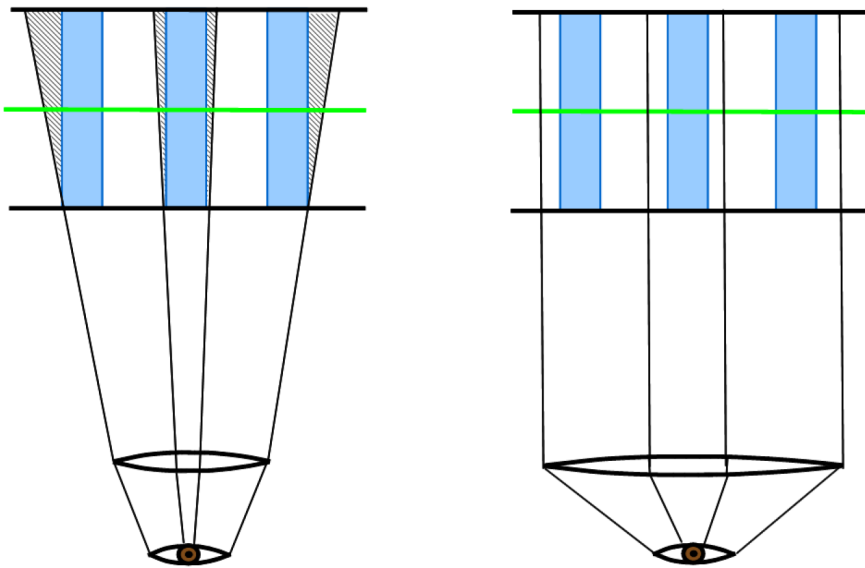
exactly orthogonal to the field of view, with a magnification fixed by the design of the lens. This requires the lens to be as large as the field of view in the object plane.

The lens we use has a maximum object field diameter of 78 mm. This diameter is reduced by the physical sensor size of the camera to a  $65 \times 65 \text{ mm}^2$  field of view, sufficient to cover the full pipe diameter and always have a minimum of two ribs within the field of view. At the same time, the lens is not unnecessarily large, which would reduce the spatial resolution of the recordings.

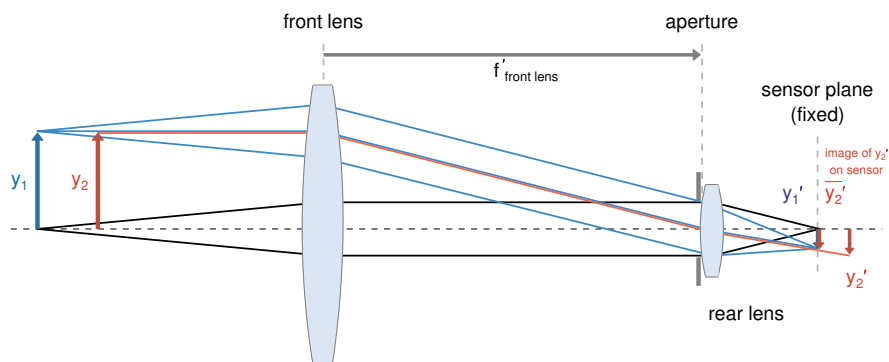
Figure 3.2a schematically shows the working principle of a telecentric lens. Figs 3.3a and 3.3b show the different images as obtained in practice. Note that the telecentric image shown in here is obtained with a different size telecentric lens, smaller in diameter than the one that was eventually used in the measurements. The photo unfortunately does not fully capture the situation as depicted in Fig. 3.2a but the different viewing angle on the rib clearly shows the working principle; the perspective present in the "normal" image has vanished in the photo taken with the telecentric lens.

Although the magnification is not a function of distance to the object plane, the telecentric lens does have a variable focal distance and focal depth. The latter can be varied between 10 and 2 mm, depending on the aperture used. In the measurements, a large aperture is used, with a corresponding thin focal depth, which is of the same thickness as the illuminated region of the flow (see Section 3.1.2).

Figure 3.3 reveals stripes and smudges on the surface of the pipe. The largest smudges were seen on the outer surface of the pipe and removed before any measurements were done. The horizontal lines are scratches on the inner surface of the pipe. They were created by the sliding contact with the ribs when positioning them inside the pipe and in the current setup cannot be avoided entirely. However, treating the inner surface with a polishing agent did improve the image quality significantly.

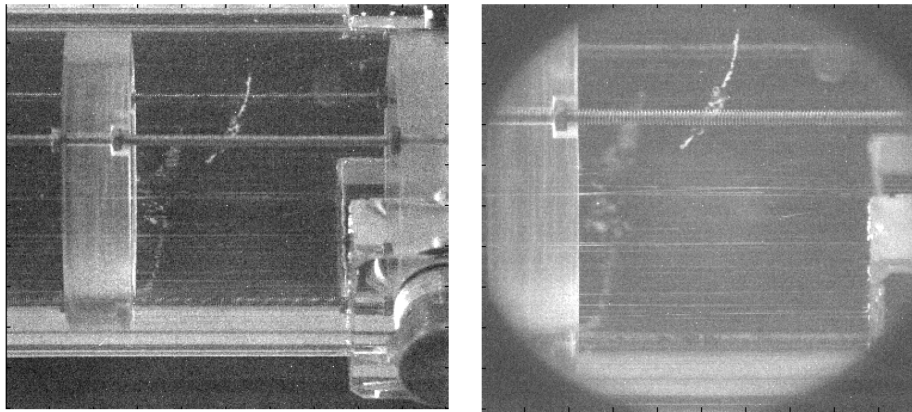


(a) Schematic representation of the use of a normal (left) and telecentric (right) lens to study flows in ribbed pipes. The blue areas are optically non-transparent ribs, gray areas represent shadow regions and the green line the PIV light sheet plane.



(b) Optical beam path of a telecentric lens; objects of the same size  $y_1$  and  $y_2$  with different working distances are depicted with the same size on the sensor plane (from: [www.vision-doctor.com/en/telecentric-lenses.html](http://www.vision-doctor.com/en/telecentric-lenses.html)).

Figure 3.2: Principles of a conventional lens and a telecentric lens.



(a) Typical image as made using a normal lens (focal distance 105 mm).

(b) Typical image as made using a telecentric lens (smaller diameter lens than that used in measurements).

Figure 3.3: Typical images produced by a conventional lens and a telecentric lens.

### 3.1.2 Recording images: camera & light source

Both the static and dynamic behaviour of the flow are of interest. A temporal resolution sufficient to capture the significant dynamic flow features, in particular the shedding motion of vortical structures, is thus required. Based on the dynamic pressure measurements (Section 2.7.3), the expected significant shedding motions have a frequency up to 400 Hz. To capture motion at this frequency, a high-speed camera is used (Photron Fastcam APX-RS). It has a maximum frame rate depending on the frame size. In full frame mode, the maximum recording frequency is 5 kHz. The full camera view is, due to the fixed size of the lens, slightly larger than the pipe diameter. This allows reducing the frame size and imaging at frequencies up to 6 kHz. Recordings covering only half the pipe diameter are made as well, allowing for an even higher frame rate, up to 12 kHz. The parameters used during the experiments are indicated in Table 3.1.

The number of consecutive images that can be recorded is limited by the internal memory of the camera (8 GB). Using cropped images thus leads to a higher total number of recordings. The limited memory results in a trade-off between recording frequency and recording duration.

The light source is a dual-cavity Nd:YLF laser (Litron LDY 304). The laser emits a pulsed beam, which is transformed to a thin ( $\sim 1.5$  to 2 mm) and wide ( $\sim 8$  cm) light sheet through the centre line of the pipe. The laser sheet is wider than the camera view to minimize the effect of a lower light intensity near the edges of

the light sheet. For both practical and safety reasons, the laser sheet is oriented vertically, illuminating the flow from above. This initially caused problems with bubbles that are present in the flow, trapped in the recirculation regions between the ribs at the top of the pipe. An improvement of the de-aeration of the flow loop (the diffusor, see Section 2.1.1) and a visual check before each measurement served to prevent the presence of trapped bubbles during the measurements. However, in some cases, small bubbles did occur, resulting in a loss of data in regions surrounding those bubbles. The laser intensity is kept low, approximately 25-30% of the maximum capacity to prevent local image saturation near the rib and pipe surfaces.

The recording frequency  $f_{cam}$ , illumination length and inter-exposure time  $\Delta t$  are each controlled separately. The recording frequency of the camera  $f_{cam}$  is determined by the desired temporal resolution of a measurement. The choice for  $\Delta t$  is determined by e.g. the flow velocities, the magnification and the image resolution. The illumination duration for each image is chosen to provide sufficient image illumination while avoiding motion blur and over-saturation. The timing of camera and laser was controlled using a system composed of two pulse generators and an initial trigger pulse provided by the user. Our experimental settings, including those of parameters  $\Delta t$  and  $f_{cam}$ , are summarized in Section 3.1.3. We also discuss our choice of  $\Delta t$  further in Section 3.1.4.

### 3.1.3 Parameter settings

The settings of all parameters related to the experiment are listed in Table 3.1. We performed PIV measurements on the longest available measurement section for each rib shape and pitch, i.e. 10 ribs for the EL geometry, 9 ribs for RL and 8 ribs for RS. No PIV was performed for a pitch of 15 mm because of the limited range of flow visible between the ribs. For each geometry, a measurement was performed at three different flow rates with both a full-frame and half-frame field of view. The flow rates for the EL and RL geometries were chosen to be 2.0, 4.5 and 7.0 l/s, with each flow rate expected to be in the fully turbulent regime based on the results of the static pressure measurements (see Section 2.4.1). For the RS geometry, the flow rates were chosen such that the bulk velocities based on the inner rib diameter approximated those of EL and RL, resulting in flow rates of 1.2, 2.9 and 4.4 l/s. Observation of a fully developed section of the flow was ensured by positioning the ribbed segment such that the ribs in view were at least 5 ribs from the first rib, and at least 1 rib from the most downstream rib.

Table 3.1: Parameters for PIV experiments

Parameter	Value	Condition
seeding particle size	$\sim 10 \mu\text{m}$	SpheriCell
particle-images per image window	8-10	$16 \times 16$ pixel interrogation window
laser sheet thickness	$\sim 2 \text{ mm}$	
magnification	0.274	fixed value
image resolution	$6.2 \cdot 10^{-2} \text{ mm/pixel}$	
camera frame size	1024 x 832 pixels 1024 x 432 pixels	full frame half frame
number of frames	7561 14563	full frame half frame
camera frame rate $f_{cam}$	1000 Hz 2000 Hz 3500 Hz 2000 Hz 4500 Hz 7000 Hz	full frame $V_r=2.1 \text{ m/s}$ full frame $V_r=4.7 \text{ m/s}$ full frame $V_r=7.3 \text{ m/s}$ half frame $V_r=2.1 \text{ m/s}$ half frame $V_r=4.7 \text{ m/s}$ half frame $V_r=7.3 \text{ m/s}$
exposure time delay $\Delta t$	440 $\mu\text{s}$ 190 $\mu\text{s}$ 120 $\mu\text{s}$	$V_r=2.1 \text{ m/s}$ $V_r=4.7 \text{ m/s}$ $V_r=7.3 \text{ m/s}$
processing window size	32 x 32 pixels 16 x 16 pixels	first iteration second iteration
processing window overlap	75%	

### 3.1.4 Exposure time delay

As mentioned in the previous sections, both the camera recording frequency  $f_{cam}$  and inter-exposure time  $\Delta t$  depend on the flow velocity. The inter-exposure time  $\Delta t$  is chosen such that a particle travelling at  $V_r$  travels a distance corresponding to 14 pixels. Assuming a parabolic flow profile, the maximum mean velocity is roughly 1.3 times the bulk velocity; taking into account temporal velocity

fluctuations, a maximum displacement of  $\sim 20$  pixels is plausible. Our a-priori knowledge about the flow inspires us to provide the PIV algorithm with a pre-shift of 8 pixels in axial direction, resulting in an effective displacement of  $\sim 12$  pixels instead of 20. With an initial window size of  $32 \times 32$  pixels, this means that a displacement is within the measurable range of 16 pixels. However, it does not comply with the optimization criteria for PIV, (8 pixels, (Adrian and Westerweel, 2011)) in the fastest flowing regions.

Another factor playing an important role in the determination of a proper setting of  $\Delta t$  is the out-of-plane motion that leads to a loss of correlation. With a 2-mm thick light sheet, the design rule of 8 pixels displacement allows for an out-of-plane velocity of the same magnitude as the total axial velocity component. The presence of large velocity gradients is a third feature putting limitations on  $\Delta t$ . With the observed particle image diameter of  $\sim 3$ -4 pixels, the third design rule allows for a shear intensity up to  $\sim 2000 \text{ s}^{-1}$  for  $V_r = 7.3 \text{ m/s}$ . In practice, this value is slightly exceeded in some cases (see Section 4.2) and the valid vector yield in the regions of highest shear is somewhat lower than desired.

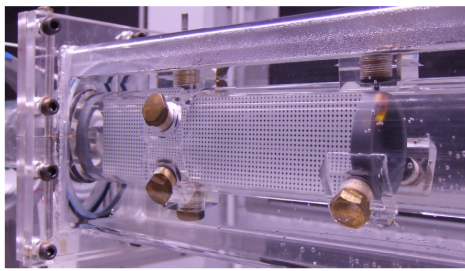
### 3.1.5 Calibration

The optical box ensures a fairly undistorted optical path from the camera to the image plane. Because of the telecentric lens, there is no variation in magnification within the image, provided that the camera, optical box and pipe are properly aligned. To determine the parameters needed to map the image plane exactly onto the camera chip and to be able to focus the lens on the image plane, a calibration is required. This calibration is performed by placing a calibration target inside the pipe, with its marked surface located exactly at the centre plane of the pipe.

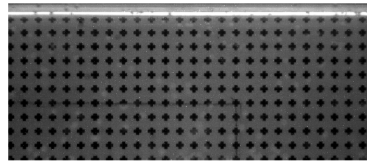
Figure 3.4 shows the calibration geometry and a typical calibration image. Calibration images were obtained for both the  $1024 \times 832$  and  $1024 \times 432$  pixel images to automatically incorporate the image cropping in the calibration. Both calibrations, using second-order image back-projection (Adrian and Westerweel, 2011), resulted in a calibration function with only small corrections apart from the magnification, confirming a proper alignment of camera, box and flow. In addition, we find that the image near the pipe walls is only marginally distorted.

### 3.1.6 Water quality

A total volume of  $\sim 150 - 200 \text{ l}$  of water flows in the closed loop. In preparatory experiments, we used pump an old sewer pump made of cast iron, which led to the presence of rust particles in the flow. The loop was also situated in an area



(a) Photo of the calibration target placed inside the pipe and optical box.



(b) Typical calibration image, in this case for half the pipe diameter with  $1024 \times 432$  pixels.

Figure 3.4: Image calibration to enable PIV measurements.

with direct sunlight, causing algae to grow. After these preliminary experiments, the pump was replaced and the flow loop moved to an area with only artificial light. The system was then flushed multiple times to remove all debris, but this proved less effective than expected. The water was refreshed every few experiments and the rusty colour was eventually fully removed, but small flakes of algae kept appearing throughout the whole experimental campaign, somewhat degrading the optical quality of the recordings.

## 3.2 Image pre-processing

Before applying the PIV algorithms, the flow recordings require pre-processing. Ideally, the images consist of bright particles on a dark and uniform background. In reality, sources of camera noise (such as thermal noise and dark currents) are always present but for typical PIV experiments relatively small. Other sources of noise are experiment-specific, such as light reflections from surfaces, due to both direct scattering from the light source and light scattered from particles onto a surface. Light source fluctuations also influence the outcome of the algorithms. The following paragraphs shortly describe the image enhancement steps applied before further evaluation of the data.

### 3.2.1 Normalization, background subtraction and enhancement

The image series can be divided into a stationary background and a fluctuating signal, where the latter corresponds to moving particles as well as fluctuating noise components. A single Nd:YLF laser has a low pulse-to-pulse energy

variation. However, the two laser pulses corresponding to the two image frames of an image pair, originating from the commonly used dual Nd:YAG laser with two separate laser cavities (used in the present measurements) can have a significant intensity difference (typically 10%). Because of this, the 2 image frames are normalized and enhanced independently from each other. First, each image is normalized with its own standard deviation as a first step to minimize the effect of global light intensity fluctuations. In doing so, care is taken to exclude pixels that reach saturation at any of the images from the corresponding image of the image pair in the time series, in order to avoid a bias in the normalization.

The stationary part of the normalized images, which is caused predominantly by reflections on the rib structure and which is bright in comparison with the fluctuating component, is removed using a background subtraction method. With a perfectly constant light source, the background can be obtained by taking the minimum occurring value of each pixel from the corresponding images over a sufficient time span. In the current work, a quantile value is used instead of the minimum to take into account the influence of intensity fluctuations, thus avoiding under-prediction of the background intensity. A quantile of 0.5 would be equivalent to the often used median pixel value, while a quantile of 0 or 1 reproduces the minimum and maximum, respectively. We use a quantile of 0.05 based on the data yield of the resulting images. The algorithms determining the displacement field and data yield are discussed in Sections 3.3 and 3.4, respectively.

Local variations in light intensity, particle density and particle size all negatively influence the image contrast. One method to improve and normalize the local contrast is to use a min-max filter (Adrian and Westerweel, 2011). This filter normalizes the image contrast locally. In a small area, typically  $3 \times 3$  to  $13 \times 13$  pixels, the minimum and maximum intensities of the envelope are determined and smoothed. Using those envelope values, the image is normalized to achieve a constant difference between the maximum and minimum image intensities (Adrian and Westerweel, 2011). To obtain the desired effect, the filter size should be larger than the small reflections from the particles but smaller than the large size variations in intensity. A filter area of  $9 \times 9$  pixels was selected based on the optimal resulting data yield. In practice, a filter area of 10 instead of 9 pixels was used accidentally. However, the effect of this asymmetry in the filter was shown to be of minimal influence. The min-max filter is applied after the background subtraction. In this manner, the otherwise dominant effect of static reflections does not influence the local normalization operation.

### 3.2.2 Image masking

The images contain boundaries between flowing and non-flowing regions. A distinction can be made between physical and optical boundaries. The physical boundaries are the pipe surface and ribs. Optical boundaries occur where the ribs or connecting rods obstruct the view to the object plane, without being a physical obstruction to the flow in that plane. In both cases, it is beneficially to know the location of the boundary before the application of the PIV algorithms (see Section 3.3). In the current work, the non-flowing regions are identified manually by drawing a mask onto the images, covering rib walls, ribs and connecting rods. Since the location of the boundaries does not depend on the flow but only on the geometry used, a single mask is drawn for each measurement set.

## 3.3 Image correlation with boundaries

For the image correlation, a two-step approach is used (Adrian and Westerweel, 2011). It is based on an image interrogation area of  $32 \times 32$  pixels in the first step and a refined grid with  $16 \times 16$  pixel interrogation areas in the second step, both with a window overlap of 75%. As mentioned in Section 3.1.3, a pre-shift of 8 pixels in the streamwise direction is applied to all data sets. After each interrogation step, a validation procedure is applied, which is described in more detail in Section 3.4.

Even when it is assumed that the image pre-processing and enhancement provide a near-perfect image, applying a basic PIV algorithm occasionally results in erroneous flow displacements near flow/non-flow boundaries. A bias towards zero displacement or, in the present case, towards the initial pre-shift, is introduced by the finite size of the interrogation windows.

This bias can be avoided by using masks for non-flow regions and applying an adjusted interrogation procedure, as described by Theunissen et al. (2008). This method is largely adopted in the current work, with only some minor changes. The procedure differs from the regularly applied cross-correlation by a weighed normalization, which accounts for the presence of non-flow regions. Interrogation areas with a mask overlap of 50% or more are considered as invalid and no displacement vector is assigned.

## 3.4 Vector validation

The results of the first interrogation step are validated before they are used as the initial displacement (pre-shift) for the second, refined, interrogation step.

Subsequently, the results of the refined interrogation are validated as well before being used in further data processing.

The most common validation method is the normalized median filter (Westerweel and Scarano, 2005; Adrian and Westerweel, 2011). This method has the underlying assumption that each vector has a certain coherence with the surrounding vectors. Thus, a single erroneous vector can be detected by comparison with its neighbouring vectors. Isolated erroneous vectors are removed very effectively by the normalized median method, even in the presence of erroneous vectors in the direct neighbourhood of the vector that is evaluated. However, a problem arises when patches of erroneous vectors are present. In practice, this can occur when there is a region of the flow where the signal is poor, for example due to a large scratch on the pipe surface or a large impurity in the flow (e.g. dirt flakes), blocking the view onto the laser sheet. As mentioned in Section 3.1.6, these conditions are indeed encountered for the current recordings. To identify patches of erroneous vectors, an iterative validation method is introduced in which the first iterations don't use a normalized median filter but a sorted median filter.

### 3.4.1 Sorted median filter

As with the normalized median filter, the sorted reference values are determined for both displacement components separately.

An  $N \times N$  neighbourhood is used, with  $N$  an odd integer, thus evaluating a symmetrical surrounding. Excluding regions corresponding to masked regions, the values within the neighbourhood are sorted into bins of which the number and width are based on the neighbourhood size and standard deviation of the values within the  $N \times N$  neighbourhood, respectively. The median of only the values within a bandwidth of 1 bin around the most occurring bin(s) is further used for validation. The difference between this sorted median value with the original displacement field is computed, transformed to a residual as a vector norm and normalized with the  $q$  quantile of the  $N \times N$  neighbourhood of these residuals. This methodology is similar to the normalized median method, with the additional use of a quantile  $q$  as opposed to the median value in the determination of normalization factor. Here,  $q$  is typically smaller than 0.5, resulting in a normalization less influenced by the presence of multiple spurious vectors in the neighbourhood. The validity of the vector is then determined by applying a threshold  $L$  on the residual.

Threshold  $L$  is very large for the first iteration, and smaller but still significantly larger than used for a typical normalized median validation for the remaining iterations.

The effectiveness of the sorted median method is based on a few assumptions.

First, the spurious vectors must be uncorrelated and thus not originate from e.g. an unmasked solid boundary. Uncorrelated spurious vectors result in random values, which can be distinguished from the true values, of course provided that sufficient correct vectors are present in the  $N \times N$  neighbourhood.

Since the bin size depends on the standard deviation of the values in the neighbourhood, the presence of many outliers would increase the bin size significantly. This would mean that whether or not a vector is considered an outlier depends partially on other, random valued, spurious vectors. The use of multiple iterations within a validation step neutralizes this effect.

Every additional iteration, taking into account only vectors that were accepted in the previous iteration step, results in a decrease of the standard deviation and thus a decrease of the bin size for the sorting operation. This converges quickly – usually within a few iterations – to a steady situation in which no additional vectors are detected.

### 3.4.2 Validation procedure

Both the initial and refined interrogation step of the PIV algorithm can produce erroneous "vector patches", since they are computed using the same image pairs. The validation after the first interrogation step can be relatively coarse: the removal of some non-spurious vectors, as long as all spurious ones are removed, does not appear to decrease the quality of the final result. Because the result of the first interrogation step only serves as initial displacement field for the refined step, it is smoothed before use, decreasing the accuracy while increasing the robustness of the vector field.

In the validation after the refined interrogation is performed, it is more important to find a proper balance between the robustness and accuracy of the method. Therefore, choosing the proper threshold values for the validation steps has a higher priority.

Sorted median validation is very suitable for detecting multiple and strong outliers. However, in order to further use the resulting data, we would need to perform a detailed assessment of the accuracy of the method compared to existing methods, which has not been done in the current study. Therefore, for the validation of the results of the second interrogation, a two-fold method is used: first, a sorted median validation is used, ensuring the removal of erroneous patches. The use of a relatively large threshold and  $7 \times 7$  pixel neighbourhood ensures that only spurious vectors are removed. This is followed by a more traditional normalized median filter (Adrian and Westerweel, 2011), using a  $3 \times 3$  neighbourhood and a threshold value of 2.5.

Rejected values are replaced in the same way as is done in the more common normalized median validation procedure, i.e. using the average value of the non-rejected neighbouring values.

### 3.4.3 Validation treatment at boundaries

It is not only the cross-correlation operation that requires additional care regarding the presence of boundaries in the image; the validation operations as described in Section 3.4.2 also need adjustments in the presence of masked areas. First of all, the normalized median filter requires adaptation when vectors are adjacent to a masked interrogation window, since the median is usually computed using the surrounding vectors. The adapted algorithm first computes the median value of the non-masked vectors in the assigned median range (e.g.  $3 \times 3$  or  $5 \times 5$ ). The same adaptation is used for the median of the residuals. In the vector replacement, the mask is used as well, and only the valid vectors are used to compute the replacement. This is also the case for the regular replacement algorithm; the only difference in this respect is that in the adapted algorithm, the minimum number of valid surrounding vectors depends on the location of the wall. Without this implementation, most vectors next to the masked regions will in all cases be rejected for replacement, leading to a significant loss of data at crucial locations within the image, for example near the edges of the ribs.

When using the validation and replacement steps iteratively, the implemented adaptations have an additional advantage. In most cases, after data replacement, there are many vectors that cannot be replaced due to the presence of too many invalid neighbours. When the non-replaced vectors are taken into account in the validation step and treated as if they are mask locations, validation of neighbouring vectors improves significantly. In this manner, the "patches" of erroneous vectors, as discussed in Section 3.4, are thus shrunk due to erosion. The iterative loop is continued until no holes or erroneous vectors are present in the data. With sufficient data quality, one or two iterations are required to reach this condition. Only small regions require more iterations. These are regions in which for example a scratch on the pipe surface or a strong reflection from a rib deteriorate the image quality such that multiple vectors can not be detected properly.

When using the converged vector field as a displacement offset for a finer grid, again the mask must be taken into account. When only the vector output is interpolated and used as a window shift, the interpolated values at the edges of the mask will include the zero values inside the mask and thus lead to an erroneous pre-shift. This can be solved by using the median of the vector field, with the mask included as described above. The median has valid values slightly

"inside" the masked regions as well, which for the interpolation appears to yield proper results also for windows partially overlapping with the mask. The interpolated displacement also provides a displacement at locations far inside the masked area, but since the interrogation procedure includes a mask as well, these values are omitted and do not appear to further influence the results.



## Chapter 4

# PIV: time-averaged patterns and profiles

In Chapters 4 and 5 we present the results and interpretations of the PIV measurements as introduced in Chapter 3, focussing on the mean flow properties (Chapter 4) and dynamic behaviour (Chapter 5), respectively.

### 4.1 Mean velocity fields for ribbed sections

Figures 4.1, 4.2 and 4.3 display the mean axial and radial components of the velocity for rectangular ribs (EL geometry) at various pitches.

The overall structure is that of a core flow with mixing layers over the ribs and a recirculatory flow in the cavities in between the ribs. We also see that the mixing layer between these two regions is much thinner for the shorter pitch geometry, penetrating less into the cavity. This is accompanied by an increase in axial variation in the core region. The radial (vertical) velocity reveals an inflow in the cavities at the downstream side, at first glance independent of pitch. The recirculation flow in the cavity changes in both shape and strength with increasing pitch.

The vector fields obtained from the recorded images have regions that can not be resolved due to image blockage. The ribs themselves cause non-visible regions in which we expect strong gradients in both axial and radial direction. This makes it difficult, if not impossible to obtain meaningful results within those regions from the present data. This is different for the region blocked by the presence of a connecting rod between the camera and the object plane. The small dimension

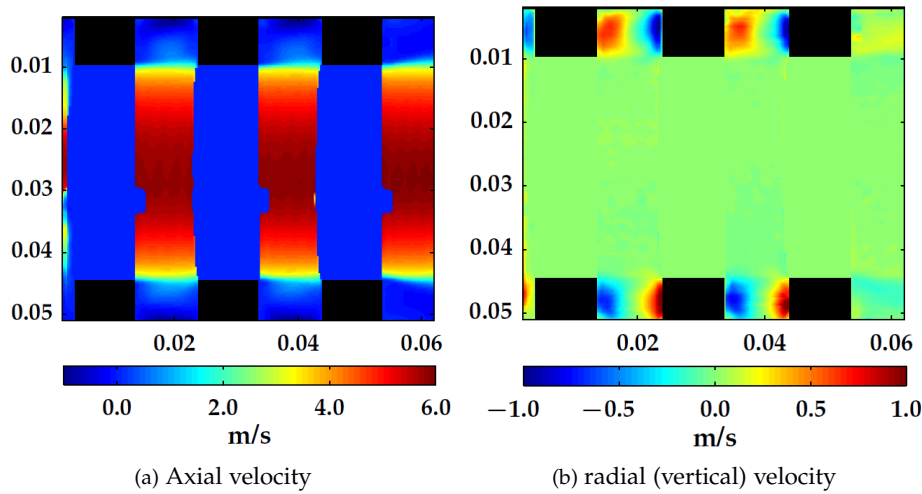


Figure 4.1: Mean axial (a) and wall-normal (b) velocity for rectangular ribs (EL geometry),  $p = 20$  mm,  $Re_r = 1.6 \times 10^5$ . Dimensions in metres, direction of the flow from left to right.

of this blocked region in a direction with relatively low velocity gradients allows for a data reconstruction. This reconstruction is performed on the instantaneous velocity fields using a spline interpolation method based on the first 2 available data points on both sides of the blockage. In all contour plots, the physical presence of ribs within the object plane is indicated by black regions. These are the regions where, also after reconstruction of the blocked regions, no data is available due to the blockage of view due the presence of the ribs.

Contour plots in the following sections are shown for the upper half of the pipe only, which is justified by the flow symmetry shown in Figs 4.1 to 4.3.

#### 4.1.1 Reynolds number dependency

Once normalized with  $V_r$ , the contours of the measurements on ribbed sections of the EL geometry at the three Reynolds numbers appear to be identical (not shown here). However, the measurements on the RL geometry do display a Reynolds number dependency. This is illustrated in Figs. 4.4 and 4.5 for the upper half of the pipe's cross section,  $p = 25$  mm and  $p = 40$  mm. The figure shows the RL results for  $Re_r = 7.3 \times 10^4$ ,  $1.6 \times 10^5$  and  $2.5 \times 10^5$ , each with their colour range adjusted to the corresponding Reynolds number. The figure also includes results for the EL geometry at  $Re_r = 1.6 \times 10^5$  (Figs 4.4a and 4.5a, respectively).

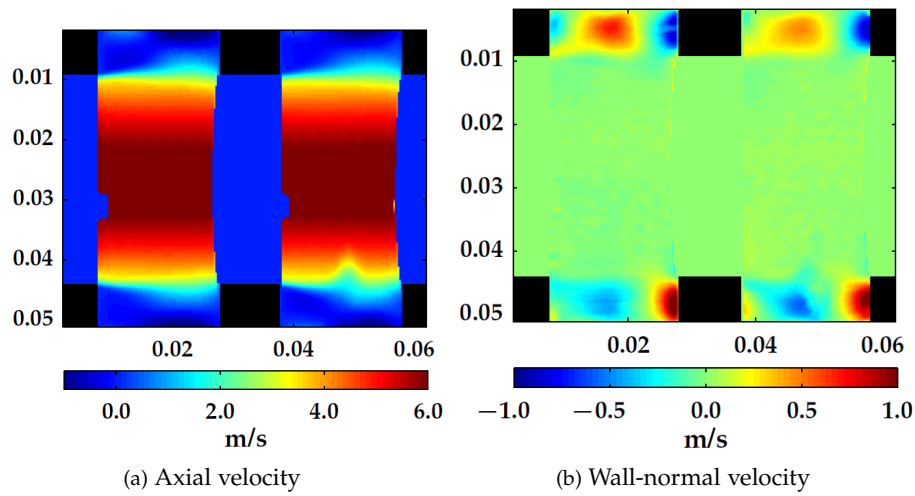


Figure 4.2: Mean axial (a) and radial (b) velocity for rectangular ribs (EL geometry),  $p = 30$  mm,  $Re_r = 1.6 \times 10^5$ . Dimensions are in metres, direction of the flow from left to right. Note: the "wiggly" in the lower right-hand corner of the images is identified as an artefact of the measurement and not further discussed.

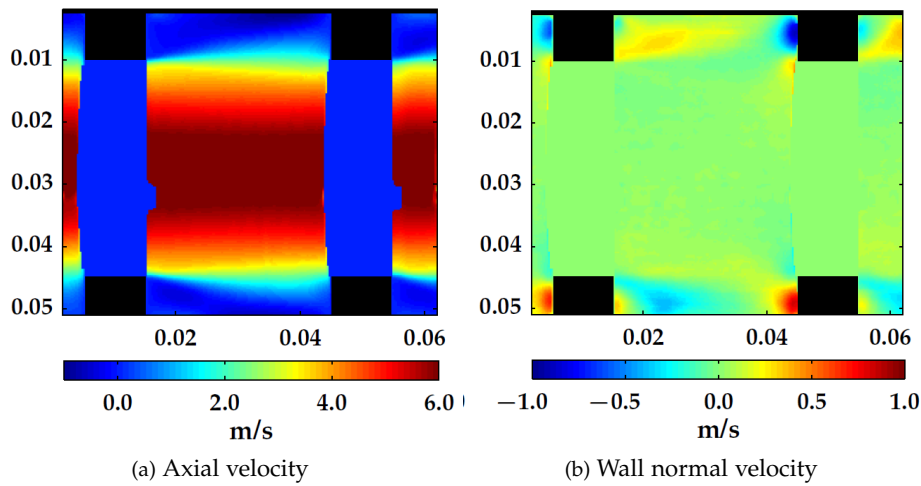


Figure 4.3: Mean axial (a) and radial (b) velocity for rectangular ribs (EL geometry),  $p = 40$  mm,  $Re_r = 1.6 \times 10^5$ . Dimensions in metres, direction of the flow from left to right.

In the figure it is clearly visible that, for the RL geometries, the shear layer separating the cavity and the core region of the flow is wider than for the EL geometry. Furthermore, an increase in shear layer thickness with increasing Reynolds number is visible. The occurrence of this Reynolds number dependency is not surprising, given the results regarding the RL ribs obtained from the static pressure measurements in Chapter 2.4, which indicate a Reynolds number dependency of the pressure loss only for the RL geometries.

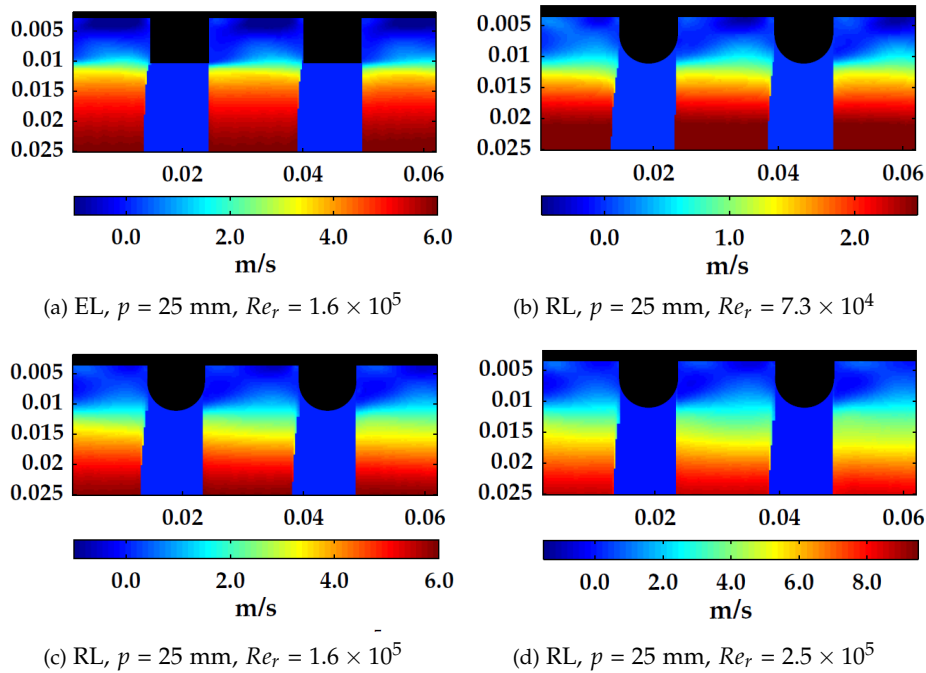


Figure 4.4: Axial velocities in RL (left) and EL (right) geometries for different Reynolds numbers and  $p = 25$  mm. Dimensions in metres, flow direction from left to right. The region downstream of the second rib suffers from measurement artefacts.

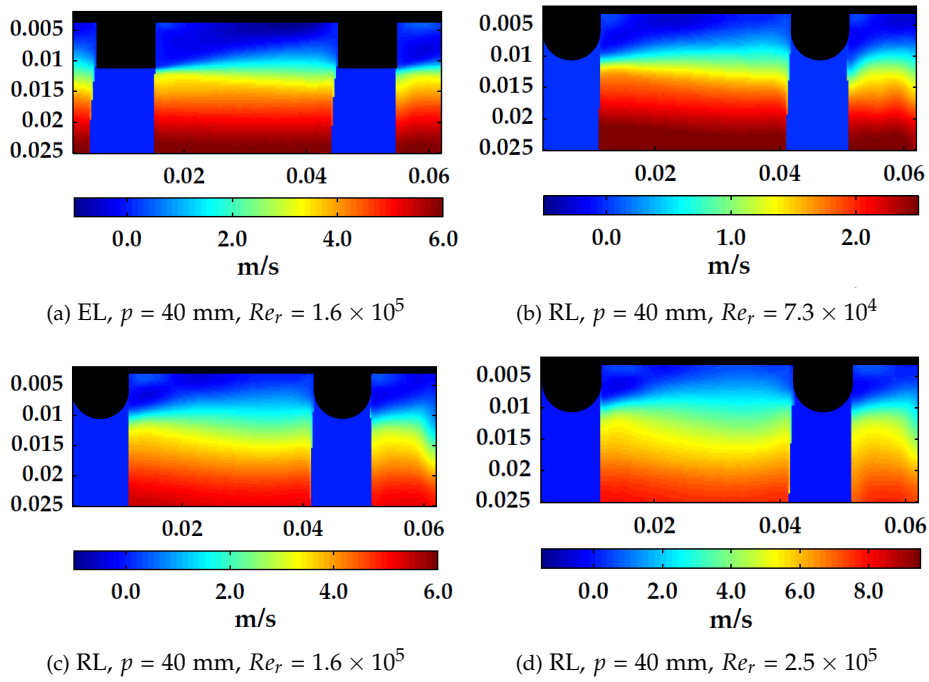


Figure 4.5: Axial velocities in RL (left) and EL (right) geometries for different Reynolds numbers and  $p = 40$  mm. Dimensions in metres, flow direction from left to right. The region downstream of the second rib suffers from measurement artefacts.

## 4.2 Shear stresses of the mean flow

The mean flow can be described by characteristic structures or properties of which three are discussed below: horizontal shear, Reynolds shear stress and Q criterion.

### 4.2.1 Horizontal shear of the mean flow

The 2D mean velocity fields are used to compute the mean shear  $S$ , of which we use the horizontal component, computed as:

$$S = \frac{\partial U}{\partial y}. \quad (4.1)$$

Figs. 4.6 and 4.7 provide a comparison of the horizontal shear at a single Reynolds number between the rectangular and rounded ribs at all available pitches. The

vertical shear component is in the major part of the flow (with the exception of the recirculation zones within the cavities) much smaller and mostly negligible with respect to the horizontal shear component.

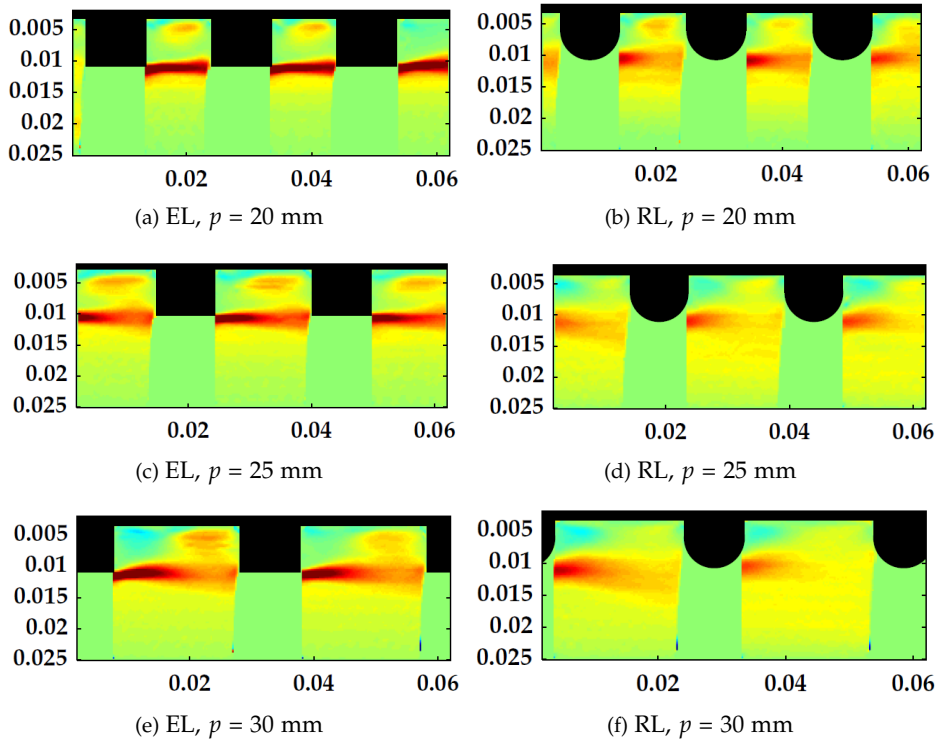


Figure 4.6: Mean horizontal shear  $\frac{\partial U}{\partial y}$  for  $Re_r = 1.6 \times 10^5$  and different rib geometries and pitches 20 - 30 mm. Dimensions in metres, flow direction from left to right.

The shear layers, which were also visible in the axial velocity contours, are now emphasized clearly. With an origin at the rib trailing edge, the layers separate the cavity and core regions from each other. The shear layer and thus this separation in regions become less defined in downstream direction. As previously observed, the shear layer is thinner for the EL geometry compared with RL. This also coincides with a stronger shear magnitude for EL with respect to RL.

The direction with which the shear layers separate from the rib appears to depend slightly on the pitch of the geometry, both for EL and RL. However, no dependency of spreading rate or shear strength on the pitch is visible.

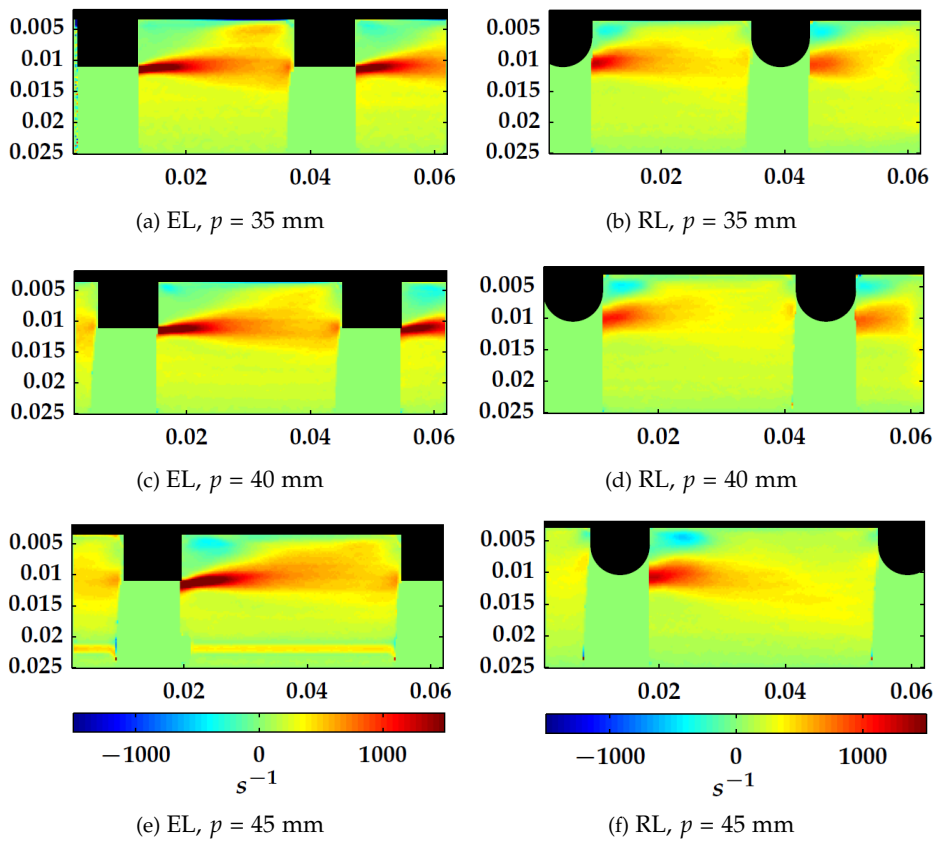


Figure 4.7: Mean horizontal shear  $\frac{\partial U}{\partial y}$  for  $Re_r = 1.6 \times 10^5$  and different rib geometries and pitches 35- 45 mm. Dimensions in metres, flow direction from left to right.

#### 4.2.2 Mean Reynolds stresses

A quantity strongly correlated to the regions of high shear is the Reynolds stress  $\tau$ , which for two-dimensional data can be represented as:

$$\tau = -\rho \overline{u'v'} \quad (4.2)$$

The Reynolds stress is the effective mean stress due to the contribution of turbulent fluctuations, and its spatial variation thus visualizes the distribution of the impact of turbulence. Figs. 4.8 and 4.9 show the mean Reynolds stress for the same set of geometries as depicted in Figs. 4.6 and 4.7.

The strongest Reynolds stresses are located at the regions of high shear as visible

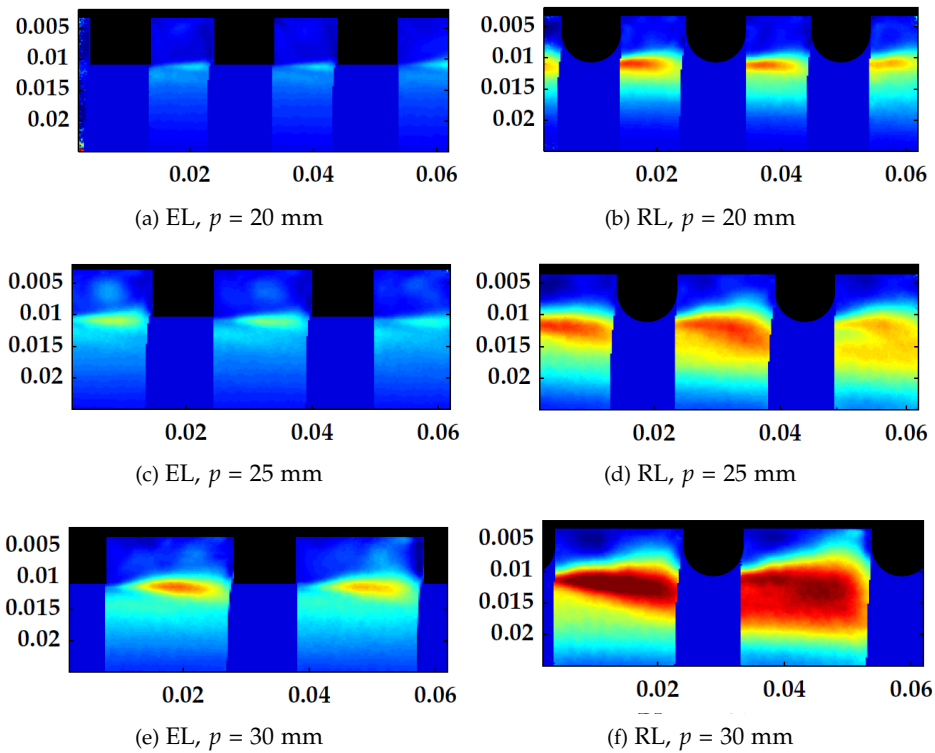


Figure 4.8: Reynolds stress  $-\overline{\rho u'v'}$  for  $Re_r = 1.6 \times 10^5$  and different geometries and pitches 20 - 30 mm. Dimensions in metres, flow direction from left to right.

in Figs. 4.6 and 4.7. Different than the horizontal mean shear, the Reynolds stress magnitude is strongly impacted by the changes in pitch. A more quantitative analysis of this dependency is provided in Section 4.6.2.

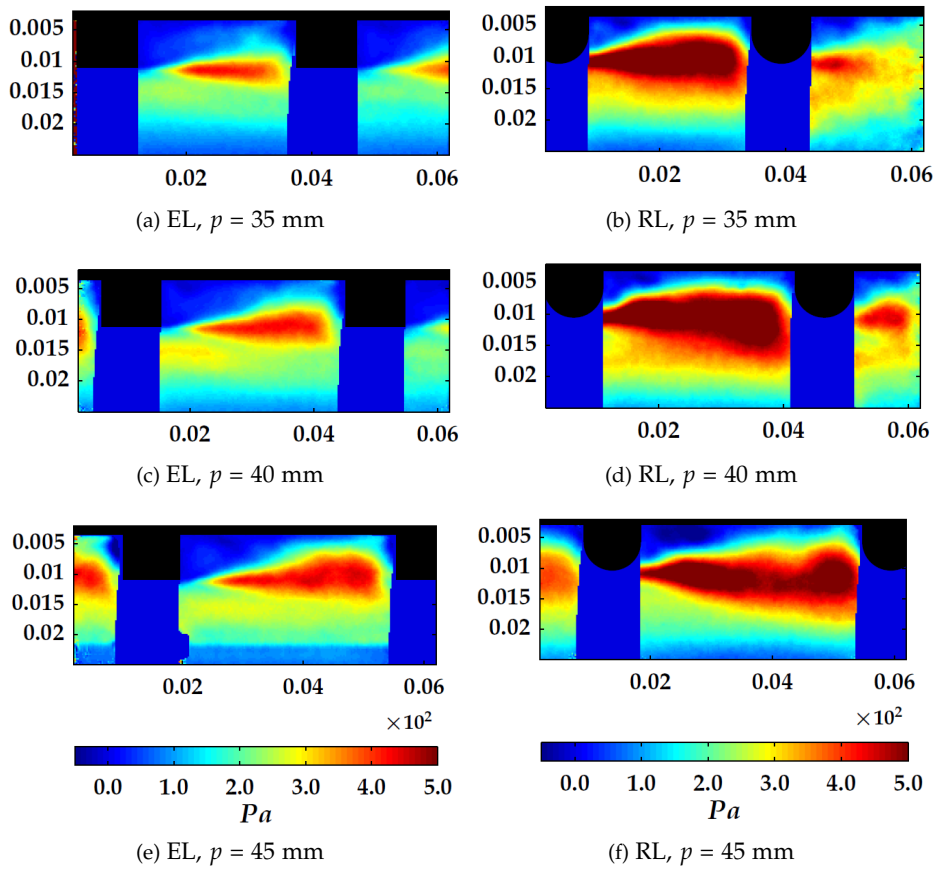


Figure 4.9: Reynolds stress  $-\rho\overline{u'v'}$  for  $Re_r = 1.6 \times 10^5$  and different geometries and pitches 35-45 mm. Dimensions in metres, flow direction from left to right.

### 4.2.3 The $Q$ criterion

Yet another parameter that can be used to visualize the characteristics of the mean flow is the so-called  $Q$  criterion, in a two-dimensional flow representation expressed as:

$$Q = \frac{1}{4}\omega^2 - \left( \left( \frac{\partial u}{\partial x} \right)^2 + \left( \frac{\partial v}{\partial y} \right)^2 + \frac{1}{2} \left( \frac{\partial u}{\partial y} + \frac{\partial v}{\partial x} \right)^2 \right) \quad (4.3)$$

A positive value for  $Q$  can be interpreted as rotation prevailing over irrotational shear. It can thus reveal the regions with strong rotation, without the concealing effect of strong shear regions as would be the case with using the vorticity.

The  $Q$  criterion is shown in Fig. 4.10 for EL (left panels) and RL (right panels) ribs at a single bulk Reynolds number, but for different pitches. The figure shows only a single cavity for each geometry. The streamlines are superimposed on the contours of  $Q$ , identifying the exact location of the cavity recirculation zones. For a clearer identification of the regions with strong rotation, the colour range in the panels of Fig. 4.10 is adjusted for each pitch.

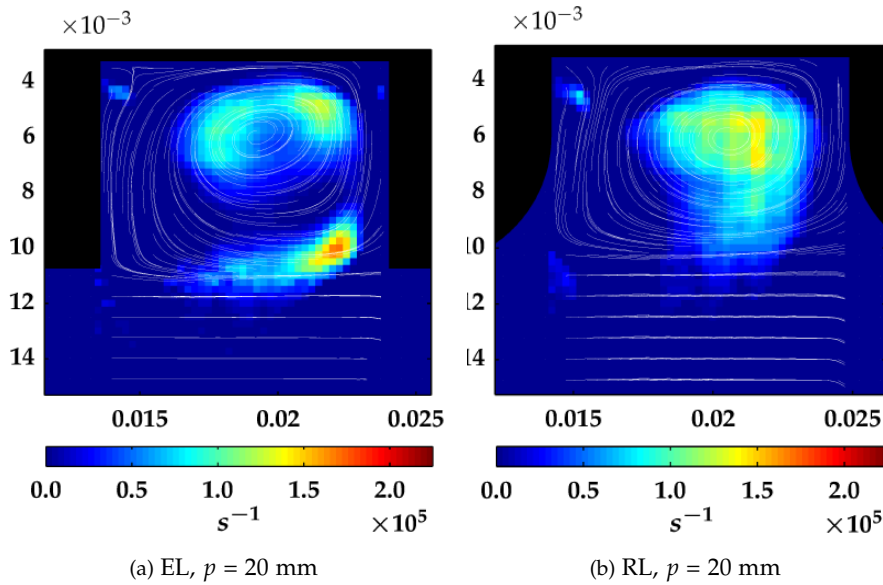


Figure 4.10: Mean-flow  $Q$  criterion for  $Re_r = 1.6 \times 10^5$  for EL and RL, with  $p = 20$  mm, superimposed with streamlines of the mean flow. Dimensions in metres, flow direction from left to right.

Other than the magnitude of the shear layer at separation or the Reynolds stresses, the maximum magnitude of  $Q$  decreases with increasing pitch (note the differences in the colour range of the panels in Figs. 4.10 and 4.11). The locations of strong rotation and the corresponding streamline patterns revealing the distribution of the recirculation zones show large differences between EL and RL for  $p > 20$  mm.

Figure 4.10 reveals that the strongest rotation zones are indeed solely related to the recirculating zones within the cavity. For the flow patterns within the cavity themselves, no clear trends are visible yet, requiring further investigation.

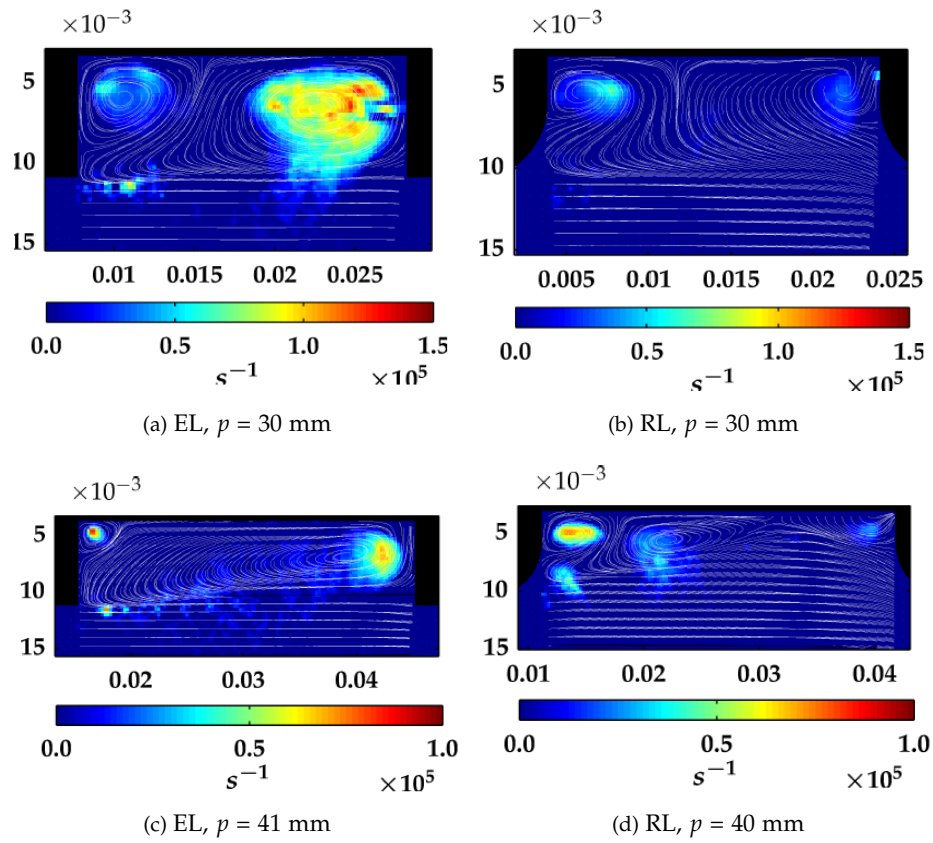


Figure 4.11: Mean-flow Q criterion for  $Re_\tau = 1.6 \times 10^5$  for EL and RL, with  $p = 30$  and  $40$  mm, superimposed with streamlines of the mean flow. Dimensions in metres, flow direction from left to right.

### 4.3 Cavity flow pattern evaluation

The recirculation regions are crudely visualized by the  $Q$  criterion in Section 4.2.3. In Figs. 4.12 and 4.13, the streamline patterns for the EL geometries and  $Re_r = 1.6 \times 10^5$  are shown, visualizing the flow patterns within the cavity more clearly. In all cases, a large recirculation zone at the downstream side of the cavity is present, stretching with increasing pitch and covering most of the cavity area. A much smaller secondary recirculation zone is present in the upstream corner of each cavity. Exceptions to this pattern are the cases with a 30 and 45 mm pitch, where the secondary recirculation region is much larger, almost spanning the full depth of the cavity. For  $p = 45$  mm, a third recirculation centre appears. For  $p > 30$  mm, the core region enters the cavity area, penetrating deeper with increasing pitch.

The location of the centre of the major recirculation region is stagnant in the axial direction. However, its location does change in wall-normal direction, with initially an increase in wall-normal position followed by a slight decrease from 30-35 mm. The 30-mm pitch geometry was shown to be the first geometry behaving as intermediate rough flow, as concluded from static pressure measurements. Both the sudden change in pattern and the core flow entering the flow from this pitch onwards are very likely related to this regime transition.

For the RL geometry, Figs 4.14 and 4.15 show the streamline patterns for different pitches and Reynolds numbers. The streamline patterns for RL do not display the discontinuous trends in recirculation patterns with pitch observed for EL. Compared to the results for EL, the distinction between cavity recirculation zones and core flow is less clear. For  $p > 35$  mm, the major recirculation zone in the downstream half of the cavity becomes irregular and separates into multiple regions for all Reynolds numbers. With  $Re_r \geq 1.6 \times 10^5$ , this disappearance occurs already at  $p = 35$  mm.

A feature present for all RL geometries is the downstream shift of the main stagnation point at the pipe wall with increasing Reynolds number. Besides the location of this stagnation point, the direction with which the flow approaches the stagnation also displays a Reynolds number dependency slightly influenced by the pitch.

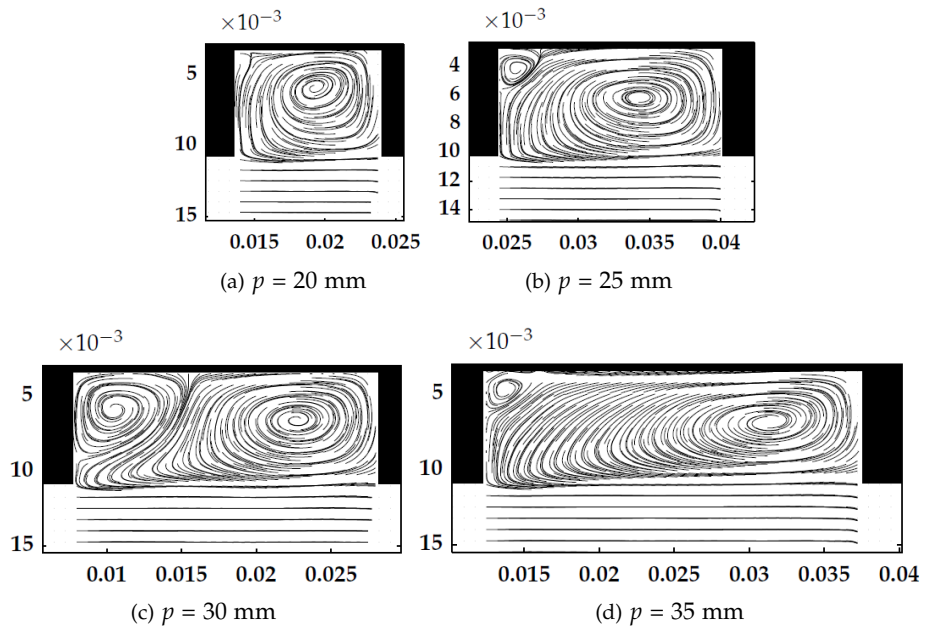


Figure 4.12: Mean flow streamlines for the EL geometry at  $Re_r = 1.6 \times 10^5$ ,  $p = 20$ -35 mm. Similar to all contour plots, the dimensions are in metres and the flow direction is from left to right.

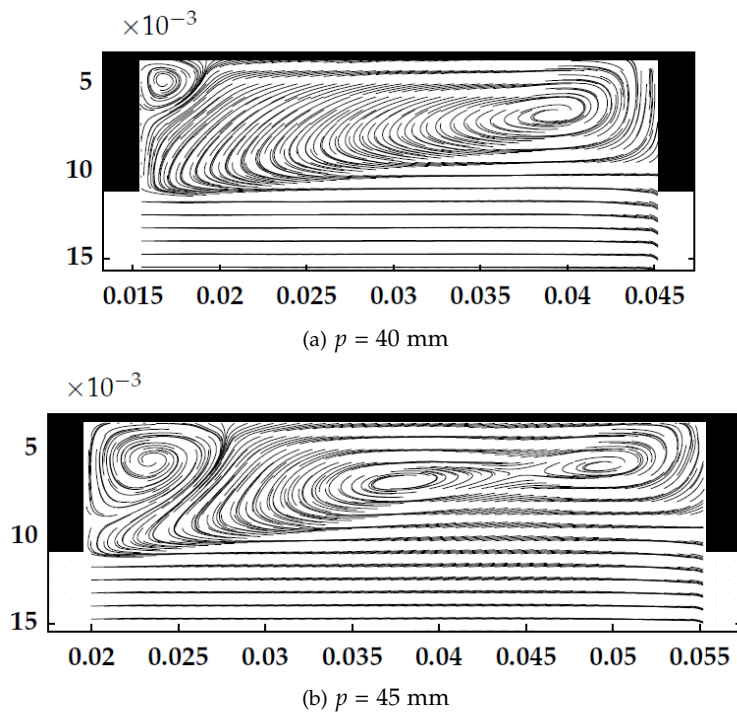


Figure 4.13: Mean flow streamlines for the EL geometry at  $Re_r = 1.6 \times 10^5$ ,  $p = 40$ - $45$  mm. Similar to all contour plots, the dimensions are in metres and the flow direction is from left to right.

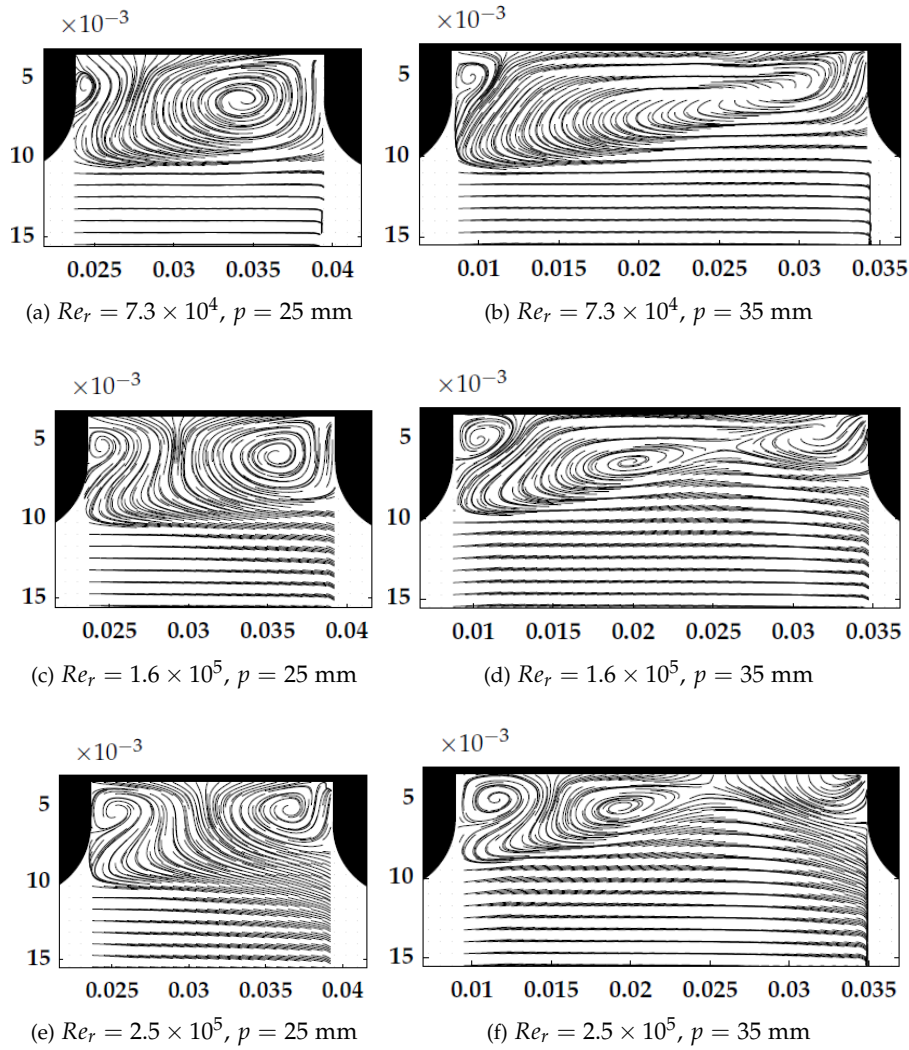


Figure 4.14: Mean flow streamlines for the RL geometry with  $p = 25$  mm (left panels) and 35 mm (right panels). Dimensions in metres and flow direction from left to right

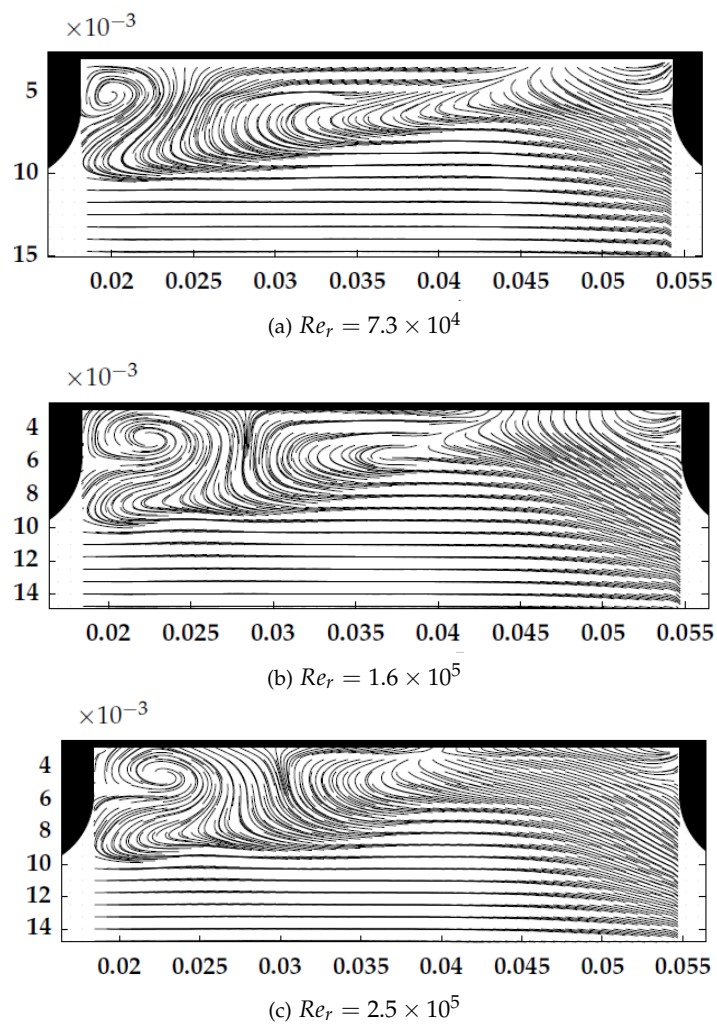


Figure 4.15: Mean flow streamlines for the RL geometry with  $p = 45$  mm. Dimensions in metres and flow direction from left to right

## 4.4 Flow axisymmetry

The rib elements are fixed to the inside of the pipe by means of connecting rods, thus breaking the axisymmetry of the geometry (see Section 2.1.2). However, the flow measurements only include a two-dimensional cross section of the pipe. The question is whether the results obtained are a good representation of the full circumference of the geometry.

To answer this question, we evaluate the axisymmetry of the flow due to the rods by comparing the two halves of the velocity field. The rods are located at three azimuthal locations (see Fig. 2.2b), although in a few exceptional cases the construction is  $180^\circ$  rotated. This configuration enables an evaluation of the extent of the non-axisymmetry of the flow.

In Figs. 4.16 and 4.17, the radial velocity superimposed with streamlines for the full cross section is displayed for  $p = 25, 30, 35$  and  $40$  mm. To be able to compare both image halves properly, the sign of the velocity in the lower image half has been reversed.

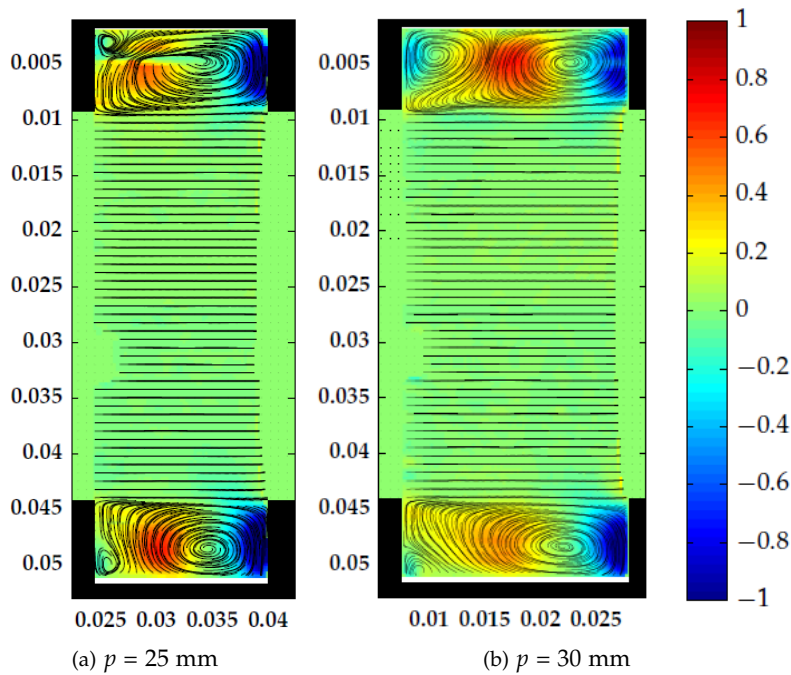


Figure 4.16: Mean flow streamlines superimposed on the mean radial velocity for a single cavity.  $Re_r = 1.6 \times 10^5$ ,  $p = 25 - 30$  mm, dimensions in metres and flow from left to right.

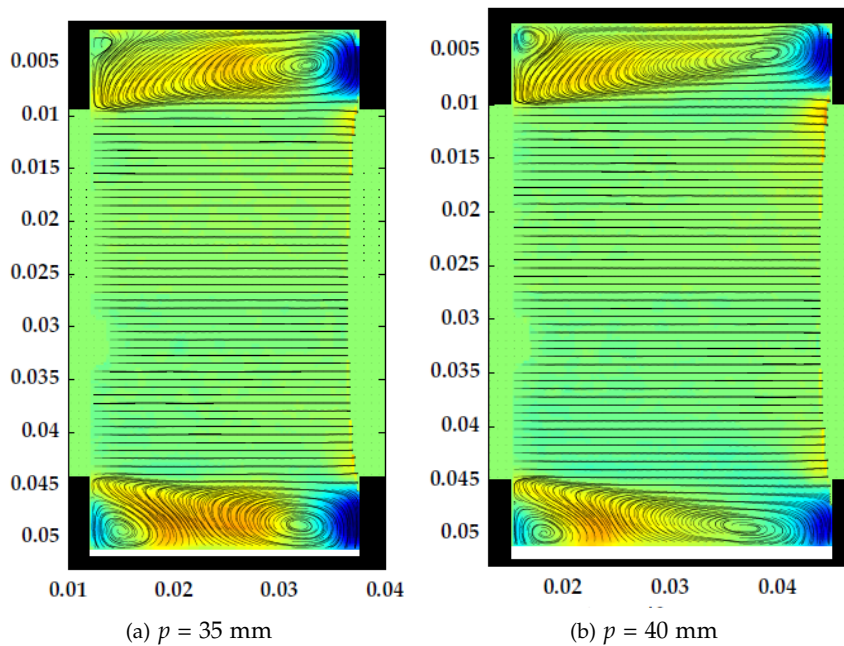


Figure 4.17: Mean flow streamlines superimposed on the mean radial velocity for a single cavity.  $Re_r = 1.6 \times 10^5$ ,  $p = 35 - 40$  mm, dimensions in metres and flow from left to right. Color scale according to Fig. 4.16

The comparison shows that the flow is indeed not fully axisymmetric. Especially the secondary recirculation region, in the upstream corners of the cavity, displays a clear asymmetry. This asymmetry is present for a pitch of 30 mm and larger, with the impact decreasing with increasing pitch. The region of strong shear separating the core and cavity, and the core flow region itself do not display any asymmetry, suggesting that there is no significant azimuthal flow component present.

#### 4.4.1 Azimuthal flow

A non-axisymmetric flow implies that an azimuthal velocity component must be present. Although the azimuthal velocity itself cannot be computed based on the two-dimensional flow field, the gradient of this velocity component can be computed using the continuity equation for an incompressible flow. The azimuthal velocity gradient is computed using a cylindrical coordinate system, implying an on average decreasing amplitude towards the centre of the pipe.

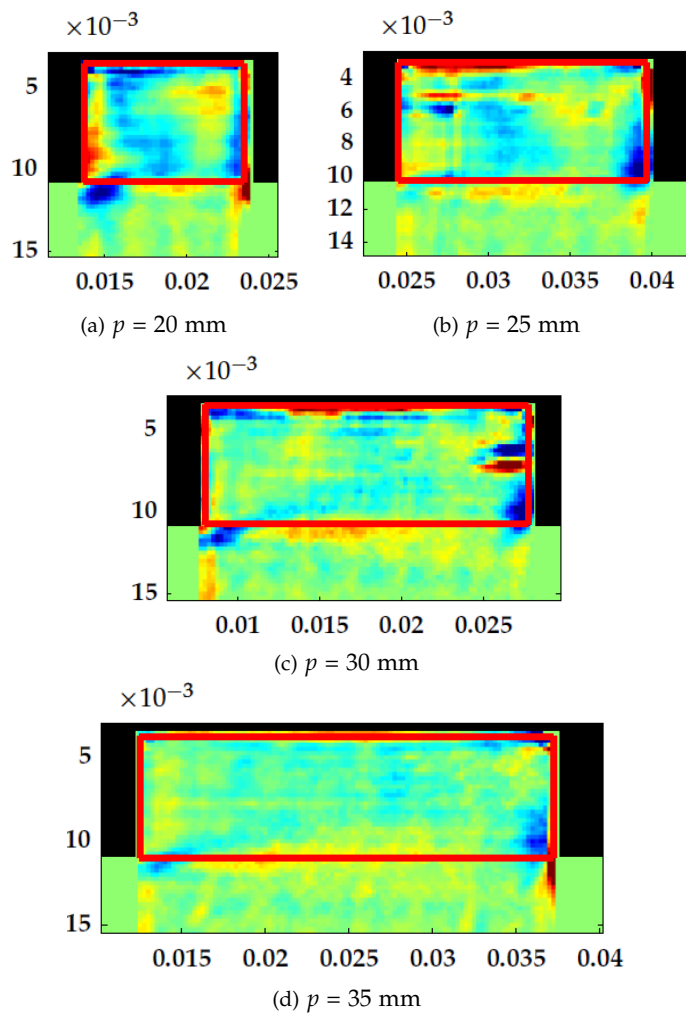


Figure 4.18: Azimuthal velocity gradient  $\frac{1}{r} \frac{\partial V}{\partial \theta}$  for  $p = 25 - 35$  mm. the EL geometry.  $Re_r = 1.6 \times 10^5$ , dimensions in metres, flow from left to right. Color scale according to Fig. 4.19

Figs. 4.18 and 4.19 show the corresponding patterns of the mean azimuthal gradient within the cavity region. Although the gradients are somewhat noisy and some artefacts are visible due to a poor data quality near the edges and due to reflections on the rod located behind the image plane, the results reveal the presence of azimuthal gradients in the mean flow within the cavity. The

core region of the flow does not display these gradients and is therefore not displayed. For the larger pitch geometries ( $p = 35\text{-}40\text{ mm}$ ), the azimuthal gradient magnitude decreases and a strong gradient is present only near the upstream and downstream cavity sides.

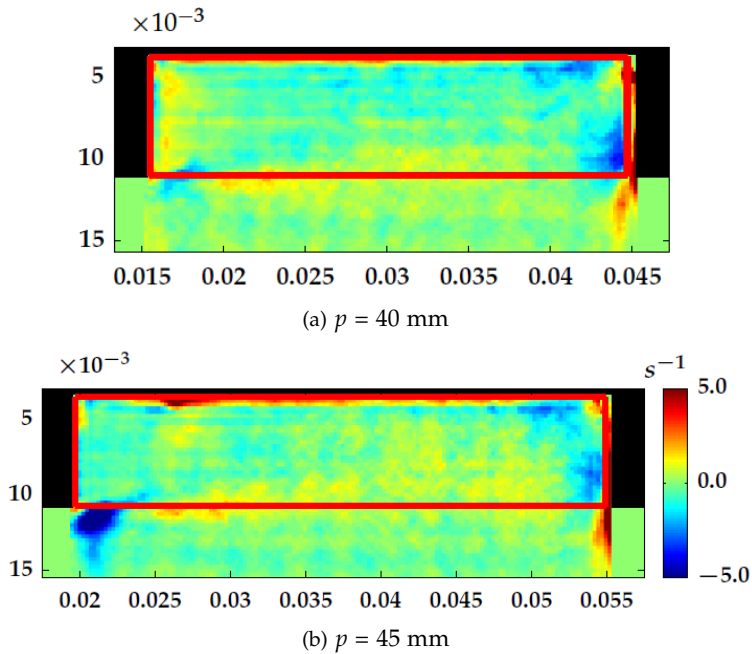


Figure 4.19: Azimuthal velocity gradient  $\frac{1}{r} \frac{\partial V}{\partial \theta}$  for  $p = 40 - 45\text{ mm}$ . the EL geometry.  $Re_r = 1.6 \times 10^5$ , dimensions in metres, flow from left to right.

Based on the layout of the ribs and connecting structure, a few assumptions regarding the direction of flow and gradient for the otherwise ambiguous results can be made.

The positioning of the rods causes the azimuthal flow to have a pattern that repeats every  $120^\circ$ , as indicated in a simple sketch in Fig. 4.20. Within each  $120^\circ$  segment, the flow pattern is assumed to be a stagnation point flow associated with the rod positions, yielding a zero azimuthal velocity at the centre location and at the location of the rods, regardless of the direction or magnitude of the azimuthal circulation. A flow in azimuthal direction nearly approaching a rod or symmetry plane will thus decelerate, while fluid moving away from a rod or plane of symmetry will likely accelerate. The cavity region of the top half of the image plane is, as indicated in Fig. 4.20, located relatively close to a rod. A larger area with a positive azimuthal velocity gradient – or acceleration – thus

probably relates to a flow direction away from the rod, whereas a region with a negative azimuthal gradient – or deceleration – relates to motion towards the rod. Following this line of thought, a flow pattern as illustrated schematically in Fig. 4.21 becomes a likely candidate.

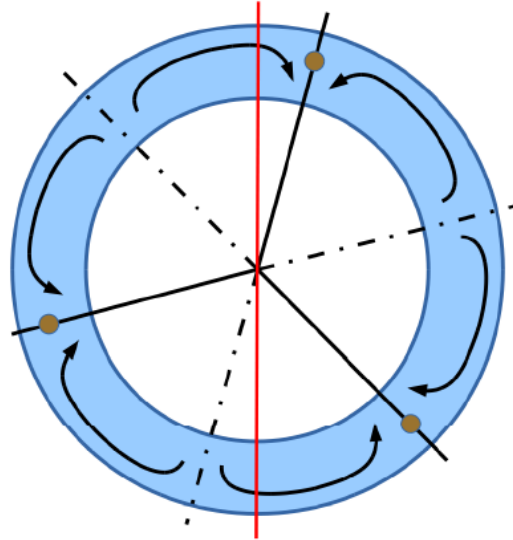


Figure 4.20: Schematic azimuthal triple symmetry for the configuration used in most measurements, with the observer on the left hand side of the image, the brown dots denoting the rib-connecting rods and the red line indicating the image plane.

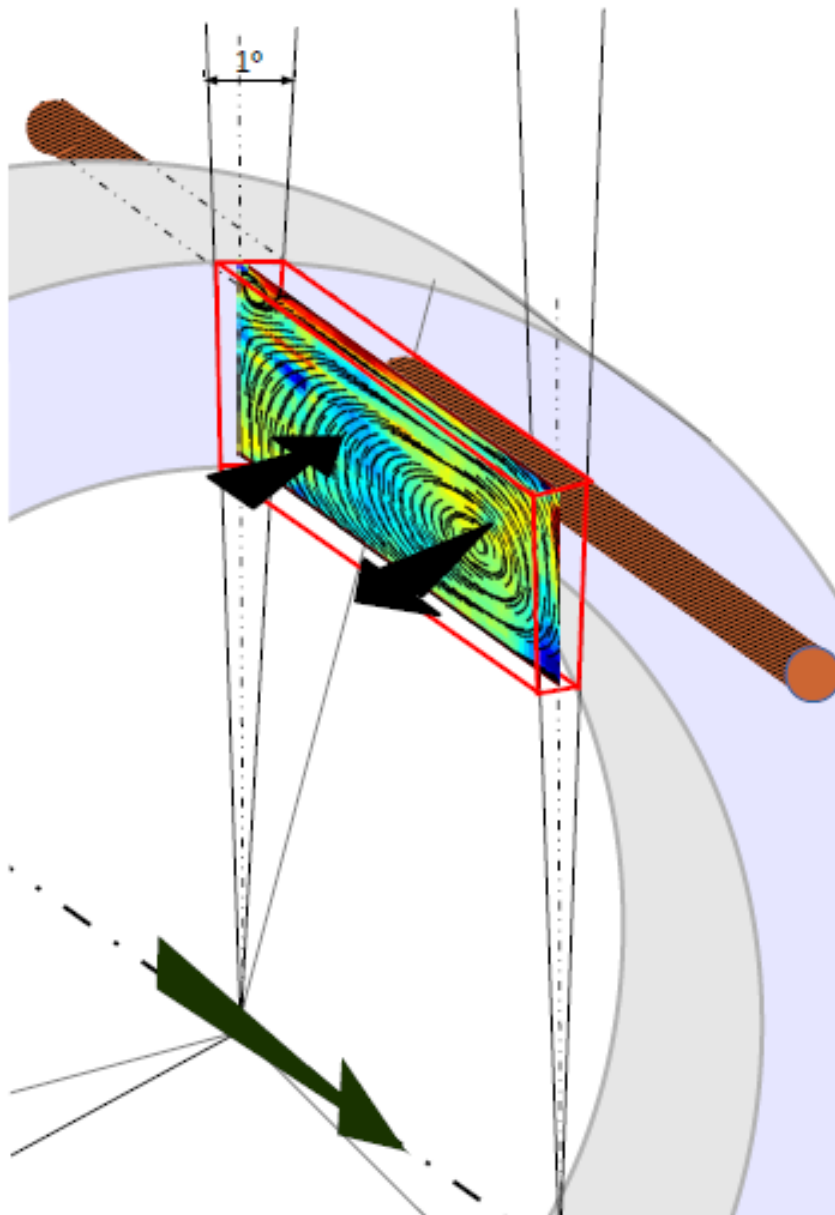


Figure 4.21: Azimuthal flow direction and direction of acceleration/deceleration as assumed based on the geometry and azimuthal gradient magnitude. The green arrow is the overall flow direction.

### 4.4.2 Cavity fluxes

The impact of the secondary flow in azimuthal direction is further evaluated by considering a control volume consisting of a  $1^\circ$  wedge of the cavity volume. The total volume flux or mass flux (equivalent due to the fluid's incompressibility) towards this control volume is by definition zero. The sum of the in-plane (radial and axial) fluxes towards the volume therefore always equals the sum of all local azimuthal mass fluxes within the same control volume. Because the flow is not consistently fully resolved up to the cavity walls, the control volume is slightly smaller than the actual cavity as indicated by the red rectangles in Fig. 4.18.

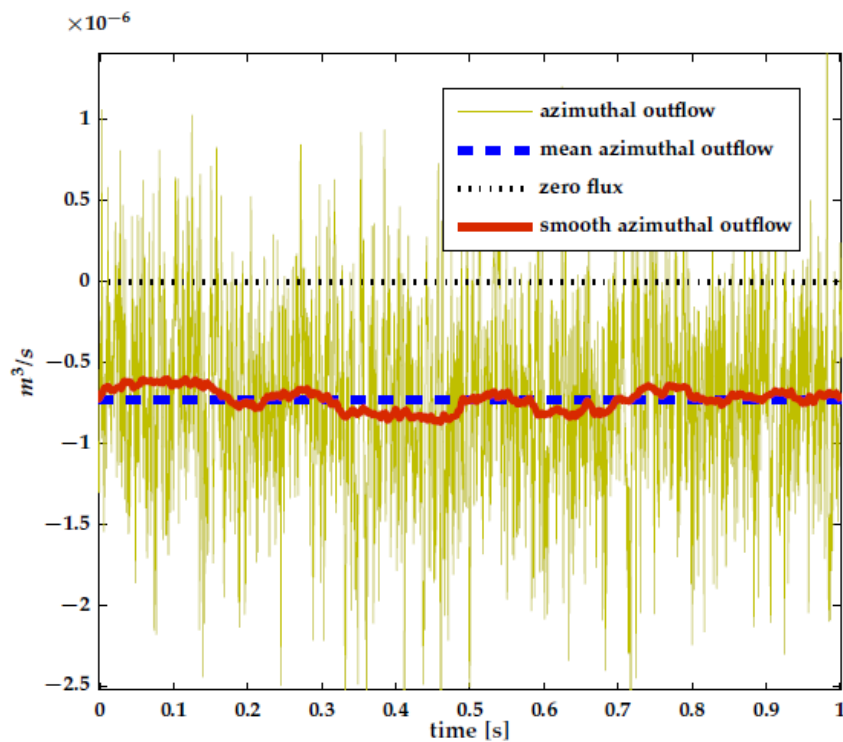


Figure 4.22: Instantaneous, smoothed and mean volume flux. The flux is directed outward in azimuthal direction and inward in radial direction with respect to the control volume in the cavity. The smooth line is obtained by a moving average with a span of 0.01 s.

Figure 4.22 displays the total azimuthal volume flux directed out of the control volume for a typical case ( $p = 35$  mm,  $Re_r = 1.6 \times 10^5$ ). The total in-plane

flux towards the control volume is virtually identical and not displayed. In an instantaneous sense, this volume flux fluctuates strongly. Once a temporal low-pass filter is applied, the presence of a steady, non-zero in-plane volume flux becomes clear. For the filter length, 0.01 s is used, which is short enough not to remove fluctuations associated with shedding behaviour. This steady component is strongly present for the short-pitched EL geometries but becomes less pronounced with increasing pitch. Both the absolute value and the value with respect to the mean amplitude of the fluctuations decrease gradually.

The mean in-plane volume flux over the control volume can be expressed as a mean outflow velocity in radial direction, which can be compared with the local wall-normal velocity at the cavity open surface. In Fig. 4.23, this mean outflow velocity, normalized with the flow bulk velocity, is depicted as a function of the rib pitch.

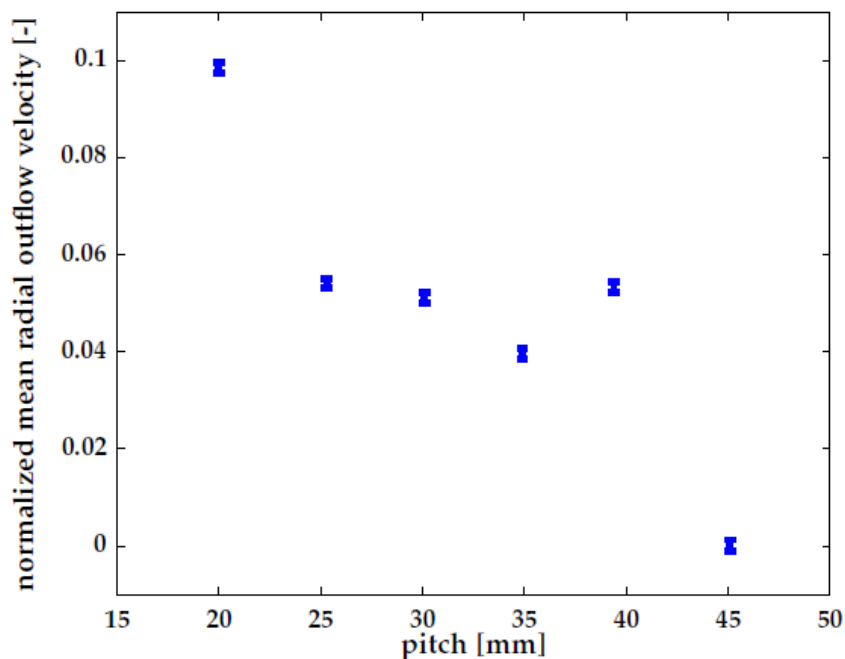


Figure 4.23: Mean radial outflow velocity normalized with the bulk velocity  $V_b$  as a function of pitch.  $Re = 1.6 \times 10^5$ .

The segmented flow pattern as suggested by Fig. 4.20 would result in a more or less opposite behaviour in the lower half of the images: a mean azimuthal volume flux towards the cavity and away from the cavity in radial direction.

However, the computed fluxes based on a control volume in the lower cavity (not shown) result in a mean flux in the same directions and of similar magnitudes as those of the top half of the images. The match between the computation based on in-plane velocities and the azimuthal flux by means of continuity is poorer, which is caused by a poorer image quality and therefore data quality in the lower half of the images. Although the data quality is not optimal and the decreasing trend with pitch is not perfectly clear, this result suggests that the simplified pattern in Fig. 4.20 is not a complete model for the tertiary flow patterns. This does not contradict the assumption regarding the flow directions in a plane close to a rod that is used to derive the assumed flow directions in Fig. 4.21 but does reveal the complexity of the flow and the need to further evaluate the three-dimensionality. The velocity magnitudes in azimuthal direction can be estimated from the volume flux. For  $Re_r = 1.6 \times 10^6$ , they are  $\sim 1$  ml/s. As this is 3 orders of magnitude smaller than the bulk velocity, the azimuthal flows caused by the rods are considered to be a minor influence in terms of disturbance to the axisymmetry of both the instantaneous and mean flow.

## 4.5 Mean flow for orifice flows

In Figs 4.24 and 4.25, the axial velocity component of the mean flow and corresponding mean Reynolds stresses for the single-rib or single-orifice measurements are shown. The orifice, which is typically just at the edge of the field of view, is indicated with a black silhouette within each image.

The maximum Reynolds stress and its evolution in axial direction are very different for the different orifice geometries. Note that all contour plots in Fig. 4.25 correspond to the same Reynolds number and all refer to the same colour contour range.

Some differences become clear after looking at the corresponding streamline patterns in Fig. 4.26.

The layout of the recirculation region also changes with geometry. The length varies, the centre of the recirculation shifts and two geometries even show a distinctly different pattern: geometry B does not have any significant recirculation region whereas geometry G displays a relatively large recirculation region that is split into two separate circulation motions.

### 4.5.1 Orifice flow patterns and pressure loss

The results in Section 2.5 reveal that the shape of the orifice or rib is a very significant parameter in the static pressure loss.

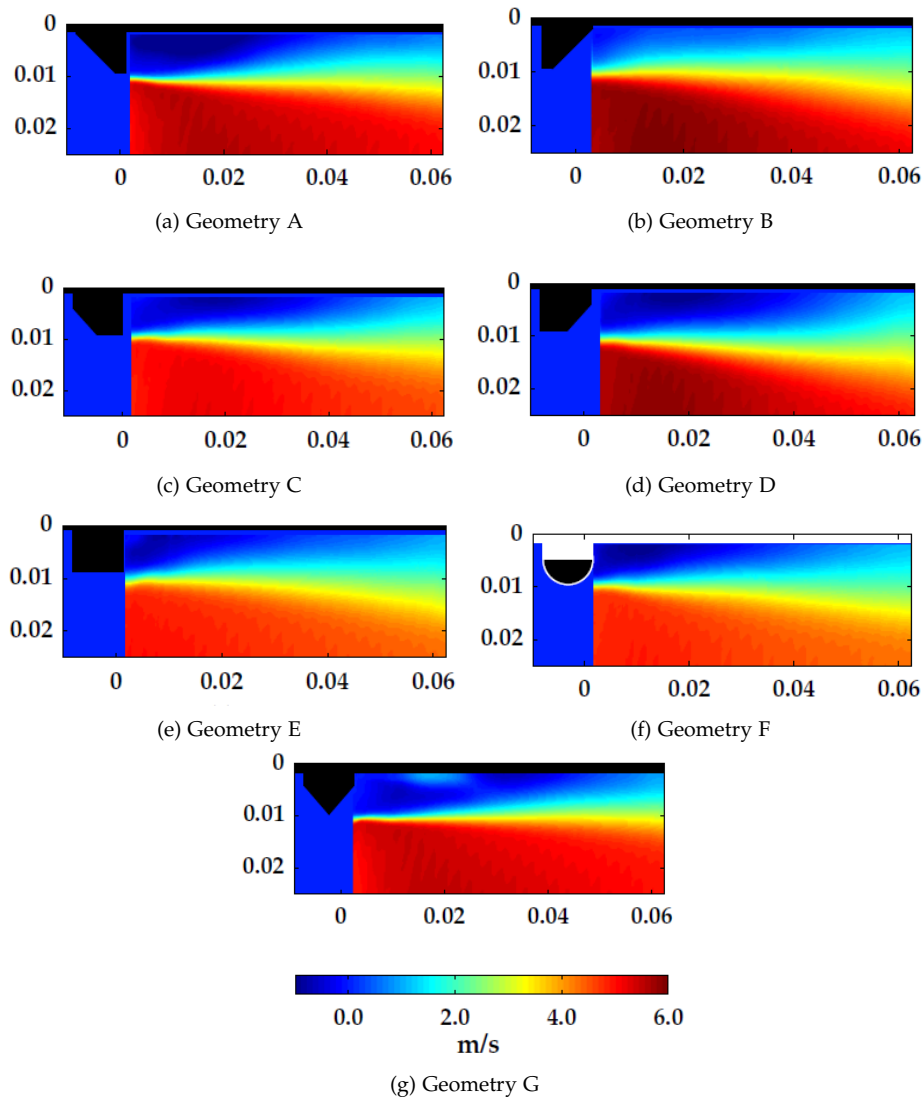


Figure 4.24: Mean axial velocity for all single-orifice geometries. Rib geometries are shown in black and referred to according to Table 2.5.  $Re_r = 1.6 \times 10^5$ , flow direction from left to right.

The correction factors for the Chisholm correlation, required to match the measured pressure losses with the correlation for a thin orifice, are shown in Table 2.5. These factors would change the *vena contracta* or the effective contraction

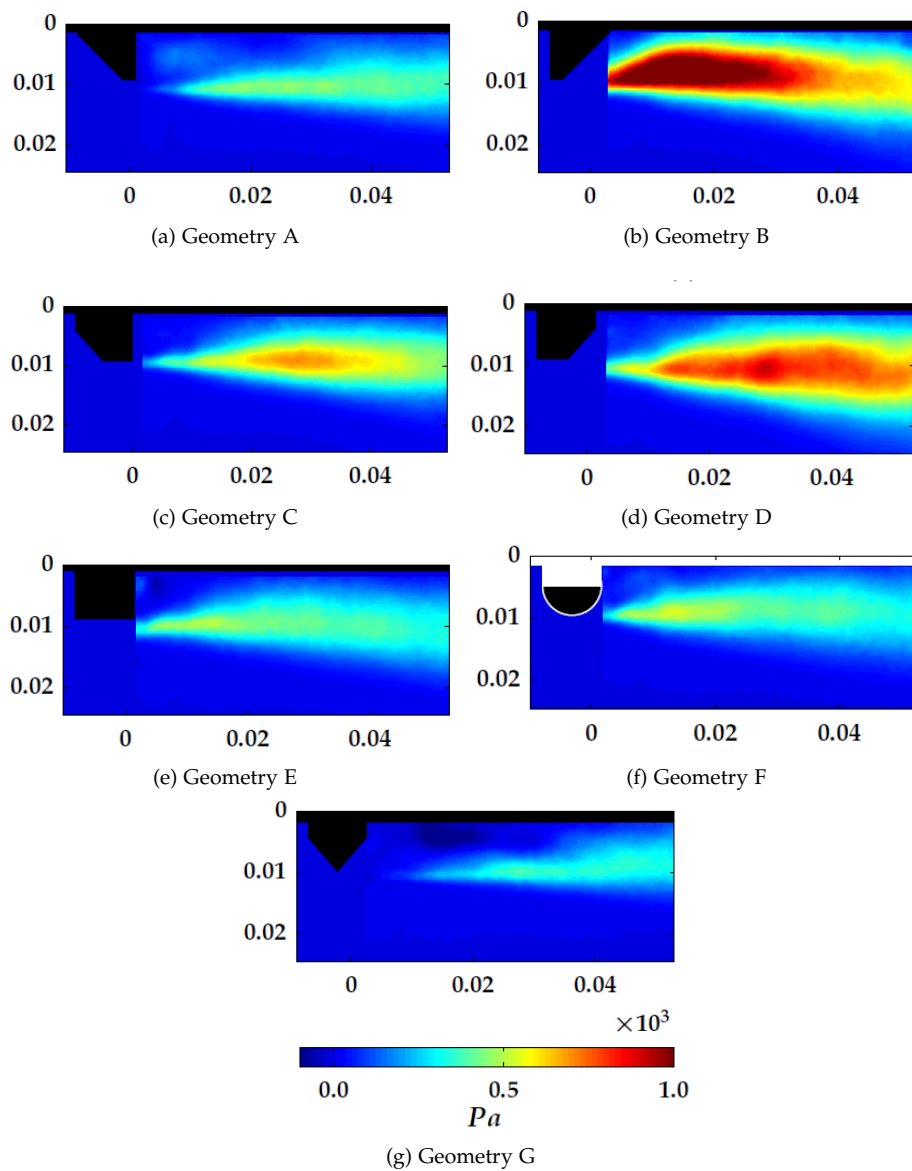


Figure 4.25: Mean Reynolds stress for all single-orifice geometries. Rib geometries are shown in black and referred to according to Table 2.5.  $Re_r = 1.6 \times 10^5$ , flow direction from left to right.

diameter of the flow. If this was indeed the mechanism causing the significant

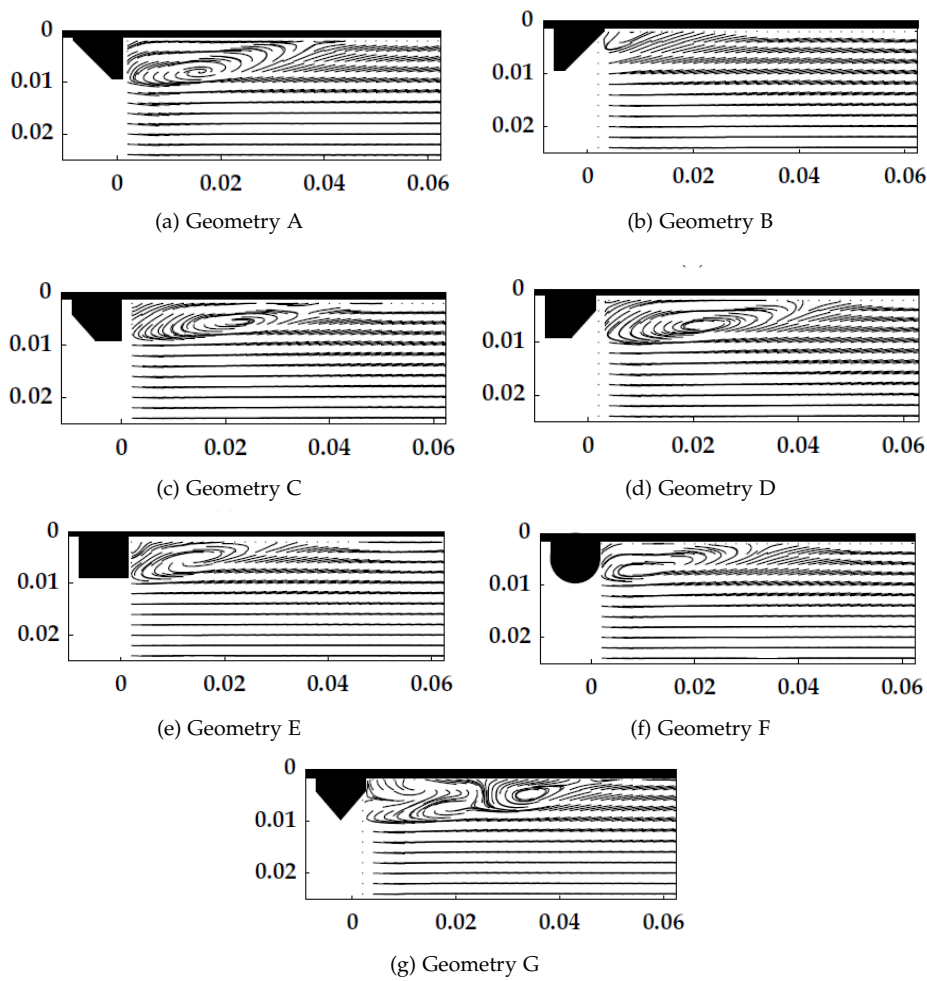


Figure 4.26: Streamlines for all single-orifice geometries. Geometries are referred to according to Table 2.5,  $Re_r = 1.6 \times 10^5$  and flow direction from left to right.

differences between the different orifice geometries, this variation in contraction should appear clearly in the streamline patterns in Fig. 4.26. Although the flow pattern is not resolved within the orifice itself, the streamlines downstream of the orifice do not suggest the presence of strong variations in this contraction diameter.

The Reynolds stresses as shown in Fig. 4.25 do show some correlation with the static pressure results: the two geometries with significantly higher Reynolds stresses, B and D, correspond to the orifices with the largest static losses. However,

this correlation between Reynolds stress magnitude and pressure drag does not hold for the other geometries. The Reynolds stresses are a significant factor in the total drag but other flow aspects have impact as well, such as the shape, size, strength and even presence of the recirculation area as well as the flow at the upstream side of the orifice, which is not included in the current measurements. The direction of the streamline separation the recirculation region with the main flows shows a correlation with the static pressure loss as well. This is best visualized for geometries A, C and E in Fig. 4.24. The pressure loss increases with this separation direction further towards the centre of the pipe, with otherwise very similar streamline patterns present. For geometry G, the effect of the flow around the orifice geometry penetrates less deep into the centre region of the flow, the region of high Reynolds stress is located further downstream with respect from the orifice and the recirculation region itself is very different, in comparison with the other geometries. Geometry F has the least static pressure loss when studied as a single orifice, which does not fit the trend of geometries A, C and E. We have not further investigated a causal relation between the orifice shape and the resulting flow behaviour and static pressure loss.

#### 4.5.2 Comparison of orifice flow and fully developed ribbed flow

As was already observed from the static pressure measurements, the flow losses for orifice geometries E and F, that is those corresponding to the geometries of the ribbed segments, do not display the same behaviour as the corresponding ribbed sections.

Figure 4.27 displays, side to side, the mean axial velocity, mean Reynolds stress and streamline pattern for orifice geometry E versus a ribbed section of type EL with  $p=40$  mm. Although the images clearly show some resemblance, the differences stand out. In the axial velocity fields, the largest difference is visible in the core region: the fully developed ribbed flow has a significantly higher velocity at the centre of the pipe and a significantly lower velocity closer to the rib crest than the orifice flow, which has, closely downstream of the orifice, an axial velocity that is almost uniform across the inner rib diameter. The mean Reynolds stress also displays large differences in the core region of the flow. Where the orifice flow has negligible Reynolds stresses over a large part of the core diameter, the fully developed flow shows a gradual decrease of stresses towards the pipe centre. However, the magnitude of the mean Reynolds stresses is remarkably similar between both geometries, certainly in comparison with the large differences in Reynolds stresses observed for the different orifice geometries

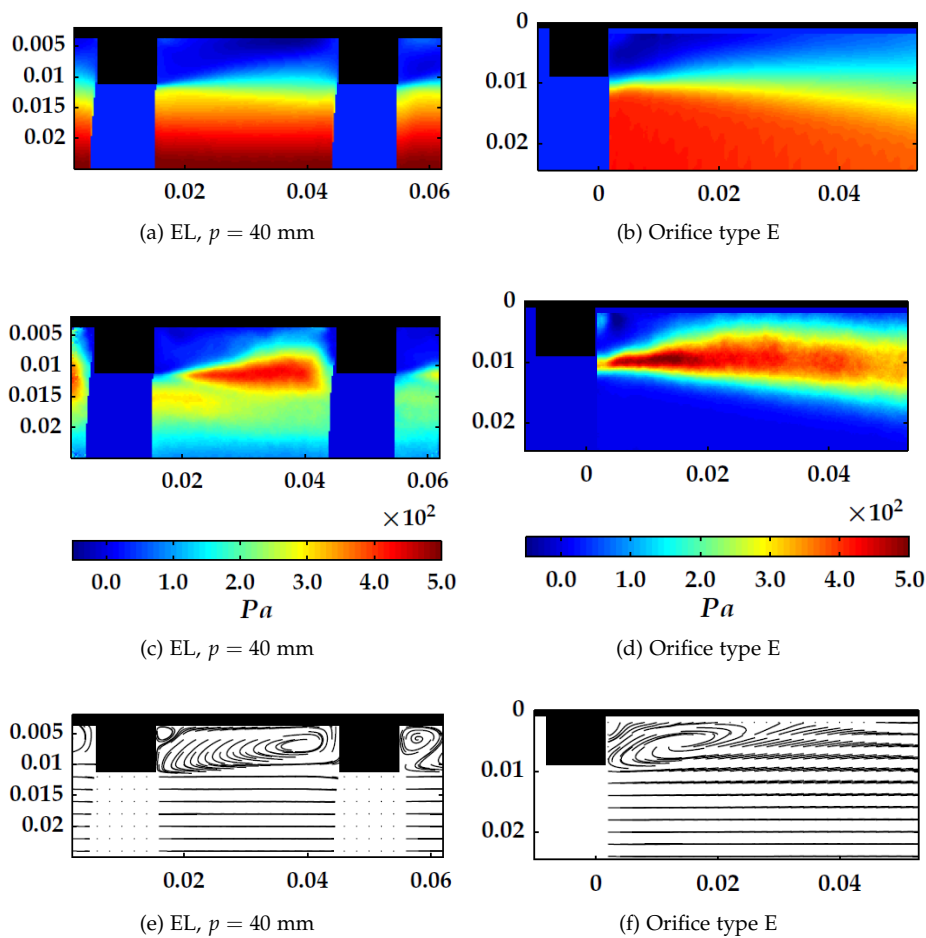


Figure 4.27: Comparison between the axial velocity, mean Reynolds stress and streamline pattern for ribbed section EL (left) and single-orifice geometry E (right). The colour range for the velocity plots is identical to that of Fig. 4.24.  $Re = 1.6 \times 10^5$ , dimensions in metres and flow from left to right.

in Fig. 4.25.

The recirculation motion is very different between both situations in Figs 4.27e and 4.27f, which is an expected result of the impingement on the successive ribs for EL versus the presence of a redeveloping boundary layer for the orifice geometry.

Figure 4.28 displays a similar one-to-one comparison of a RL-type ribbed section

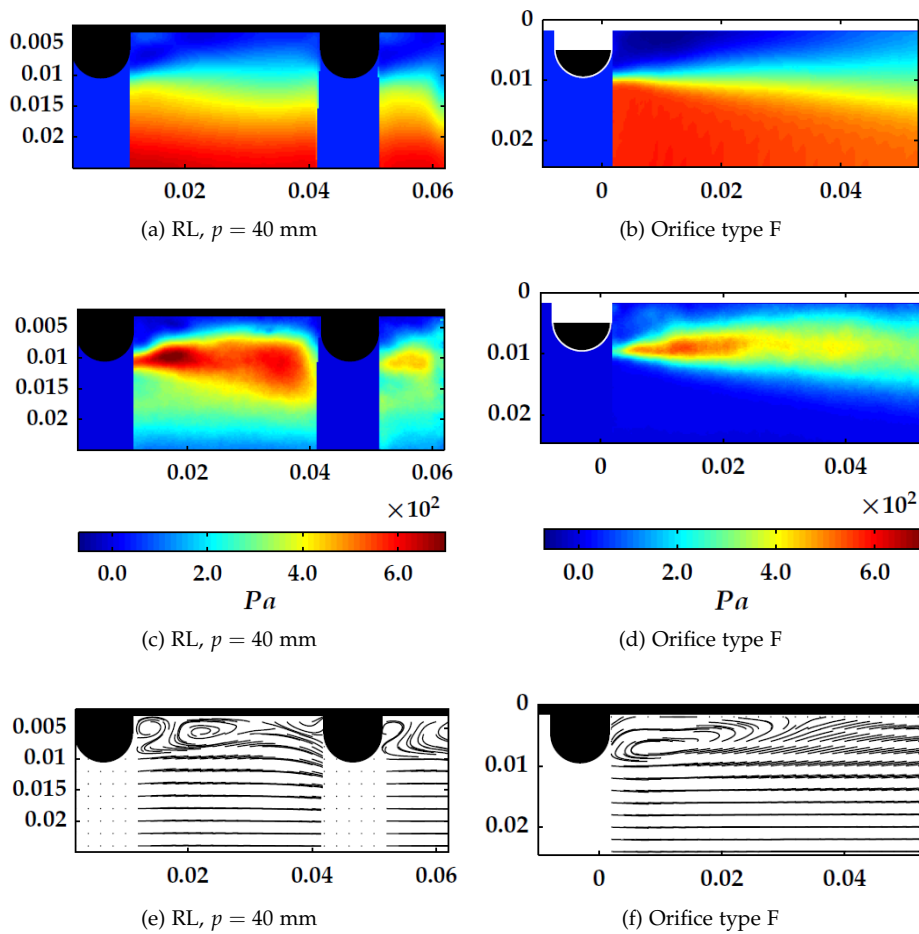


Figure 4.28: Comparison between the axial velocity, mean Reynolds stress and streamline pattern for a RL-type ribbed section and orifice geometry F. The colour range for the velocity is identical to that in Figure 4.24,  $Re = 1.6 \times 10^5$ , dimensions in metres and flow from left to right.

and F-type orifice. For these geometries, the differences are more profound than for EL versus E. RL lacks a sharp shear layer at the downstream side of the rib, separating the core region from the cavity that is present for orifice F. The Reynolds stress magnitude also differs more between the developed flow and the orifice than was the case for the rectangular geometries. However, the location of the maximum Reynolds stress does coincide for the rib and orifice geometry. The

differences between rib and orifice in the core region of the flow are similar to those described for the rectangular ribs.

## 4.6 Local mean profiles

For a more quantitative comparison of the flow properties and the differences in these properties for the different rib configurations, this section analyses the mean flow through one-dimensional time-averaged profiles. Two main types of profiles are distinguished: local and spatially averaged in axial direction. This section focuses on mean local profiles, and mostly analyses the qualitative differences and similarities between flows through different configurations. Section 4.7 discusses spatially averaged profiles, and introduces the results in non-dimensional units.

### 4.6.1 Local velocity profiles

Figure 4.29 shows the mean local axial and radial velocities obtained at three axial positions within the cavity; at  $\frac{1}{4}$ th,  $\frac{2}{4}$ th and  $\frac{3}{4}$ th of the cavity width. As before, because of the Reynolds number independency of the results, plots for the EL geometry are only depicted for a single Reynolds number, whereas the results for RL, which display a Reynolds dependency, include all three Reynolds numbers in the figures. For EL, Figs. 4.29 and 4.30 include the local time-averaged velocities for a selection of pitches (between  $p = 20$  to 45 mm). Figs. 4.31 and 4.32 include two geometries ( $p = 25$  & 45 mm) at two Reynolds numbers.

As also observed in Section 4.1, for EL geometries, the axial velocity shows little variation with axial position in the core region of the flow, while further towards the cavity crest height the axial variation increases. The wall-normal velocity is negligible over the whole core region. Within the cavity, both axial and wall-normal velocities are relevant, strongly varying with axial location. The axial variation extends further toward the core region for the geometries with a larger pitch, which is in line with the observed mean flow patterns in Sections 4.1 and 4.3.

For RL geometries with a short pitch ( $p = 25$  mm, Figs 4.31a and 4.32a), the same observation as for EL is valid: the axial variation is mostly limited to the cavity region. For larger pitch (Figs 4.31b and 4.32b), the axial variation (for EL only significant in and slightly above the cavity region) extends much further into the core region. This trend is also in line with the patterns as observed in Sections 4.1 and 4.3.

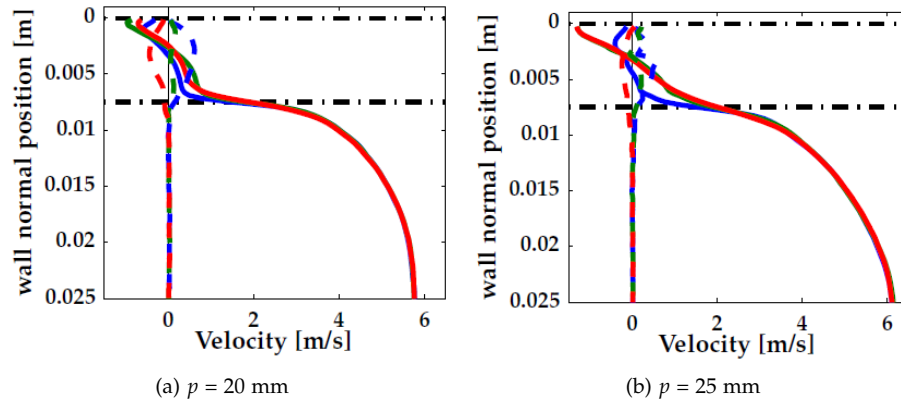


Figure 4.29: Mean axial (solid lines) and radial (dashed lines) velocity for EL geometries.  $Re_r = 1.6 \times 10^5$ ,  $p = 20$  and  $25$  mm. Blue: upstream quarter; green: cavity centre; red: downstream quarter. Data for  $p = 45$  mm not available up to the centre line (wall-normal positions  $> 0,022$  m).

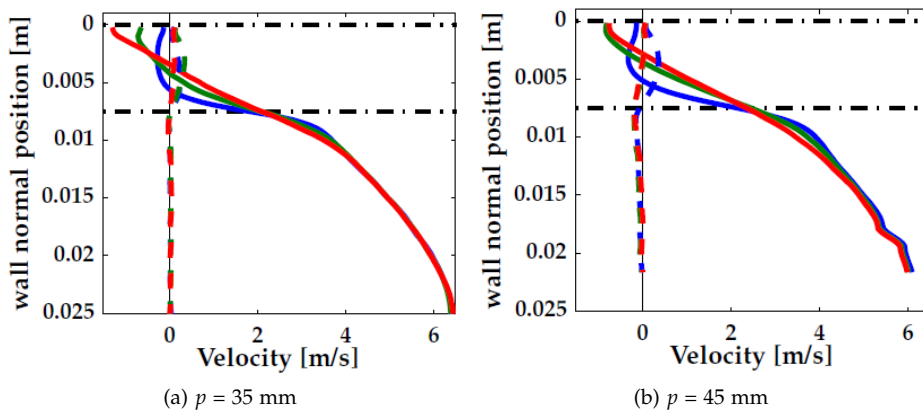


Figure 4.30: Mean axial (solid lines) and radial (dashed lines) velocity for EL geometries.  $Re_r = 1.6 \times 10^5$ ,  $p = 35$  and  $45$  mm. Blue: upstream quarter; green: cavity centre; red: downstream quarter. Data for  $p = 45$  mm not available up to the centre line (wall-normal positions  $> 0,022$  m).

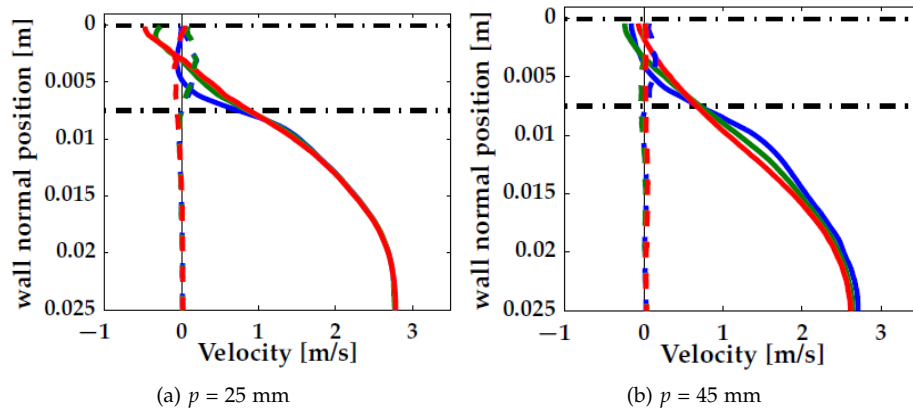


Figure 4.31: Mean axial (solid lines) and radial (dashed lines) velocity for RL geometries.  $Re_r = 7.3 \times 10^4$ . Blue: upstream quarter; green: cavity centre; red: downstream quarter. Data for  $p = 45$  mm is not available up to the centre line (wall-normal positions  $> 0.022$  m).

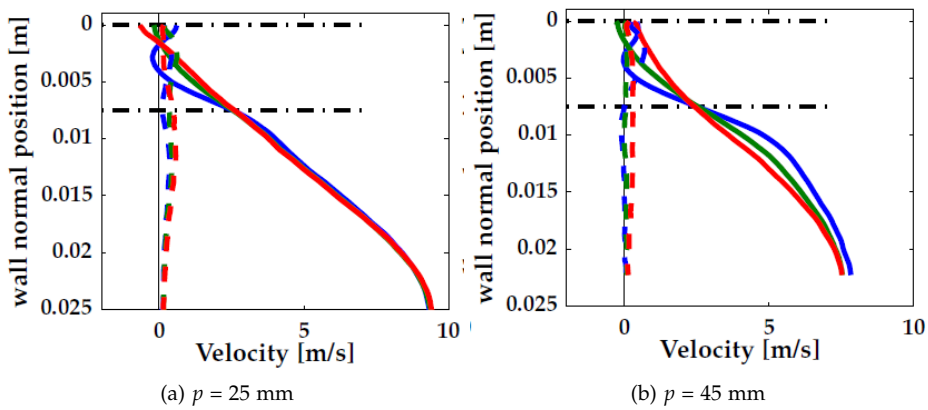


Figure 4.32: Mean axial (solid lines) and radial (dashed lines) velocity for RL geometries.  $Re_r = 2.5 \times 10^5$ . Blue: upstream quarter; green: cavity centre; red: downstream quarter. Data for  $p = 45$  mm is not available up to the centre line (wall-normal positions  $> 0.022$  m).

### 4.6.2 Local mean Reynolds stress profiles

Similar to the velocity profiles, Figs 4.33 and 4.34 depict the Reynolds stress at three axial positions for EL and RL, respectively.

In the centre region of the pipe, the Reynolds stresses display axially invariant behaviour. For the larger pitch geometries, this stress profile in the core region is linear, decreasing towards zero at the centre of the pipe. The length of this linear and axially invariant section of the stress profile decreases with increasing pitch. For the shortest pitch geometries, the centre-most region of the profile is not linear, although it is axially invariant. Instead, its slope decreases more gradually towards the zero value at the pipe centre. Closer towards the rib crest, the linear profile vanishes and the differences between the axial positions increase, with these axial variations becoming stronger for larger pitch. The blue lines in Fig. 4.33, corresponding to the most upstream location within the cavity, display two local maximums above the rib crest height for  $p > 20$  mm: one at the wall-normal distance of the rib crest and one further towards the core of the flow. The second peak disappears for the two further downstream stress profiles, while the first and largest peak remains and, for most pitches, grows in magnitude. For RL in Fig. 4.34, a similar feature seems present, although less pronounced with only a "bump" rather than a local maximum present at the upstream quarter profile. In addition, the magnitude increase of the main peak in downstream direction is not present; for  $p = 45$  mm, even a strong decrease is visible. The second stress peak, located further from the rib crest, seems to be associated with the interaction of the flow with the ribs further upstream than that directly upstream of the cavity in view. A further analysis of this flow aspect can be found in Chapter 5.

Within the cavity, the Reynolds stresses depend on the axial position, as would be expected due to the recirculation patterns. At the pipe wall, the stresses decay to zero. Although not clearly visible in Figs 4.33 and 4.34, the stresses within the cavity do locally obtain negative values as well.

The magnitude of the Reynolds stress strongly depends on the pitch, with a factor  $\sim 4$  increase between  $p = 20$  mm and  $p = 45$  mm. The presence of this strong geometric dependency was already observed in the contour plots of Section 4.2.2. The presence of a strong shape influence, visible in the differences between the Reynolds stress for EL and RL, was previously observed as well. The influence of rib shape on the Reynolds stresses is best observed by comparing the otherwise identical configurations in Figs 4.33b and 4.34c, and Figs 4.33f and 4.34d, respectively.

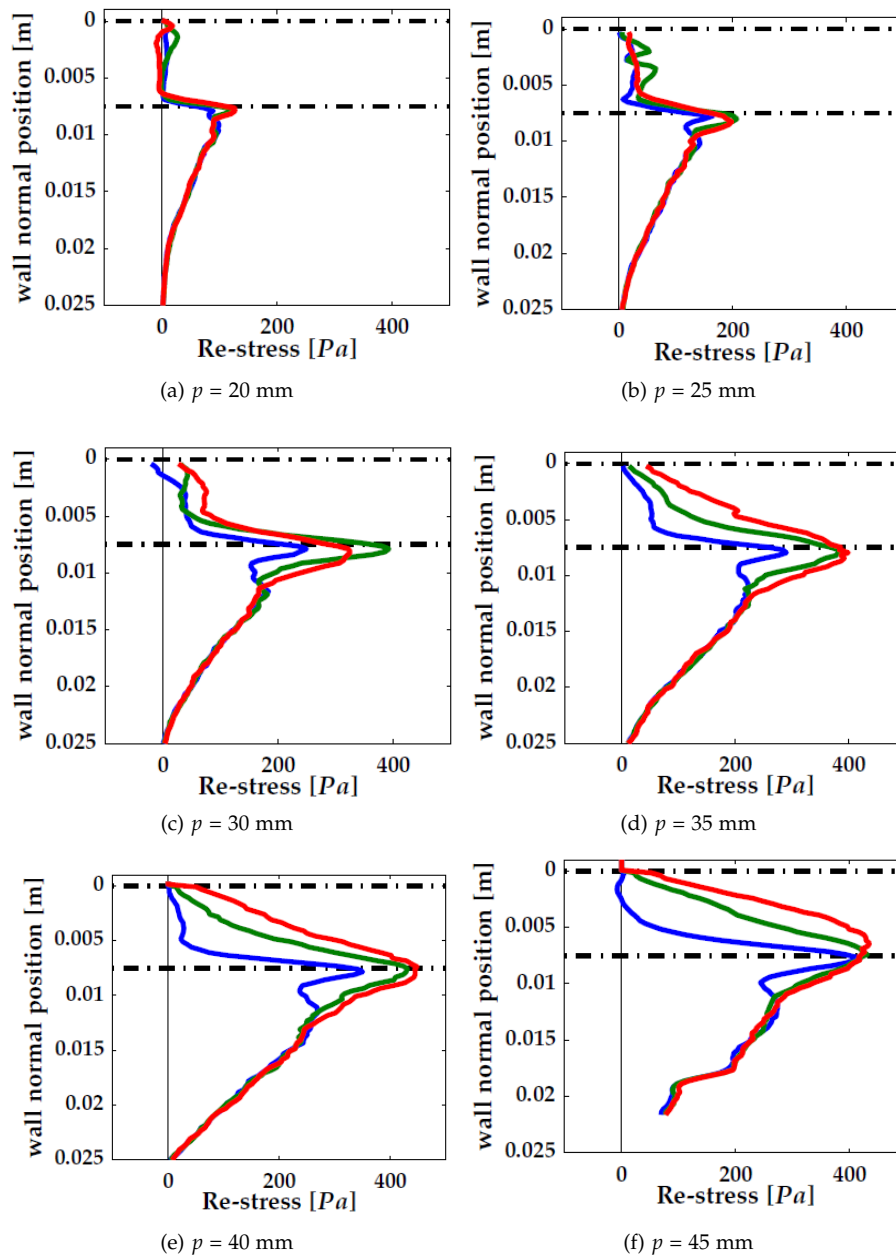


Figure 4.33: Reynolds stress at three axial locations for rectangular ribs (EL geometry) at  $Re_r = 1.6 \times 10^5$ . Blue: upstream quarter; green: cavity centre; red: downstream quarter. Data for  $p = 45$  mm not available up to the centre line (wall-normal positions  $> 0,022$  m).

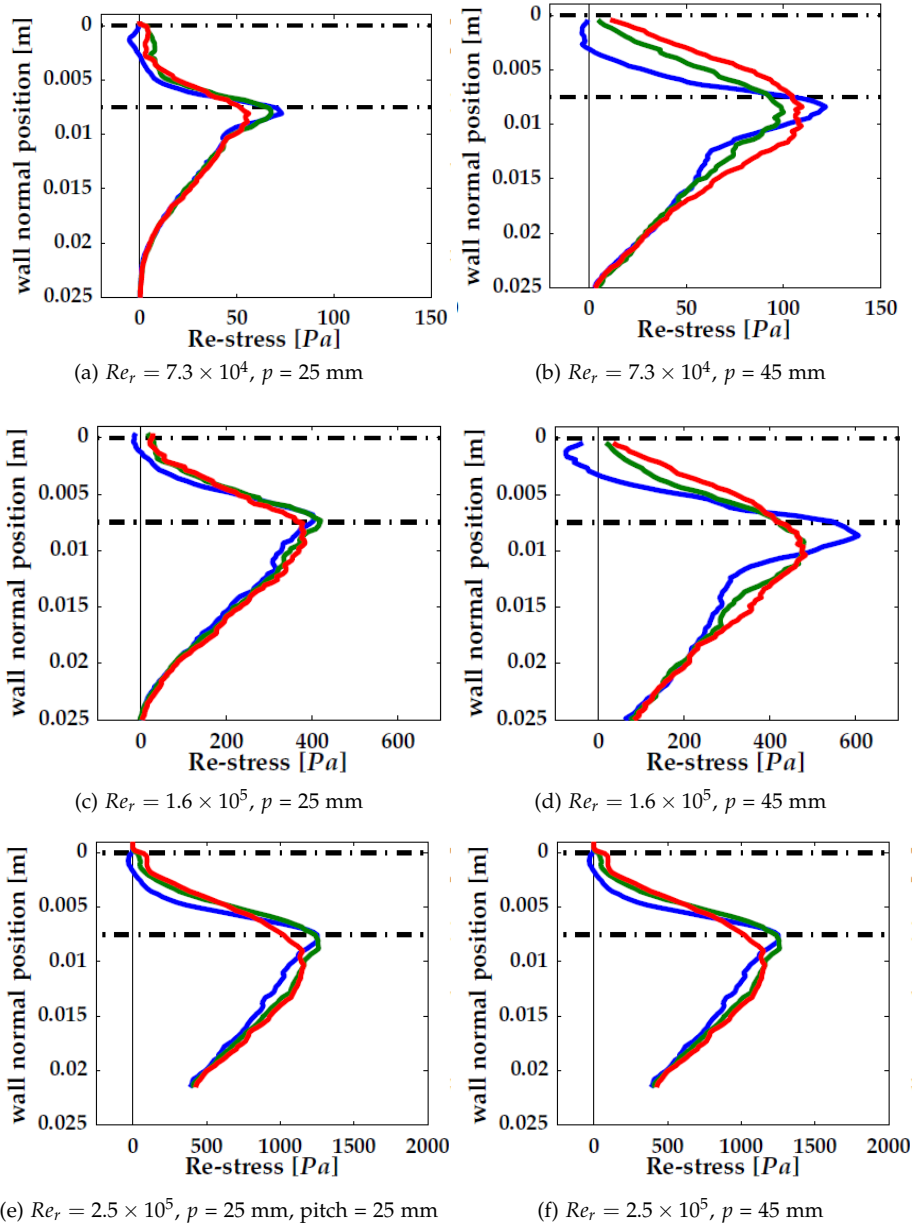


Figure 4.34: Reynolds stress at three axial locations for rounded ribs (RL geometry). Left column:  $p = 25$  mm; right column:  $p = 45$  mm. Blue: upstream quarter; green: cavity centre; red: downstream quarter. Data in panels e and f not available up to the centre line.

## 4.6.3 Local profiles for orifice flows

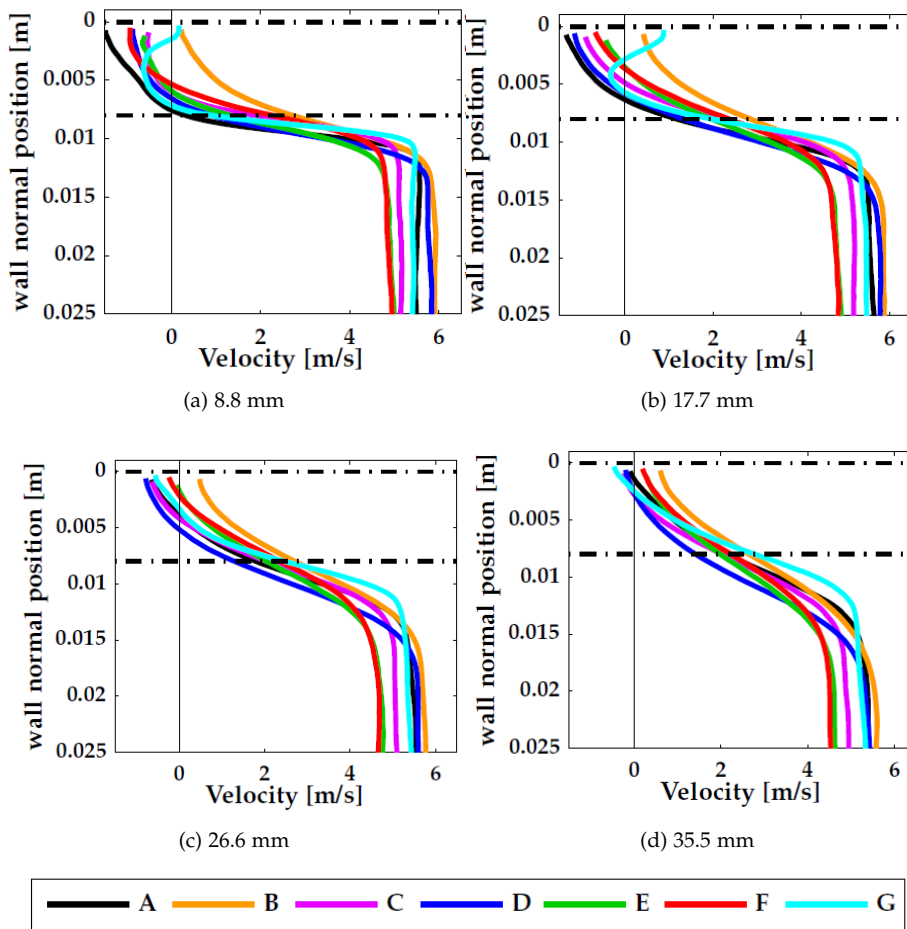


Figure 4.35: Axial velocity profile at four axial locations for the six types of orifices studied. The axial positions are chosen to match the 1/4th, 2/4th, 3/4th and 4/4th cavity length for a 45-mm pitch geometry.  $Re_r = 1.6 \cdot 10^5$ .

Local axial velocity profiles are determined for the orifice flows at four different positions downstream of the single orifice, with the axial position corresponding to the distance from the upstream rib of 1/4th, 2/4th, 3/4th and 4/4th cavity length for a 45-mm pitch geometry. The axial velocity profiles for the different geometries show similar trends, distinctly different from those obtained for the fully developed flow in Figs 4.29 and 4.31.

Initially, close to the orifice, the profiles consist of a plug flow in the core region and a strong gradient towards the rib crest height. Further downstream, a gradual shift occurs, with the uniform velocity core region decreasing in diameter and a less steep axial velocity gradient from the pipe wall up to this uniform core. Although the velocity profiles for the different orifice geometries differ somewhat in shape, the spatial development in axial direction of these profiles in the region above the orifice crest height is similar. Within the measured axial distance, the flow profiles do not reach a fully developed state, and the inner core region remains at uniform velocity, resulting in axial velocity profiles distinctly different from those corresponding to the ribbed sections in Figs 4.29 and 4.31.

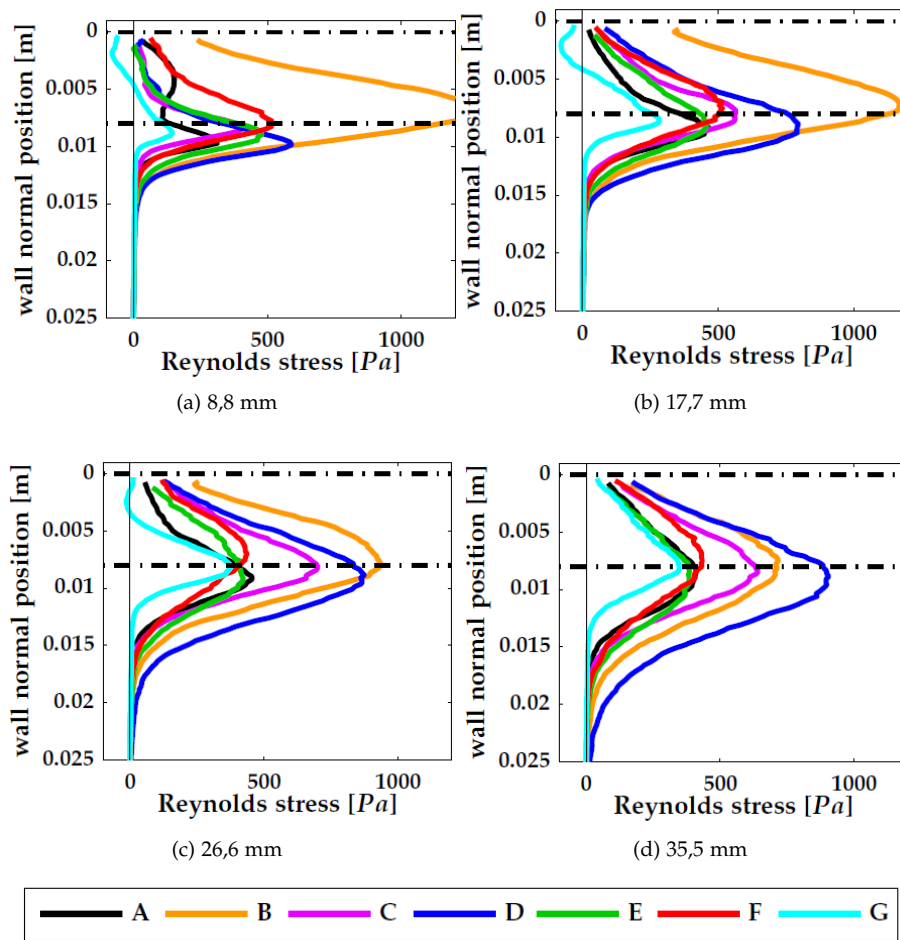


Figure 4.36: Reynolds stress profile at four axial locations for the six types of orifices studied. The positions match 1/4th, 2/4th, 3/4th and 4/4th cavity length for a 45-mm pitch geometry.  $Re_r = 1.6 \cdot 10^5$ .

The Reynolds stress profiles for different axial locations show strong variations, both with geometry and axial position. The differences in peak magnitude were already clearly observable in Fig. 4.25. Apart from a few similarities (all stress profiles show a strong peak around rib crest height and are decreasing towards zero at the pipe wall and core region; all geometries show an increase in peak width further from the orifice), the spatial evolution in axial direction of the Reynolds stresses in Fig. 4.36 is very different for the different geometries, in

contrast to what we find for the axial velocity in Fig. 4.35. Differences are present in the direction of the shift of the peak location, the growth or decrease of the peak magnitude and the growth rate of the peak width. The Reynolds stress profiles for orifice flows differ strongly from those obtained for EL and RL geometries. In the core region, no linear decreasing stress towards zero at the centre of the pipe is present, but rather a large core region without any significant turbulent stress, in comparison with the stresses caused by the rib.

## 4.7 Axial spatial averaging

The mean (as opposed to the local) properties of the fully developed periodic flow can be best observed using a spatial average in axial direction. The averaging can be performed over 1 or more full periods of the geometry. For the orifice flows, no relevant equivalent for a spatial average is possible or meaningful. Therefore, the next paragraphs only focus on the fully developed ribbed flows.

### 4.7.1 Spatial averaged axial velocity

Figure 4.37 displays the spatially averaged velocity for all EL geometries at  $Re_r = 1.6 \times 10^5$ . In the spatial average, the regions in which the view is blocked must be included as well. This is achieved by linearly interpolating in axial direction over the blocked region corresponding to the inner diameter of the ribs. Assuming a linear change across the thickness of the ribs is a rather coarse approach, especially very close to the rib edge, where the direction of the flow changes significantly with location. However, slightly further away from the rib edge, the radial velocity is very small compared to the axial component, and a nearly parallel flow is present, which justifies a linear interpolation across the blocked region.

Evidently this procedure is not applicable to the geometries with rounded ribs, in which the flow is not expected to be nearly parallel over the thickness of the rib. As no reliable method to infer the velocities in the blocked region based on the available data is available, only results for EL are shown.

As expected, the mean wall-normal velocity is always virtually zero. The axial velocity displays a maximum at the pipe centre, increasing with pitch. This corresponds to a shift from a profile with very sharp axial velocity gradients at rib height and shallow gradients further towards the core to a profile with less steep axial velocity gradients around rib height but extending much further towards the core with increasing pitch, a shape already observed in the local profiles in Fig. 4.29. The velocity becomes zero at approximately half the rib height for all

itches and thus becomes negative for the region below half the rib height. The velocity is not resolved all the way to the surface, so the figures do not show the very thin viscous layer with zero velocity at the wall surface.

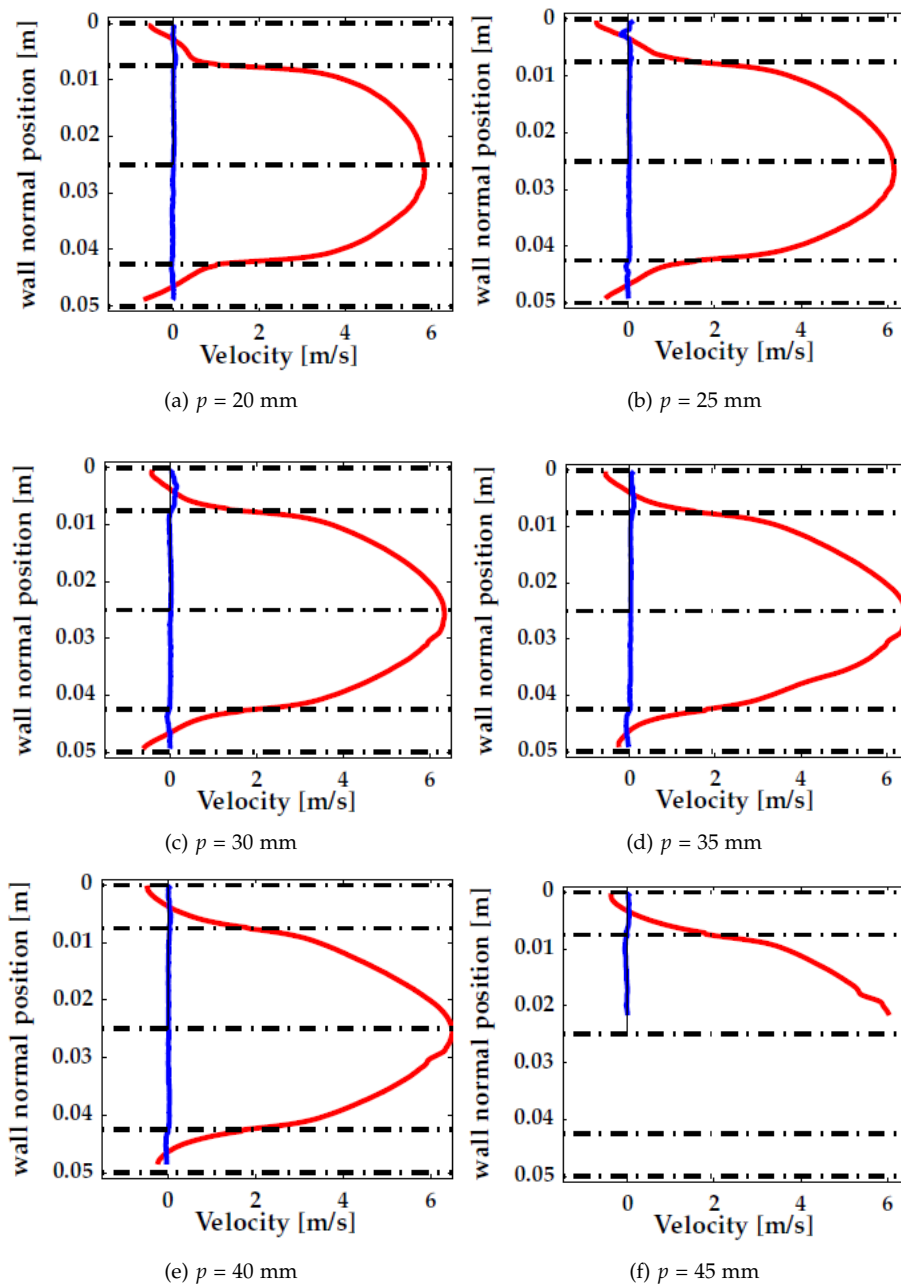


Figure 4.37: Axially spatially averaged axial (red) and wall-normal (blue) velocity for the EL geometry at  $Re_r = 1.6 \times 10^5$ .

### 4.7.2 Bulk velocity

A bulk velocity directly comparable with data obtained from flow-meter measurements can be calculated by integrating the spatially averaged axial velocity across the full cross-section of the pipe. This bulk velocity is required for flow scaling, further explained in Section 4.7.6. Fig. 4.38 displays this bulk velocity calculated based on both image halves separately, as well as the bulk velocity calculated from the flow meter data for all available EL measurements. The results display some differences, believed to be mainly caused by the deviations from axisymmetry present in the flow as identified in Section 4.4 and the difference in measured time (the pressure measurements have a much longer duration than the high-speed imaging). The bulk velocities are also less sensitive to errors introduced by extrapolation up to the pipe wall for the lower image half and interpolation over any blocked area. Overall, the agreement is reasonable, with less than 5.5% difference between the average bulk flow based on the velocity fields and that computed with the flow-meter data.

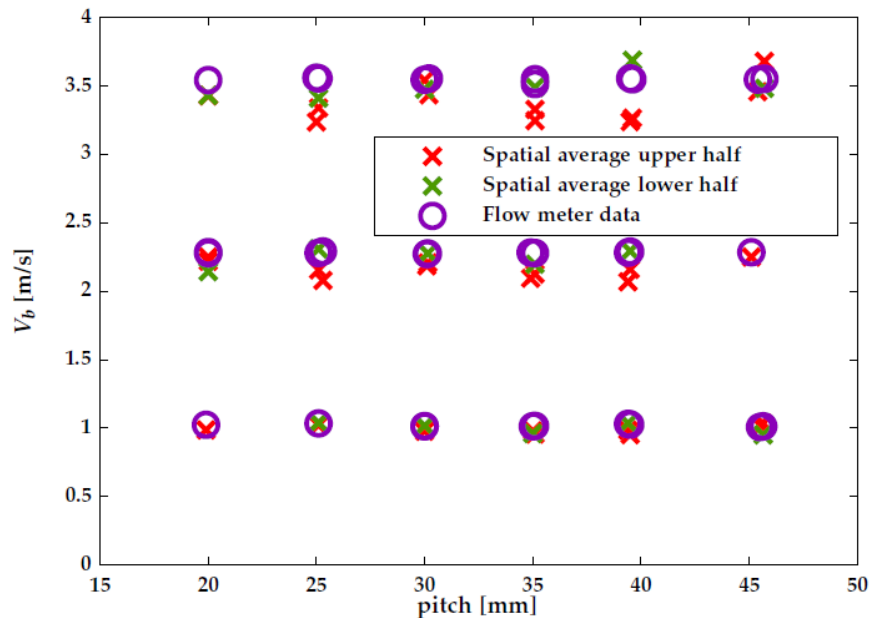


Figure 4.38: Bulk velocity  $V_b$  for all available EL measurements. Comparison between PIV results for the upper ( $\times$ ) and lower ( $\times$ ) halves of the velocity field and the flow meter results ( $\circ$ ). The three horizontal rows of data correspond to  $Re_r = 7.3 \times 10^4$  (bottom),  $1.6 \times 10^5$  (middle) and  $2.5 \times 10^5$  (top).

### 4.7.3 Axial spatial averaging of turbulent stresses

When computing the effective spatially averaged mean stress on the flow, two components are taken into account: the axially averaged Reynolds stresses and the dispersive stresses. The averaged Reynolds stresses were defined earlier as  $\tau = -\rho\overline{uv}$  (Eq. (4.2)). The dispersive stresses are the apparent stresses in the flow induced by the axial spatial variation rather than the temporal variation, defined as:

$$\theta = -\rho\overline{U'V'} \quad (4.4)$$

$$U'(x, y) = U(x, y) - \overline{U}, \quad V'(x, y) = V(x, y) - \overline{V} \quad (4.5)$$

with the overlines indicating an averaging operation in axial direction.

The Reynolds stresses, dispersive stresses and their sums are shown in Fig. 4.39. The Reynolds stress profiles display a linear increase from zero at the centre of the pipe to a maximum at approximately the rib crest, in contrast to the local stress profiles in Fig. 4.33, which showed deviations from the linear slope far above the crest. The dispersive stresses have a negligible magnitude above the rib height, only contributing significantly to the total stresses within the cavity region, corresponding to the region with a significant wall-normal velocity.

With a linear decrease from approximately the crest height to the pipe centre and a less structured decrease from the maximum towards the pipe wall, the total stresses are very similar to those obtained for staggered and aligned blocked arrays computed by Coceal et al. (2006).

In the lower pipe half, in some cases a "bump" is present in the stress profile (approximately at wall-normal position 0.03, -0.035 m). This is a result of the interpolation across the region blocked from view by the connecting rods of the ribs and not a physical feature of the flow itself. For  $p = 45$  mm, this feature is visible in the upper pipe half at a wall-normal position of approximately 0.02 m.

### 4.7.4 Mixing length

From the Reynolds stress and gradient of the axial velocity, the effective mixing length as a function of wall-normal position can be computed. The definition for the mixing length is given in Eq. (1.14). Following the arguments by Coceal et al. (2006) discussed in Section 1.4.5, a linear profile of the mixing layer expressed by the relation

$$l_m = \kappa(y - d) \quad (4.6)$$

is equivalent to fitting a logarithmic velocity profile with the parameters  $\kappa$  and  $d$ , which are the von Kármán constant and displacement height, respectively.

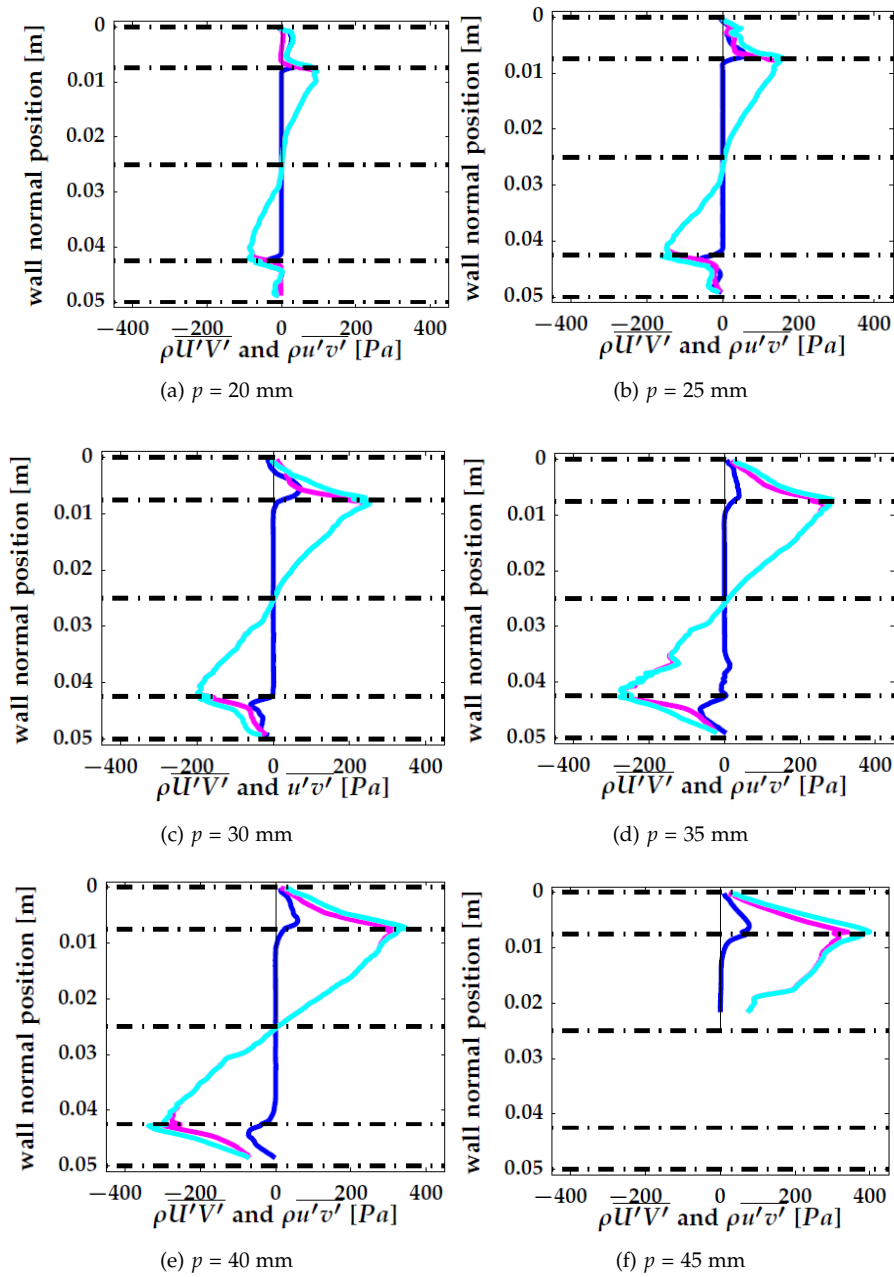


Figure 4.39: Spatially averaged Reynolds stress (magenta), dispersive stress (dark-blue) and total stress (light blue) for EL geometries at  $Re_r = 1.6 \times 10^5$ .

Combining this approach with the argument by Castro (2009) and Leonardi and Castro (2010) that the von Kármán constant  $\kappa$  might, in models describing very rough flows, not be an exact constant, the values for both  $\kappa$  and  $d$  can be obtained by fitting a line to the effective mixing length profiles. This is done in Fig. 4.40 for three geometries at Reynolds number  $1.6 \times 10^5$ . For comparison, the optimal displacement height  $d$  assuming  $\kappa$  to be 0.41 is also fitted.

The logarithmic region is not expected to extend far towards the centre of the pipe or within the cavity region, and indeed the linear region of the effective mixing length  $l_m$  occupies only a small region of the flow.

Figure 4.40 also includes a profile of the effective mixing length based on the total stresses rather than on the turbulent stresses only, thus including the effect of the spatial variation of the mean flow:

$$l_{m,tot} = \frac{\sqrt{\langle u'v' \rangle + \overline{U'V'}}}{dU/dy} \quad (4.7)$$

As can be seen in the figure, the profiles corresponding to the two mixing length definitions are identical in the region above the rib crest. Only in the cavity region, differences become visible.

The fit of Eq. (4.6) assuming  $\kappa$  to be 0.41 does not consistently provide a proper match to the data. This is clearly visible for example in Fig. 4.40d, where the green line indicates the fit without constraints for  $\kappa$ , and the magenta line the fit with  $\kappa = 0.41$ . Further evaluation of the data therefore uses the freely fitted mixing length model, omitting the fixed value for  $\kappa$ .

#### 4.7.5 Von Kármán constant and displacement length

Figure 4.41 displays the resulting values for  $\kappa$  as obtained by the fit to the mixing length using Eq. (4.6). When available, the result is also shown for the lower half of the pipe cross-section, indicated by crosses instead of circles. The different colours in Fig. 4.41 represent the results corresponding to different Reynolds numbers. Fig. 4.42 shows the corresponding results for the displacement height  $d$ .

Significant scatter is observed in the results for both parameters. However, an increase of  $\kappa$  with rib pitch and to a lesser extent with Reynolds number is evident.

The displacement height  $d$  decreases with increasing pitch. For a pitch of 20 mm,  $d$  is larger than 7.5 mm, which is the crest height of the ribs. For all other geometries,  $d$  is either at rib crest height or below that, penetrating slightly into the cavity.

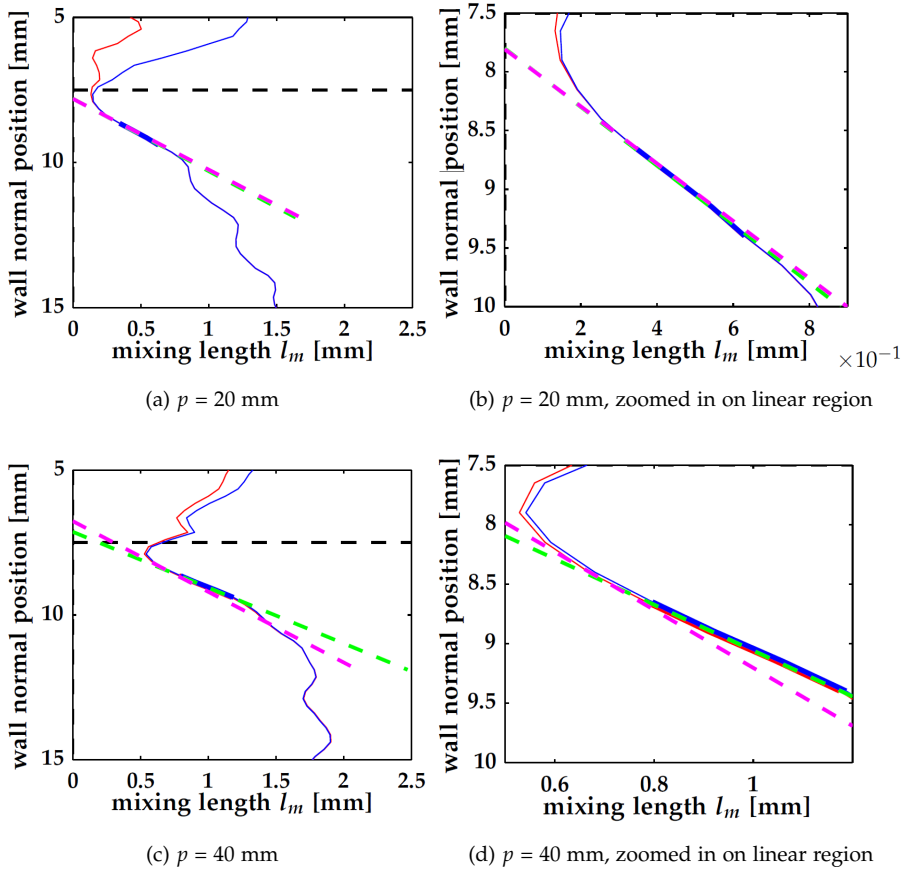


Figure 4.40: Effective mixing lengths  $l_m$  (blue) and  $l_{m,tot}$  (red). The black dash line indicates the rib crest height. The green dashed line represents the fit of Eq. (4.6) to the linear region of the mixing length. The magenta line represents the same fit, but assuming  $\kappa = 0.41$ .

Please note that  $\kappa$  and  $d$  are not mutually independent as they are determined as two fitting parameters in the same procedure.

With the limited number of data points, it is challenging to find the exact values of the various variables. The displacement height can be adequately described as a function of  $\kappa$  by the following relation:

$$d = A\kappa + f(p), \quad (4.8)$$

with  $A \approx 0.003$  m or 3 mm. Fig. 4.43 is similar to Fig. 4.42 but shows  $d - A\kappa$

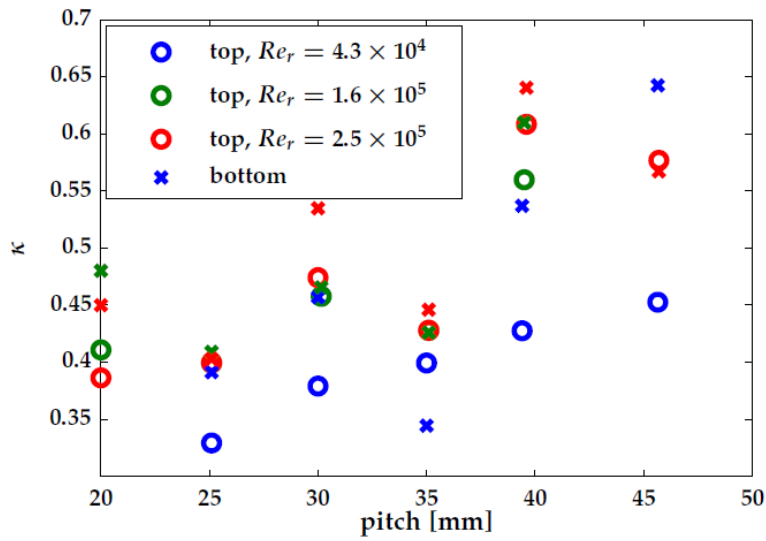


Figure 4.41: Von Kármán constant  $\kappa$  obtained by fitting Eq. (4.6) for rectangular ribs (EL geometry). Open symbols: upper half of the pipe; crosses: lower part of the pipe.

rather than  $d$ . Although some scatter is still present, the pitch dependency is less disorganized than in the original graph.  $A$  is determined by minimizing the differences of  $d - A\kappa$  between all cases with  $Re_r = 1.6 \times 10^5$  and  $2.5 \times 10^5$ .

The exact functionality  $f(p)$  remains undetermined, with too many options possible for the limited amount of available data points. The results in Fig. 4.43 do however suggest a separation in two regions, below and above a pitch of 35 mm.

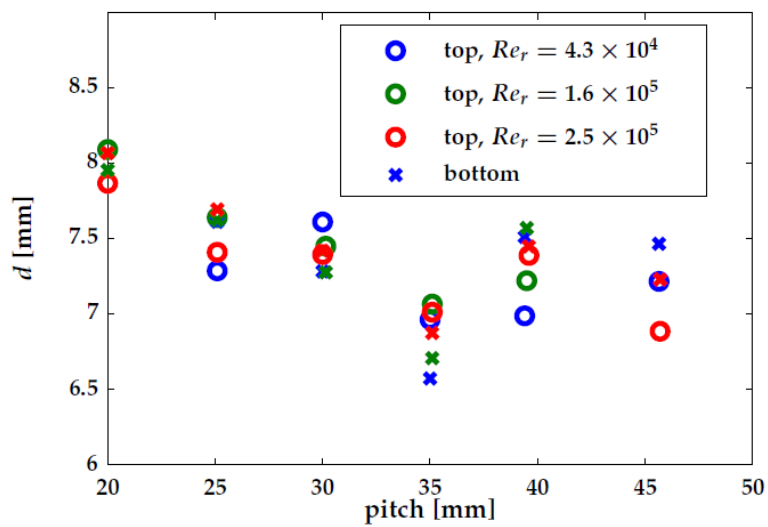


Figure 4.42: Displacement height  $d$  obtained by fitting Eq. (4.6) for rectangular ribs (EL geometry). Open symbols: upper half of the pipe; crosses: lower part of the pipe.

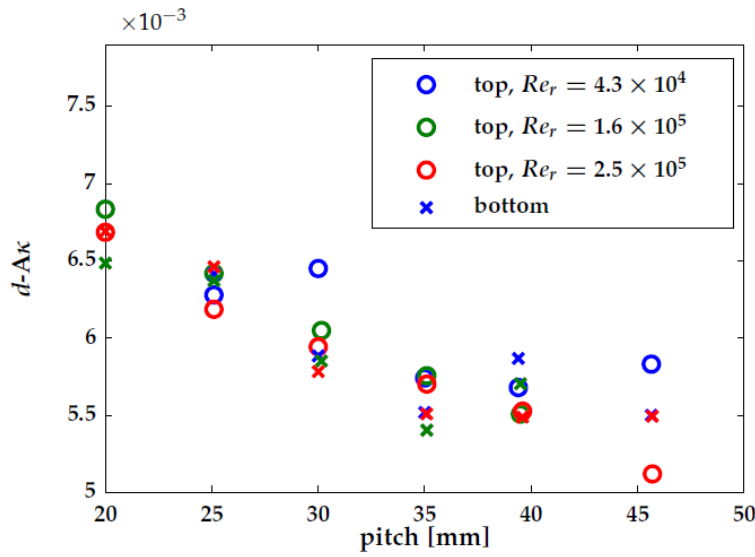


Figure 4.43: The relation  $f(p) = d - A\kappa$ , defined in Eq. (4.8). Open symbols: upper half of the pipe; crosses: lower half of the pipe.

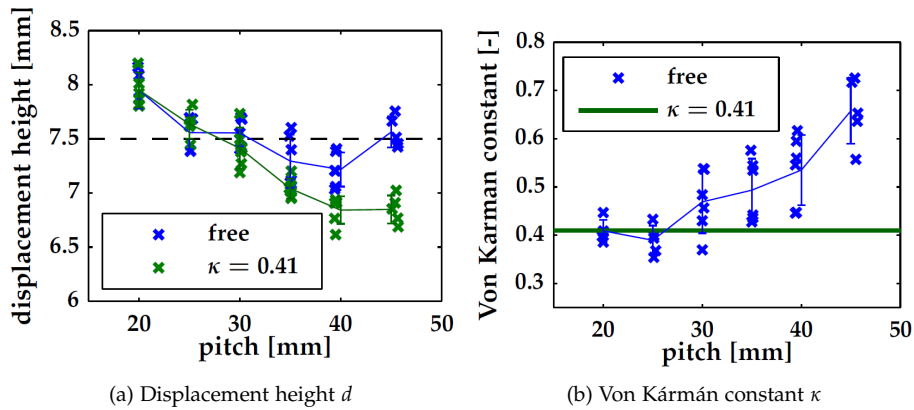


Figure 4.44: Displacement height  $d$  (a) and von Kármán constant  $\kappa$  (b) as obtained by the two procedures to fit Eq. (4.6): without (blue) and with (green) forcing  $\kappa = 0.41$ .

### 4.7.6 Logarithmic region

The obtained values for  $\kappa$  and  $d$  are used as input parameters in the full description of a rough-wall layer (see Section 1.4):

$$u^+ = \frac{1}{\kappa} \ln(y-d)^+ + C - \Delta U^+ + \frac{1}{\kappa} \Pi\left(\frac{y}{\delta}\right) \quad (4.9)$$

The velocity profile is fitted to the logarithmic region of the flow, thus omitting the last term in Eq. (4.9), resulting in Eq. (1.10).

The remaining equation has two independent unknowns: the friction velocity  $u_\tau$  and the roughness function  $\Delta U^+$ . For  $C$ , a constant value of 5.1 is adopted.

Eq. (1.10) is valid for the region with a logarithmic velocity profile only. For a smooth wall, this region would be between  $y^+ = 30$  and  $y/\delta \approx 0.15$  with  $\delta = R$  (see Section 1.2). For the current flow, the start of the logarithmic region is naturally located further away from the pipe wall. The fitted region uses ranges from 1 mm above the rib crest to approximately  $(y-h)/r = 0.15$ , with  $h$  the rib crest height and  $r$  the inner radius of the ribs.  $u_\tau$  and  $\Delta U^+$  are obtained by minimizing the norm between the fitted profile and the axial velocity averaged in axial direction within this range.

For all geometries, a proper fit can be obtained, with a logarithmic profile extending over the full fitting range and in most cases even further. Fig. 4.45 shows a typical example of the result of the fit. The  $x$  axis of the plot represents  $(y-d)^+$ , depicted in logarithmic scale, thus by definition resulting in a linear representation of the logarithmic region.

A friction velocity  $u_\tau$  and roughness function  $\Delta U^+$  are derived for every measurement on the EL geometry using this fitting procedure.

The total friction is calculated based on the obtained friction velocity, using the height at which the computed wall shear stress acts (see Section 1.4.3) as effective radius rather than the pipe radius  $R$ . This is logically the same height as the displacement height  $d$ , which is by definition the virtual origin of the logarithmic layer. In accordance with the method in Coceal et al. (2006), the effective wall shear stress acting on the pipe surface is obtained by extrapolating from  $d$  to the wall. The effective wall shear stress can now be described by:

$$u_\tau^* = u_\tau \sqrt{\frac{R}{R-d}} \quad (4.10)$$

Using  $\tau_0 = \rho u_\tau^{*2}$ , based on Eq. (1.2) and  $\Delta p = 2\tau_0/R$ , the pressure loss per meter is obtained. This pressure difference can be converted to a friction factor similar to the results of the pressure measurements in Section 2.4.4, such that the results can be compared directly.

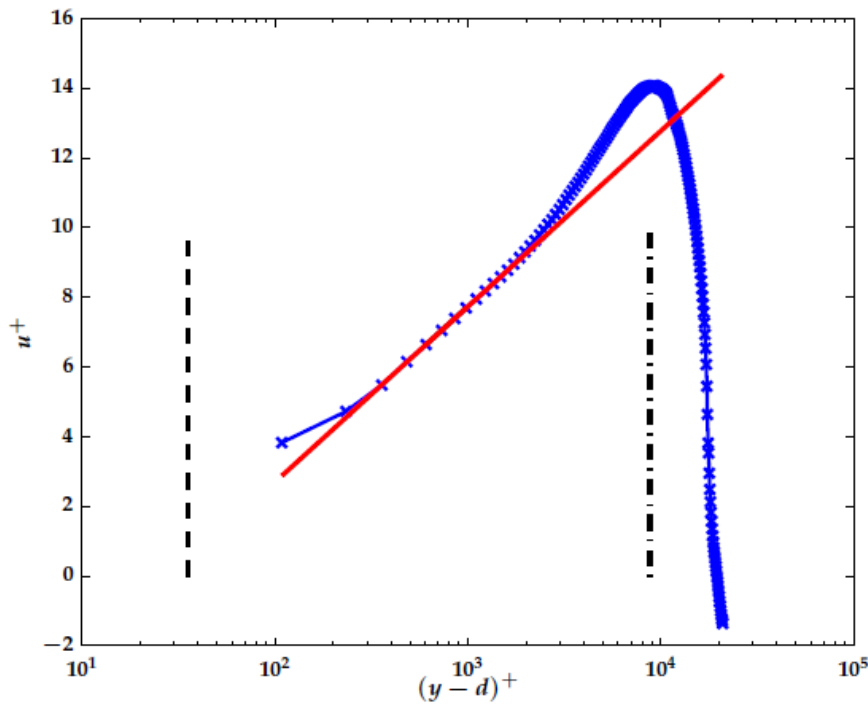


Figure 4.45: Spatial average velocity represented in logarithmic form for  $Re_r = 1.6 \times 10^5$  and  $p = 30$  mm. The dotted and dash-dotted black lines indicate the rib crest height of the upper rib cross section and centre line of the pipe, respectively. The red line is a fit to Eq. (4.9).

In the computation of the friction factor, a bulk velocity is required. For this velocity, the bulk velocity based on the flow meter measurements can be used. Another option is to use the bulk velocity based on the spatially averaged velocity profile, in which case the profile of the pipe half corresponding to that of the measured friction velocity is used. These velocities do show some variation as shown in Section 4.7.2.

As was determined in Section 4.7.5,  $\kappa$  and  $d$  may yield different results for the two halves of the measured cross section of the velocity field, which is a feature likely related to asymmetry of the flow. It is logical to assume a direct relation between the bulk velocity based on the measured velocity profile of the corresponding pipe half and the friction velocity obtained by fitting Eq. (4.9) to that same profile. A comparison between the results of both methods of including the bulk velocity

shows indeed that the latter option provides more consistent results.

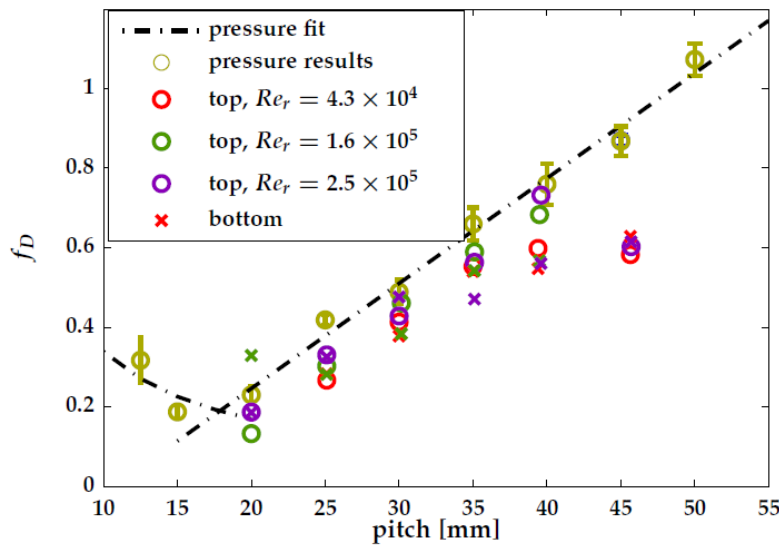


Figure 4.46: Friction factor as a function of pitch for rectangular ribs (EL geometry) as obtained from PIV measurements. Open circles: upper half of the pipe; crosses: lower half of the pipe. Also included are the friction factors derived from the pressure measurements and fitted trend as shown before in Fig. 2.13b.

Figure 4.46 shows the computed friction factor  $f_D$  for all measured cases, using the bulk velocity based on the corresponding velocity profiles. Included is the data as obtained from the pressure measurements shown in Section 2.4.4. The agreement between the two data sets is satisfactory up to a pitch of 35 mm, with the friction factor based on PIV measurements only slightly underestimating the friction factor based on direct pressure measurements. For larger pitches, the two friction factors start to deviate more. The results for the bottom half of the pipe, separately indicated in the figure, show overall less agreement with the pressure measurements than those obtained at the top half.

#### 4.7.7 Roughness function

Together with the friction velocity  $u_\tau$ , the roughness function  $\Delta u^+$  is obtained by fitting Eq. (1.10) to the measured velocity profiles. The roughness function serves as an offset to the logarithmic and outer layer caused by the effects of roughness in the inner layer, and is a function of geometry.  $\Delta U^+$  is typically positive. Fig.

4.47 displays  $\Delta u^+$  versus pitch for different Reynolds numbers.

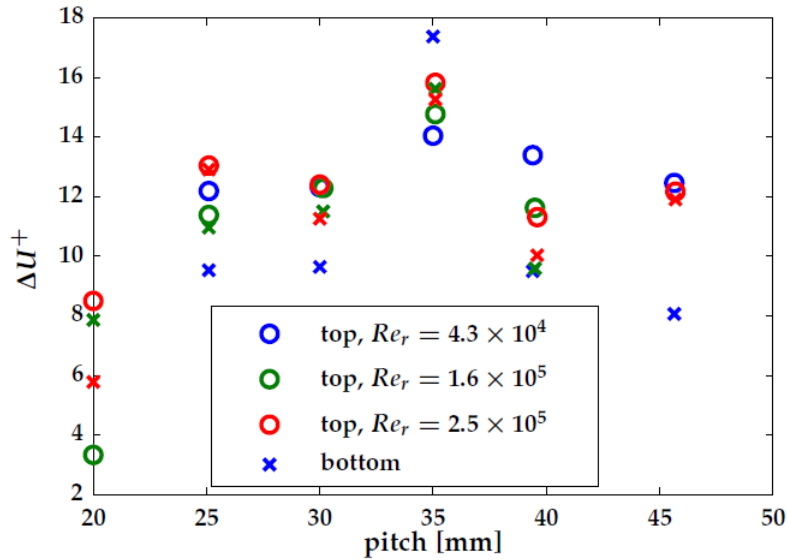


Figure 4.47: Roughness function  $\Delta u^+$  as a function of pitch. Open circles: upper half of the pipe; crosses: lower half of the pipe.

Jackson (1981) and Perry et al. (1969) suggest a roughness function for a ribbed surface of d-type roughness based on the displacement height (previously introduced in Eq. (1.11):

$$\Delta U^+ = \frac{1}{\kappa} \ln(h-d)^+ + B' \quad (4.11)$$

However, Jackson (1981) and Perry et al. (1969) assume, a priori, a positive value for  $h-d$  and fixed value for  $\kappa = 0.4$ . For the current results, these conditions do not apply and Eq. (1.11) is not directly applicable, as in a few cases  $h-d$  results in a small negative value. This is resolved by adding a small offset to the rib height. Instead of 7.5 mm, a slightly larger height  $h$  of 8.1 mm is substituted in Eq. (4.11). This guarantees a positive value for  $h-d$  for all results. Fig. 4.48 shows the measured and fitted values for  $\Delta U^+$  for both top and bottom halves of the pipe's cross section. The fitted values are computed using Eq. (4.11) with a fixed value for  $B'$  of 0. The dashed line is the fit obtained by Perry et al. (1969) with  $B' = -0.4$ . The agreement between the values obtained for  $\Delta U^+$  using Eq. (4.11) and those obtained from fitting to the logarithmic region is strong, certainly given the fact that Eq. (4.11) is designed to apply to d-type roughness only, while

these results show a agreement for all included measurements.

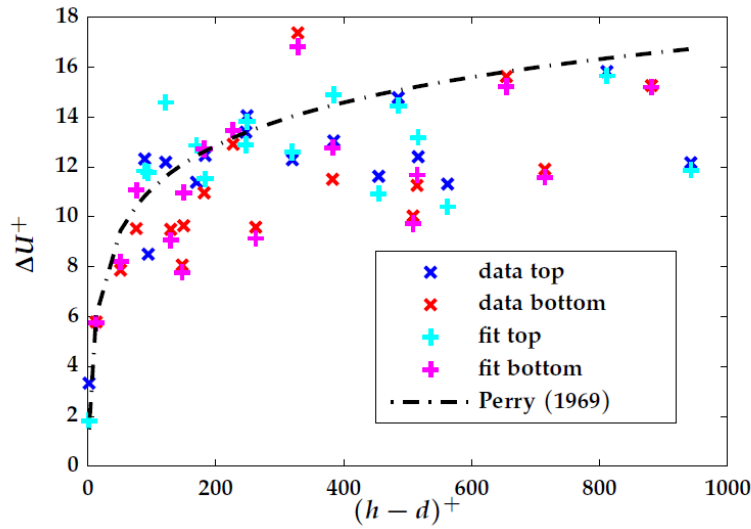


Figure 4.48: Measured ( $\times$ ) and fitted ( $+$ ) values of  $\Delta u^+$ . Fits obtained by fitting the data to Eq. (4.9) and by using Eq. (4.11) with  $B'=0$  and  $h=8.1$  mm. Dashed line: fit obtained by Perry et al. (1969) with  $B'=-0.4$ .

#### 4.7.8 Additive constant

The combined effect of the roughness function and the displacement height can be described as a single parameter, called the "additive constant"  $F$  and defined as

$$F = u^+ - \frac{1}{\kappa} \ln \left( \frac{y-d}{h} \right) \quad (4.12)$$

which, using Eq. (4.9) and omitting the last term describing the outer region, can be transformed to:

$$F = C - \Delta U^+ + \frac{1}{\kappa} \ln(h^+) \quad (4.13)$$

Coleman et al. (2007) report this additive constant  $F$  (referred to as  $B$  in their publication) for channel flows with two-dimensional rib roughness. Fig. 4.49 compares their results with ours: the non-black symbols show  $F$  as a function of relative pitch as calculated using the fitted  $\Delta U^+$  and  $\kappa$  from the current study (see

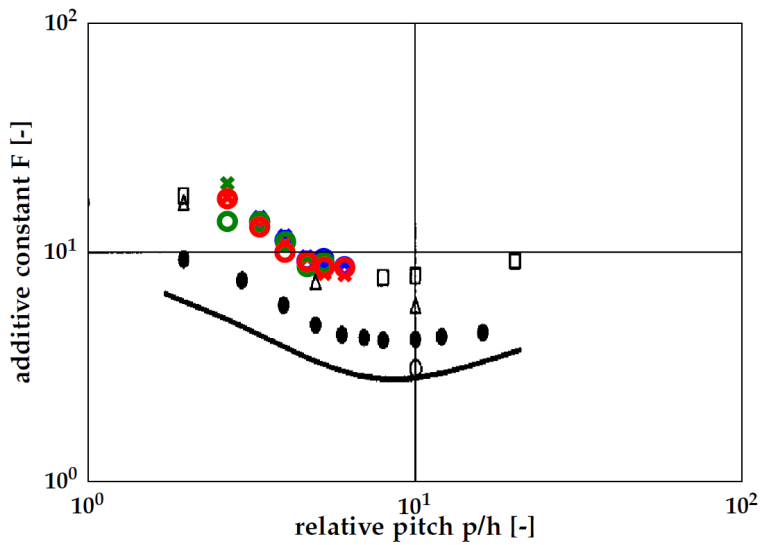


Figure 4.49: Additive constant  $F$  compared with the results for two-dimensional ribs from Coleman et al. (2007). The three colours correspond to the three Reynolds numbers investigated (blue =  $Re_r = 4.3 \times 10^4$ ; green =  $Re_r = 1.6 \times 10^5$ ; red =  $Re_r = 2.5 \times 10^5$ ). The black symbols correspond to results from studies for two-dimensional rectangular rib roughness on one side of a channel flow as included in Coleman et al. (2007). They correspond to the following relative rib heights:  $\bullet$ :  $h/H = 0.09$  (free surface flow);  $\square$  and  $\triangle$ :  $h/H = 0.1$ ;  $\circ$ :  $h/H = 0.06$ ; solid line: theoretic limit for  $h/H = 0$ .

Sections 4.7.5 and 4.7.7); the black symbols are the results reported by Coleman et al. (2007).

The relative roughness height of the current measurements is with  $h/R = 0,3$  significantly higher than that of the reported results from Coleman et al. (2007) in Fig. 4.49. In contrast to these results, we don't use a fixed value for  $\kappa$ , which enables the application of Eq. (4.9) to adequately describe the flow profiles for large relative roughness. However, the magnitude and trend of the additive constant in Fig. 4.49 matches the results reported in Coleman et al. (2007) well.

## 4.8 Summary of results and preliminary conclusions

We studied flows through pipe sections containing one or multiple ribs of various shapes. The observed flows show characteristics universally present for all geometries, such as a separating shear layer, flow impingement and recirculating

regions within the cavity. They also display a strong dependency on both rib pitch  $p$  and rib shape. For the rectangular (EL) geometries, the behaviour is, within the observed velocity range, independent of Reynolds number whereas for rounded (RL) geometries, the flow changes significantly as a function of Reynolds number.

The axially averaged Reynolds stresses and axially averaged velocity profiles allow us to compute the mixing length, which is used to derive the displacement height  $d$  and von Kármán constant  $\kappa$ . The latter value is not forced to be a constant as is commonly done in literature, but allowed to vary with pitch. This results in a much better agreement of the logarithmic region of the measured velocity profiles with the fitted velocity profile according to the theory for rough-walled flows.

The flows show asymmetry between the top and bottom halves of the pipe's cross section. This is attributed to azimuthal secondary flows induced by the rod structure which is present to keep the ribs in place. The asymmetry is largely confined to the cavity regions and only marginally influences the flow beyond the cavity crest height. However, as observed for the fitting of the logarithmic layer, the differences in "local" velocity above the rib are not entirely negligible.

Although allowing the von Kármán constant  $\kappa$  to vary enables a proper fit to the mixing length profile and thus to obtain  $d$ , the question remains how to interpret the scaling of the logarithmic layer.  $\kappa$  becomes a function of the geometry, with relatively large deviations from the commonly accepted range of 0.38-0.42, especially for large-pitch geometries (see Fig. 4.44b).

A fit to the logarithmic layer of the axially averaged velocity profiles results in the friction velocities and hence in the friction factors, which are computed based on the "local" bulk velocities. We find a reasonable agreement with the friction factors obtained in Chapter 2.4.4, as can be seen in Fig. 4.46. However, the friction factors obtained by using the fitting method for the geometries with a larger pitch are lower than those derived from pressure measurements. This deviation approximately coincides with the deviation of  $\kappa$  from the constant value 0.41.

Fitting the obtained velocity profiles to the rough-wall description yields, next to the friction velocity, a roughness function  $\Delta U^+$ . In Section 4.7.7, this function is expressed as a function of the displacement height  $d$ , a method adopted from Perry et al. (1969). We find reasonable agreement between the measured and computed roughness function. Agreement with the data for d-type roughness from Perry et al. (1969) is also reasonable.

The displacement height  $d$  and roughness function  $\Delta U^+$  are influenced by our choice to dismiss the universal value of  $\kappa = 0.41$ . Thus, the agreement of the results with those for d-type roughness by Perry et al. (1969) for the intermediate-

type roughness currently studied is remarkable.

The roughness parameter  $F$ , as introduced in Section 4.7.8, is another approach to parametrize the effect of wall roughness on the flow. The results match the trends of  $F$  versus pitch  $p$  as reported by Coleman et al. (2007) for different roughness studies.

The comparison with both the results of Perry et al. (1969) and Coleman et al. (2007) confirm the validity of the approach to consider the ribbed geometries as a wall roughness, despite their large roughness height. The use of a non-universal interpretation of  $\kappa$  enables the common parametrization of a rough-wall flow to be extended to larger relative roughness heights and relatively large roughness spacings.

However, care must be taken to use and interpret the resulting parameters. The friction factor derived from the fitted velocity profile does not comply with the measured friction factor when the rib spacing increases and  $\kappa$  starts deviating. It must be noted that, based on the current data, the friction factor, when it is forcibly computed with a fit based on  $\kappa = 0.41$ , also does not improve the agreement of the friction factor calculations with the direct pressure measurements.

The need to significantly adjust  $\kappa$  in order to properly fit a logarithmic region is due to the adaptation in the slope of the mixing length profiles. This implies that for geometries with a larger pitch, either the Reynolds stresses or the mean gradient  $dU/dy$ , or both, do not scale with velocity and position as they would in a "normal" rough flow. Typical for the flows through these larger pitched geometries in comparison with shorter-pitch geometries is the increase in the axial variation of the mean flow velocities beyond the cavity region. In Section 4.7.4, the spatial variation of the flow was taken into account by including the dispersive stresses in the computation of the mixing length. This contribution was negligibly small in the linear region of the mixing length profile. It thus does not directly influence the fit of the logarithmic region. However, the axial flow variation can also *indirectly* influence the process of transport of energy, both on large and small scales. Therefore, the mean and instantaneous patterns within the flow are analysed in more detail in Chapter 5.



## Chapter 5

# PIV: temporal fluctuations

Chapter 4 provided characteristics of the mean flow and presented the mean effects of flow fluctuations. This chapter focuses on the fluctuations themselves. Sections 5.1 and 5.2 use a statistical approach. Section 5.4 discusses instantaneous coherent structures more quantitatively.

### 5.1 Statistical analysis of the flow dynamics: joint probability density functions

Among the results discussed in Section 4.6 are the Reynolds stresses; the result of all instantaneous contributions  $-u'v'$  of the turbulent fluctuations  $u'$  and  $v'$  to the total apparent stress.

To gain more insight into these fluctuations, we compute the joint probability density function or **jpdf** of the terms  $u'$  and  $v'$  for every position in the flow. Additionally, the corresponding contribution to the total Reynolds stress  $-\rho\overline{u'v'}$  is computed. Figs 5.1a and 5.1b provide an example of a jpdf and corresponding contribution to the Reynolds stresses for a single position in the flow.

Each jpdf can be approximated by an ellipsoid parametrized by its orientation, position on the axis and elongation, with each of these parameters depending on the position within the flow. The ellipsoid parameters fitted to each jpdf, together with the fluctuation strength and occurrence rate of the most frequent occurring fluctuation, are a simple method of characterizing the jpdfs, allowing for an analysis of the spatial distribution of the characteristics of the stress generation within the flow.

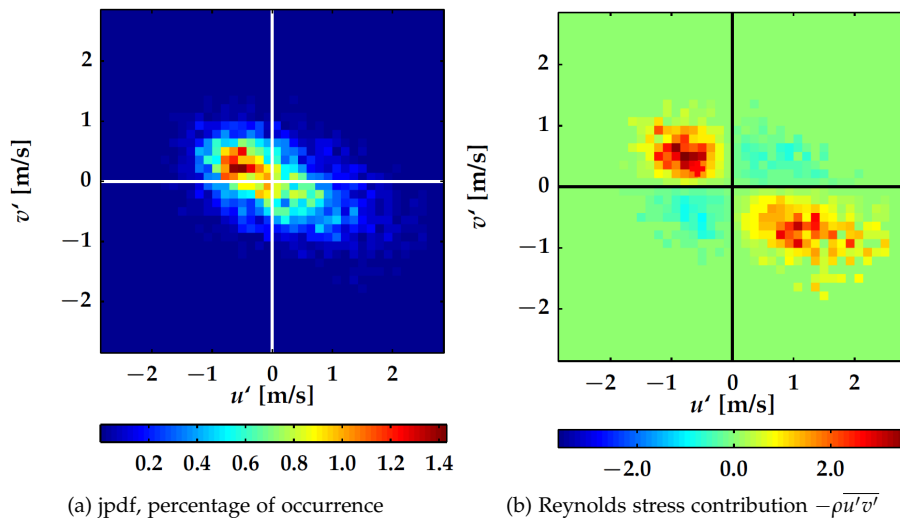


Figure 5.1: Example of a jpdf (a) and corresponding Reynolds stress contribution (b). Case: EL geometry,  $p = 25$  mm,  $Re_r = 1.6 \times 10^5$ . Position: rib-crest height and axial cavity centre.

### 5.1.1 Parameterization of the jpdf

The lengths of the principal axes of the fitted ellipse relate to the local turbulent intensity. The ratio between the length of the major ( $a$ ) and minor ( $b$ ) principle axes is an indicator for the degree of turbulent isotropy. The latter is expressed using the eccentricity of the ellipse:

$$\varepsilon = \sqrt{1 - \frac{b^2}{a^2}} \quad (5.1)$$

The orientation of the principal axis is the direction of the strongest anisotropy, and thus directly related to the direction in which the highest number of strong fluctuations occur. Furthermore, a maximum occurrence rate further away from the origin of the jpdf points at a more intermittent flow, in which frequent but relatively weak fluctuations are balanced by much less frequent but much stronger fluctuations in the opposite direction.

The ellipse parameters are determined by fitting a binary version of each jpdf, with a threshold defined such that 95% of the fluctuations are taken into account. This means that 5% of the fluctuations are excluded. These include occasional very strong fluctuations, which individually contribute relatively strongly to

the total Reynolds stresses. Much more than all other obtained characteristics, the location of the origin of the ellipse is sensitive to the threshold used for its determination. This is explained by the fact that the fluctuations falling in the cut-off percentage, i.e. 5% in the current situation, are not symmetrically distributed but mostly located on the opposite side of the graph with respect to the peak of the distribution. Hence, the origin of the ellipse is a function of the employed threshold; this property is best illustrated with a strongly non-symmetric jpdf. Fig. 5.2 shows an example of such a jpdf, with ellipsoids fitted for various thresholds. Indicated are the ellipse centres and edges.

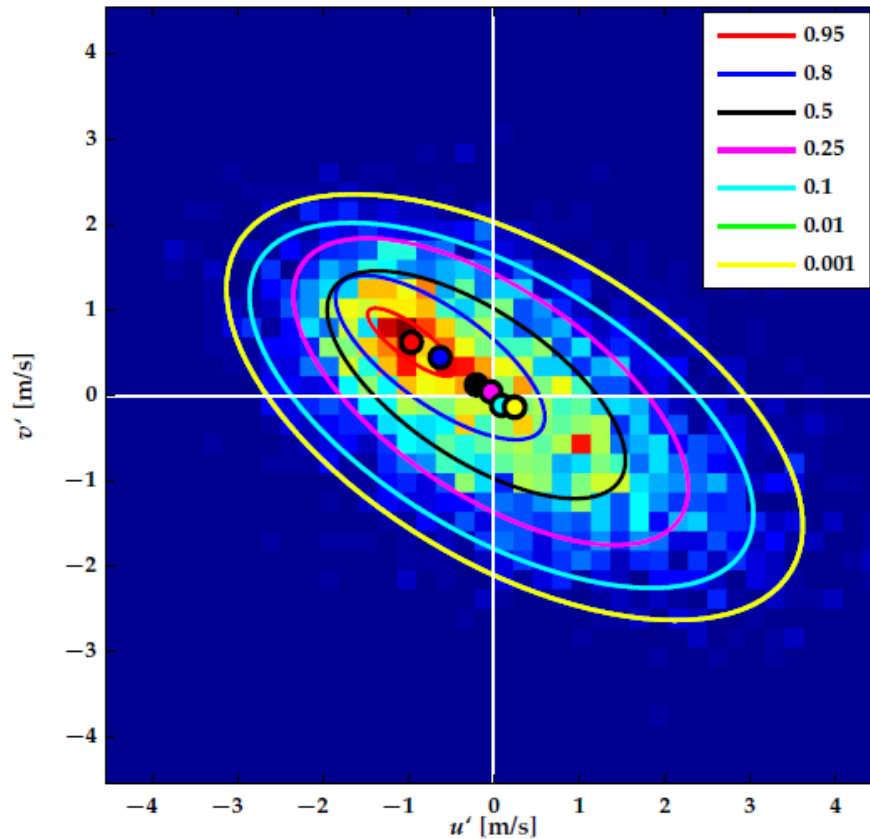


Figure 5.2: Effect of threshold fraction on the jpdf ellipsoid origin (circles) and size (lines). The lines for threshold fractions 0.01 and 0.001 overlap due to the limited resolution of the distribution. The major and minor axes are not shown for clarity.

Due to the observed sensitivity to the chosen threshold, the origin of the ellipse is

only partially useful for data comparison. The same applies to the absolute length of both principal axes, although their ratio is not a threshold-sensitive parameter. The peak location of the jpdf describes the asymmetry of the fluctuations and is, different from the ellipsoid origin, insensitive to the applied threshold.

### 5.1.2 Spatial evolution

Figures 5.3 and 5.4 visualize the jpdfs at different wall-normal positions for a single axial position. The plots include the fitted ellipse, the major and minor axes, the ellipsoid centre and the location of the most occurring fluctuation of the distribution. The plots show visually that the fitted ellipsoids match the jpdf characteristics well, capturing their shape correctly throughout the domain, thus enabling a further analysis based on ellipsoid parameters and peak location only. Figures 5.5a to 5.6b show the ellipsoid properties for a single measurement case. The plots display, respectively, the major and minor axis lengths, orientation, origin and peak location. The latter is obtained using a sub-pixel accuracy method, using a Gaussian fit to a  $3 \times 3$  neighbourhood around the maximum bin.

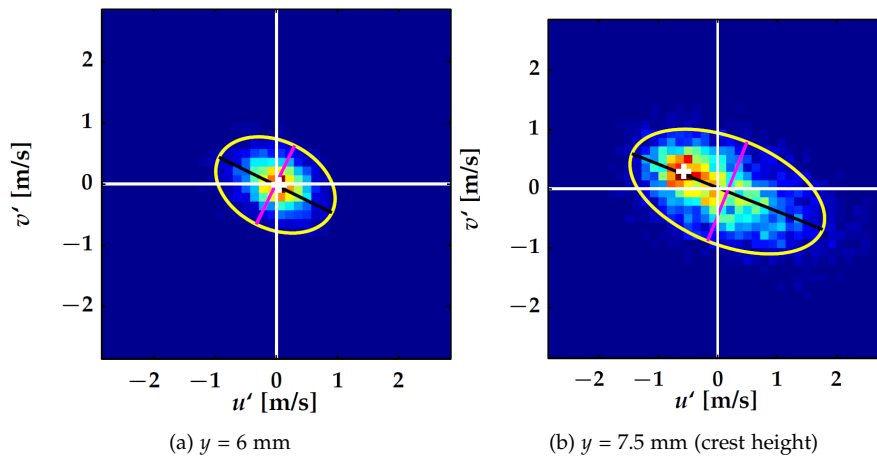


Figure 5.3: Jpdf evolution versus wall-normal position  $y$ . Case: EL geometry,  $p = 25 \text{ mm}$ ,  $Re_r = 1.6 \times 10^5$ . Position: axial cavity centre.

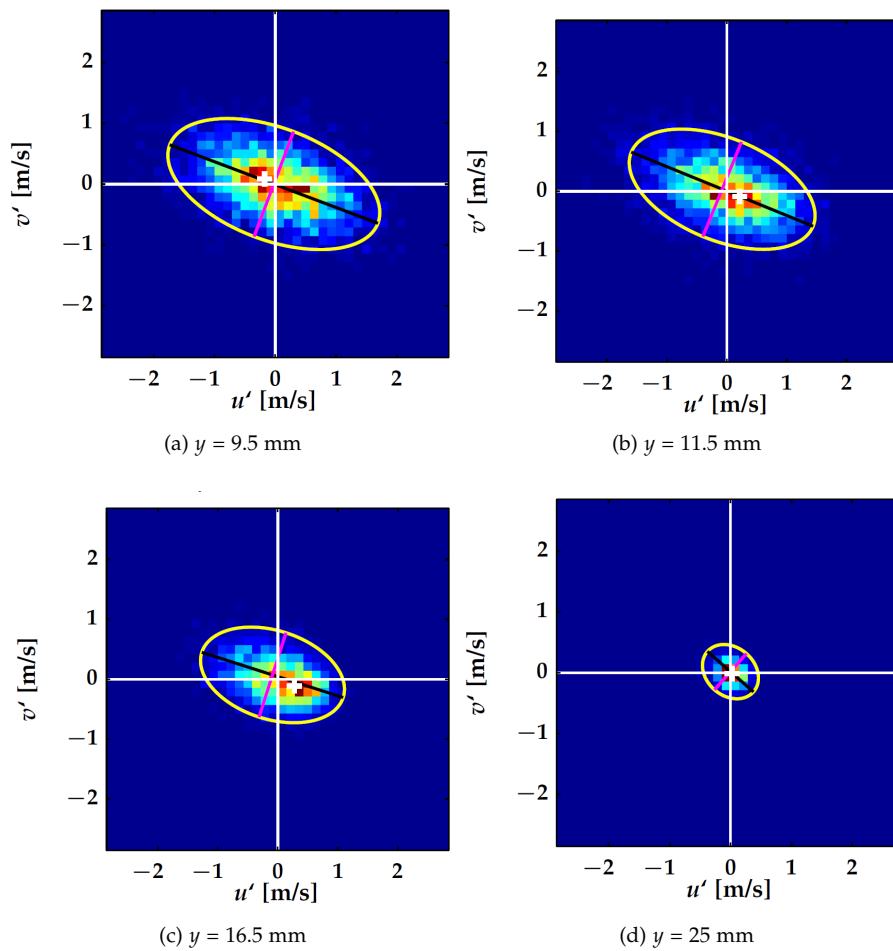
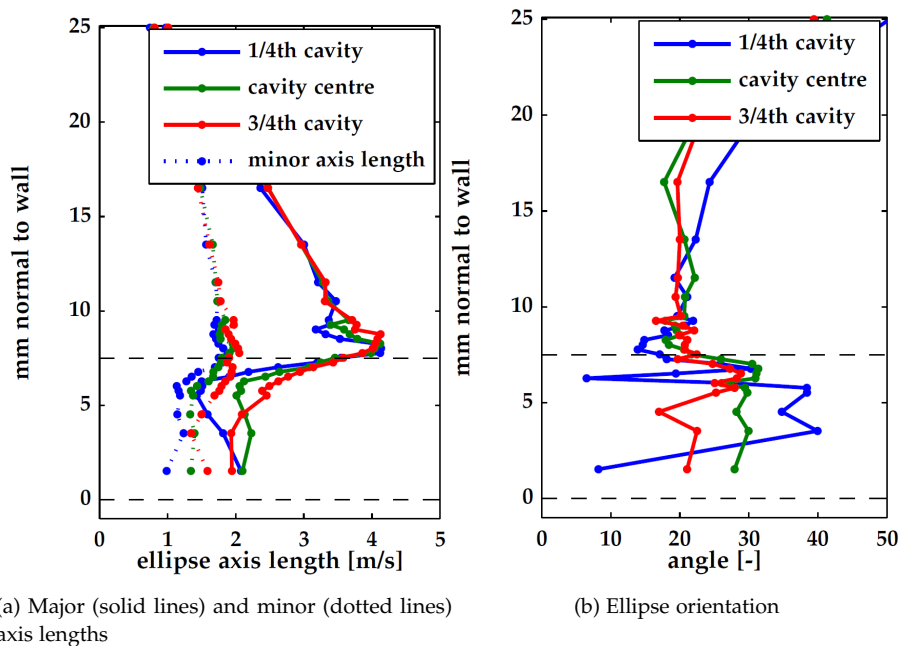


Figure 5.4: Jpdf evolution versus wall-normal position  $y$ . Case: EL geometry,  $p = 25$  mm,  $Re_\tau = 1.6 \times 10^5$ . Position: axial cavity centre. Continuation of Fig. 5.3

The orientation of the ellipse is defined as the angle of the major axis with the horizontal axis, positive when rotated in clockwise direction and by definition between  $-90^\circ$  and  $+90^\circ$ . In some regions of the domain, the ellipse is nearly circular, leading to ambiguity and uncertainty in the ellipsoid angle. However, in the regions with a significant jpdf elongation, the angle is well determined.

Even with the application of the sub-pixel accuracy method, the accuracy with which the peak location is determined is somewhat limited. This is a result of the resolution of the jpdf, which, in turn, is related to the size of the recorded data

series. Despite these limitations in accuracy, the variables describing the ellipsoids provide a robust indication of the behaviour of the turbulent fluctuations.



(a) Major (solid lines) and minor (dotted lines) axis lengths

(b) Ellipse orientation

Figure 5.5: Ellipse properties versus wall-normal position. Case: EL geometry,  $p = 25$  mm,  $Re = 1.6 \times 10^5$ .

The major and minor axis lengths show, as would be expected, behaviour mirroring that of the Reynolds stresses. The decreasing eccentricity towards the centre of the pipe is also a logical result: since the Reynolds stresses disappear, the positive and negative contributions to the Reynolds stresses must balance each other, leading to a symmetric distribution.

The orientation varies slowly from a  $20^\circ$  to a  $40^\circ$  angle when moving from above the rib crest to the centre of the pipe. At the centre, as mentioned above, the angle is difficult to determine due to the loss of eccentricity. In the region at crest height, corresponding to location of the shear layer separating the cavity region from the core flow, the angle changes more rapidly. Within the cavity, the angles corresponding to different axial locations with respect to the rib show a large variation. However, since the ellipsoid eccentricity is very small in this region, the orientation within the cavity region must be interpreted with care.

The ellipse centre location (for clarity shown only for the centre axial position)

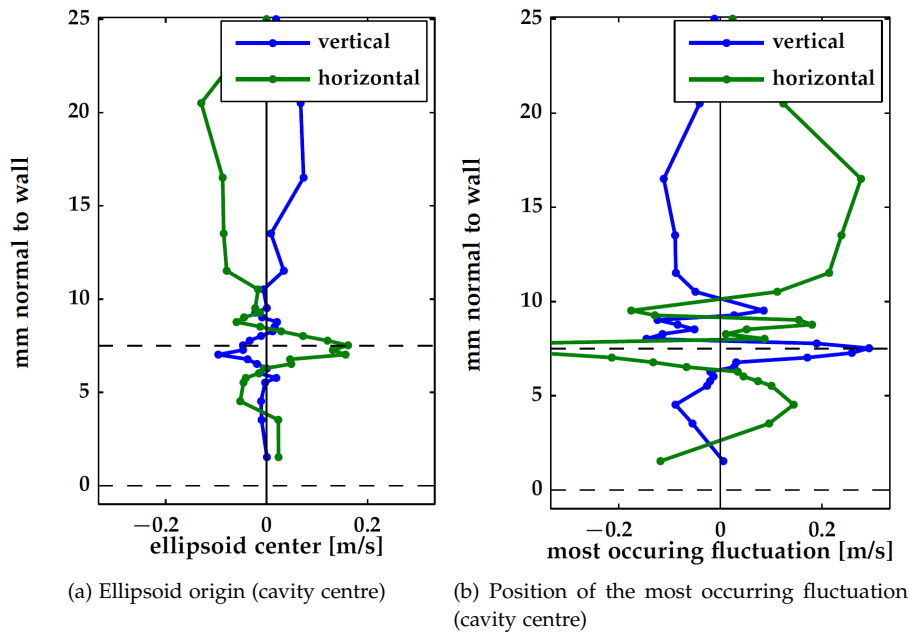


Figure 5.6: Ellipse properties versus wall-normal position. Case: EL geometry,  $p = 25$  mm,  $Re = 1.6 \times 10^5$ . (Continuation of Fig. 5.5)

shows small variations when moving in axial direction, except for the region deeper into the cavity. The position of the centre in vertical and horizontal direction is in general of opposite sign, indicating a bias towards negative  $u'v'$ , thus positively contributing to the total Reynolds stresses. This feature is further elaborated in Section 5.2.

The peak location shows behaviour that mirrors that of the ellipsoid centre, but with larger amplitudes. The centre of mass of the distribution is by definition located at the origin. Thus, a peak on one side must be balanced by another peak or larger area of lower values on opposite side, the latter of which is the case.

### 5.1.3 Dependence on pitch and Reynolds number

Qualitatively, the behaviour displayed in Figs. 5.5 and 5.6 is observed for all geometries. Quantitatively, however, the parameters depend on geometry, Reynolds number and axial position.

The ellipse parameters fitted to the jpdfs can be compared using their characteristic values in the region above the cavity crest. Within the cavity region, the

behaviour is too irregular to capture in a few describing parameters.

Figures 5.7a and 5.7b display the maximum major and minor axis length, respectively, as a function of pitch. The plots are based on the results for three axial locations (1/4th, 2/4th and 3/4th of the cavity width) of all available data for rectangular ribs (EL geometry). Similarly, Fig. 5.7b displays the same results for the minor axis. The results inside the cavity region are not included for the reason mentioned above.

We find that the maximum length of the major axis increases with both Reynolds number and pitch, which is not a surprising result given the relation between the total Reynolds stresses and the pitch and Reynolds number, as discussed in Section 4.6.2. The minor axis length displays very similar behaviour, with a magnitude approximately a factor two smaller than that of the major axis. The eccentricity of the distribution is thus independent of both pitch and Reynolds number.

Figure 5.7c displays the mean ellipsoid angle obtained at the axial position at the cavity centre, and in wall-normal direction between the rib crest height and  $y = 15$  mm. This is the region where the ellipse orientation is relatively constant. There does not appear to be a trend in how the orientation of the distribution depends on Reynolds number but the angle as a function of wall-normal position clearly depends on the rib pitch. Although reproducible for all three measured Reynolds numbers, the difference in orientation is only  $5^\circ$ . The maximum angle occurs for  $p = 30-35$  mm, corresponding to the geometric range in which more trends change, such as the friction factors obtained from PIV measurements deviating from those directly measured in Fig. 4.46.

The ellipse centre and strength of the most occurring fluctuations display behaviour that is too complex to capture in a single parameter and are therefore not included in Fig. 5.7.

For all measured Reynolds numbers and pitches we observe a similar overall pattern as visible in Fig. 5.6b, with a sharp transition between a negative and positive value slightly above rib crest height, further towards the centre, followed by more but smaller fluctuations. Symmetry between the vertical and horizontal component is again encountered and the sign of the large peak around the rib crest is opposite of the one towards the core region of the flow.

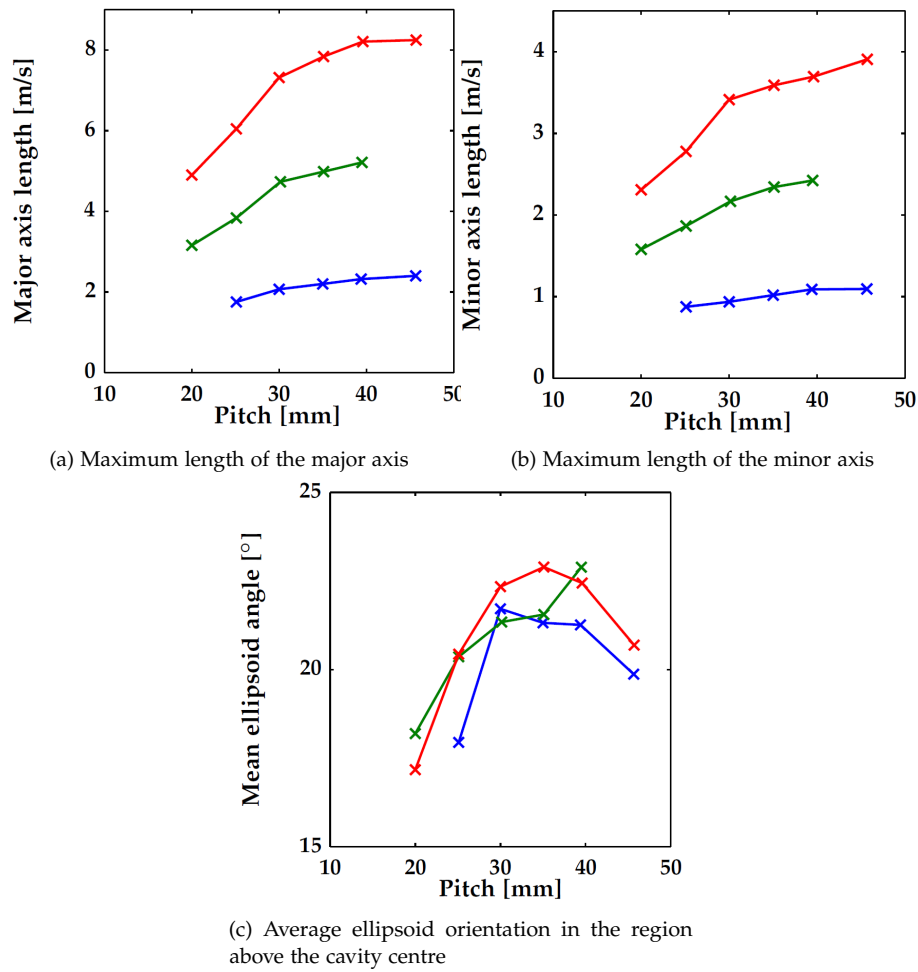


Figure 5.7: Jpdf parameters as a function of pitch. Case: rectangular ribs (EL geometry).  $Re = 7.3 \times 10^4$  (blue),  $1.6 \times 10^5$  (green),  $2.5 \times 10^5$  (red).

## 5.2 Quadrant analysis

Thus far, in Sections 5.1.2 and 5.1.3, focus was on the distribution of the occurring fluctuations. The next step is to evaluate the contribution of these distributions to the Reynolds stresses. The jpdf can directly be transformed to a distribution of the contribution (see e.g. Fig. 5.1b).

These contributions are categorized in quadrants Q1 to Q4. Different defini-

tions for these quadrants are possible; in the current work, they are identified according to layout shown in Fig. 5.8, with the  $y$ -axis positive from the pipe wall inwards towards the centre. This definition is conform most literature concerning quadrants.

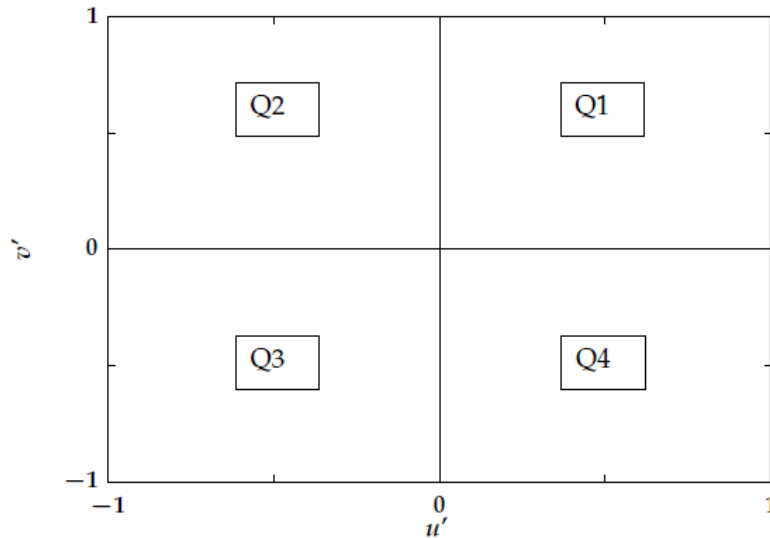


Figure 5.8: Schematic layout of the 4 quadrants Q1-Q4.

By definition, the contribution to the Reynolds stresses from quadrants 1 and 3 are negative, whereas quadrant 2 and 4 contribute positively to the total stresses. According to the results in Chapter 4.6.2, the net Reynolds stresses are mainly positive, although some small regions with net negative stresses are present. This implies that the contributions of quadrant 2 and 4 should outweigh those of the other two quadrants.

### 5.2.1 Results per quadrant

The contributions of the quadrants to the Reynolds stresses are shown in Fig. 5.1b. The Reynolds stress contribution, defined as  $-\rho u'v'$ , are by definition positive for Q2 and Q4, and negative for the other two quadrants. The total contribution of each quadrant as a function of position is depicted in Figs 5.9a and 5.10a for the EL geometry with 25 and 40-mm pitch, respectively. The total Reynolds stress at every available point, as previously shown in Fig. 4.33, is included for comparison. Although the negative contributions of Q1 and Q3 are certainly not

negligible, they are outweighed by the positive contributions of Q2 and Q4.

In Fig. 5.9a, the contributions of Q1 and Q3 are similar to each other and independent of wall-normal location. However, the contributions of Q2 and Q4 differ with respect to each other. In the bulk region, the contribution of Q2 is consistently larger than that of Q4. This trend decreases a few mm above the rib crest. Slightly above the rib crest, Q4 becomes stronger instead, which remains the situation further towards the wall and into the cavity. Deeper within the cavity, the trends are unclear and, opposed to the situation in the rest of the domain, no longer similar at the various axial positions (not shown here).

In Fig. 5.10a, the same behaviour is visible for larger pitch, with an even more distinct difference around the rib crest height than in the 25 mm case. In the latter case, the trend extends much further into the cavity, corresponding to a Reynolds stress profile with less axial variations for this geometry than for the shorter-pitched cases.

Panels 5.9b and 5.10b show the relative contributions of the four quadrants to the Reynolds stresses. As could be expected based on the ellipsoid shape of the *jpdfs* the contributions of Q1 and Q3 approximately mirror the behaviour of the contributions of Q2 and Q4 at a lower intensity. The relative contributions of the negative versus the positive quadrants are not strongly influenced by the geometry, although the absolute contributions differ significantly.

Figures 5.9c and 5.10c show the fraction of occurrence of each quadrant. Comparing these plots with their corresponding contribution in Figs 5.9a and 5.10a reveals a strong skewness. The regions in which the contribution of Q2 exceeds that of Q4, Q2 occurs less frequent. Vice versa the same is valid; where the Q4 contribution is larger, Q2 events occur more frequently. This implies that the less occurring event, whether it is sweeps or ejections, is stronger. In addition, the Q1 and Q3 events are not occurring equally often, although their contributions match very well. Figs 5.9d and 5.10d illustrate this feature; they show the contribution of each quadrant as if they each would be occurring continuously. They therefore show the relative strength of an average event, rather than the average contribution. The profiles look similar to those of the total contribution, but exaggerate the differences between the quadrants.

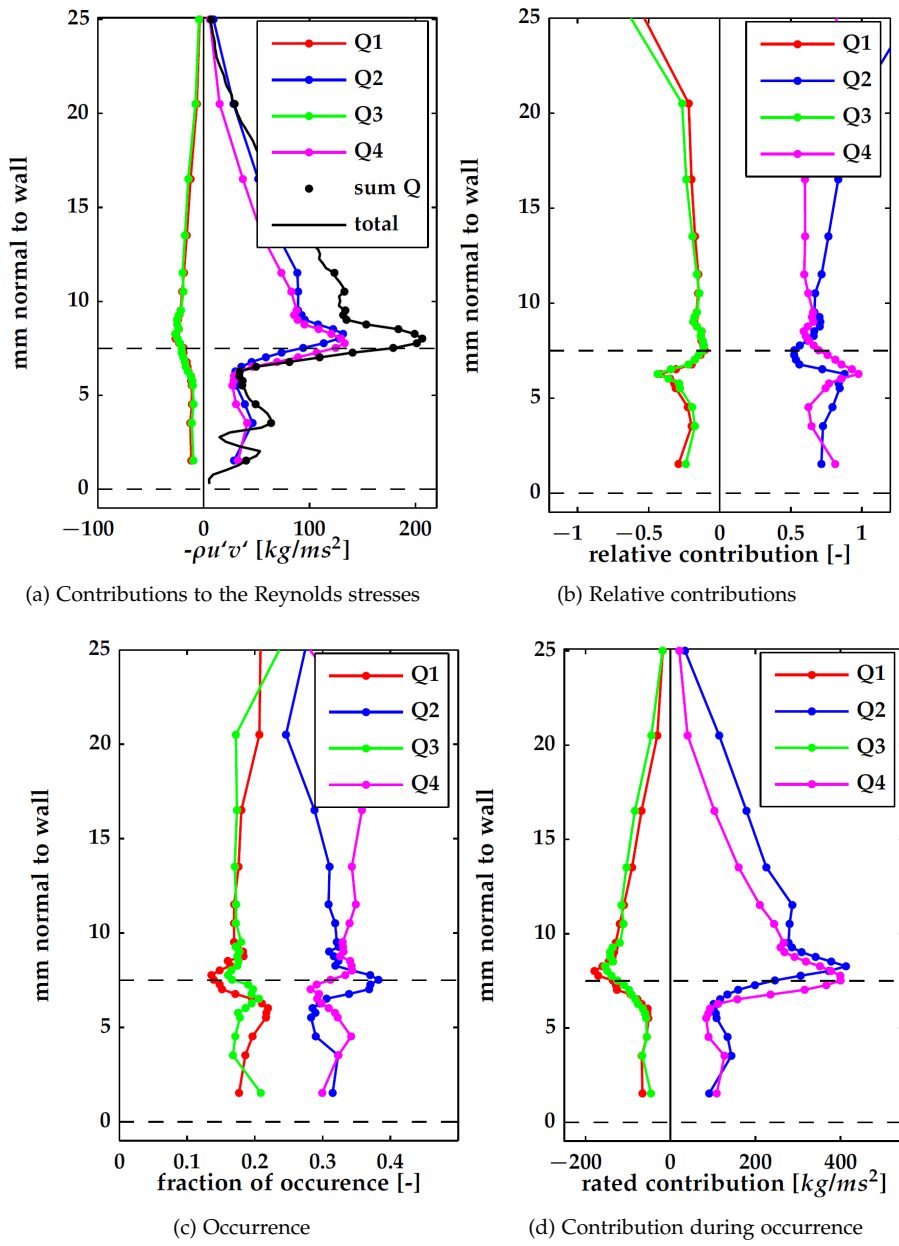


Figure 5.9: Quadrant analysis at cavity centre for  $Re_\tau = 1.6 \times 10^5$ , EL geometry,  $p = 25$  mm.

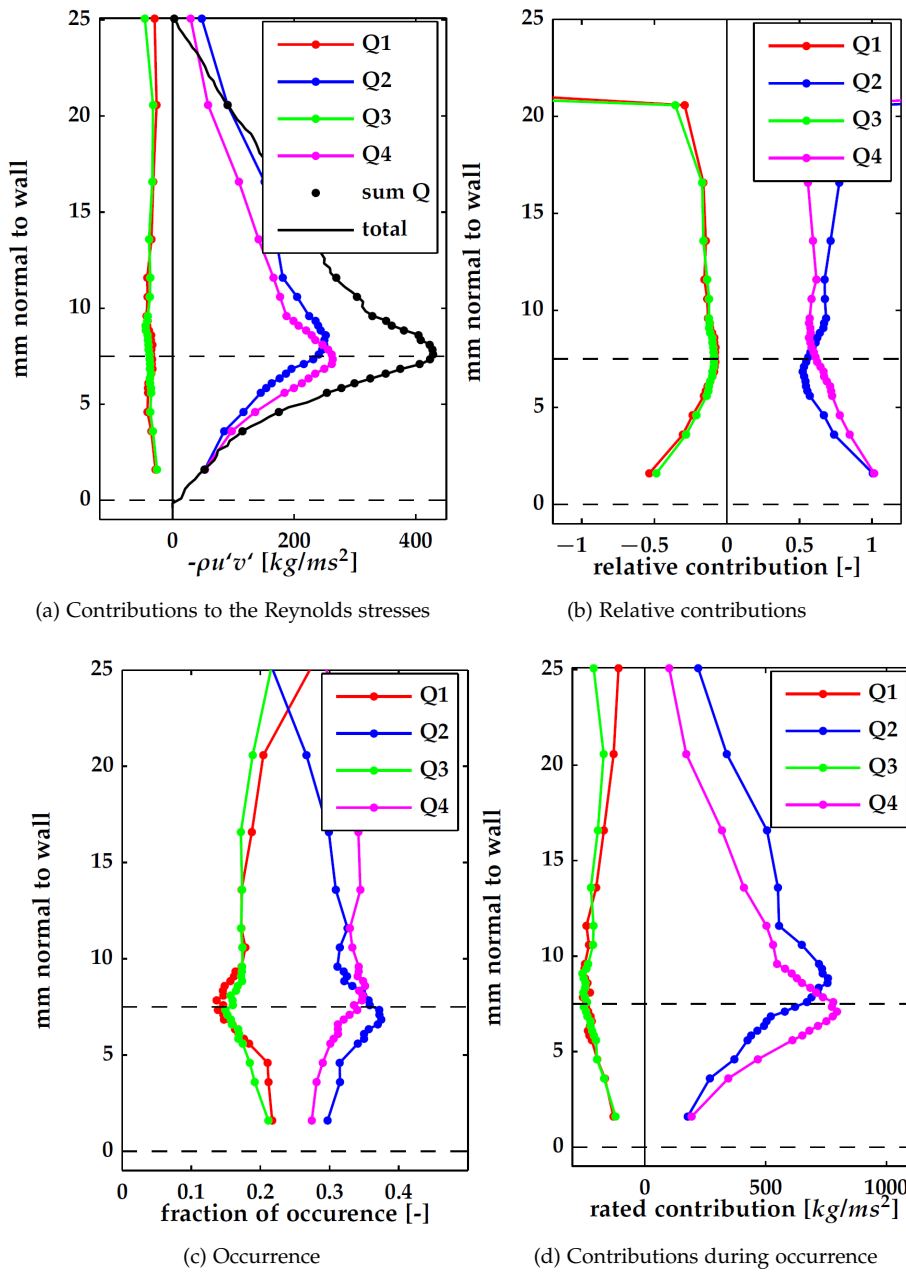


Figure 5.10: Quadrant analysis at cavity centre for  $Re_r = 1.6 \times 10^5$ , EL geometry,  $p = 40$  mm.

## 5.2.2 Interpretation of the quadrant analysis

Quadrants 2 and 4 are referred to as ejections and sweeps, respectively. A Q2 event is a fluctuation in negative axial direction and positive wall-normal direction. In a boundary flow, this is typically a path of low-momentum fluid "ejected" out into the higher-momentum region further from the wall, hence the name. Q4 events, or sweeps, represent the opposite motion: a high-momentum patch of fluid moving towards the wall into the lower-momentum region, thus "sweeping" the low-momentum region along. It may be clear that both motions increase the mixing of high and low-momentum regions, and thus act as a positive stress on the flow.

The fluctuations contributing to Q2 or Q4 do not necessarily relate to larger-scale motions, which can be interpreted as large-scale sweeps and ejections. However, given results for flat wall boundary layers (e.g. Adrian (2007)), such large-scale motions are likely to occur. The region with the strongest fluctuations is the shear layer, including the outer region of the cavity and the outer layer of the flow core.

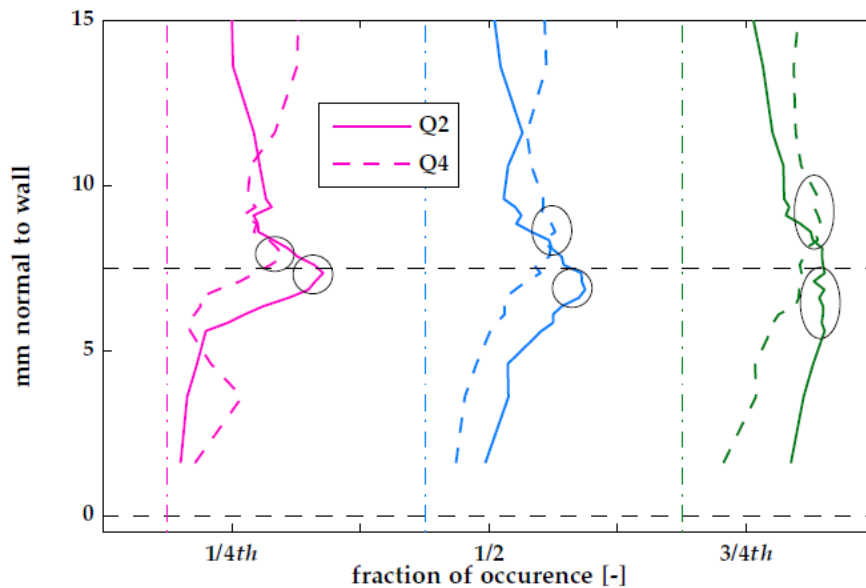


Figure 5.11: Fraction of occurrence of Q2 (solid lines) and Q4 (dashed lines) around the rib crest height, displayed for three axial locations: 1/4th, 1/2nd and 3/4th of the cavity. Data for the EL geometry,  $p = 40$  mm,  $Re = 1.6 \times 10^5$ .

The skewness between the occurrence and the contribution of the various quad-

rants in the shear region is related to the dynamics of the shear layer. The two peaks of maximum occurrence for Q2 and Q4 move further apart while moving in downstream direction above the cavity, mimicking the spreading rate of the shear layer. This moving apart of the peaks is visualized in Fig. 5.11, with the peaks emphasized by circles. The scale is equal for all three profiles, with the vertical lines included in the graph corresponding to an occurrence of 1/4th. Fig. 5.11 therefore not only shows the position of the peaks but also reveals a flattening of the occurrence overall.

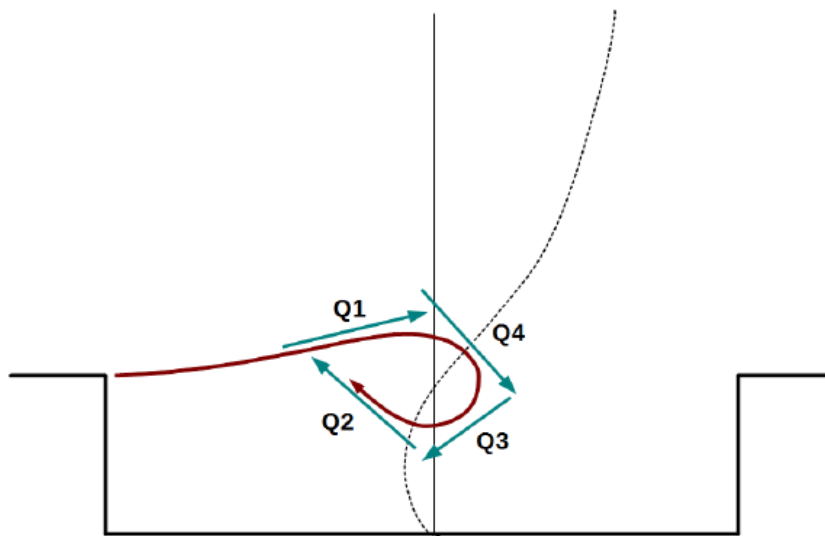


Figure 5.12: Sketch of the mechanism of quadrant occurrence in a vortex shed from the cavity edge.

The location where most Q2 events take place is at the inner side of the shear layer, the side closest to the pipe wall, facing the cavity. Most Q4 events are located on the top side of the shear layer. These characteristics are explained using a strongly simplified model of the shear layer motion. Imagine the shear layer to consist of a train of inward-rolling vortices, rotating anti-clockwise at the top half of the pipe and clockwise at the bottom half. These vortices represent an instantaneous motion and the representation is thus a motion relative to the mean velocity. A sketch of this situation is given in Fig. 5.12.

The motion of the vortex is divided in 4 parts, each with a direction corresponding

to one of the quadrants, as indicated in the sketch. Taking into account that the visualized vortex is "rolling" forward, the axial velocity corresponding to Q3 is likely to be small with respect to the mean velocity. The section corresponding to Q1 is moving faster in the absolute sense, but is also likely to be close to the mean velocity, thus contributing little to relative velocity differences. The two remaining segments of the vortex correspond to Q2 and Q4, with Q2 located at the wall side half of the vortex, and Q4 at the pipe-centre side of the vortex. These characteristics are in agreement with the peaks of the occurrence profiles in Figs 5.9c and 5.10c.

The motion segment corresponding to Q2 can penetrate the strong shear zone trailing behind the vortex and reach into the bulk region. This event will happen less often than the overall occurrence of Q2 events below the shear layer, as only strong motions will be able to penetrate the layer. However, when it happens, the contribution to the Reynolds stresses must be relatively strong, due to the high velocity difference with the mean flow above the shear layer. Similarly, strong Q4 motions penetrate further into the cavity, where they have a larger contribution to the total Reynolds stresses. The presence of these vortical motions thus clarifies the initially counter-intuitive mismatch between the occurrence and Reynolds stress contribution. These observations confirm that the Reynolds stress contributions allocated to sweeps and ejections indeed correspond to large-scale motions.

## 5.3 Dynamic flow behaviour

The predicted presence of a vortical shedding motion is confirmed by the skewness between the occurrence and contribution of Q2 and Q4. The pressure fluctuations discussed in Chapter 2.7 reveal a periodic impingement and strengthen the conclusion that periodic shedding is present.

The individual vortices must be identifiable in the instantaneous vector fields and the periodicity must be present in the temporal resolved data as well. We focus on these two aspects in the following sections.

### 5.3.1 Vortex identification

Direct observation of vortices is possible using individual snapshots of the vorticity field. However, since the vortices are embedded in a strong shear region, they are obscured by strong shear and therefore difficult to distinguish robustly.

A method often used to better visualize vortices is the subtraction of a characteristic velocity (e.g. Wang et al. (2007)). By using different velocities, each

characterizing a different flow region, different structures can be recognized in the velocity field. For the current flow, the method by Wang et al. (2007) cannot be applied robustly as the velocity in the shear region containing the vortices of interest fluctuates too much to use the mean flow as the relevant reference velocity, whereas the local spatial gradients vary too much to depend on a reference velocity based on an instantaneous spatial average.

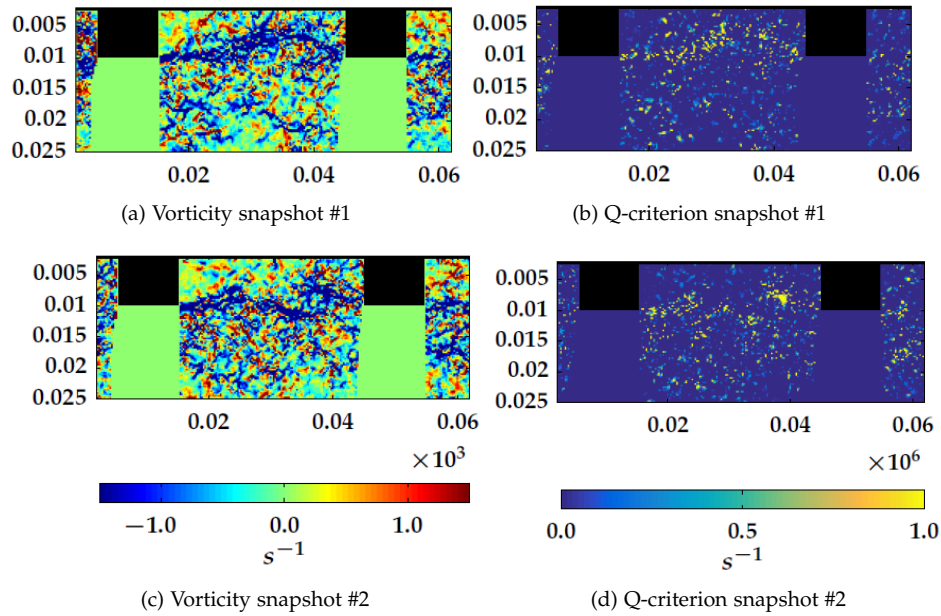


Figure 5.13: Vorticity and Q criterion for 2 uncorrelated snapshots. EL geometry,  $p = 40$  mm,  $Re = 1.6 \times 10^5$ . Dimensions in meters, flow direction from left to right.

The Q criterion, as previously used for the mean flow in Section 4.2.3, separates rotating motion from pure shear. This same method can be applied to instantaneous flows. Fig. 5.13 shows the vorticity and Q criterion for the same two snapshots.

Both vorticity and Q criterion from a single snapshot result in a noisy image. In the vorticity snapshots, the shear layer is clearly visible, but no individual vortices embedded in this layer can be identified, as the shear component is dominant. The Q criterion performs better in this aspect, but also in Figs 5.13b and 5.13d no clear, well-defined vortices can be distinguished. Although observing series of these snapshots might reveal patterns to the viewer, the results are too irregular in strength, shape and contrast to use as a good basis for a quantitative evaluation

of the dynamics of the flow.

## 5.4 Coherent structures

The simplified vortex model sketched in Section 5.2.2 serves as a plausible explanation for the computed quadrant occurrences and contributions. However, this mechanism requires confirmation from the actual data. In this Section we look at structures within the flow, rather than their statistical footprint.

### 5.4.1 Instantaneous quadrant structures

As mentioned in Section 5.3.1, the detection of individual vortices directly from the instantaneous vorticity or  $Q$  criterion is difficult. However, the footprint of the vortices is visible in the total contributions and occurrences of the four quadrants discussed in Section 5.2.

Figure 5.14a shows the four quadrants for a typical snapshot. The snapshot is the same as depicted in Figs 5.13a and 5.13b and corresponds to the same data series for which the profiles of Fig. 5.10 are obtained. Besides the quadrants, the four remaining images show the instantaneous Reynolds stresses (Fig. 5.14b), axial velocity (Fig. 5.14e) as well as the wall-normal (Fig. 5.14c) and axial (Fig. 5.14d) components of the relative velocity, all corresponding to the same snapshot.

The first observation is that there is much coherence between areas contributing to a specific quadrant. Especially Q2 and Q4, the quadrants positively contributing to the Reynolds stresses, consist of large connected regions rather than scattered small patches. This zone coherence characterizes the motions as large-scale fluctuations as was previously concluded in Section 5.2.2.

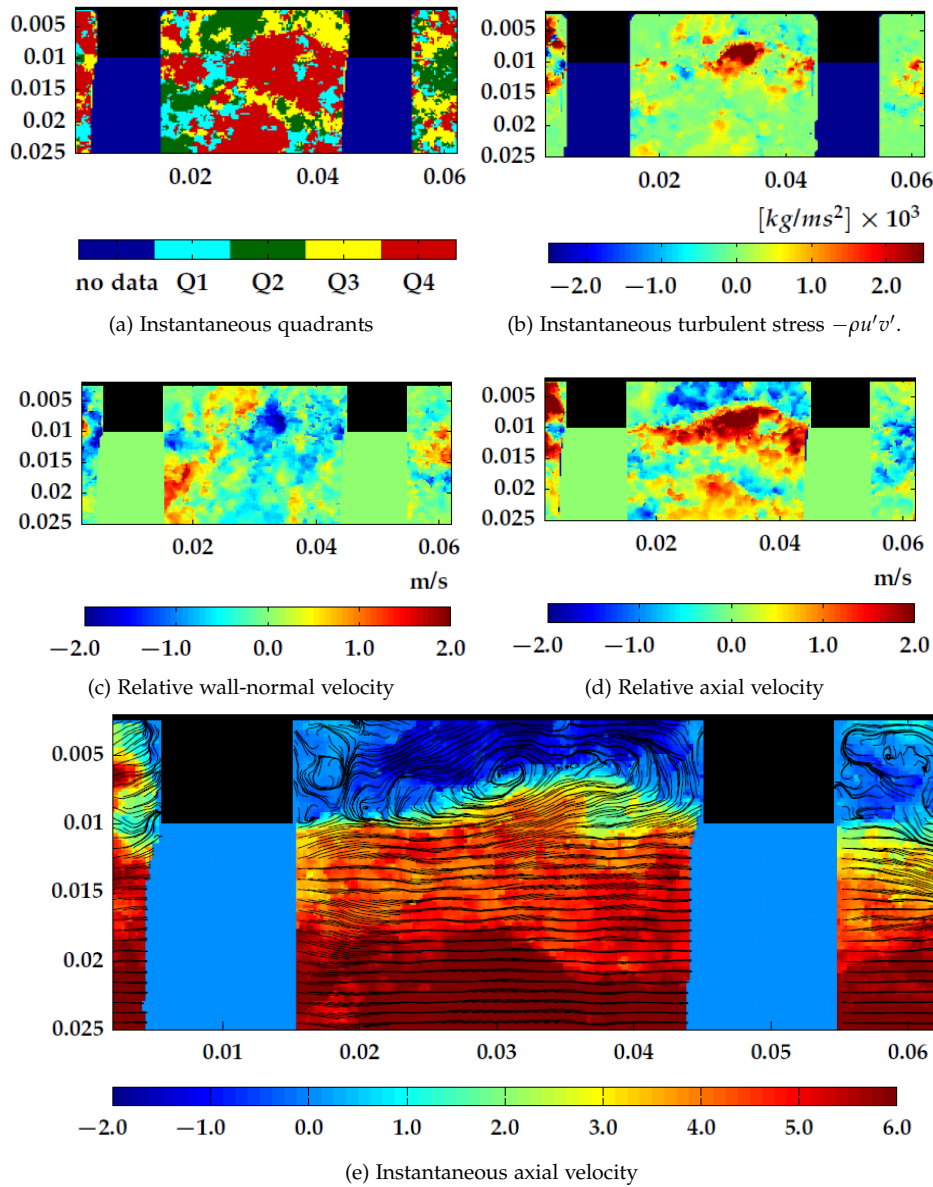


Figure 5.14: Different representations of a typical snapshot (EL geometry,  $p = 40$  mm,  $Re = 1.6 \times 10^5$ ). The snapshot is the same as shown in Figs 5.13a and 5.13b. Dimensions in metres, flow direction from left to right.

The pattern visible in Fig. 5.14 is a good example of how the large-scale vortical motions at rib crest height contribute to the Reynolds stresses by a sweeping motion, or Q4 region, penetrating into the cavity. The region of highest stress in Fig. 5.14b corresponds to a part of a large coherent Q4 region in Fig. 5.14a. As expected for such a motion, the high-stress region is not located in the centre of the Q4 region but at the boundary, where it "touches" regions corresponding to the other three quadrants. The arrangement of these regions corresponds to the simple model of Section 5.2.2. Together they correspond to a vortical motion, as visualized by the streamlines in Fig. 5.14e.

The Q1, Q2 and Q3 events in the same area also contribute to the stresses, although much less than the Q4 segment. The pattern visible in this particular snapshot is exemplary for a pattern encountered often within the same measurement series. Other patterns are encountered as well. Figs 5.14 to 5.17 show the quadrants, instantaneous turbulent stresses and instantaneous streamlines for a number of uncorrelated snapshots. Each figure is a typical example of a significant contribution to the Reynolds stresses:

- Fig. 5.14 depicts a strong Q4 event.
- Fig. 5.15 is an example of a the flow truly resembling the idealized schematic model of Section 5.2.2, with a vortex resulting in a strong contribution to the Reynolds stresses through both a Q2 and Q4 event.
- Fig. 5.16 shows an event in which Q2 is dominant in the region where the average Q2 contribution is strongest.

The fourth type of typical snapshots is provided in Fig. 5.17. This snapshot might seem unexpected, as it is clear that the simplified vortex model of Section 5.2.2 is not fully applicable. This type of behaviour is observed in a relatively small number of snapshots. Rather than an ejection from the vortex above the cavity, a Q2 "zone" flow originating from the regions upstream of the ribs in the image flows into view. This feature is related to strong fluctuations of the whole bulk region and cannot be explained using a single vortex model based on a simplified shear layer shedding from a single rib. The interaction of multiple ribs upstream of the imaged section of the flow apparently causes very strong ejection events, which survive far beyond the first rib they encounter.

The relative contribution to the Reynolds stresses of this event is very strong, suggesting that it is relatively rare compared to the "normal" shear layer behaviour. The zone corresponding to the Q2 event in this and similar snapshots is very big compared to those observed closer to the rib crest height. Similar large zones corresponding to a Q4 event are observed but do not contribute as much to the Reynolds stresses.

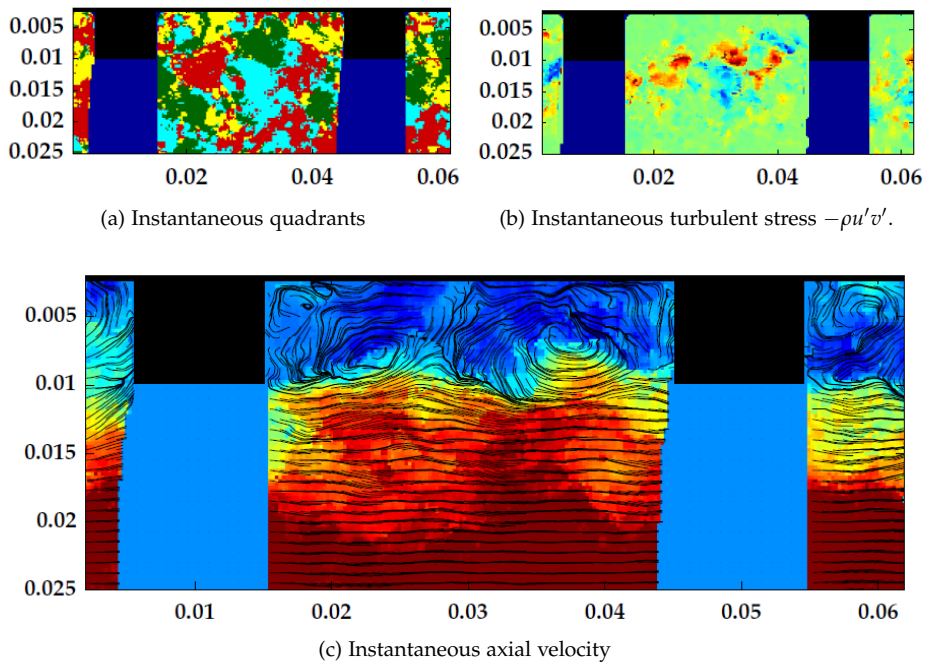


Figure 5.15: Instantaneous snapshot showing a strong Q2 and Q4 event. The colour scales are the same as those in Fig. 5.14. Case: EL geometry,  $p = 40$  mm,  $Re = 1.6 \times 10^5$ . Dimensions in metres, flow direction from left to right.

The depicted snapshots represent typical patterns during high-impact events and thus show large contributions to the Reynolds stresses. At many time instances however, the maximum occurring Reynolds stress in the image is much lower. Although those snapshots do, in total, certainly contribute to the total stresses, they less clearly show specific patterns, and no representative example can be identified.

The patterns are currently identified manually, based on the orientation of the quadrant zones in each image. A quantitative analysis based on the contribution or occurrence of each structure type is therefore out of reach.

The strong Q2 and Q4 events near the shear layer are often located directly next to a recirculation as visualized by the streamlines in the corresponding figures. Although this seems a logical situation, it is important to bear in mind that the contributions to the Reynolds stresses are computed based on the relative velocities, whereas the depicted streamline patterns are those of the absolute instantaneous velocity field.

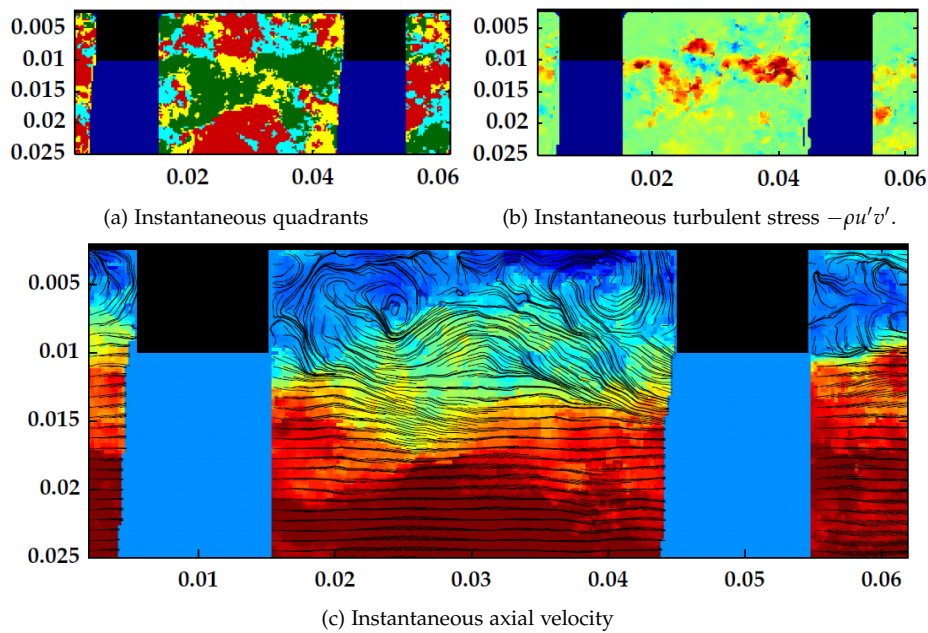


Figure 5.16: Instantaneous snapshot showing a dominant Q2 event. The colour scales are the same as those in Fig. 5.14. Case: EL geometry,  $p = 40$  mm,  $Re = 1.6 \times 10^5$ . Dimensions in metres, flow direction from left to right.

The mean flow field within the cavity has, for the EL geometry used in the above examples, a single large recirculation region accompanied by a very small recirculation in the upstream cavity corner (see Fig. 4.3). All smaller recirculation cells, such as visible in Figs 5.15 and 5.16 are thus temporary structures.

A notable feature is the link between the core velocity and ejection events. In the depicted cases, a relatively low core velocity (in the pipe half under observation) is often present when a Q2 event or ejection event with a strong Reynolds stress contribution occurs. This correlation is observed for most strong Q2 events, although not exclusively. This feature suggests that either the strong ejection is caused or enhanced by the core motion or vice versa, or, most likely, both. In any case, the presence of multiple ribs in series acts as an amplifier to these motions.

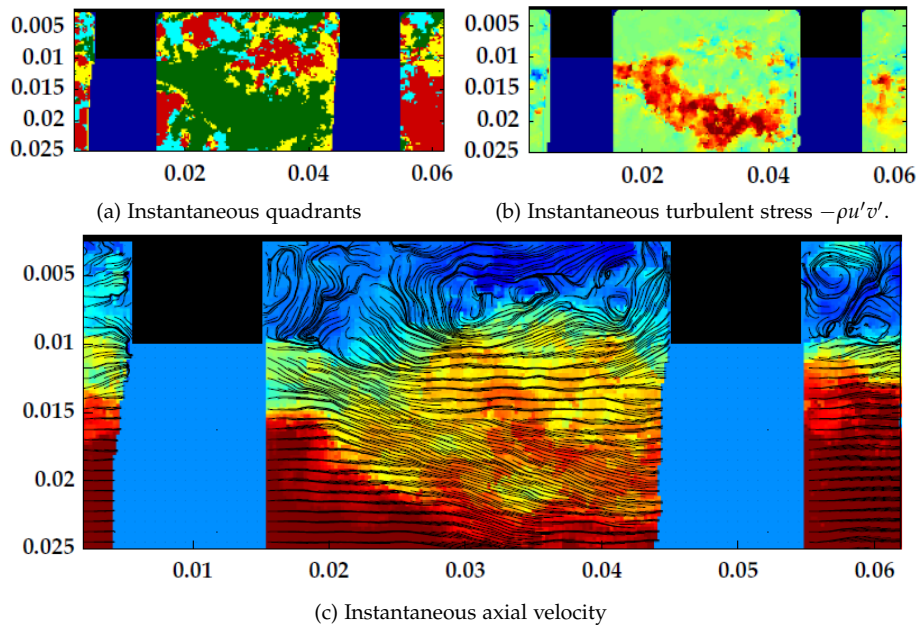


Figure 5.17: Instantaneous snapshot showing a dominant Q2 event in the core region. The colour scales are the same as those in Fig. 5.14. Case: EL geometry,  $p = 40$  mm,  $Re = 1.6 \times 10^5$ . Dimensions in metres, flow direction from left to right.

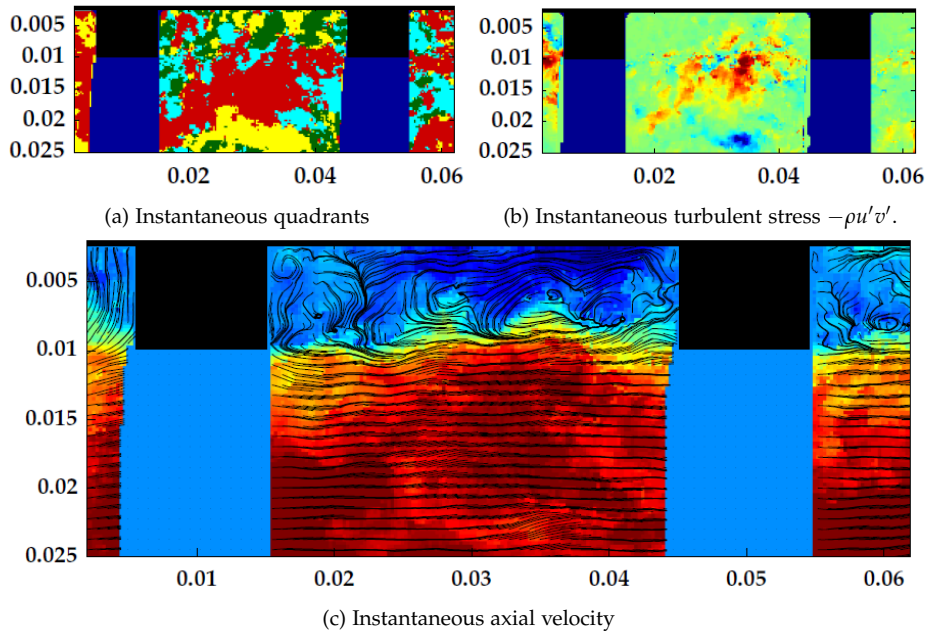


Figure 5.18: Example of a vortex train. The colour scales are the same as those in Fig. 5.14. Case: EL geometry,  $p = 40$  mm,  $Re = 1.6 \times 10^5$ . Dimensions in metres, flow direction from left to right.

### 5.4.2 Match with the simplified model

Visible vortical structures in the shear layer can be identified that exactly match the simplified vortex model shown in Fig. 5.12. Although these structures are clearly not the only dominant feature in the flow, they certainly exist. Since their presence is typically related to strong instantaneous stresses, it is inferred that they contribute significantly to the total stresses as well.

Figure 5.18 shows a snapshot with a pattern matching the characteristics of the model. A train of vortices is visible, some of which have a relatively strong contribution to the stresses.

The question remains whether these vortical structures can indeed be explained according to the simple vortex shedding model of Section 5.2.2. The rib edges certainly create a shear layer and the instability of this layer results in vortical structures such as visible in Fig. 5.18. However, even in this example, a large part of the core region of the flow corresponding to the Q4 quadrant connects all sweep events in the shear layer to the motion of the core region. The strong interaction between those vortices, the large-scale instability of the core region and the recirculation in the cavity is thus what eventually creates the largest and strongest contributions to the total stresses.

### 5.4.3 Variation versus geometry

All instantaneous quadrant distributions shown in Figs 5.15-5.18 are from the same measurement series, with a pitch of 40 mm and  $Re = 1.6 \times 10^5$ . Based on the results of the time-averaged contributions and occurrences discussed in Section 5.2, similar patterns are expected for all geometries and Reynolds numbers. Quantitative results are not derived in the current work but differences are expected to arise, such as the occurrence rate of specific patterns and differences in the balance between the quadrants.

### 5.4.4 Distribution within quadrants

The analysis thus far has revealed the occurrence and the total and average contributions of fluctuations in the different quadrants. We found that the quadrants do not contribute equally to stresses. The ejection events are more intermittent compared to the contributing sweeps. In order to confirm and quantify these effects, a probability distribution function (pdf) of each quadrant can be computed. The fraction of occurrence is now sorted by its contribution to the Reynolds stresses, with a separate pdf generated for each of the four

quadrants. Typical results for the occurrence of each quadrant are provided in Fig. 5.19.

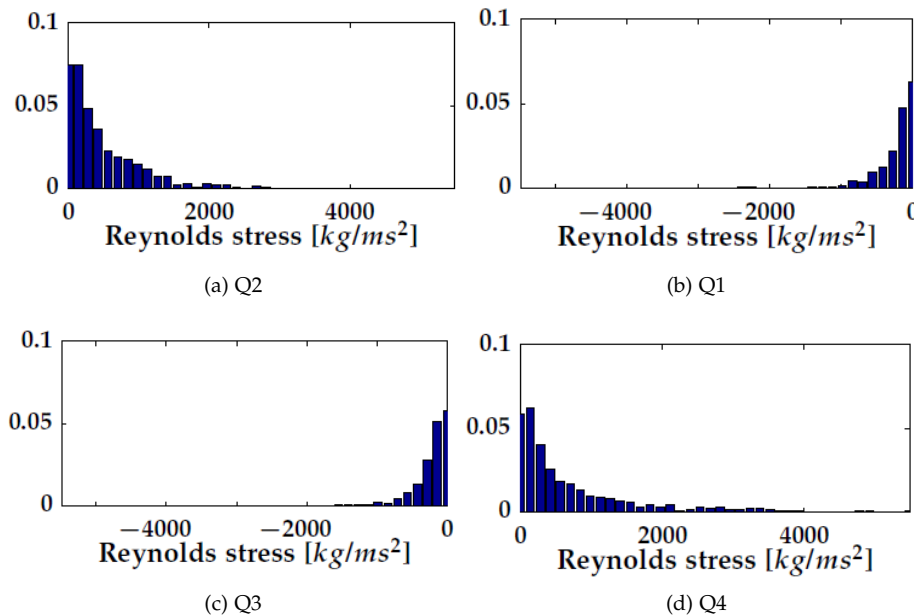


Figure 5.19: Example of the pdf of the fraction of occurrence of each stress contribution for all four quadrants. EL geometry,  $p = 40$  mm,  $Re = 1.6 \times 10^5$ .

As expected, the distribution is narrower for quadrants Q1 and Q3 than for Q2 and Q4. Otherwise, the histograms provide little clarity. Since the emphasis is on the differences in the distributions of occurrence and contributions of the two dominant quadrants, the comparison between two quadrants is visualized by subtracting the joint distribution of Q4 from that of Q2. This result is depicted for both the fluctuation occurrence and corresponding Reynolds stress contributions at four wall-normal positions in Figs 5.20 and 5.21, respectively.

The results are noisy and irregular but still show a clear trend; within the cavity, weak ejection events (Q2) dominate over weak sweeps (Q4) but stronger events occur more often as sweeps. At crest height, the trend is similar, although the differences between the quadrants are less pronounced here. Further towards the centre of the pipe, the trend is reversed: for the weak events, sweeps dominate while strong events occur more frequently as an ejection.

Naturally, the contributions and occurrences of events display similar behaviour. However, the contributions provide a better indicator of the importance of scarce strong events. Figs 5.20 and 5.21 clarify how a quadrant occurring less can still

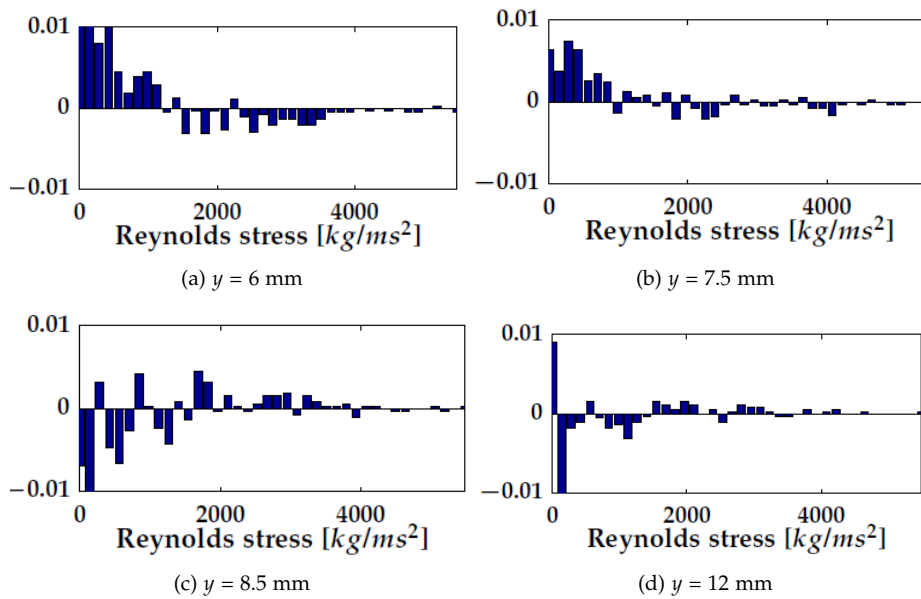


Figure 5.20: Fraction of occurrence of Q2 minus fraction of occurrence of Q4 for 4 wall-normal positions. EL geometry,  $p = 40$  mm,  $Re = 1.6 \times 10^5$ .

be the largest contributor to the total stresses; by having a distribution displaying more strong events. These results complement our findings based on visual inspection of the quadrant and Reynolds stress fields in Section 5.4.1 and the asymmetry of the fitted ellipsoid in Section 5.1. They support the assumption in the description of the simplified vortex model (Section 5.2.2) that the shear layer, on average, acts as a shield to weaker events, only letting strong events pass. This mechanism is valid for both ejections from below the shear layer and sweeps approaching from above.

Of course, the shear layer itself is not a stagnant entity. It is created by the time average of a very chaotic flow. Although instantaneously shear layers are visible as well, their position varies largely with time, and in many instances no well-defined shear layer is visible at all.

The shielding effect is thus not necessarily a property of the physically present layers, but rather a statistical property of the flow as a whole.

A good method to visualize the shift in distribution of both Q2 and Q4 with wall-normal position is by calculating a cumulative probability distribution. Figs 5.22a and 5.22b ( $p = 40$  mm) and 5.23a and 5.23b ( $p = 25$  mm) show the cumulative distributions of the contributions to the Reynolds stresses for both these quadrants.

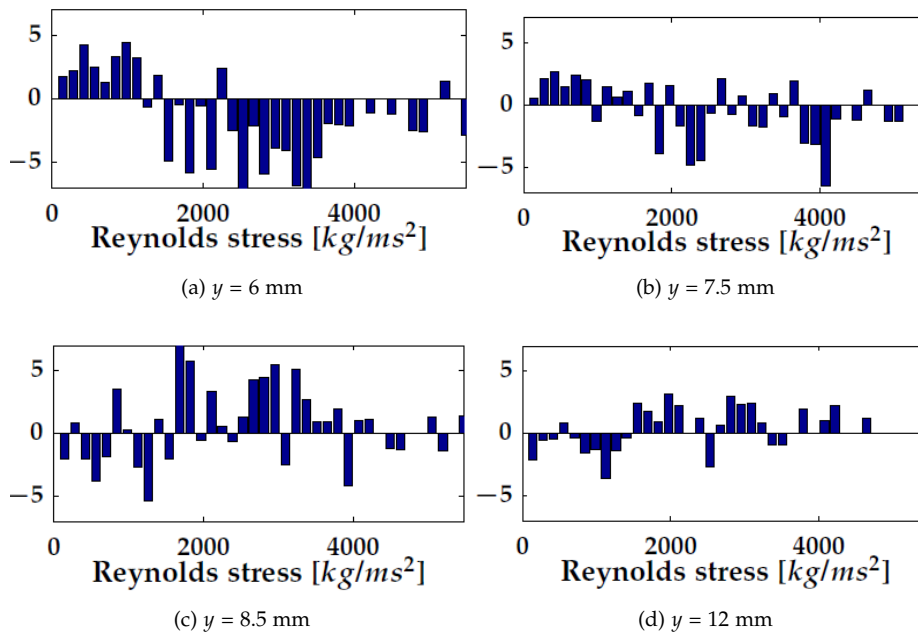


Figure 5.21: Contribution of Q2 minus contribution of Q4 organized by event strength for 4 wall-normal positions. EL geometry,  $p = 40$  mm,  $Re = 1.6 \times 10^5$ .

The values have been normalized with the total positive contribution and, thus, Q2 and Q4 add up to a value of 1. This provides the opportunity to emphasize the relative differences between both distributions while maintaining the relative difference in total contribution between the two quadrants.

The spatial evolution of the cumulative distribution is depicted from deep into the cavity (dark lines) to the centre of the pipe (yellow lines). The behaviour of the events can be divided in several zones, as was already visible in the spatial profiles discussed in Section 5.2.

Both the ejections and sweeps very close near the pipe wall contribute approximately half the stress, with all contributions caused by weak events. Further upwards, closer to the shear layer, the ejections contribute less but more of the contributing events are of medium strength. Simultaneously, the sweeping events become stronger, mainly due to an increase of strong events.

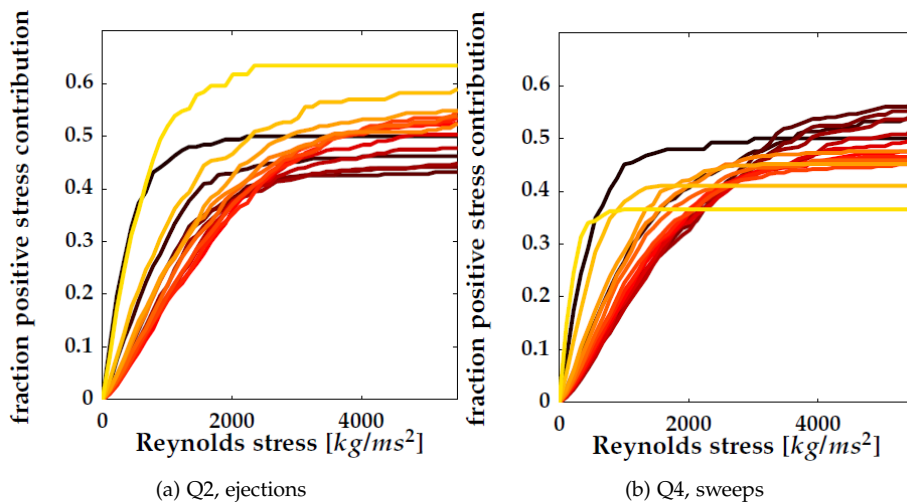


Figure 5.22: Normalized cumulative distribution of the contribution to the Reynolds stresses. EL geometry,  $p = 40$  mm,  $Re = 1.6 \times 10^5$ . Lighter colours signify increasing wall-normal location, from inside the cavity (black) to the centre of the pipe (yellow).

Near the centre of the pipe (yellow lines), there is a strong tendency towards a larger relative contribution of ejections, all attributed to small fluctuations. However, these contributions are all very small compared to those in the high-shear region.

Within the cavity (black to dark red lines), the sweeps contribute more, an effect that is mostly due to high-strength fluctuations. Above the cavity (bright red lines), the ejections have a larger contribution. There is, however, no observable difference in the distribution of the fluctuation strengths between sweeps and ejections for this region.

We do not observe major differences as we move from  $p = 40$  mm (Figs 5.22a and 5.22b) to  $p = 25$  mm (Figs 5.23a and 5.23b).

Small differences can be seen in the overall shape of the distributions, which are directed less towards high strength fluctuation for the 25-mm pitch compared with the 40-mm pitch results in Fig. 5.22. The absolute fluctuation strengths are smaller than for the 40-mm pitch case and the differences between the distributions of sweeps and ejections are more emphasized.

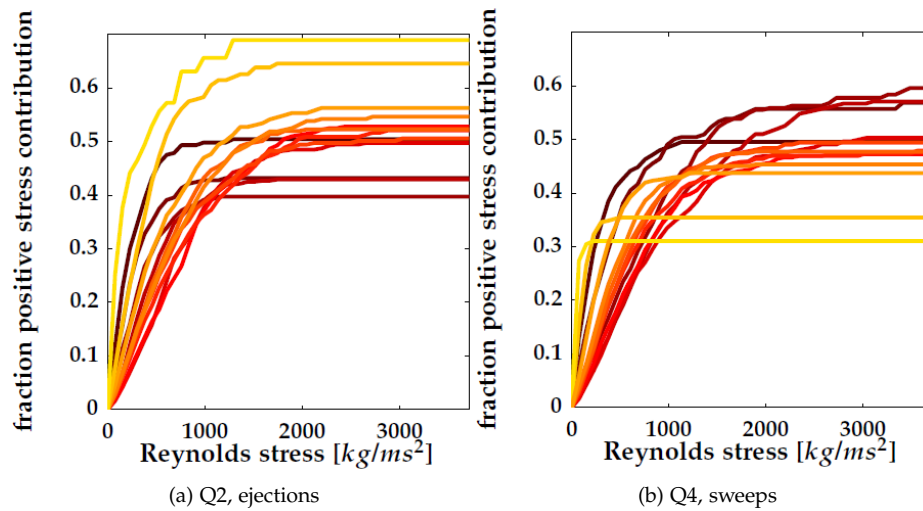


Figure 5.23: Normalized cumulative distribution of the contribution to the Reynolds stresses. EL geometry,  $p = 25$  mm,  $Re = 1.6 \times 10^5$ . Lighter colours signify increasing wall-normal location, from inside the cavity (black) to the centre of the pipe (yellow). The two innermost points (corresponding to the two darkest lines in Fig. 5.22), located in a strong recirculation region within the cavity, are removed for clarity.

## Chapter 6

# Conclusions

This chapter summarizes the conclusions of this research, followed by several recommendations for further research.

- A fully developed flow through a ribbed pipe can be established with only a few ribs. For the Reynolds numbers and rib size studied in this thesis, at most 5 ribs are sufficient to reach the fully developed state (see Section 2.4.1).
- For the ribbed sections studied in this thesis, the sand grain roughness derived using the Colebrook friction correlation and the full pipe diameter yields unrealistic relative roughness values, far extending beyond the radius of the pipe (Fig. 2.9 and 2.10). When on the other hand the friction factor is calculated using the inner diameter of the ribs rather than the full pipe diameter, the calculated equivalent values for the sand grain roughness have a physical realistic value (see Fig. 2.11 and table 2.4). These results highlight the impact of the choice of frame of reference; for very rough walls, the wall position is not trivial.
- The friction factor of a fully developed flow over rectangular ribs is a function of rib pitch, but Reynolds number independent (Fig. 2.9). However, the fully developed flow over rounded ribs (Fig. 2.10) is Reynolds number dependent. This behaviour is linked to a Reynolds number dependency of the flow detachment point at the ribs and the resulting impact on the flow dynamics for rounded ribs. The flow detachment for the rectangular ribs is triggered at the leading edge of the ribs. Somewhat counter-intuitive, the absolute friction for a ribbed section with rounded ribs is, in comparison with rectangular ribs with the same inner diameter and pitch, significantly

higher. Also the trend with which the friction depends on the rib pitch is very different (see Figs. 2.13a and 2.14a). This implies that for practical applications in which optimization of mixing (e.g. heat exchange) or minimization of friction is relevant, the roughness shape can have important consequences.

- The trends in Figs. 2.13a, 2.14a and 2.15a are based on a relatively small range of pitches. Extrapolation to larger pitch results in a continuously increasing pressure loss per rib. A result that can logically not persist when the ribs move further apart and the flow will reestablish a developed state before the next rib is encountered. The limit case, with infinite pitch, is the single rib pressure loss (see Fig. 2.17). How the pressure loss changes with rib pitches for  $p > 50$ ,  $p < \infty$  mm is unknown. Further research into this regime would be recommended.
- Pressure drop evaluation of a single rib is not suitable as an indicator for the friction of a ribbed section, as can be seen comparing Figs. 2.9 and 2.10 with Fig. 2.17, showing opposite results for the rib shapes E and F, the rib geometries matching those used for the ribbed sections. The flow patterns, and especially the direction of the shear layer separation, for the flow over a single rib do show similarities with those of ribbed sections (see Figs. 4.27 and 4.28). Further evaluation of the similarities and differences in flow patterns between single rib geometries and ribbed section shows more differences. The local mean flow in axial direction shows a much more "plug-flow" like behaviour for the single orifices in comparison with the developed ribbed flows. Also a strong axial variation of the flow over the whole pipe diameter is observed for the orifice flow, showing a redevelopment not present for the ribbed geometries (see Figs. 4.35 and 4.29 and 4.31). The Reynolds stress profiles show even stronger differences for the orifice flows compared with the developed ribbed flows. No linear stress region towards the core of the flow is present for the orifice flows (see Fig 4.36).
- To enable PIV measurements of the flow, an optically accessible ribbed section is designed. The design allows the rib geometry and pitch to be set manually (see Fig 3.1), and provides optical access to the regions in between the ribs, but not the region within each rib. The use of a telecentric lens optimizes the field of view, and removes "shadow regions" (see Fig. 3.2a). Although proven very useful, the design has some disadvantages, such as a low efficiency in set-up adjustment. The structure holding the ribs in place also has some effects on low velocity azimuthal flow patterns

(see paragraph 4.4), which would ideally be avoided. A revision of the rib-placement mechanism is therefore strongly recommended for future continuation of this or similar studies.

- With physical and optical boundaries and significant image deterioration due to impurities in the flow, obtaining useful results with particle image velocimetry (PIV) is a challenge. With a (manually created) image mask, integrated in the PIV-algorithms, the issues regarding the effect of boundaries are handled (sections 3.3 and 3.4.3). For artefacts caused by flow impurities an adjusted iterative variant of the normalized median filter, called the sorted median filter, is introduced (see Section 3.4.1). With these algorithms, PIV can be applied successfully to a challenging flow.
- The mean axial and wall-normal velocities show, in line with the pressure measurements, a Reynolds number independent behaviour for the EL-geometry, and a Reynolds number dependent behaviour for the RL geometry (see Fig. 4.5). Also the mean shear and Reynolds stress show Reynolds number independent and dependent behaviour for respectively EL and RL ribbed sections.
- The mean horizontal shear stress shows a less defined and thicker shear layer, with a lower maximum shear for the RL geometry (see Fig. 4.6). However, the Reynolds stresses show a much larger intensity for the RL geometry in comparison with the EL geometry (see Fig. 4.8). The larger pressure loss measured for the RL geometry mentioned above seems to be associated with an increased level of fluctuations positively contributing to flow stresses. The Reynolds stresses in Figure 4.8 show, for both the EL and RL geometries, an increase in Reynolds stress intensity with rib pitch. This trend can, similar to the trend with Reynolds number, be associated with the increase in pressure loss per rib with increasing pitch as observed during the pressure measurements.
- The mean flow velocity profiles show a strong influence of the rib pitch on the velocity distribution for both rectangular and rounded ribs (see Figs. 4.29 and 4.31). For the RL geometry a similar variation is visible as a function of Reynolds number. Axial variation of the axial velocity is mostly limited to the cavity. The core region of the flow does not vary significantly in axial direction.
- Local Reynolds stress profiles show a strong axial variation in the cavity-region and around the shear layer separating from the ribs. Further towards the core region the axial variation disappears and the Reynolds stress

shows a linear trend towards the center of the pipe, just as in regular fully developed turbulent pipe flow.

- The mean velocity profiles, calculated by averaging the local velocity profiles over one pitch length in axial direction, show an axial velocity profile strongly depending on the rib pitch. The spatially averaged radial velocity becomes virtually zero (see Fig 4.37), an observation which is in line with paragraph 4.4, which evaluates whether the azimuthal flow induced by the rib mounting significantly affects the flow.
- Reynolds stress profiles averaged in axial direction show a linear trend towards the pipe core. In the cavity region, in addition to the Reynolds stresses, the dispersive stress becomes apparent. Outside the cavity region this dispersive stress, which is the result of the spatial, rather than temporal, fluctuations in the flow, is negligible (See Fig. 4.39).
- Based on the axially averaged Reynolds stress profiles and axial velocity profiles the friction velocity is determined for every measurement with the EL-geometry (paragraphs 4.7.4, 4.7.5 and 4.7.6). In this analysis, the von Kármán constant is not a fixed value. Instead the constant is determined by fitting a linear relation to the mixing length. (See Fig. 4.40) and thus adjusted in order to obtain the best fit to the data. The resulting von Kármán constants are scattered around the commonly accepted value of 0,4 for ribs at low pitch, but increase significantly for higher pitched ribs (See Fig. 4.41).
- The effective wall shear stress, calculated based on the previously determined friction velocity and translated from the effective radius to the pipe radius, results in the determination of the friction factor, which can be compared directly to the friction factor derived based on pressure measurements (see Fig. 4.46). The results show a large agreement up to a pitch of 35 mm.
- Evaluation of the temporal fluctuations by making joint probability distributions, show a dependency of the fluctuation strength and directions on the rib pitch and local position in the flow (see Figs. 5.3, 5.4 and 5.7). The results are in agreement with the Reynolds stress patterns and intensities observed earlier.
- The Quadrant analysis in paragraph 5.2 further clarifies the trends observed in the Reynolds stress patterns. The stresses are caused by a combination of sweeps and ejections. Just underneath the shear layer separating the cavity region from the core region the sweeps (Q4-events) dominate in

contribution. Above the shear layer, the ejections (Q2-events) contribute the most to the stresses. This is vice-versa for the number of occurrences for both events: The largest contribution to the stresses is caused by fewer, but on average stronger, events (see Figs. 5.9 and 5.10). The radial position of the peaks of average contribution of both sweeps and ejections depend on the axial position relative to the upstream rib crests. They are initially close together, moving apart further downstream (see Fig. 5.11).

- Both the radial and axial distribution of the ejections and sweeps support the hypothesis that a train of vortices, shed by the ribs, are a strong contributor to the stresses (see Fig. 5.12). Based on the dynamic pressure measurements for the rectangular rib geometry (see paragraph 2.7.2 and Fig. 2.21), these vortices are implied to be primarily consisting of a vortex shedding motion with two vortices simultaneously present between the leading edges of two ribs (second harmonic). This conclusion can be drawn for the EL-geometry with all pitches studied both with dynamic pressure and PIV (i.e.  $p = 20\text{-}50$  mm), but is, based on the dynamic pressure alone, also valid for  $p = 15$  mm.
- Instantaneous snapshots confirm the existence of the 2-vortex pattern (see Fig. 5.15), but also show that this simple model does not describe the full dynamics of the flow (see Figs. 5.14, 5.16 and 5.17).

## 6.1 Outlook

The results show interesting patterns, but also provide more new questions than answers. Based on the results and conclusions above, the following suggestions for further research are proposed:

- Taking into account the large contribution to the stresses by distinct larger scale patterns, and the very large roughness-to-pipe-diameter ratio, the observation that the flow scaling is in line with the theory for flow over rough walls, and that the friction velocity can still be used to calculate the flow friction, is not a trivial result. Further research into the use of the rough wall flow model for very rough flows, and the required adjustments, such as the use of a non-constant von Kármán constant, is required to understand this phenomenon better.
- Due to practical limits with the field of view, the analyses based on the axially averaging of the PIV results is only studied for rectangular ribs (EL-geometry). Especially the derivation of the friction-behaviour would be

very interesting to perform for rounded ribs (RL-geometry) as well. Will the modelling conform the theory for rough-wall flows result in a similar match with the friction derived from pressure measurements as for the EL-geometry?

- The geometries studied in this work cover a limited range of pitches. The trends observed in the friction versus rib-pitch results cannot be extrapolated, as the trends observed up to  $p/D = 1$ ;  $p = 50$  mm show no convergence towards infinite pitch. Further study would be able to determine how the friction further evolves with larger pitches, and how these trends depend on the rib shape, height and Reynolds number.
- We started this work with in mind the better understanding of boiling flows in ribbed cryogenic LNG transport tubes. So far we are not conclusive on the better design of such tubes; nevertheless, we have shone much light on the flow phenomena in the single-phase flow regime. Clearly, the validity of our results in the two-phase regime is still open and worth investigating with the new perspective on roughness we gained.

# Appendix A

## Pressure tap location

As mentioned in Section 2.3.4, the pressure tap downstream of the ribbed pipe segment is, for some measurements with the EL geometry, located within the redevelopment length from the last rib of the segment. We apply a correction for the effect on the measured pressure loss.

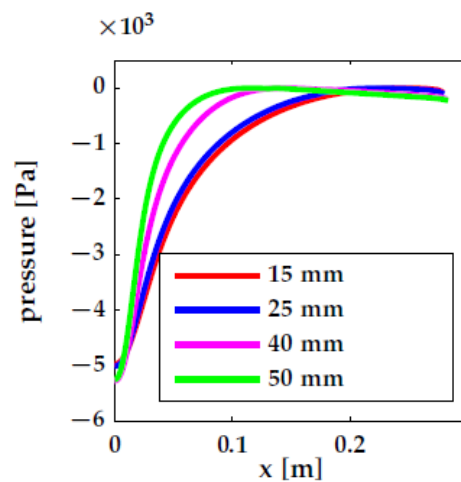


Figure A.1: Pressure recovery downstream of the ribbed pipe segment. CFD-calculation for EL geometry with 7 ribs and  $p = 15, 25, 40$  and  $45$  mm.  $V_b = 2.15$  m/s.

Within the FLUVAWINT project, CFD calculations were performed for a few experimental cases with a ribbed section EL geometry of 7 ribs by A. Twerda. The pressure recovery downstream of the last rib of the ribbed pipe segment as obtained from this CFD calculation for EL geometry at  $p = 15, 25, 40$  and  $50$  mm

and a bulk velocity  $V_b = 2.15 \text{ m/s}$  is shown in Fig. A.1. The recovery distance is a function of pitch. The magnitude of the pressure recovery is proportional to  $V_b^4$  (concluded based on results not shown) and shows no dependency on the rib-pitch. This is the proportionality expected based on a simple Bernoulli approximation, similar to the case of a single orifice.

The simulations do not capture the full dynamics of the flow, and a deviation of the total pressure loss with respect to the measurements is observed for the rib sections with a pitch of 40 and 50 mm (Fig. A.2).

However, the scaling behaviour of the pressure recovery in the redevelopment region, which is not dominated by shear layer dynamics and rib-wall interaction, is assumed to be predicted reasonably well.

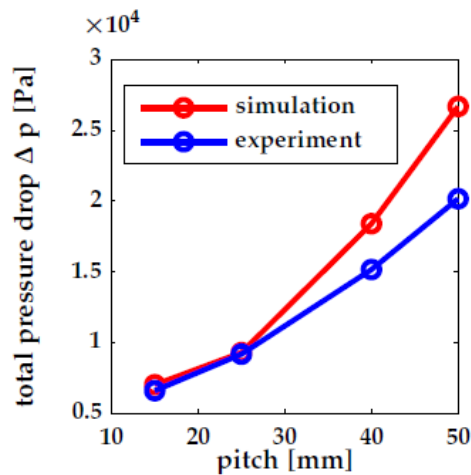


Figure A.2: Total pressure drop  $\Delta p$  at a bulk velocity,  $V_b = 2.15 \text{ m/s}$ , for EL geometry with 7 ribs

The pressure recovery behaves very similar for different rib pitches, as can be seen in Figure A.1. We define the recovery-half-distance  $x_h$  as distance downstream of the ribs at which half of the pressure overshoot has recovered. The recovery half-distance for all numerical simulations is shown in Figure A.3. Included is a linear fit to the data;

$$x_h \approx e - f * \text{pitch}, \quad (\text{A.1})$$

with  $e = 0.07 \text{ m}$  and  $f = 0.8$ .

In Figure A.3 we also included the recovery half-width for a sudden expansion (from on Teyssandiert and Wilson (1974)) for comparison. A sudden expansion

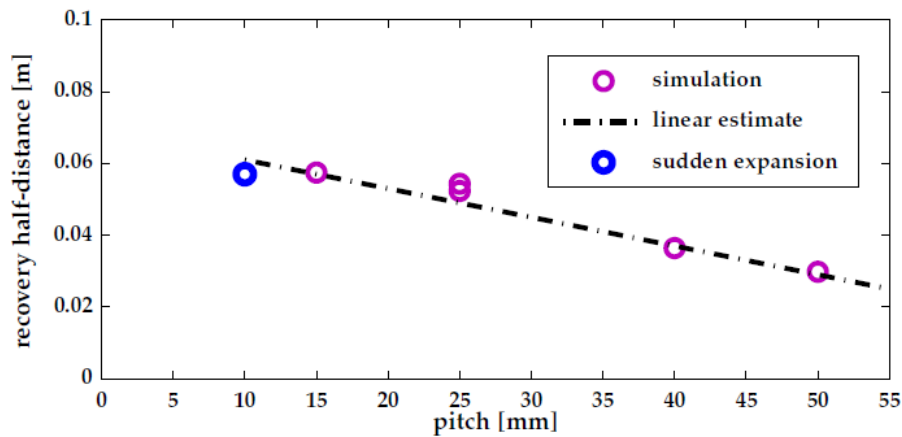


Figure A.3: Pressure recovery half-distance as a function of rib-pitch

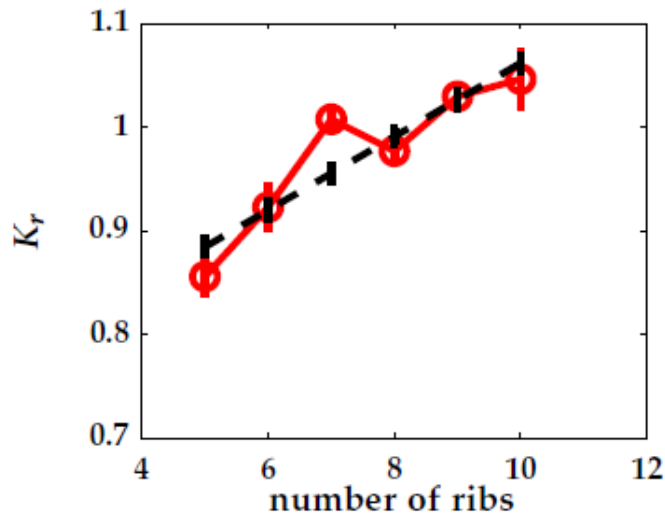
can be seen as the EL geometry with a pitch of 10 mm. As the ribs are 10 mm wide, this leaves no cavities. The results obtained with the numerical computation are in line with this limiting case.

This, in combination with the well-matched total pressure loss over the the ribbed section, indicates that for the small pitch values the pressure recovery correction is reasonably trustworthy. For the larger pitch, the recovery strength and half width are determined with less certainty.

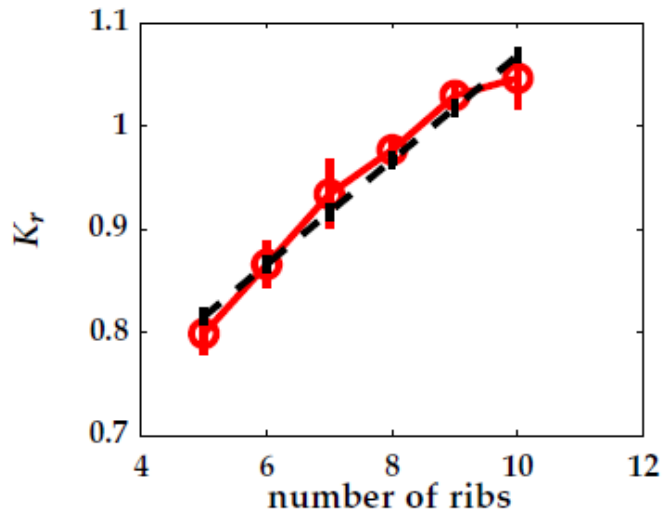
The relation between total pressure loss and the number of ribs should be linear once the fully developed region has been established. For the data-series obtained with some measurements.

Without correction for the tap location this is not the case when including measurements performed relatively close to the downstream pressure tap. Figure A.4a is an example of a geometry for which this was the case. In this example the 3 points on the left correspond to measurements with the ribbed segment placed relatively close to the downstream pressure tap, while the other points are obtained from measurements performed with a segment placed more upstream within the test section. The discontinuity in their trend is a result of the effect of pressure recovery, which is not evenly present in all points. This discontinuous behaviour is found for all data sets including measurements both close and far from the downstream tap location. The available datasets are used to obtain the correction parameters.

Using these scaling parameters, a correction for the total pressure loss over the ribbed segment is applied to all measurements with rectangular ribs. This correction is zero for the majority of the measurements, which were performed



(a) uncorrected



(b) corrected

Figure A.4: Original nondimensional pressure loss  $K_r$  vs number of ribs and the same result corrected for the pressure recovery when applicable, for a geometry with 25 mm pitch at  $Re_b = 1.65 \times 10^5$

with ribs located sufficiently far from the downstream pressure tap to fall outside the range for which the correction is required.

For the RL geometries ribs we applied no tap location correction. For these measurements the pressure tap was always located beyond the pressure-recovery region. The absence of discontinuous behaviour for all rounded data sets justifies this decision.



## Appendix B

# Overheating correction

For the case of a 45-mm pitch, measurements were performed before the overheating incident with 4, 5, 6 and 7 ribs, while measurements with 8, 9 and 10 ribs were performed afterwards.

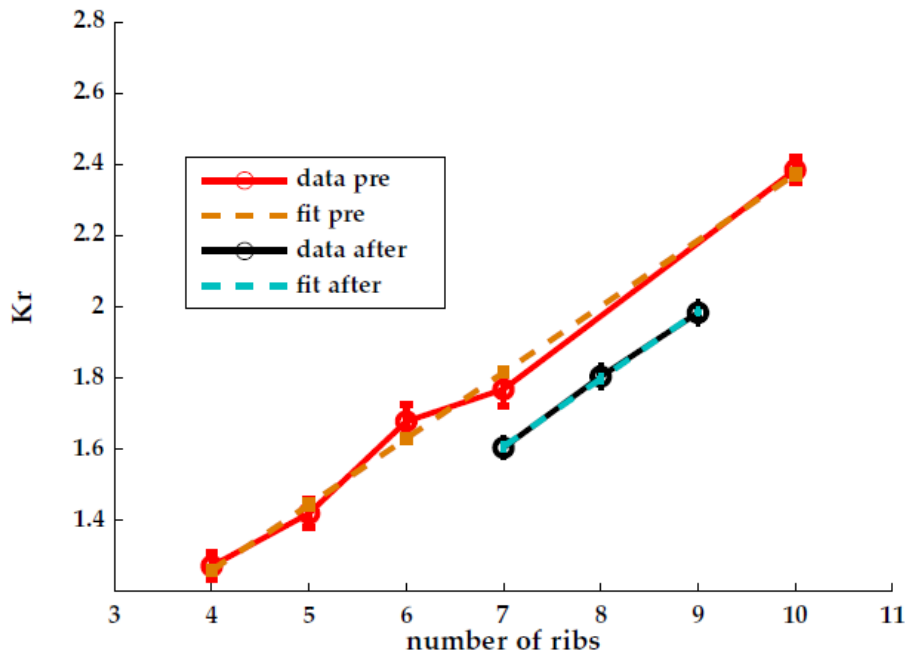


Figure B.1: Non-dimensional pressure loss  $K_r$  for  $p = 45$  mm before and after the overheating incident and subsequent adjustment of the outer rib diameter.

Without the incident, the obtained values of  $K_r$  for these points are expected to form a straight line, since the test section is long enough to include the same entrance and exit effects for all cases, as explained Section 2.4.

In Fig. B.1, it can be seen that there is a clear distinction between the measurements before (in red) and after (in black) the rib adaptation. However, the decrease in  $K_r$  and thus in pressure drop appears to be independent of the number of ribs in the test section. When fitting a line through both data sets, the slope is almost the same. This implies that the effect is limited to the first rib only, where the approaching flow has a relatively high velocity near the wall.

For the other geometries, i.e. other values for the pitch, no comparison as for  $p = 45$  mm is possible due to a lack of data either before or after the adaptation. However, the few single-point comparisons that could be made suggest a similar trend but with a decreasing absolute effect with decreasing pitch.

For the analysis of the data in this thesis, the absolute pressure loss over the ribbed test section is only an intermediate result. As long as the calculation of the pressure loss per rib ( $K_r'$ ) is not based on a mix of data before and after the adjustment of the ribbed section, the results can be interpreted equally. This has been done for all measurements reported throughout this thesis. No absolute correction is applied to the intermediate results for  $K_R$  or  $K_b$  (e.g Fig. 2.6).

## Appendix C

# Line fit method to the dynamic pressure spectrum

The power spectrum of the dynamic pressure, normalized with the bulk velocity  $V_r$  of the flow, is presented as a contour plot, with the colours representing the spectrum magnitude. Linear trends crossing the origin are clearly visible. In all plots, multiple lines can be distinguished, one of which is always in the very low frequency range (0-30 Hz).

The fact that a line crossing the origin is sought is used as input in the detection method. A discrete set of the possible line positions is transformed to binary matrices representing a small wedge in the direction of the line (see Fig. C.1a). Each wedge represents a specific linear trend of the frequency with respect to the bulk velocity. The binary image of each wedge is interpolated to the same grid as the spectrum (Fig. C.1b) and the result is multiplied with the normalized power spectrum (Fig. C.1d).

The values of the resulting matrix are summed, yielding a scalar value representing the correlation of the binary wedge with the contour plot. This scalar is plotted versus the wedge angle (Fig. C.2a). The peak values in this graph represent the angle at which the wedge corresponds to a linear trend in the contour graph. We apply this procedure to each geometry (EL,  $p = 15 - 55$ ), and calculate these peaks as a function of pitch (Fig. C.2). The results are further discussed in Section 2.7.2.

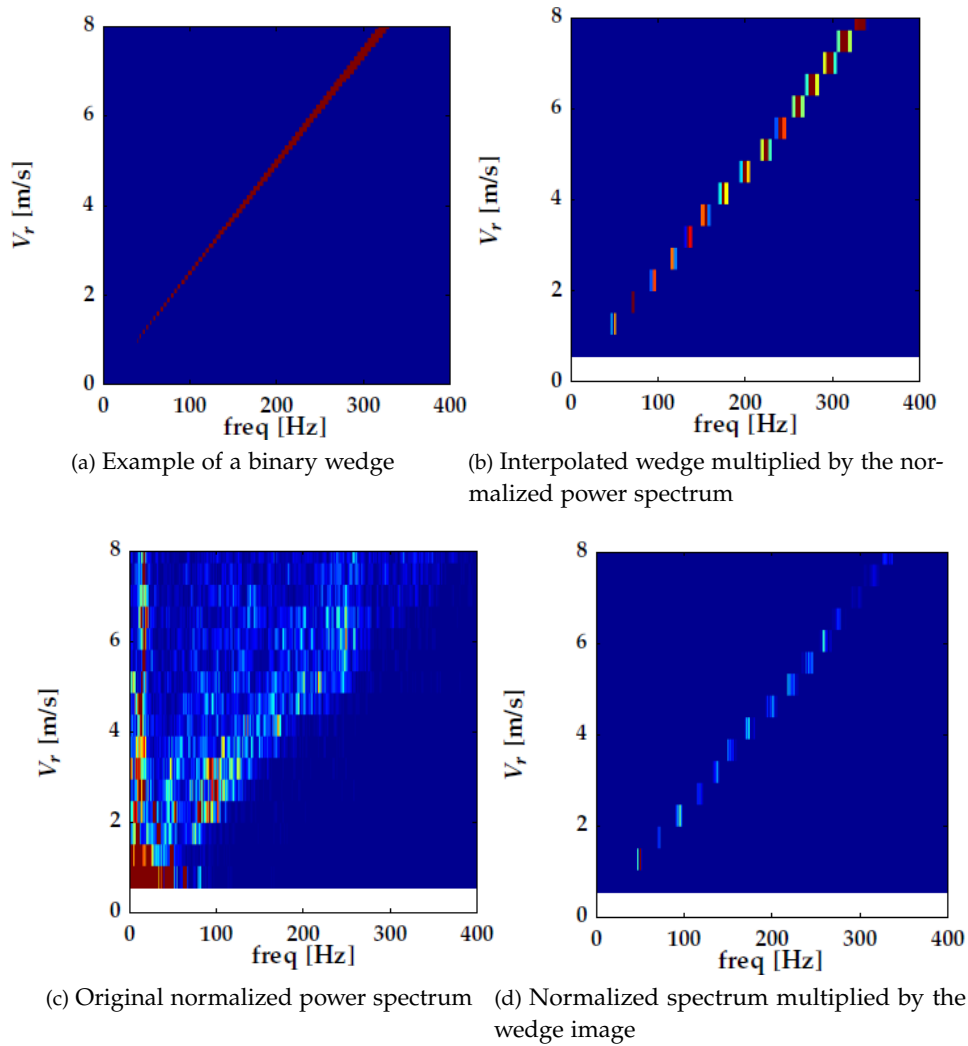
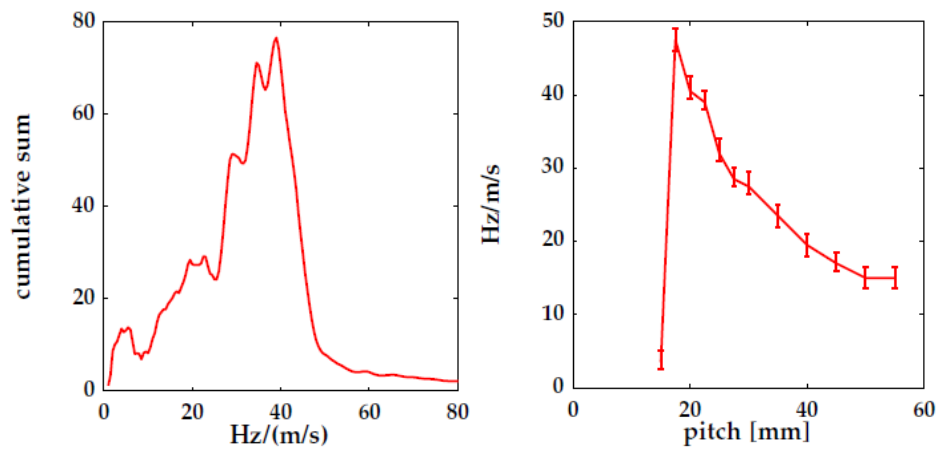


Figure C.1: Example of the line fit method to determine the harmonics in the dynamic pressure spectrum for  $p = 22.5$  mm.



(a) Correlation scalar versus linear trend of the spectrum for  $p = 22.5$  mm

(b) Peak location slope versus pitch

Figure C.2: Scalar describing the linear frequency trend ( $p = 22.5$  mm and peak of this function as a function of pitch.



# Bibliography

- R.J. Adrian. Hairpin vortex organization in wall turbulence. *Physics of Fluids*, 19 (041301):1–16, April 2007.
- R.J. Adrian and J. Westerweel. *Particle Image Velocimetry*. Cambridge University Press, 2011.
- R.J. Adrian, C.D. Meinhart, and C.D. Tomkins. Vortex organisation in the outer region of the turbulent boundary layer. *Journal of Fluid Mechanics*, 422:1–54, 2000.
- C.E. Brennen. *Cavitation and bubble dynamics*. Oxford University Press, 1995.
- N.D. Cardwell and P.P. Vlachos. Developing and fully developed turbulent flow in ribbed channels. *Experiments in Fluids*, 50:1357–1371, 2011.
- I.P. Castro. Rough-wall boundary layers: mean flow universality. *Journal of fluid mechanics*, 585:469–485, 2007.
- I.P. Castro. Turbulent flow over rough walls. In B. Eckhardt, editor, *Advances in Turbulence XII*. Springer-Verlag, 2009.
- H. Cheng, P. Hayden, A.G. Robins, and I.P. Castro. Flow over cube arrays of different packing densities. *Journal of Wind Engineering*, 95:715–740, 2007.
- D. Chisholm. *Two-phase flow in heat exchangers*. Longman Higher Education, 1983.
- O. Coceal, T.G. THomas, I.P. Castro, and S.E. Belcher. Mean flow and turbulent statistics over groups of urban-like cubical obstacles. *Boundary layer Meteorology*, 121:491–519, 2006.
- O. Coceal, A. Dobre, T.G. Thomas, and S.E. Belcher. Structure of turbulent flow over regular arrays of cubical roughness. *J. Fluid Mech*, 589:375–409, 2007.

- F. Colebrook, C. Turbulent flow in pipes, with particular reference to the transition region between the smooth and rough pipe laws. *Journal of the Institution of Civil Engineers*, 11:133,156, 1939.
- S.E. Coleman, V.I. Nikora, S.R. McLean, and E. Schlicke. Spatially averaged turbulent flow over square ribs. *Journal of Engineering Mechanics*, 133:194–204, 2007.
- J. Cui, V.C. Patel, and C.L. Lin. Large eddy simulation of turbulent flow in a channel with rib roughness. *International Journal of Heat and Fluid Flow*, 24: 372–388, 2003.
- H.A.R. De Bruin and C.J. Moore. Zero-plane displacement and roughness length for tall vegetation, derived from a simple mass conservation hypothesis. *Boundary-Layer meteorology*, 31:39–49, 1985.
- C.M. de Silva, N. Hutchins, and I. Marusic. Uniform momentum zones in turbulent boundary layers. *Journal of Fluid Mechanics*, 786:309–331, 2016.
- M. Fossa and G. Guglielmini. Pressure drop and void fraction profiles during horizontal flow through thin and thick orifices. *Experimental Thermal and Fluid science*, 26:513–523, 2002.
- J. Fröhlich, C.P. Mellen, W. Rodi, L. Temmerman, and A. Leschziner. Highly resolved large-eddy simulation of separated flow in a channel with streamwise periodic constrictions. *J. Fluid Mech*, 526:19–66, 2005.
- J. C. Han, L.R. Glicksman, and W.M. Rohsenow. An investigation of heat transfer and friction for rib-roughened surfaces. *International journal for heat and mass transfer*, 21:1143–1156, 1978.
- P.S. Jackson. On the displacement height in the logarithmic velocity profile. *Journal of Fluid Mechanics*, 111:15–25, 1981.
- W. Jianhua, A. Wanzheng, and Z. Qi. Head loss coefficient of orifice plate energy dissipator. *Journal of Hydraulic Research*, 48(4):526–530, 2010.
- J. Jiménez. Turbulent flows over rough walls. *Annual Review of Fluid Mechanics*, 36:173–196, 2004.
- R. Karwa, S.C. Solanki, and J.S. Saini. Heat transfer coefficient and friction factor correlations for the transitional flow regime in rib-roughened rectangular ducts. *International Journal of Heat and Mass transfer*, 42:1597–1615, 1999.
- P.K. Kundu and I.M. Cohen. *Fluid Mechanics*. Academic Press, 4th edition, 2008.

- P.K. Kundu, I.M. Cohen, and D.R. Dowling. *Fluid Mechanics*. Academic Press, 5th edition, 2012.
- J.H. Lee, H.J. Sung, and P. Krogstad. Direct numerical simulation of the turbulent boundary layer over a cube-roughened wall. *Journal of Fluid Mechanics*, 669: 397–431, 2011.
- S. Leonardi and I.P. Castro. Channel flow over large cube roughness: a direct numerical simulation study. *J. Fluid Mech.*, 651:519–539, 2010.
- S. Leonardi, P. Orlandi, and R.A. Antonia. Properties of d- and k-type roughness in a turbulent channel flow. *Physics of FLuids*, 19, 2007.
- O.I. Lyer and S.L. Ceccio. The influence of developed cavitation on the flow of a turbulent shear layer. *Physics of Fluids*, 14:3414–3431, 2002.
- E. Naudascher and D. Rockwell. *Flow induced vibrations: An engineering guide*. Dover Publications, 1994.
- F.T.M Nieuwstadt. *Turbulence, Introduction to theory and applications of turbulent flows*. Springer International Publishing, 2016.
- J. Nikuradse. Strömungsgesetze in rauhen rohren. *VDI-Forschungsheft*, 361, 1933. In translation, NACA TM 1292, 1950.
- A. E. Perry, W. H. Schofield, and P. N. Joubert. Rough wall turbulent boundary layers. *Journal of Fluid Mechanics*, 37(2):383–413, 1969.
- D. Pokrajac, L.J. Campbell, V. Nikora, C. Manes, and I. McEwan. Quadant analysis of persistent spatial velocity perturbation over square-bar roughness. *Experiments in Fluids*, 42:413–423, 2007.
- S. B. Pope. *Turbulent flows*. Cambridge University Press, 2000.
- D. Rockwell. Prediction of oscillation frequencies for unstable flow past cavities. *Journal of Fluids Engineering*, pages 294–299, 1977.
- D. Rockwell and E. Naudascher. Review-self-sustaining oscillations of flow past cavities. *Journal of Fluids Engineering*, 100:152–165, 1978.
- M.K. Roul and S.K. Dash. Numerical modeling of pressure drop due to single-phase flow of water and two-phase flow of air-water mixtures through thick orifices. *Int. Journal of Eng. Trends and Technology*, 3(4):544–551, 2012.

- D.N. Ryu, D.H. Choi, and V.C. Patel. Analysis of turbulent flow in channels roughened by two-dimensional ribs and three-dimensional block. part i: Resistance. *Int. Journal of Heat and Fluid Flow*, 28:1098–1111, 2007.
- H. Schlichting. *Boundary-Layer Theory*. McGraw-Hill Book company, 7th edition, 1979a.
- H. Schlichting. *Boundary-Layer Theory*, chapter XXb-XXc, pages 600–609. McGraw-Hill Book company, 7th edition, 1979b.
- H. Schlichting and K. Kersten. *Boundary-Layer Theory*. Springer, 8th edition, 2001.
- H. Tennekes and J.L. Lumley. *A first course int turbulence*. The MIT Press, 17th edition, 1999.
- R.G. Teyssandiert and M.P. Wilson. An analysis of flow through sudden enlargements in pipes. *Journal of Fluid Mechanics*, 64:85–95, 1974.
- R. Theunissen, F. Scarano, and M.L. Riethmuller. On improvement of piv image interrogation near stationary interfaces. *Experiments in Fluids*, 45:557–572, 2008.
- E. van Bokhorst and M. van Osch. Impact of boiling liquid on fluid-vapor-wall interaction in lng transfer systems. In *2nd Trondheim Gas Technology Conference*, 2011.
- J. van der Putte. corrugation profiles. Private communication, November 2015a.
- J. van der Putte. Results of water flow measurements on 4 inch lng transfer hoses. Private communication, November 2015b.
- L. Wang, J. Hejcik, and B. Sundén. Piv measurement of separated flow in a square channel with streamwise periodic ribs on one wall. *Journal of Fluids Engineering*, 129:834–841, 2007.
- L. Wang, M. Salewski, and B. Sundén. Turbulent flow in a ribbed channel: Flow structures in the vicinity of a rib. *Experimental Thermal and Fluid Science*, 34: 165–176, 2010.
- R.L. Webb. Heat transfer and friction in tubes with repeated-rib roughness. *International Journal for heat and Mass Transfer*, 14:601–617, 1971.
- J. Westerweel and F. Scarano. Universal outlier detection for piv data. *Experiments in Fluids*, 39:1096–1100, 2005.
- F.M. White. *Fluid mechanics*. McGraw-Hill, 6th edition, 2008.

